



**Institute for Space and
Nuclear Power Studies**



NEUP | Nuclear Energy
University Programs
U.S. Department of Energy



THE UNIVERSITY of
NEW MEXICO

Graphite Oxidation Simulation in HTR Accident Conditions – 3rd Year and Final Technical Report

Mohamed S. El-Genk, Jean-Michel Tournier and Boyce Travis

Institute for Space and Nuclear Power Studies

MSC01 1120

1 University of New Mexico, Albuquerque, NM 87131-0001

Technical Report ISNPS-UNM-1-2012*

Institute for Space and Nuclear Power Studies (ISNPS)

** Third Year and Final Technical Report for DOE NEUP Grant No. 00044825
00002, Project No. 09-830 to University of New Mexico.*

Project Title: Graphite Oxidation Simulation in HTR Accident Conditions

October 2012

EXECUTIVE SUMMARY

This project, started October 2009 and concluded September 2012, investigated the oxidation of nuclear graphite in Generation-IV, prismatic Very High Temperature and High Temperature gas cooled Reactors (VHTRs and HTRs) in the unlikely event of a massive air ingress accident. The completed research tasks include:

- (a) Developing and validating a modeling capability, based on chemical reactions kinetics, for the gasification rates of nuclear graphite as functions of temperature, oxygen partial pressure and fractional weight loss. The developed capability has been reported in both the 1st and 2nd year technical reports.
- (b) Developing and implementing a multi-parameter optimization algorithm for obtaining the chemical-reactions kinetics parameters of different grades of nuclear graphite from reported experimental measurements of transient weight loss and total gasification rate as functions of temperature. Results show excellent agreement of the predictions using the obtained chemical-reactions kinetics parameters with reported measurements for different grades of nuclear graphite. Most comparison results are included in the 2nd year technical report. Results of remaining comparisons are included in this report.
- (c) Comparing chemical-reactions kinetics parameters of nuclear graphite grades of IG-110, IG-430, NB-18, and NBG-25. These parameters include: (i) specific activation energies of adsorption of oxygen and desorption of CO gas and their Gaussian-like distributions and the corresponding rate constants; (ii) specific activation energy and the corresponding rate constant for the desorption of CO₂ gas; (iii) specific activation energy and corresponding rate constant for the formation of stable [CO] surface complexes; and (iv) initial surface area of free active sites. The values of the chemical reactions kinetics parameters are almost independent of the size of filler particles, but depend on materials of the particles. Nuclear graphite grades with petroleum coke filler particles (IG-100 and NBG-25), regardless of their size (medium of super fine), have similar chemical kinetics parameters. They are different from those of nuclear graphite grades with coal coke filler particles (IG-430 and NBG-18). The initial specific surface area of free active sites of nuclear graphite grades of IG-110, IG-430, NB-18, and NBG-25 decreases inversely proportional to square root of the initial mass of specimens in experiments (0.25 – 50 grams). Further work is needed to examine this finding for larger masses of nuclear graphite.
- (d) Developing a Sherwood number correlation for calculating the oxygen diffusion velocity in the boundary layer at high temperatures. At such temperatures, graphite gasification solely at the external surface is limited by oxygen diffusion in the boundary layer. At low and intermediate temperatures, gasification is controlled by the chemical-reactions kinetics and oxygen diffusion into the open volume pores. The correlation is based on an extensive database of measurements for forced-convection heat and mass transfer at $0.006 \leq Re \leq 2.42 \times 10^5$ and $0.68 < Sc < 2,000$ (Table 2.1), and the gasification of a V483T nuclear graphite cylinder (300 mm long and 200 mm in diameter) at 1141 to 1393 K in ascending cross-flow of nitrogen gas containing 5 vol. % oxygen, at $533 \leq Re \leq 1660$. The correlation is within $\pm 8\%$ of the compiled experimental database for laminar, turbulent and combined convection and the calculated total gasification fluxes based on this correlation are within $\pm 10\%$ of reported measurements for different size specimens of nuclear graphite grades of NBG-18, NBG-25, IG-11, IG-110, and IG-430.

- (e) Developing multi-dimensional readout tables of the gasification rates of different grades of nuclear graphite and a Generic Interface for coupling the gasification readout tables to 3-D thermal-hydraulics and mass diffusion capabilities in the Finite-Element code CD-Adapco STAR-CCM+, for transient gasification analysis of NBG-18 nuclear graphite in a helium coolant channel of a prismatic HTR or VHTR fuel element. Gasification results using STAR-CCM+ are successfully compared with those obtained using a developed multi-species diffusion and flow model on the Matlab®/Simulink® platform.
- (f) Demonstrating the usefulness of a developed model on the Matlab®/Simulink® platform for NBG-18 graphite gasification in 0.8 m long helium coolant channel in hexagonal fuel element of a VHTR or an HTR. The analyses use a Generic Interface to couple the multi-species diffusion and flow model in the coolant channel to the readout tables of the CO and CO₂ production fluxes as functions of temperature, oxygen partial pressure and weight loss fraction. The model handles up to 5 gaseous species in the bulk gas flow (He, N₂, O₂, CO and CO₂) and accounts for the heat released in the exothermic production of CO and CO₂ gases. Results include the local rise in graphite temperature, the local and total graphite weight loss and the productions of CO and CO₂ gases and the extent of gasification along the flow channel, as a function of the graphite initial temperature and that of the entering atmospheric air flow (800 K to 1100 K) and the air inlet Reynolds number (5 to 20). Results demonstrated the fidelity of interfacing the readout tables of graphite gasification with the multi-species diffusion and flow model and confirmed that the graphite local weight loss is non-uniform along the flow channel. The non-uniformity is caused by the increase in graphite local temperature due to the heat released by the exothermic production of CO and CO₂ gases, as well as the gradual depletion of oxygen in bulk gas flow along the channel. At high initial temperatures, graphite gasification is limited to a short section near the entrance of the channel due to the high local gasification rate and the fast depletion of oxygen in the bulk gas flow. Results clearly show that neglecting the heats of formation for CO and CO₂ gases significantly over estimates the total graphite loss in the helium flow channel.
- (g) Performing thermal-hydraulics analyses of a hexagonal fuel element with and without helium coolant bypass flow and of a full height VHTR 1/6th core by implementing a simplified methodology into STAR-CCM+ commercial software. This methodology markedly decreases the numerical meshing requirement and computation time without compromising the accuracy of the results. The simplified methodology couples a 1-D helium flow in coolant channels to 3-D heat conduction in the graphite and fuel compacts. The local heat transfer coefficient along the coolant channels is determined using a Nusselt number correlation developed and validated in the 2nd year technical report. The helium bypass flow cools the edges of the fuel element, but raises the temperature everywhere else in the elements. Results confirmed the fidelity and usefulness of the developed simplified methodology for future thermal-hydraulics analysis of VHTR or HTR cores.

The First Section of this report provides an introduction and the objectives of the work completed during the 3rd and Final Fiscal Year of this DOE-NEUP Contract. The details on the performed work and the obtained results are presented in Sections 2 – 6.

TECHNICAL TASKS AND SUMMARY OF COMPLETED WORK

Task (1): Develop a chemical kinetics model, with temperature-dependent material properties and chemical reaction database.

A Chemical reactions kinetics model for the gasification of graphite has been developed and validated with experimental results from the literature. The model includes only four chemical reactions for desorption of oxygen, formation of [CO] stable complexes, and desorption of CO and CO₂ gases. The results and details of the model development and validation and the methodology developed for determining the chemical kinetics parameters of the primary reactions as well as of the initial surface areas of active sites are included in the 1st Year Technical Report issued Oct. 2010 and in a Journal Article [M. S. El-Genk and J.-M. Tournier, “Development and Validation of a Model for the Chemical Kinetics of Graphite Oxidation,” *J. Nuclear Materials* **411**, 2011, 193 – 207].

Task (2): Implement developed model using Simulink solver and perform single effect analysis of graphite oxidation for different geometries and at different temperatures

Simulations of the gasification of NGB-18 nuclear graphite in a typical helium flow channel (80 cm long) with atmospheric air is performed using the chemical kinetics parameters obtained using the multi-parameter optimization algorithm developed and implemented successfully in Task (3). The gasification analysis is performed for air inlet Reynolds number of 5, 10 and 20 and initial graphite and inlet air temperatures from 800 K – 1100 K. The analysis accounts for the released heat of formation of the CO and CO₂ gases during graphite gasification and resulting increase in the surface temperature of the graphite sleeve. Completed work and results are included in the 3rd Year and Final Technical Report issued Oct. 2012.

Task (3): Perform model validation and benchmarking using reported experimental data for different graphite geometries at different temperatures and oxidant partial pressure.

We completed the validation of the model results with reported experimental measurements of the gasification rates for different grades of nuclear graphite at different temperatures and weight loss fractions. The model validation is complete for nuclear graphite grades: IG-110, IG-430, NBG-18 and NBG-25. The calculations compared well with the experimental measurements of the total gasification rate and transient weight loss reported by different researchers in Germany and the Republic of Korea. The reported measurements are for a wide range of temperatures that covers all three modes of graphite gasification, including the diffusion-limited mode at high temperatures. The experiments employed different sizes of the graphite test specimens.

The results on the model development and validation are included in the 2nd Year Technical Report issued Oct. 2011 and have been published in two recent Journal Articles and a conference Proceedings Article [M. S. El-Genk and J.-M. Tournier, “Comparison of Oxidation Model Predictions with Gasification Data of IG-110, IG-430 and NBG-25 Nuclear Graphite,” *J. Nuclear Materials*, **420**, 2012, 141 – 158; M. S. El-Genk and J.-M. Tournier, “Validation of an Oxidation Model for NBG-18 Nuclear Graphite,” *J. Nuclear Engineering and Design*, **250**, 2012, 142 –

155; and M. S. El-Genk and J.-M. Tournier, “Comparison of Gasification Kinetics Parameters of Different Types of Nuclear Graphite” *Proceedings of 12th International Congress on Advances in Nuclear Power Plants (ICAPP’12)*, **paper No. 12022**, Chicago, 24 – 28 June 2012].

For the diffusion-limited mode of graphite gasification, we developed a Sherwood number correlation for calculating the oxygen diffusion velocity through the boundary layer. The developed correlation is based on an extensive experimental database for laminar, combined and turbulent convection heat and mass transfer at Reynolds numbers from as low as 0.1 to $> 4 \times 10^4$. The correlation is within $\pm 8\%$ of the compiled experimental database comprising > 800 data points. It is also consistent with the reported gasification rate measurements in experiments with different grades of nuclear graphite. Two papers on this part of our research have been published in a recent Journal Article and a conference Proceedings Article [El-Genk, M. S. and J.-M. Tournier, “Sherwood Number Correlation for Nuclear Graphite Gasification at High Temperatures,” *J. Progress in Nuclear Energy*, **62**, 2013, 26 – 36; and M. S. El-Genk and J.-M. Tournier, “Diffusion Velocity Correlation for Nuclear Graphite Gasification at High Temperatures and Low Reynolds Numbers” *Proceedings of 12th International Congress on Advances in Nuclear Power Plants (ICAPP’12)*, **paper No. 12023**, Chicago, 24 – 28 June 2012].

Task (4): Identify suitable commercial CFD code (will likely be CD-adapco) and perform preliminary T-H analysis of HTR without graphite oxidation

In this task, we have developed an effective methodology for performing thermal-hydraulics analysis of prismatic core helium cooled reactors without graphite gasification. This methodology has been implemented successfully in STAR-CCM+ and the results are compared with those of a full 3-D analysis of a prismatic fuel element, with and without bypass helium flow and of a full height $1/6^{\text{th}}$ core. The developed methodology implemented in STAR-CCM+ commercial software results in significant savings in numerical meshing requirements and computation time compared to full 3-D thermal hydraulics analysis of a typical VHTR core. The details on the development and validation of the simplified methodology for thermal-hydraulics analysis are included in the 2nd Year Technical Report issued Oct. 2011 and published in a Journal Article and a conference Proceedings Article [B. W. Travis and M. S. El-Genk, “Numerical Simulation and Turbulent Convection Heat Transfer Correlation for Coolant Channels in a Very-High-temperature Reactor,” *J. Heat Transfer Engineering*, **34** (1). 2013, 1 – 14; and Travis, B. W. and M. S. El-Genk, “A Heat Transfer Correlation for Flow Channels in a Prismatic Core VHTR,” *Proceedings 15th International Conference on Emerging Nuclear Energy Systems (ICENES-2011)*, San Francisco, CA, 15 – 19 May 2011].

The results of validating the effectiveness of the developed computational methodology for performing the thermal-hydraulics analysis of a prismatic fuel element and a full height $1/6^{\text{th}}$ VHTR core are included in the 3rd Year and Final Technical Report issued Oct. 2012 and in a recent conference Proceedings Article [B. W. Travis and M. S. El-Genk, “An Effective Thermal-Hydraulics Methodology for Prismatic Core HTGR and VHTR,” *Proceedings of 12th International Congress on Advances in Nuclear Power Plants (ICAPP’12)*, **paper No. 12061**, Chicago, 24 – 28 June 2012].

Task (5): Develop and test a generic interface for coupling the developed graphite oxidation kinetics model to the STAR-CCM+

The developed Generic Interface couples the developed transient multi-species diffusion and flow model to the readout tables of the CO and CO₂ production fluxes as functions of temperature, oxygen partial pressure and weight loss fraction. This model's results are compiled into multi-columns readout tables every 10 K incremental rise for temperatures from 800 K to 1250 K and oxygen partial pressure every decade from 10⁻³ Pa to 10⁴ Pa, with additional values of 300 Pa, 3 kPa and 21.4 kPa. These results are for seven different fractions of graphite weight loss, $X = 0.0001, 0.01, 0.02, 0.04, 0.06, 0.08$ and 0.10.

These tables are generated using the chemical-reactions kinetics model that has been developed and validated in this research for the gasification of the different grades of nuclear graphite. Readout tables for gasification are generated for NBG-18 nuclear graphite, and also for NBG-110 nuclear graphite. As a prelude to testing the fidelity of coupling the readout tables to a codes such as STAR-CCM+ for conducting a safety analysis of a VHTR or HTR, we developed and investigated the robustness of interfacing the readout tables for NBG-18 with a model for graphite gasification in single flow channel of a typical VHTR hexagonal fuel element. This effort was completed successfully. Results demonstrated the use and implementation of a Generic Interface for coupling of the readout tables to the gasification model of an 80-cm long single channel using atmospheric air flow. The analysis has been carried out using the Matlab/Simulink Platform at air inlet Reynolds number = 5, 10 and 20 and temperatures from 800 K – 1100 K.

The model results of the values of the CO and CO₂ molar fluxes [mole/m².s] are collected into seven, 2-D readout tables of 46 x 11 elements, one table for each weight loss fraction. These 2-D readout tables are then loaded into a 3-D table block in Simulink with an index i corresponding to a temperature in [K], index j corresponding to a $\log_{10}(P_{O_2})$ in [Pa], and index k corresponding to a local weight loss fraction, X . Linear interpolation and extrapolation are used of the tabulated values in the 3-D readout table. Good interpolation and extrapolation accuracies are obtained using logarithmic values of the CO and CO₂ molar fluxes and of the oxygen partial pressure. The transient multi-species diffusion and flow model handles a bulk gas mixture of up to 5 species (He, N₂, O₂, CO and CO₂, $n = 5$) during the transient gasification along the graphite flow channel, with atmospheric air entering from the bottom. The channel is initially filled with helium at atmospheric pressure, prior to introducing the air flow.

At the start of the simulated gasification transient, $t = 0$, hydrodynamic conditions caused by purging the helium initially present in the flow channel with the introduced atmospheric air flow generate a sonic pressure wave. This wave, simulated using the ODE23s numerical solution technique of Matlab/Simulink, increases the CPU time. To accelerate transient calculations, a reflective impedance introduced at the exit of the channel effectively damped the sonic wave in less than 200 ms of real transient time. Beyond this short startup time, the reflective impedance is no longer needed, thus turned off. The time to fully purge the helium from the flow channel and replace it with air is in the tens of seconds, depending on the values of T_o and Re_{in} . For example, at $T_o = 900$ K and $Re_{in} = 20$, the air inlet velocity is 13 cm/s and a complete purging of the helium gas from the 80 cm-long flow channel, by the atmospheric air takes < 7s of real time, increasing to ~ 30s at $Re_{in} = 5$. This time is much smaller that the actual gasification time to reach 10% weight loss at the entrance of the simulated gasification of nuclear graphite in the flow channel. Such time

varies from a few to hundreds of hours, depending on the initial temperature and the air inlet Reynolds number.

The developed model accounts for the heat released in the production of CO and CO₂ gases at the surface of the graphite sleeve in the flow channel. The heat balance at the graphite surface comprises the enthalpies of formation of the CO and CO₂ gases, the convective heat transfer between the bulk gas flow and the surface of the graphite sleeve in the flow channel, and heat conduction in the graphite sleeve. The results show strong effect of the heats of reactions on the graphite gasification along the channel, thus they could not be neglected. The heats of reactions increase the local graphite temperature, which accelerates the gasification process. Once oxygen in the bulk gas mixture is depleted, the local graphite gasification ceases.

Results showed that the gasification rate and graphite temperature are not affected by increasing the number of radial numerical mesh elements in the graphite sleeve from 2 to 9. By contrast, the axial change in graphite temperature is large and increases with the time of gasification and the values of T_o and Re_{in} . In performed gasification transient, when the local weight loss at the entrance of the channel reaches 10% ($t = t_{10}$) the graphite local surface temperature is highest near the flow channel entrance and decreases rapidly with distance into the channel due to the depletion of oxygen in the bulk gas mixture and hence, the decrease in the local gasification rate. At an initial temperature of 1100 K, the local gasification rate is very high and oxygen in the channel is fully depleted within a small distance from the flow channel entrance, $z = 20$ cm.

The obtained results for the gasification of NBG-18 in the 80 cm-long flow channel of a prismatic VHTR include the values of t_{10} (time to reach 10% weight loss at the entrance of the flow channel) and the total graphite weight loss as functions of initial graphite and inlet air flow temperature, $T_o = 800 - 1100$ K, and the inlet air Reynolds number, $Re_{in} = 5, 10, \text{ and } 20$. When $T_o = 800$ K, $t_{10} = 159$ and 100 hrs at $Re_{in} = 5$ and 20, respectively. At an air inlet Reynolds number of 20, $t_{10} = 10$ hrs, when $T_o = 850$ K, and only 30 minutes, when $T_o = 1100$ K. When $T_o = 1000$ K, $t_{10} = 1.1, 1.5$ and 2 hrs for $Re_{in} = 20, 10$ and 5 respectively. When $T_o < 840$ K, graphite gasification is more uniform along the flow channel and t_{10} is almost independent of Re_{in} . The obtained transient results agree with those obtained in Task (6) using the commercial software package STAR-CCM+ until the oxygen in the bulk gas mixture flow is depleted. **The results of the work done in this task are detailed in the 3rd Year and Final Technical Report.**

Task (6): Couple the graphite oxidation model with STAR-CCM+ and perform analysis of air ingress event for a prismatic core HTR

The coupling of the readout tables of graphite gasification is being exercised to demonstrate the fidelity of the coupling process to the STAR-CCM+ Code. Results for a single flow channel in a VHTR or HTR prismatic fuel element are compared successfully to those obtained using the transient gasification model on the Simulink platform in Task (5). The objective of this task was not to carry out a full accident analysis, but rather demonstrate the coupling of the readout tables to STAR-CCM+ code, which could be duplicated by the users of other reactor safety codes for conducting future analysis of a VHTR in case of an air ingress accident.

To demonstrate the proper implementation of the User Code Field Functions, the identical geometry of the flow channel of NBG-18 graphite, simulated in the Matlab/Simulink model in Task (5) is modeled in 3-D in STAR-CCM+ Code. Three different numerical mesh grids are

developed and implemented into the numerical analysis to examine the effects on the solution convergence and the accuracy of the results.

Because the GUI in some CFD codes such as STAR-CCM+ is not capable of loading multidimensional arrays (2-D or 3D) or readout tables, a subroutine is developed in C programming language to perform the linear interpolation and extrapolation on the weight loss fraction. This is based on using seven individual 2-D readout tables. This subroutine also performs linear interpolation and extrapolation on temperature and oxygen partial pressure in each 2-D table. The STAR-CCM+ code requires loading 7 individual 2-D tables for the CO₂ gas mass flux, and another 7 for the CO gas mass flux. When results from the C subroutines developed in this task are compared to those using a single 3-D readout table in Simulink, the differences in the gasification results are insignificantly small. The subroutines are loaded as User Code Field Functions in STAR-CCM+ to calculate the mass fluxes of CO, CO₂ and O₂ at the surface of the graphite sleeve in the NBG-18 flow channel at various conditions. The results of the STAR-CCM+ gasification model are in excellent agreement with the transient results obtained in Task (5) above, until the oxygen in the bulk gas mixture is fully depleted or a 10% weight loss is achieved at the entrance of the graphite channel. Results are compared for different initial graphite and inlet air temperatures, T_o , and air inlet Reynolds number, Re_{in} , of 5, 10, and 20. Details and results of the work carried out under this task are included in the 3rd Year and Final Technical Report.

TABLE OF CONTENT

EXECUTIVE SUMMARY	II
TECHNICAL TASKS AND SUMMARY OF COMPLETED WORK	IV
LIST OF FIGURES	XII
LIST OF TABLES	XVIII
LIST OF TABLES	XVIII
1. INTRODUCTION	1
2. SHERWOOD NUMBER CORRELATION FOR NUCLEAR GRAPHITE GASIFICATION AT HIGH TEMPERATURE	1
2.1 DIFFUSION-LIMITED GASIFICATION OF NUCLEAR GRAPHITE	6
2.2 DEVELOPED SHERWOOD NUMBER CORRELATION	8
2.2.1 <i>Comparison with other Sherwood number correlations</i>	12
2.2.2 <i>Application to nuclear graphite gasification</i>	14
2.3 SUMMARY	18
2.4 NOMENCLATURE	20
3. VALIDATION OF GASIFICATION MODEL FOR NBG-18 NUCLEAR GRAPHITE	22
3.1 NUCLEAR GRAPHITE OXIDATION MODEL.....	22
3.1.1 <i>Elementary reactions in chemical kinetics model</i>	23
3.1.2 <i>Specific activation energies</i>	26
3.1.3 <i>Oxygen diffusion velocity</i>	26
3.1.4 <i>Oxidation model input parameters</i>	28
3.2 OXIDATION EXPERIMENTS OF NBG-18 NUCLEAR GRAPHITE	30
3.2.1 <i>Test specimens</i>	30
3.2.2 <i>Effective surface area in experiments</i>	32
3.3 MODEL VALIDATION FOR NBG-18 NUCLEAR GRAPHITE	35
3.3.1 <i>Reported measurements by Chi and Kim (2008)</i>	37
3.3.2 <i>Reported measurements by Hinssen et al. (2008)</i>	37
3.4 PARAMETRIC ANALYSES.....	39
3.4.1 <i>Effects of temperature and oxygen partial pressure</i>	39
3.4.2 <i>CO and CO₂ production rates</i>	43
3.4.3 <i>Total gasification rate</i>	45
3.5 SUMMARY	47
3.6 NOMENCLATURE	49

4. CHEMICAL KINETICS PARAMETERS OF NUCLEAR GRAPHITE GASIFICATION ...	51
4.1 CHEMICAL-REACTION KINETICS MODEL PARAMETERS	52
4.2 GASIFICATION EXPERIMENTS	53
4.3 CHEMICAL KINETICS PARAMETERS	58
4.4 MICRO-STRUCTURAL PARAMETERS	63
4.5 EFFECT OF GRAPHITE MASS	66
4.6 EFFECT OF GRAPHITE MASS ON TOTAL GASIFICATION RATE	67
4.7 SUMMARY	72
4.8 NOMENCLATURE	74
5. TRANSIENT GASIFICATION OF NBG-18 NUCLEAR GRAPHITE IN A VHTR FLOW CHANNEL.....	75
5.1 GEOMETRY AND PROBLEM STATEMENT	79
5.2 READOUT TABLES OF NBG-18 GASIFICATION	82
5.3 MULTI-SPECIES DIFFUSION AND FLOW MODEL	83
5.3.1 <i>Governing equations</i>	84
5.3.2 <i>Solution implementation</i>	88
5.4 GASIFICATION RESULTS AND DISCUSSION	90
5.4.1 <i>Graphite gasification</i>	93
5.4.2 <i>Production of CO and CO₂ gases</i>	95
5.4.3 <i>Effects of Re_{in} and T_o</i>	96
5.5 COUPLING OF GASIFICATION MODEL WITH STAR-CCM+ CFD CODE.....	101
5.5.1 <i>3-D and 2-D numerical mesh grids considered in STAR-CCM+</i>	101
5.5.2 <i>Implementation of gasification model in STAR-CCM+</i>	103
5.5.3 <i>Comparison of Matlab/Simulink and STAR-CCM+ results</i>	106
5.6 SUMMARY	110
5.7 NOMENCLATURE	112
6. THERMAL-HYDRAULICS ANALYSES OF 1/6 PRISMATIC VHTR CORE AND OF FUEL ELEMENT WITH BYPASS FLOW	114
6.1 NUMERICAL ANALYSIS	119
6.1.1 <i>Numerical meshing approach</i>	121
6.1.2 <i>Material properties</i>	124
6.1.3 <i>Thermal-hydraulics analysis conditions</i>	124
6.2 RESULTS AND DISCUSSION	125
6.2.1 <i>Fuel element analysis without a bypass flow</i>	128
6.2.2 <i>Effects of helium bypass flow and heat generation in burnable poison rods</i>	128
6.2.3 <i>Thermal-hydraulics analysis of a full height 1/6th core</i>	136
6.3 SUMMARY	140
6.4 NOMENCLATURE	142

7. SUMMARY AND CONCLUSIONS.....	143
8. REFERENCES	145
APPENDIX A – PUBLICATIONS BASED ON COMPLETED RESEARCH.....	152
A-1. REFEREED JOURNAL PAPERS	152
A-2. REFEREED CONFERENCE PROCEEDINGS PAPERS	152
A-3. CONFERENCE PROCEEDINGS PAPERS	153
A-4. TECHNICAL REPORTS	153

LIST OF FIGURES

Chapter 2:

Figure 2.1.	Gasification Modes of Nuclear Graphite in Different Temperature Ranges.	2
Figure 2.2.	Developed Sherwood Number Correlation for Laminar Convection ($0.006 < Re < 1,000$).	9
Figure 2.3.	Developed Sherwood Number Correlation for Turbulent Convection ($2 \times 10^4 < Re < 2.42 \times 10^5$).	9
Figure 2.4.	Sherwood Number Correlation for Entire Range of the Compiled Database.	11
Figure 2.5.	Sherwood Number Ratio in the Laminar, Combined and Turbulent Convection Regimes.	11
Figure 2.6.	Comparison of Present Sh Correlation with those of Hilpert (1933) and McAdams (1954).	13
Figure 2.7.	Comparison of Present Sh Correlation with Graetz Solution for Laminar Flow. ...	13
Figure 2.8.	Comparison of the Calculated and Measured Diffusion-limited Gasification Fluxes for Different Grades of Nuclear Graphite.	16

Chapter 3:

Figure 3.1.	Determined Specific Activation Energy Distributions for NBG-18 Nuclear Graphite Test Specimens. (a) Adsorption; (b) Desorption.	25
Figure 3.2.	Estimates of Oxygen Diffusion Velocities in NBG-18 Nuclear Graphite Experiments.	27
Figure 3.3.	Comparison of Model Results with Reported Measurements for NBG-18 in the Experiments of Chi and Kim (2008): (a) Transient Weight Loss; (b) Transient Gasification Rate; (c) Arrhenius Curve of Total Gasification Rate.	33
Figure 3.4.	Comparison of Model Results with Reported Measurements for NBG-18 in the Experiments of Chi and Kim (2008); (a) Weight Loss Fraction; (b) Total Gasification Rate.	34
Figure 3.5.	Comparison of Model Results of the Total Gasification Rate with Reported Measurements for NBG-18 in the Experiments of Hinssen et al. (2008): (a) Specimen 1 (*); (b) Specimen 2 (†); (c) Specimen 3 (⊥).	36
Figure 3.6.	Comparison of Model Results with Reported Total Gasification Rates for NBG-18 Test Specimens in the Experiments of Hinssen et al. (2008) in Dry Air.	38
Figure 3.7.	Model Predictions of Gasification Rate for NBG-18 Test Specimens of Chi and Kim (2008).	40

Figure 3.8.	Calculated Time to Reach a Given Weight Loss for NBG-18 Test Specimens of Chi and Kim (2008).....	40
Figure 3.9.	Calculated Time to Reach 40% Weight Loss for the NBG-18 Test Specimens of Chi and Kim (2008).....	41
Figure 3.10.	Results of Effect of Temperature on Weight Loss of NBG-18 Test Specimens of Chi and Kim (2008): (a) $P_{O_2} = 21$ kPa; (b) $P_{O_2} = 2.1$ kPa.....	42
Figure 3.11.	Results of Effects of Temperature and P_{O_2} on the CO_2 Production Rate for NBG-18 Nuclear Graphite Specimens.....	44
Figure 3.12.	Results of Effects of Temperature and P_{O_2} on the CO Production Rate for NBG-18 Nuclear Graphite Specimens.....	44
Figure 3.13.	Results of Effects of Temperature and P_{O_2} on the Total Gasification Rate for NBG-18 Nuclear Graphite Specimens.....	46

Chapter 4:

Figure 4.1.	Gaussian-like Distributions of the Specific Activation Energies for Adsorption of Oxygen for Different Grades of Nuclear Graphite (<i>Numbers in Parentheses Refer to the Specimen Numbers Listed in Table 4.2</i>).....	56
Figure 4.2.	Gaussian-like Distributions of Specific Activation Energies for Desorption of CO Gas for Different Grades of Nuclear Graphite. (a) IG-110 and NBG-25; (b) IG-430 and NBG-18 (<i>Numbers in Parentheses Refer to the Specimen Numbers Listed in Table 4.2</i>).	57
Figure 4.3.	Gaussian-Distribution Most Probable Specific Activation Energies. (a) For Adsorption of Oxygen; (b) For Desorption of CO Gas (<i>Numbers in Parentheses Refer to the Specimen Numbers Listed in Table 4.2</i>).....	59
Figure 4.4.	Standard Deviations of Specific Activation Energies for the Gasification of Different Grades of Nuclear Graphite. (a) Adsorption of Oxygen; (b) Desorption of CO Gas (<i>Numbers in Parentheses Refer to the Specimen Numbers Listed in Table 4.2</i>).	60
Figure 4.5.	Specific Activation Energies for Forming Stable (CO) complexes and for Desorption of CO_2 for Different Nuclear Graphite Grades (<i>Numbers in Parentheses Refer to the Specimen Numbers Listed in Table 4.2</i>).....	61
Figure 4.6.	Chemical Kinetics Rate Constants k_a^o for Adsorption of Oxygen and k_b^o for Forming Stable (CO) Complexes (<i>Numbers in Parentheses Refer to the Specimen Numbers Listed in Table 4.2</i>).	61
Figure 4.7.	Chemical Kinetics Rate Constant k_d^* for Desorption of CO_2 (<i>Numbers in Parentheses Refer to the Specimen Numbers Listed in Table 4.2</i>).....	62

Figure 4.8.	Chemical Kinetics Rate Constant for Desorption of CO Gas during Gasification of Different Grades of Nuclear Graphite (<i>Numbers in Parentheses Refer to the Specimen Numbers Listed in Table 4.2</i>).....	62
Figure 4.9.	Size and Shape of Nuclear Graphite Specimens in Gasification Experiments of Kim, Lee and No (2006), Fuller and Okoh (1997), Chi and Kim (2008) and Hinssen <i>et al.</i> (2008).	64
Figure 4.10.	Effect of ASA_0 on Gasification Rate after 5 Hours at 873 K for Different Grades of Nuclear Graphite (<i>Numbers in Parentheses Refer to the Specimen Numbers Listed in Table 4.2, and Other Numbers Refer to the Graphite Specimens in Figure 4.9</i>).....	65
Figure 4.11.	Specific Area of Free Active Sites, s_m^o as a Function of Specimen Mass, for Different Grades of Nuclear Graphite.	65
Figure 4.12.	Comparison of Reported Measurements with Present Calculations of the Total Gasification Rates from Different Grades of Nuclear Graphite. Calculations Use Recommended Chemical-Reaction Kinetics Parameters in Table 4.3 and Eqs. (4.2) and (4.3) for s_m^o	68
Figure 4.13.	Calculated Arrhenius Curves of the Total Gasification Rate in Flowing Atmospheric Air for Different Graphite Grades and Initial Masses. (a) IG-110 Nuclear Graphite; (b) NBG-18 Nuclear Graphite.	69

Chapter 5:

Figure 5.1.	A Cut-away View in a Prismatic Core VHTR (McDonald et al., 2004).	76
Figure 5.2.	Transverse Cross-sectional View of a Prismatic Fuel Assembly or Element.	77
Figure 5.3.	VTHR or HTR TRISO Fuel Particle, Fuel Compact and Prismatic Assemblies (INL, 2007).....	77
Figure 5.4.	Comparison of Model Results with Reported Measurements for NBG-18 in the Experiments of Chi and Kim (2008): (a) Transient Weight Loss; (b) Transient Gasification Rate; (c) Arrhenius Curve of Total Gasification Rate.....	78
Figure 5.5.	Single-Channel Fuel Module and Equivalent Graphite Annulus in a Prismatic VHTR or HTR Fuel Assembly.....	80
Figure 5.6.	Cross-Sectional Views of a Flow Channel and Equivalent NBG-18 Graphite Sleeve.	81
Figure 5.7.	Block-Diagram of Multi-Species Transient Flow and Diffusion Model Developed Using the Matlab/Simulink® Platform.	83
Figure 5.8.	Computational Grid for the Gasification of NBG-18 Nuclear Graphite in a Single Channel of a VHTR or HTR Prismatic Fuel Assembly.	89

Figure 5.9.	Calculated Graphite Local Loss along the Flow Channel at Different Times in the Gasification Transient.....	91
Figure 5.10.	Axial Distribution of Oxygen Partial Pressure in Flow Channel in the Gasification Transient.....	91
Figure 5.11.	Axial Distributions of Graphite Surface Temperature and Bulk Gas Temperature in the Gasification Transient.....	92
Figure 5.12.	Axial Distribution of Gasification Flux in Flow Channel in the Gasification Transient.....	92
Figure 5.13.	Transient CO ₂ and CO Total Productions and Production Ratio in Gasification Transient.....	94
Figure 5.14.	Effects of T_o and Re_{in} on Graphite Total Loss versus Gasification Time in a Flow Channel of a Prismatic VHTR or HTR Fuel Assembly.....	97
Figure 5.15.	Dependence of Gasification Time to Reach 10% Weight Loss at Channel Entrance, t_{10} , on both T_o and Re_{in}	97
Figure 5.16.	Effects of T_o and Re_{in} on Graphite Total Loss and Gasification Time, t_{10}	98
Figure 5.17.	Effects of Heats of Formation of CO and CO ₂ Gases on the Graphite Total Loss and Gasification Time, t_{10}	99
Figure 5.18.	Effects of T_o and Re_{in} on Axial Distributions of Graphite Loss and Temperature Rise along the Flow Channel.....	100
Figure 5.19.	View of 2-D Numerical Mesh Grid Used in the Transient Analysis of the Gasification of an Axi-Symmetric NBG-18 Graphite Sleeve in CD-Adapco STAR-CCM+.....	102
Figure 5.20.	Block-Diagram of Multi-Species Transient Flow and Diffusion Model and Gasification Generic Interface Developed on CD-Adapco STAR-CCM+.....	104
Figure 5.21.	Effect of Weight Loss on Axial Distribution of Oxygen Concentration in Flow Channel during Gasification at 950 K.....	107
Figure 5.22.	Axial Distribution of Weight Loss in Flow Channel during Gasification at 950 K.....	107
Figure 5.23.	Effect of Weight Loss on Axial Distributions of Oxygen, CO and CO ₂ Mass Fractions during Gasification at 950 K.....	108

Chapter 6:

Figure 6.1.	TRISO Particle, Fuel Compact, and a Prismatic Fuel Element or Assembly (Kiryushin et al., 1997; MacDonald et al., 2003; Schultz et al., 2004).	116
Figure 6.2.	A Quadrant of a Prismatic VHTR Core (Kiryushin et al., 1997; MacDonald et al., 2003; LaBar et al., 2004; Schultz et al., 2004).	117

Figure 6.3.	Cross-Sectional View of a VHTR Prismatic Fuel Element Showing the Burnable Poison Rods, a Single Flow Channel Model, Fuel Compacts, and Standard and Small Helium Coolant Flow Channels.....	119
Figure 6.4.	Radial and Axial Cross-Sectional Views of Numerical Mesh Grid Used in the Full 3-D Thermal-Hydraulics Analysis of a Prismatic VHTR Fuel Element.....	120
Figure 6.5.	A Close-Up of the Implemented Numerical Mesh Grid in a Prismatic VHTR Fuel Element with a Helium Bypass Flow.....	122
Figure 6.6.	Radial Cross-Sectional View of the Numerical Mesh Grid Used in the Thermal-Hydraulics Analysis of a Full Height 1/6 Core.....	123
Figure 6.7.	Calculated Temperature Contours in the Fuel Element Without Bypass Helium Flow, 4 cm above Bottom.	126
Figure 6.8.	Calculated Temperature Contours in the Fuel Element without Bypass Flow, 4 cm above Bottom.....	127
Figure 6.9.	Calculated Transverse Temperature Fields, 55 cm from the Top of the Prismatic Fuel Element, with and without Bypass Flow and for Different Heating Rates of the Corner Poison Rods.....	129
Figure 6.10.	Calculated Radial Temperature Distributions along the 0° Coordinate in Fuel Element with 100% Power in Burnable Poison Rods, with and without Bypass Flow (55 cm from Top of Element).	131
Figure 6.11.	Calculated Radial Temperature Distributions along the 0° Coordinate in Fuel Element with 25% Power in Burnable Poison Rods, with and without Bypass Flow (55 cm from Top of Element).	131
Figure 6.12.	Calculated Radial Temperature Distributions along the 0° Coordinate in Fuel Element without Bypass Flow, but Different Powers in the Burnable Poison Rods (55 cm from Top of Element).	132
Figure 6.13.	Calculated Radial Temperature Distributions along the 30° Coordinate in Fuel Element with and without Bypass Flow and Different Powers in the Burnable Poison Rods (55 cm from Top of Element).....	132
Figure 6.14.	Calculated Temperatures Using a Full 3-D Analysis of a Prismatic Fuel Element with Helium Coolant Bleed Flow (3% of Total) in the Control Rod Channel (at 20 and 55 cm from Entrance).	134
Figure 6.15.	Calculated Temperatures Using the Simplified Methodology and a Full 3-D Analysis of a Prismatic Fuel Element with Helium Coolant Flow (3% of Total) in Control Rod Channel (at 55 cm from Entrance).	134
Figure 6.16.	Calculated Temperatures Using the Simplified Analysis Methodology of a Prismatic Fuel Element with Helium Flow in the Control Rod Channel and Interstitial Bypass Flow (at 55 cm from Entrance).	135

Figure 6.17. Calculated Radial Temperature Field at Mid-Plane in the Thermal-Hydraulics Analysis of a Full Height VHTR 1/6 Core with Constant Volumetric Heat Generation in Fuel Compacts, and No He Bypass Flow. 137

Figure 6.18. Calculated Axial Temperature Distributions in the Thermal-Hydraulics Analysis of a Full Height VHTR 1/6 Core with Constant Volumetric Heat Generation and No Helium Bypass Flow..... 138

LIST OF TABLES

Table 2.1.	Compiled Database for Laminar, Combined and Turbulent Convection Regimes...5	
Table 2.2.	Test Conditions and Setups of the Gasification Experiments that Used Test Specimens of Different Grades of Nuclear Graphite.15	
Table 3.1.	Setups and Conditions in the Experiments of NBG-18 Nuclear Graphite Gasification (Chi and Kim, 2008; Hinssen et al., 2008).29	
Table 3.2.	Determined Kinetics and Micro-Structural Parameters for NBG-18 Nuclear Graphite Specimens in Gasification Experiments (Chi and Kim, 2008; Hinssen et al., 2008).31	
Table 4.1.	Test Conditions and Setups in Reported Gasification Experiments of Nuclear Graphite (Chi and Kim, 2008; Fuller and Okoh, 1997; Hinssen <i>et al.</i> , 2008).....54	
Table 4.2.	Kinetics and Micro-Structural Parameters for Different Grades of Nuclear Graphite.55	
Table 4.3.	Recommended Oxidation Kinetics Parameters for Different Grades of Nuclear Graphite.64	
Table 5.1.	Recommended Oxidation Kinetics Parameters for Different Grades of Nuclear Graphite (El-Genk and Tournier, 2012c).82	
Table 6.1.	Material Properties Used in the Thermal-Hydraulics Analysis (Travis and El-Genk, 2013) (the Temperature, T is in Kelvin).118	
Table 6.2.	Parameters Used in the Thermal-Hydraulics Analysis of a Full Height 1/6 Core.124	

1. INTRODUCTION

A massive air or steam ingress in High Temperature Reactors (HTRs), nominally operating at 600 – 950°C (McDonald et al., 2003; LaBar et al., 2004; INL, 2007) is a design-basis accident requiring the development and validation of graphite oxidation and erosion models. Such models are important for assessing the impact on the potential fission products release from the coated TRISO fuel particles, predict the rates of erosion and assess the integrity of the graphite core and reflector blocks as well as the supporting graphite columns in the lower plenum of prismatic core HTRs. Some studies have shown that a graphite burn-off of only 10% could decrease its structural strength by as much as 50% (Fuller and Okoh, 1997; Kim et al., 2008). Nuclear graphite materials share many similarities but also differences in the microstructure, volume porosity, impurities, type and size of filler coke particles, graphitization and heat treatment temperatures, and the thermal and physical properties (El-Genk and Tournier, 2011). These as well as the temperature and oxygen partial pressure strongly affect the oxidation kinetics and the gasification rate of graphite.

Several graphite oxidation models and simulation approaches, with varying degrees of sophistication, have been reported for investigating the graphite oxidation during air and steam ingress accidents in HTRs (Takeda, 2004; Li and No, 2006; Kim et al., 2008; Yu et al., 2008). These models typically use empirical correlations for determining the local gasification rate of the graphite and predicting the gaseous product fractions. The empirical relationships use constant values of the activation energy and oxidation coefficient determined based of a best fit of the experimental data. However, this straightforward approach does not give insight into the various physical processes taking place and not monitored in the experiments.

The nature and progression of graphite oxidation are quite complex. They primarily depend on the temperature, the partial pressure of oxidant and the availability of active sites for oxidation and surface complexes, which change with burn off, the type of graphite, and other coupled transport processes. As a result, accurate predictions of the graphite oxidation rates remain a challenge. Modeling graphite oxidation is further complicated by the changes in the microstructure and volume pores, the surface active sites and complexes with time, temperature and the partial pressure of oxidants. A key factor adding to the complexity of graphite oxidation, which should be accounted for in the models is that activation energies of the surface free active sites and complexes are not constant but have Gaussian-like distributions. Such distributions could be directly measured in the experiments or deduced from experimental measurements of the gasification rate and the CO/CO₂ ratio using an error minimization algorithm (El-Genk and Tournier, 2011 and 2012a).

In the 1st year technical report (Technical Report No. ISNPS-UNM-1-2011, by M. S. El-Genk and J.-M. Tournier) of this project, an extensive review of the literature on graphite oxidation was performed, and a phenomenological chemical-reactions oxidation kinetics model was developed and benchmarked with oxidation data of thin films of pyrolytic graphite. The literature review of more than 500 technical papers and reports covered: (a) the manufacturing, microstructure and properties of nuclear graphite materials; (b) the oxidation processes and kinetics of graphite; (c) the available experimental data for benchmarking the graphite oxidation model; and (d) the approaches reported by various organizations for simulating the oxidation of coal char and nuclear graphite materials.

The developed chemical-reactions kinetics model in this work uses 4 elementary chemical reactions and Gaussian-like distributions of the activation energies for the adsorption of the surface free active sites and for the desorption of dissociated surface oxygen complexes (El-Genk and Tournier, 2011 and 2012a). It tracks the changes in the surface active sites, the graphite weight loss and the generation rates of CO and CO₂ with time, temperature and oxygen partial pressure. A multi-parameter optimization algorithm is developed and used to obtain the oxidation kinetics parameters and activation energy distributions from the reported experimental measurements of the gasification rates and the CO/CO₂ ratio (El-Genk and Tournier, 2011 and 2012a). The applicability of this optimization technique was demonstrated in the 1st year technical report using the detailed experimental data of Ahmed and Back for the oxidation of thin-films of pyrolytic graphite in oxygen at different temperatures. An advantage of those experiments is that the Active Surface Area (ASA) of the graphite samples was measured, and reported as a function of weight loss in the experiments. After incorporating the kinetics parameters obtained from the optimization algorithm, the developed graphite oxidation model successfully predicted the effects of temperature and oxygen partial pressure on the measured gasification rate, the CO / CO₂ production ratio, transient weight loss and absorbed oxygen surface complexes (El-Genk and Tournier, 2011).

During the 2nd Fiscal Year of this project (Technical Report No. ISNPS-UNM-1-2012, by M. S. El-Genk, J.-M. Tournier and B. Travis), the phenomenological, chemical-reactions oxidation kinetics model of graphite was benchmarked successfully with the reported gasification data for nuclear graphite grades of IG-110, IG-430 and NBG-25. The values and distributions of the specific activation energies for adsorption and desorption, the values of the pre-exponential rate coefficients for the four elementary chemical reactions and the surface area of free active sites of the graphite specimens were obtained from the reported measurements using a multi-parameter optimization algorithm (El-Genk and Tournier, 2011 and 2012a). At high temperatures, when gasification is diffusion limited, the model calculates the diffusion velocity of oxygen in the boundary layer using a semi-empirical correlation developed for air flows at Reynolds numbers ranging from 0.001 to 100 (Chapter 2 in this report). The model also accounts for the changes in the external surface area, the oxygen pressure in the bulk gas mixture and the effective diffusion coefficient in the boundary layer with weight loss. The model results of the total gasification rate and weight loss with time in the experiments agreed well with the reported measurements for the three types of nuclear graphite investigated at temperatures from 723 – 1226 K and weight loss fractions up to ~ 0.86 (El-Genk and Tournier, 2011 and 2012a).

The good agreement between the results of the developed chemical-reactions kinetics model and the experimental data strongly suggests that the phenomenological approach of predicting the gasification rate of nuclear graphite is more realistic than the empirical approach currently being used, with predictably important consequences to the safety analysis of High Temperature Gas-cooled Reactors (VHTRs and HTRs) in the unlikely event of an air ingress accident. This phenomenological approach provides thermodynamic information and intrinsic properties of nuclear graphite not reported in experiments, beyond the perimeter of a particular set of experimental conditions. It is worth noting, however, that despite the good agreement between the model results and the reported measurements, the accuracy of the calculated oxidation kinetics parameters for input to the present model would certainly be affected by the experimental uncertainties. These uncertainties stem from the inherent in-homogeneities in the porous graphite microstructure, impurities, method of cutting and preparing the test specimens, the differences in

the initial value of the ASA and its change with weight loss, and the experimental measurements of the gasification rate, flow rate and temperature. For better characterization of the reactivity of nuclear graphite, future work may include performing well-controlled desorption experiments to measure the ASA and both the values and the Gaussian-like distributions of the specific activation energies of adsorption and desorption for the different types of nuclear graphite, and provide detailed and specific experimental uncertainties.

In addition to the development and validation of the chemical-reactions kinetics model for nuclear graphite gasification, multi-dimensional readout tables of the production rate of CO and CO₂ gases during the gasification of different grades of nuclear graphite are developed. Generic interfaces are also developed for coupling these tables to a multi-species flow and diffusion model as well as to the STAR-CMM+ finite element commercial software, during the gasification of a typical helium coolant channel in a prismatic fuel element. The results are reported in Chapter 5 of this report.

Owing to the complexity and massive reactor core structure, a full core analysis requires extensive and massively parallelized computation capabilities and a relatively long time (weeks to months) to complete. These demanding requirements are mostly due to the 3-D computational fluid dynamics (CFD) simulation of the helium flow in the 10-m long channels in the reactor core. In the 2nd year technical report (Technical Report No. ISNPS-UNM-1-2012, by M. S. El-Genk, J.-M. Tournier and B. Travis), the results of 3-D numerical thermal-hydraulics code were reported (Travis and El-Genk, 2013). In this effort, a turbulent convection heat transfer correlation was developed to be used as a surrogate of full 3-D computational fluid dynamics (CFD) numerical calculations for helium coolant flow in channels of a prismatic core HTGR or VHTR. The correlation calculates the local heat length, and is developed based on the results of a 3-D thermal-hydraulics numerical analysis of a prismatic core hexagonal fuel module with a central flow channel. The heated flow channel is 1.5875 cm in diameter and 8.0 m high. In addition, the flow channel extends 1.2 m and 0.8 m into unheated top and bottom graphite reflector blocks, for a total length of 10 m. Results showed that flow mixing in the entrance region increases the local turbulent heat transfer coefficient, but its effect diminishes after a distance $z/D > 25$ into the heated section. The developed correlation is within $\pm 2\%$ of the 3-D numerical results for both uniform and chopped-cosine axial power profiles. It is comparable to those reported in the literature based on experimental measurements of the local heat transfer coefficient for gas flows in uniformly heated tubes, including entrance flow mixing (Taylor, 1967; Travis and El-Genk, 2013).

Results reported in the 2nd year technical report showed that using a simplified numerical approach that involves 3-D conduction in the graphite and fuel compacts and 1-D simulation of the helium flow in the coolant channel effectively decreases the total computation time and simplifies the meshing requirements with little effect on the accuracy of the numerical results. This simplified approach eliminates the meshing in the flow channel and determines the local heat transfer coefficient using the correlation previously developed. The simplified numerical approach runs ~ 40 times faster than the full 3-D simulation of the single channel module. The effectiveness of this simplified numerical approach for modeling a full prismatic fuel elements with and without helium bypass flow and of a full height (10 m) VHTR core is examined during the 3rd year of this project and the obtained results are detailed in Chapter 6 of this report.

The specific technical tasks completed during the 3rd year of this project and reported in the following section of this report are to:

- (a) Develop a semi-empirical Sherwood number correlation to calculate the oxygen diffusion velocity through the boundary layer at the external surface of graphite during gasification at high temperature, at which graphite gasification is limited by the oxygen diffusion through the surface boundary layer. Also implement this correlation into the chemical-reactions kinetics model developed during the 2nd year of the project for the gasification of nuclear graphite grades of IG-110, IG-430, NB-18 and NB-25 (El-Genk and Tournier, 2012a, 2012b, 2012c);
- (b) Compare the obtained chemical reaction kinetics parameters for the gasification of the above grades of nuclear graphite and recommend values for use in future safety analysis;
- (c) Perform transient gasification of NBG-18 nuclear graphite with atmospheric air in a 0.8-m long coolant channel of a VHTR prismatic fuel assembly as a function of initial graphite/air inlet temperature and inlet air Reynolds number. This analysis uses a developed Generic Interface to couple a Matlab/Simulink multi-species diffusion and flow model in the coolant channel to the developed readout tables of the CO and CO₂ production fluxes as functions of temperature, oxygen partial pressure and weight loss fraction. The readout tables are generated using the developed chemical-reactions kinetics model during the 2nd year of this project.
- (d) Demonstrate the implementation of a Generic Interface for coupling the gasification readout tables to the 3-D thermal-hydraulics and mass diffusion capabilities in CD-Adapco STAR-CCM+ commercial software, and perform transient gasification analysis of NBG-18 nuclear graphite flow channel; and
- (e) Perform thermal-hydraulics analyses of a hexagonal fuel element with and without helium coolant bypass flow and of a full height VHTR 1/6th core by implementing the developed simplified numerical simulation methodology, developed during the 2nd year of this project (Technical Report No. ISNPS-UNM-1-2012, by M. S. El-Genk, J.-M. Tournier and B. Travis), into STAR-CCM+ commercial software.

The details of these tasks and the obtained results are presented in Chapters 2 through 6. A summary is provided at the end of each Chapter as well as in Chapter 7 for the whole report. A separate nomenclature list is provided at the end of each chapter. A compiled reference list is provided at the end of the report.

2. SHERWOOD NUMBER CORRELATION FOR NUCLEAR GRAPHITE GASIFICATION AT HIGH TEMPERATURE

High-Temperature and Very High Temperature Gas-cooled Reactor (HTGR and VHTR) designs are being developed for generating electricity, at high thermal efficiency close to 50%, and the co-generation of heat for the thermo-chemical production of hydrogen fuel and a host of other industrial applications. These reactors employ nuclear graphite in the active core and the axial and radial neutron reflector regions. The circulated helium gas at high pressure of 4 – 7 MPa removes the fission heat generated in the reactor core and exits at ~ 600 – 650°C in HTGRs and 850 – 900°C in VHTRs (INL, 2007).

The safety analysis of HTGRs and VHTRs in the unlikely event of massive air ingress accident requires accurate estimates of the gasification rates and erosion of nuclear graphite components in the core, reflector and of the massive graphite support columns in the lower plenum. In such an event, gasification within the volume pores of the support columns could compromise their mechanical strength and possibly result in a collapse of the reactor core. A weight loss of as little as 10% could reduce the mechanical strength of nuclear graphite by about 50% (Fuller and Okoh, 1997; Kim et al., 2008). The ingress of air into the reactor core flow channels and subsequent weight loss or erosion of nuclear graphite could expose coated fuel particles and release the fission products trapped in the graphite surrounding the particles. Owing to the complexity of the chemical kinetics and the inherent coupling of the processes involved in the gasification of nuclear graphite, reliable estimates of the rates would be required as functions of the total flow, pressure and Re of the bulk gas-air mixture, the oxygen partial pressure and the temperature and dimensions of the nuclear graphite structure.

Gasification models reported for predicting the gasification of different nuclear graphite grades comprise Arrhenius relations of the total gasification rate in terms of the reciprocal of the graphite temperature and apparent activation energies and pre-exponential rate coefficients determined from the empirical fits of experimental measurements for small graphite specimens.

While easy to implement, this empirical approach is limited to the experimental conditions and temperatures for determining the apparent activation energies and the pre-exponential coefficients from the total gasification rate measurements. Such an approach offers little insight into the kinetics of the chemical reactions taking place and could not be used to calculate the production rates of CO and CO₂ gases nor their relative contributions to the total gasification. In addition, the large variances in reported values by different investigators of the apparent activation energy and pre-exponential coefficient in the Arrhenius rate relations, even for the same nuclear graphite grade, result in a wide range of gasification rate predictions (Kim et al., 2008; Xiaowei et al., 2004; Yu et al., 2008; Takeda, 2004; Lim and No, 2006). And since the prevailing gasification mode of the porous nuclear graphite strongly depends on temperature and Reynolds number, the values of the apparent activation energy and pre-exponential coefficients are different in different temperature ranges. This causes discontinuities at the transition among the different modes of graphite gasification (Fig. 2.1).

To avoid the inherent limitations of the empirical approach, a chemical-reaction kinetics model has recently been introduced and successfully used for calculating the gasification rates of different grades of nuclear graphite in atmospheric air over a wide range of temperatures. The model calculations have been in good agreement with the reported measurements of the total gasification rates and transient weight loss in experiments of various grades of nuclear graphite

(El-Genk and Tournier, 2011 and 2012a). The experiments used different size specimens of graphite grades NBG-18, NBG-25, IG-11, IG-110 and IG-430 (Fuller and Okoh, 1997; Xiaowei et al., 2004 and 2005; Hinssen et al., 2008; Chi and Kim, 2008; Growcock et al., 1980).

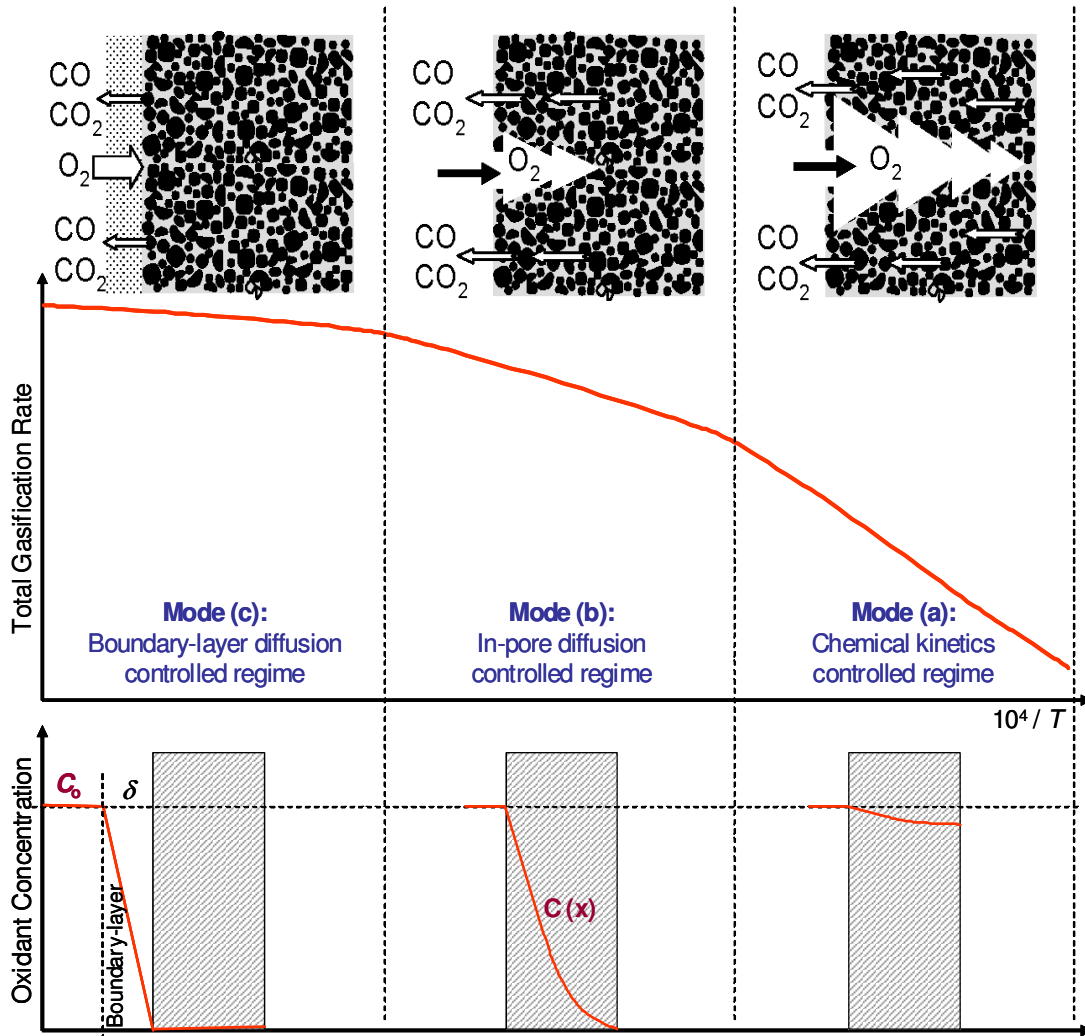


Figure 2.1. Gasification Modes of Nuclear Graphite in Different Temperature Ranges.

In addition to the microstructure and fabrication method of nuclear graphite, gasification rates partially depend on the average size of the open volume pores, the total volume porosity, and the amount of impurities that would act as catalysts for gasification, and temperature. Below 673 K, graphite gasification is insignificantly small. At temperatures up to 950 K, depending on the conditions of the bulk gas mixture and the nuclear graphite grade, gasification is mostly uniform inside the open volume pores, gradually weakening the structural strength with increased weight loss. At higher temperatures, the graphite gasification ceases within the open volume pores and shifts to corroding the external surface.

The gasification model recently developed by the authors (El-Genk and Tournier, 2011 and 2012a) employs the chemical kinetics rate and pre-exponential coefficients of four elementary reactions. These are the chemisorption of oxygen molecules to form oxygen radicals at active sites; the dissociation and adsorption of oxygen radicals to form stable complexes; the stable complexes desorption to produce CO gas; and the desorption of CO₂ gas. This model uses Gaussian-like distributions of the specific activation energies for adsorption of oxygen and desorption of CO gas, and the initial surface area of free active sites. A multi-parameters optimization algorithm (El-Genk and Tournier, 2012a) determines these quantities from reported experimental measurements of the transient weight loss and total gasification rate for the different grades of nuclear graphite at different temperatures. The model also accounts for the change in the surface area of free active sites with weight loss (El-Genk and Tournier, 2011 and 2012a). The most active sites are located at the edge positions in the basal planes of the hexagonal graphite crystals. They are abundant in the interior of the open volume pores, but relatively sparse at the external surfaces. The surface area of the active free sites, which is different for the different grades of nuclear graphite, increases with weight loss and peaks at a value of 30 – 40%.

Employing the chemical-reaction kinetics model (El-Genk and Tournier, 2011 and 2012a), instead of the empirical approach, will predictably have important consequences for the safety analysis of VHTRs and HTGRs. The model calculates the total gasification rate and the transient weight loss of graphite and the production rates of CO and CO₂ as functions of the total pressure, composition and flow rate of the bulk gas mixture, the oxygen partial pressure and the temperature, geometry and dimensions of the graphite structure. Although all or some of these quantities could be measured in the gasification experiments, others are difficult to measure directly but could be estimated reasonably accurately by the model based on the reported measurements of the total gasification rate and transient weight loss (El-Genk and Tournier, 2011 and 2012a). Examples are the surface area of the active free sites with weight loss, the fractional coverage of active free sites with surface complexes as a function of temperature and oxygen partial pressure, and the progressive transition in the total gasification rate among the three principal modes with increased temperatures (Fig. 2.1).

Graphite gasification generally proceeds in three successive processes (El-Genk and Tournier, 2011 and 2012a). These are: (a) the diffusion of oxygen to the external surface and deep into the open volume pores; (b) the adsorption of oxygen onto the surface active free sites and the simultaneous formation of C-O bonds and break up of C-C bonds; and (c) the desorption of CO and CO₂ gaseous products and their transport to the bulk gas flow. Below 673 K, graphite gasification is negligible, but, the rate increases exponentially with increased temperature. The three primary modes of graphite gasification with increasing temperature are shown in Fig. 2.1 (Walker, Jr. et al., 1959; Fuller and Okoh, 1997; Xiaowei et al., 2004; El-Genk and Tournier, 2012a; Ogawa, 1987) and discussed briefly next.

Mode (a): This mode may extend to 900 K, or even higher, depending on the gas flow rate and the total and oxygen partial pressures. In this in-pores chemical kinetics controlled mode, the rate of graphite gasification increases exponentially with increased temperature (Fig. 2.1). The gasification occurs solely inside the open volume pores within the solid graphite structure, thus does not change the outside dimensions. For the reactor safety analysis following an unlikely air ingress accident, graphite gasification in this mode degrades the mechanical strength of the graphite components in the reactor core and the lower plenum. The weight loss in the volume

pores progressively increases their sizes and the access to previously closed pores, further weakening the mechanical strength of the graphite structure. The weight loss in these pores decreases almost exponentially with distance from the external surface (Hinssen et al., 2008; Growcock et al., 1980). Therefore, in practice, mode (a) does not exist alone by itself, but in combination with the in-pores diffusion controlled Mode (b) (Fig. 2.1).

Mode (b): This mode begins to influence graphite gasification at temperatures as low as 900 K and may extend to 1123 K, depending on the gas flow rate and Reynolds number and both the total and oxygen partial pressures. Although in this mode graphite gasification still mostly occurs within the open volume pores, oxygen diffusion into these pores becomes increasingly limited with increased temperature (Fig. 2.1). This is because of the consumption of oxygen and increase in the counter-diffusion of the gasification products of CO and CO₂ gases (Fig. 2.1). Despite the exponential increase in the rates of the chemical reactions for the graphite gasification with increasing temperature, the limited oxygen penetration into the volume pores in mode (b) reduces the increase in the gasification rate with increasing temperature below that in mode (a) (Fig. 2.1). With a further increase in temperature, graphite gasification within the volume pores eventually ceases and shifts to the external surface, marking the transition to mode (c). This transition from the in-pores diffusion controlled mode (b) to the diffusion-limited mode (c) occurs gradually with increased temperature (Fig. 2.1). Thus, within the transition temperature range both modes co-exist but with different proportions.

Mode (c): This mode begins to erode the external surface of the graphite components at temperatures as low as 973 K and becomes the dominant mode of gasification at temperatures > 1123 K. This depends on the flow rate and Reynolds number of the bulk gas mixture as well as its total pressure and the oxygen partial pressure. At low values of Re, this mode begins to affect the graphite gasification at relatively lower temperatures than at high Reynolds numbers. A low Re does not necessarily mean lower gas flow rate but could also arise from the small length scale of the graphite component or the dimensions of the graphite test specimens used in gasification experiments. Examples are the experiments of Hinssen et al. (2008) and Xiaowei et al. (2004 and 2005) using dry air at almost the same total pressure and the oxygen partial pressure. The airflow rate in the experiments of Hinssen et al. (2008) was 0.125 SLPM and the used graphite test specimens were 8.0 mm in diameter and 2.69 mm high. Xiaowei et al. (2004 and 2005) used a much lower airflow rate of 0.021 SLPM and larger graphite specimens, 10 mm in diameter and 10 mm high. In these experiments (Xiaowei et al., 2004 and 2005; Hinssen et al., 2008), because the inlet air Re was so low, mode (c) began to affect the total gasification rate at temperatures as low as 973 K. Increasing the air Re via increasing its flow rate would delay mode (c) to higher temperatures, as in the gasification experiments of Chi and Kim (2008).

In mode (c), graphite gasification occurs at the external surface, thus changes the dimensions of the graphite components by erosion, thus it would not affect the mechanical strength of the graphite components. In this mode, it is not the chemical-reactions kinetics, but rather the diffusion of oxygen from the bulk gas mixture to the surface through the boundary layer that limits the gasification rate of the graphite (Fig. 2.1). The oxygen diffusion velocity in the boundary layer depends on Re, Sc, the total pressure of the bulk gas mixture and the oxygen partial pressure both in the bulk gas mixture and at the external surface of the graphite. Thus, in this diffusion-

limited mode of graphite gasification, it is important to determine the velocity or Sh for the oxygen diffusion through the boundary layer, which is the focus of this Chapter.

Table 2.1. Compiled Database for Laminar, Combined and Turbulent Convection Regimes.

Reference	Fluid	Setup	D (mm)	T_b (°C)	T_w (°C)	Re^a	Pr or Sc^a	# data
Ogawa (1987)	Nitrogen-5 vol% oxygen ^c	V483T graphite cylinder	200	875 – 1100	893 – 1100	533, 904, 1660	~ 0.71	3
Collis and Williams (1959)	Air @ 1 bar	Platinum wires	0.003, 0.009, 0.0535	20	49, 207, 313	0.006 – 144	0.68 – 0.70	109
Davis (1924)	Water @ 1 bar	Platinum wire	0.204	11	17, 31, 46	19.8 – 240	4.0 – 7.4	13
Davis (1924)	Paraffin oil	Platinum wires	0.152, 0.204	11, 17.6	16 – 68	6.7 – 120	16.7 – 35.2	20
Fand (1965)	Water @ 1 bar	Electrically heated tube	11.112	26.7	29 – 32.2	30,600 – 63,300	5.3 – 5.6	4
Hatton et al. (1970)	Air @ 1 bar	Electrically heated tubes	0.813, 1.257	20	50 – 220	16 – 46	0.68 – 0.70	24
Hilpert (1933)	Air @ 1 bar	Electrical wires	0.0198 – 1.0	20	100	2.2 – 1,604	0.692	75
Hilpert (1933)	Air @ 1 bar	Steam-heated tubes	2.99 – 150	20	100	530 – 2.42 x 10 ⁵	0.692	54
Hughes and Coy (1916)	Air @ 1 bar	Steam-heated Cu tubes	4.3 – 50.6	15	100	780 – 4 x 10 ⁴	0.693	104
Kennelly and Sanborn (1914)	Air @ up to 4 bars	Platinum wire	0.114	18.5 (1, 2, 2.8, 3.5 and 4 bars)	410, 557	11.7 – 243	0.683 – 0.691	107
King (1914)	Air @ 1 bar	Platinum wires	0.153, 0.0283	15.3	227 – 1,004	0.06 – 40.3	0.68 – 0.72	109
Piret et al. (1947)	Water @ 1 bar	Platinum and nickel wires	0.0254	25 – 53	31 – 102	0.2 – 4.2	1.7 – 5.2	46
Powell (1940)	Water vaporization in air ^b	Heated, water-saturated cyl.	1.6, 7.8, 19, 34, 60	19	29	72 – 10,000	0.609	36
Reiher (1925)	Air @ 1 bar	Liquid-cooled tubes	4.6 – 28	253	25	820 – 10,600	0.708	39
Vogtländer & Bakker (1963)	Electrolyte ^b	Mass transfer Pt electrodes	0.516 – 1.001	NA	NA	4.8 – 77	1,300 – 2,000	64

(a) Properties evaluated at wall temperature, T_w .

(b) Mass transfer experiments.

(c) Nuclear graphite gasification experiments.

One objective of this work is to develop a semi-empirical correlation for Sh that is applicable to the gasification of nuclear graphite in mode (c), in terms of both Re and Sc of the bulk gas mixture. The correlation could be used to calculate the oxygen diffusion velocity through the boundary layer in mode (c) (Xiaowei et al., 2004 and 2005; Hinssen et al., 2008; Chi and Kim, 2008; Ogawa, 1987). An experimental database (Table 2.1) is compiled of the reported measurements of the convective heat transfer coefficient for heated wires and cylinders of different diameters in air, water and paraffin oil flows at $0.006 \leq Re \leq 2.42 \times 10^5$, and $0.068 \leq Pr \leq 35.2$, and the mass transfer coefficient at $4.8 \leq Re \leq 10^4$ and Sc of 0.609 and 1,300 - 2,000.

The compiled experimental database also includes the reported average Sh values for the gasification of a cylinder of V483T nuclear grade graphite (300 mm long and 200 mm in diameter at 1141 to 1393 K in ascending cross-flow of nitrogen gas containing 5 vol. % oxygen at $533 \leq Re \leq 1660$ (Ogawa, 1987). The developed Sh correlation in this work is based on the compiled 807 data points for internal and external parallel and cross flow conditions.

The reported measurements at high temperatures of the total gasification rate in experiments with relatively small specimens of nuclear graphite are used to validate the developed Sh correlation for calculating the oxygen diffusion velocity in the chemical-reaction kinetics model (El-Genk and Tournier, 2012a). The model calculations of the total gasification rate are compared with the reported experimental measurements for different size specimens of nuclear graphite grades NBG-18 and NBG-25, IG-11, IG-110 and IG-430 in atmospheric air flow at $0.08 \leq Re \leq 30$ (Xiaowei et al., 2004 and 2005; Hinssen et al., 2008; Chi and Kim, 2008). It is worth noting that the developed Sh correlation, although applicable to internal flow and to external parallel and cross-flow conditions, is practically limited to temperatures < 1400 K. At such temperatures, the contributions on the erosion of the graphite external surface of the Boudouard reaction and of the CO/O₂ homogeneous reaction in the boundary layer are negligible.

The next section presents the implemented approach in the chemical-reaction kinetics model (El-Genk and Tournier, 2012a) for calculating the diffusion velocity of oxygen through the surface boundary layer during the gasification of nuclear graphite in the diffusion-limited mode (c) (Fig. 2.1).

2.1 DIFFUSION-LIMITED GASIFICATION OF NUCLEAR GRAPHITE

In the diffusion-limited gasification mode (c) of nuclear graphite at high temperatures (Fig. 2.1), the rate of oxygen consumption is expressed as (El-Genk and Tournier, 2012a):

$$\dot{R}_{O_2} = (A_w \sqrt{1-X}) k_m \times ([\hat{O}_2]_b - [\hat{O}_2]_w). \quad (2.1)$$

In this expression, $\sqrt{1-X}$ accounts for the decrease in geometrical surface area or erosion of the external surface area with weight loss fraction, X , for graphite cylindrical components or test specimens in the gasification experiments. The terms $[\hat{O}_2]_b$ and $[\hat{O}_2]_w$ are the average oxygen concentrations in the bulk gas mixture and at the graphite external surface, respectively; and k_m is the oxygen diffusion velocity through the boundary layer. The consumption rate of oxygen on the left-hand-side of Eq. (2.1) is sum of the rates of the elementary reactions in the chemical kinetics model for graphite gasification (El-Genk and Tournier, 2011 and 2012a). These are of the adsorption of oxygen atoms onto surface active sites to form un-dissociated C(O₂) surface complexes and of the desorption of CO₂ gas, as:

$$\dot{R}_{O_2} = \sum_i \dot{R}_{a,i} + \sum_{ij} \dot{R}_{CO_2,ij} . \quad (2.2)$$

In Eq. (2.1), the oxygen diffusion velocity in the boundary layer is expressed in terms of Sh as:

$$k_m = \text{Sh} \times D_{O_2,m} / D . \quad (2.3)$$

The values of Sh and $D_{O_2,m}$ depend on the flow conditions, properties, and the composition of the bulk gas mixture. The effective diffusion coefficient of oxygen in the boundary layer, $D_{O_2,m}$, is calculated using the first-approximation of the molecular theory of gases at low pressure (Hirschfelder et al., 1954). For a 3-component gas mixture (O_2 , N_2 and CO), the effective diffusion coefficient is given as:

$$D_{O_2,m} = \frac{1 - x_{O_2}}{x_{N_2} / D_{O_2,N_2} + x_{CO} / D_{O_2,CO}} . \quad (2.4a)$$

In this equation, the sum of molar fractions of the species in the bulk gas is unity (i.e., $x_{O_2} + x_{N_2} + x_{CO} = 1$), and the binary diffusion coefficients are calculated as (Hirschfelder et al., 1954):

$$D_{A,B} = \frac{3}{8\sqrt{2\pi}} \sqrt{\frac{1}{M_A} + \frac{1}{M_B}} \left(\frac{(R_g T)^{1.5}}{N_a P_{tot} \sigma_{AB}^2 \Omega^{(1,1)*}} \right) . \quad (2.4b)$$

The force constants are: $\sigma_A = 3.433 \times 10^{-10}$ m and $\varepsilon_A / k = 113$ K for the oxygen molecules, $\sigma_B = 3.681 \times 10^{-10}$ m and $\varepsilon_B / k = 91.5$ K for the nitrogen molecules, and $\sigma_B = 3.59 \times 10^{-10}$ m and $\varepsilon_B / k = 110$ K for the CO gas molecules. The collision integral is a function of the dimensionless temperature (kT/ε_{AB}), and the interaction force constants, σ_{AB} and ε_{AB} are given as (Hirschfelder et al., 1954):

$$\sigma_{AB} = (\sigma_A + \sigma_B) / 2 , \text{ and } \varepsilon_{AB} = \sqrt{\varepsilon_A \varepsilon_B} . \quad (2.5)$$

In the diffusion-limited mode (c) of nuclear graphite gasification at high temperatures (Fig. 2.1), other investigators (Takeda, 2004; Lim and No, 2006; Kakaç and Yener, 1995; Kim and No, 2006) used Graetz's solution (Kakaç and Yener, 1995) that is based on the similarity of heat and mass transfer to calculate Sh and hence, the oxygen diffusion velocity, k_m through the surface boundary layer. The Graetz's solution has been developed for laminar gas flow through uniformly heated tubes. It expresses the average Sh over the tube length, H as (Kakaç and Yener, 1995):

$$\text{Sh}_L = 3.66 + \frac{0.0668 \times (D/H) \text{Re Sc}}{1 + 0.04 \times [(D/H) \text{Re Sc}]^{2/3}} . \quad (2.6)$$

This expression indicates that at low Re values, Sh is constant and equal to 3.66, markedly over-predicting the oxygen diffusion velocity in the nuclear graphite gasification experiments of Xiaowei et al. (2004 and 2005), Hinssen et al. (2008), and Chi and Kim (2008) in which $\text{Re} \sim 0.1, 0.7$ and 30 , respectively. In order to match the measurements in these experiments of the total gasification rates in mode (c) for nuclear graphite grades IG-110, NBG-25, NBG-18 and IG-430 (Chi and Kim, 2008), a Sh that is $\sim 30\%$ lower than that given by Eq. (2.6) had to be used.

Similarly in order to match the reported total gasification rate measurements in mode (c) for nuclear graphite grades NBG-18 (Hinssen et al., 2008) and IG-11 (Xiaowei et al., 2004 and 2005), the oxygen diffusion velocity had to be an order of magnitude lower than that given by Eq. (2.6). Kim and No (2006) had to use a lower oxygen diffusion velocity than that based on Eq. (2.6) in order to match the total gasification rate measurements in their experiments with IG-110 nuclear graphite specimens.

These findings, confirming the inadequacy of the Graetz's expression in Eq. (2.6) for calculating the oxygen diffusion velocity in mode (c), motivated the need in the present work to develop a more applicable Sh correlation. The next section presents and discusses the Sh correlation developed in this work for determining the oxygen diffusion velocity to accurately calculate the gasification rate of nuclear graphite at high temperatures in mode (c) (Fig. 2.1).

2.2 DEVELOPED SHERWOOD NUMBER CORRELATION

An extensive database of 807 experimental data points is compiled. It includes experimental results for forced convection heat transfer coefficient for heated wires and cylinders of different diameters in air, water and paraffin oil flows at $0.006 \leq Re \leq 2.42 \times 10^5$ and $0.068 \leq Pr \leq 35.2$, and for forced mass transfer coefficient at $4.8 \leq Re \leq 10^4$ and Sc of 0.609 and 1,300 – 2,000 (Table 2.1) (Collis and Williams, 1959; Davis, 1924; Fand, 1965; Hatton et al., 1970; Hilpert, 1933; Hughes and Coy, 1916; Kennelly and Sanborn, 1914; King, 1914; Piret et al., 1947; Powell, 1940; Reiher, 1925; Vogtländer and Bakker, 1963). The forced convection heat transfer coefficient data points in the compiled database include the experimental results reported by Collis and Williams (1959), Hatton et al. (1970), Hilpert (1933), Hughes and Coy (1916), King (1914) and Reiher (1925) for atmospheric airflow. The database also includes the experimental results reported by Kennelly and Sanborn (1914) for airflows at pressures up to 4 bars, by Davis (1924), Fand (1965) and Piret et al. (1947) for water flow and those of Davis (1924) for paraffin oil flow. The mass transfer experiments involved water vaporization from heated, water-saturated cylinders in air (Powell, 1940) at $72 \leq Re \leq 10^4$, and mass transfer between platinum electrodes in sodium hydroxide electrolytes with ferri- and ferro-cyanides (Vogtländer and Bakker, 1963) at $4.8 \leq Re \leq 77$ (Table 2.1). In addition, the compiled database includes three values of the average Sh for the gasification of a cylinder of V483T nuclear grade graphite (300 mm long and 200 mm in diameter) at 1141 to 1393 K in ascending cross-flow of nitrogen gas containing 5 vol. % oxygen at $533 \leq Re \leq 1660$ (Ogawa, 1987).

Based on the similarities of heat and mass transfer, the two developed correlations in the forced laminar and forced turbulent convection regimes in this work express Sh in terms of both Re and Sc. In these correlations Sh and Sc replace Nu and Pr in the compiled database for convection heat transfer, respectively (Table 2.1). For ease of application of the present Sh correlations to the nuclear graphite gasification experiments and the safety analysis of VHTRs and HTGRs, the fluid properties in Sh, Re and Sc are evaluated at the graphite surface temperature.

The compiled experimental data, including that referenced in Table 2.1 and reported for graphite gasification in cross-flow of a mixture of nitrogen and oxygen (5 vol. %) (Ogawa, 1987), fall into three distinct regimes, namely: laminar, turbulent and combined convection. For $Re < 200$, which is the range of interest in the reported nuclear graphite gasification experiments of Chi and Kim (2008), Hinssen et al. (2008) and Xiaowei et al. (2004 and 2005), the applicable laminar-convection experimental heat transfer data of note are those of King (1914) and Collis and

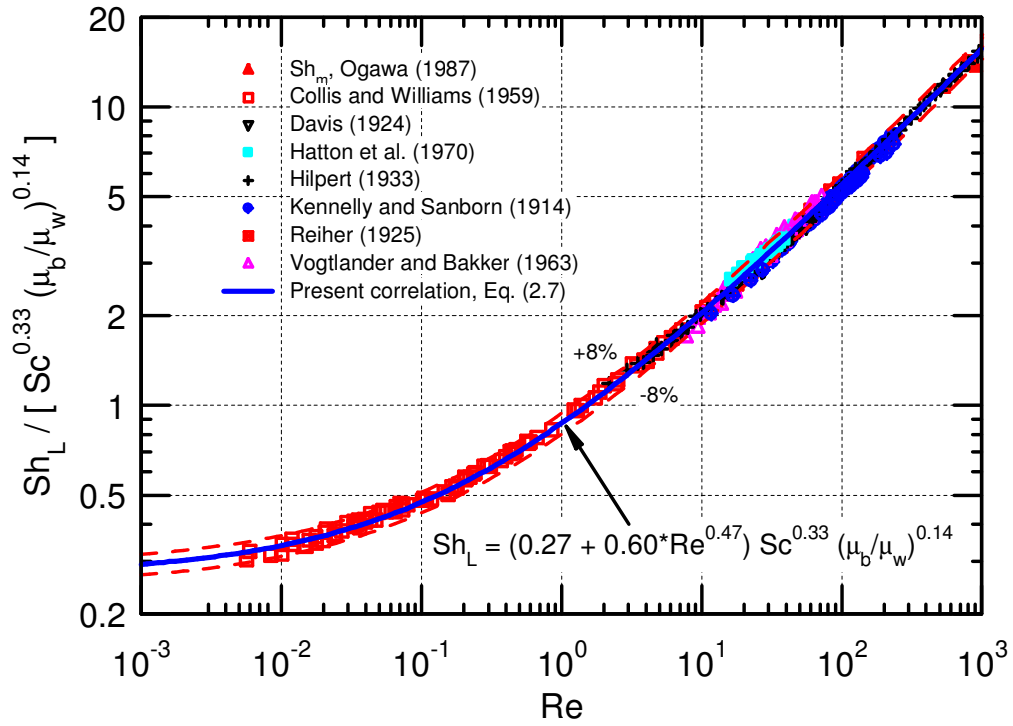


Figure 2.2. Developed Sherwood Number Correlation for Laminar Convection ($0.006 \leq Re \leq 1,000$).

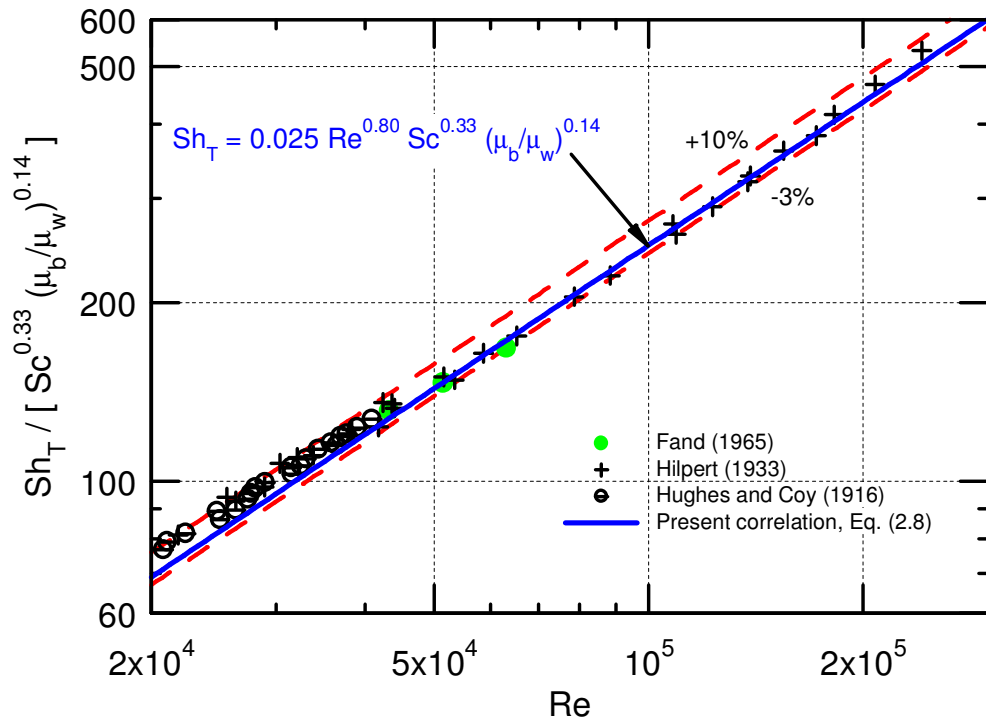


Figure 2.3. Developed Sherwood Number Correlation for Turbulent Convection ($2 \times 10^4 \leq Re \leq 2.42 \times 10^5$).

Williams (1959). The reported results of Collis and Williams, obtained in a well-controlled environment in a low-turbulence wind tunnel, are generally considered the most accurate to date at the low Re values of interest (Fig. 2.2). The results of the hot-wire anemometry experiments of King (1914) are generally consistent with those of Collis and Williams (1959), but exhibit larger scattering. King's experiments were performed with a whirling arm in an enclosed tank with interferences from draughts, both natural and induced.

The experimental results of Hilpert (1933) for atmospheric airflow are exceptional, extending over a very wide range of Re and exhibiting a high degree of consistency throughout. The values of Re in the experiments ranged from 2.2 to 1,604 for electrical heated wires, 20 μm to 1 mm in diameter, and from 530 to 2.42×10^5 for steam-heated tubes, 3 mm to 15 cm in diameter (Table 2.1). The intensity of the turbulence in Hilpert's experiments is relatively low, less than 1%, even at high Re (Fand and Keswani, 1972). Most of the compiled experimental results in Table 2.1 are consistent with those of Hilpert (1933) and Collis and Williams (1959).

The developed Sh correlation for the laminar convection ($0.006 \leq \text{Re} \leq 1,000$) is given as:

$$\text{Sh}_L = [0.27 + 0.60 \text{Re}^{0.47}] \text{Sc}^{0.33} (\mu_b / \mu_w)^{0.14}. \quad (2.7)$$

As shown in Fig. 2.2, this correlation is within $\pm 8\%$ of the compiled experimental data in Table 2.1. This correlation is also consistent with the high-temperature gasification rate measurements for different size specimens of nuclear graphite grades of NBG-18, NBG-25, IG-11, IG-110 and IG-430 in atmospheric air at $0.08 \leq \text{Re} \leq 30$ (Xiaowei et al., 2004 and 2005; Hinssen et al., 2008; Chi and Kim, 2008), as will be shown later.

In the turbulent convection regime, $\text{Re} > 2 \times 10^4$, the experimental results of Hilpert (1933), Fand (1965), and Hughes and Coy (1916) are correlated as:

$$\text{Sh}_T = 0.025 \text{Re}^{0.80} \text{Sc}^{0.33} (\mu_b / \mu_w)^{0.14}. \quad (2.8)$$

This correlation is within -3% to $+10\%$ of the compiled data in Table 2.1 and presented in Fig. 2.3. It is worth noting that in Eqs. (2.7) and (2.8), the term $(\mu_b / \mu_w)^{0.14}$ accounts for the increase in the dynamic viscosity of the gas boundary layer.

In the combined convection regime at $1,000 < \text{Re} < 2 \times 10^4$, both laminar and turbulent convections contribute to the effective value of Sh. Thus, a Sh correlation that covers all three regimes of laminar, combined and turbulent convection can be expressed in terms of the correlations for laminar and turbulent convection, Eqs. (2.7) and (2.8), using a power law as:

$$\text{Sh} = [(\text{Sh}_L)^4 + (\text{Sh}_T)^4]^{0.25}. \quad (2.9)$$

This correlation is applicable to the full range of the compiled experimental database in Table 2.1, $0.006 \leq \text{Re} \leq 2.42 \times 10^5$ and $0.68 < \text{Sc} < 2,000$. As shown in Figs. 2.4 and 2.5, Eq. (2.9) is consistent with the data of Collis and Williams (1959) and Hilpert (1933) and the great majority of the other data points in the compiled database. It is within $\pm 8\%$ of the compiled experimental database in Table (2.1) and the reported average Sh values for the gasification of a cylinder of V483T nuclear grade graphite (300 mm long and 200 mm in diameter) at 1141 to 1393 K in ascending cross-flow of nitrogen gas containing 5 vol. % oxygen at $533 \leq \text{Re} \leq 1660$ (Ogawa, 1987). The ratio $(\text{Sh} / \text{Sh}_L)$ plotted versus Re in Fig. 2.5 clearly shows the smooth transition from the laminar to the turbulent convection regime. Fig 2.5 shows that when $\text{Re} \leq 1000$ the flow is

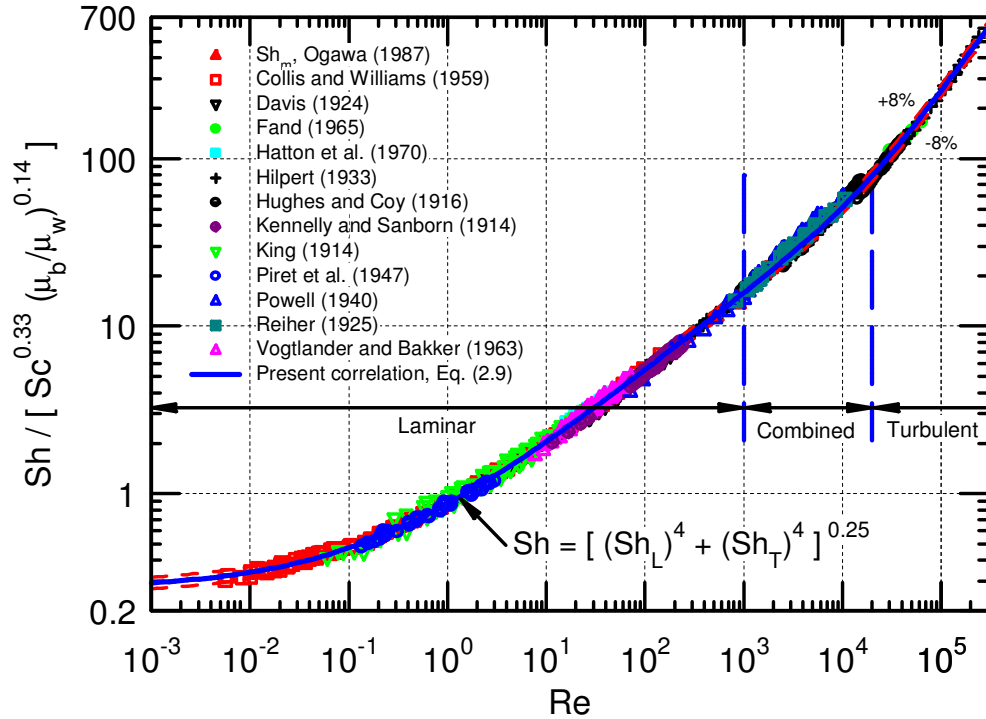


Figure 2.4. Sherwood Number Correlation for Entire Range of the Compiled Database.

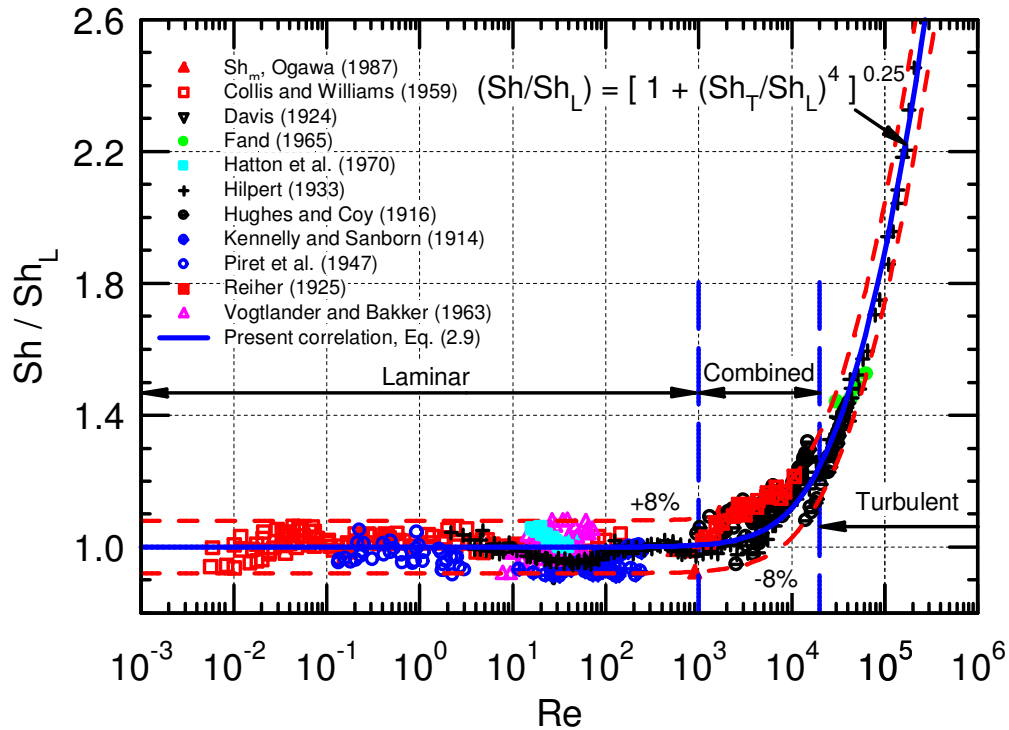


Figure 2.5. Sherwood Number Ratio in the Laminar, Combined and Turbulent Convection Regimes.

clearly laminar ($(Sh/Sh_L) = 1.0$), and $Re = 2 \times 10^4$ or $(Sh/Sh_L) = 1.25$ marks the transition to the turbulent convection regime. In this regime, Sh increases proportionally to $Re^{0.8}$ (Eq. (2.8)), versus $Re^{0.47}$ in the laminar convection regime (Eq. (2.7)).

2.2.1 Comparison with other Sherwood number correlations

This section compares the developed Sh correlation in this work, Eq. (2.9), with the well-known correlations of Hilpert (1933) and McAdams (1954), based on the similarity of heat and mass transfer, for some of the compiled forced-convection airflow data in Table 2.1. Unlike Eq. (2.9), these correlations evaluate the fluid properties at the average film temperature, which in practical applications is not known a priori. Hilpert's correlation comprises a number of expressions, each for a narrow range of Re , as (Hilpert, 1933):

$$\begin{aligned}
 Sh_f &= 0.891Re_f^{0.33}, \quad 1 \leq Re_f < 4; \\
 Sh_f &= 0.821Re_f^{0.385}, \quad 4 \leq Re_f < 40; \\
 Sh_f &= 0.615Re_f^{0.466}, \quad 40 \leq Re_f < 4000; \\
 Sh_f &= 0.174Re_f^{0.618}, \quad 4,000 \leq Re_f < 4 \times 10^4; \quad \text{and} \\
 Sh_f &= 0.0239Re_f^{0.805}, \quad 4 \times 10^4 \leq Re_f < 2.5 \times 10^5.
 \end{aligned} \tag{2.10}$$

Similarly, McAdams' correlation (McAdams, 1954) is given as:

$$\begin{aligned}
 Sh_f &= 0.32 + 0.43Re_f^{0.52}, \quad 0.1 \leq Re_f < 1000; \quad \text{and} \\
 Sh_f &= 0.240Re_f^{0.60}, \quad 1000 \leq Re_f < 5 \times 10^4.
 \end{aligned} \tag{2.11}$$

In addition to the discontinuities caused by the piecewise approach of Hilpert (1933), his correlation (Eq. (2.10)) is up to 10% higher than the present Sh correlation (Eq. (2.9)) and as much as 20% higher than the experimental data, particularly for turbulent convection ($Re > 5 \times 10^3$). McAdams' correlation, Eq. (2.11), is within -5% to $+10\%$ of the present correlation for $Re \leq 500$; and up to 33% higher than the present correlation for $1,000 \leq Re \leq 10^5$ (Fig. 2.6).

In addition to covering the entire range of the compiled database in Table 2.1, the present Sh correlation (Eq. 2.9) extends beyond the valid ranges of Hilpert's and McAdams' correlations to Re values as low as 0.006. It also provides a continuous prediction of the diffusion velocity over the entire range of the data in Table 2.1, including that of the gasification of a cylinder of V483T graphite (300 mm long and 200 mm in diameter) at 1141 to 1393 K in ascending cross-flow of nitrogen gas containing 5 vol. % oxygen at $533 \leq Re \leq 1660$ (Ogawa, 1987) to within $\pm 8\%$. The proposed correlation by Ogawa (1987) of Sh_m for the gasification of the V483T nuclear graphite is given as:

$$Sh_m = 0.689Re_f^{0.466} Sc^{1/3} \tag{2.12}$$

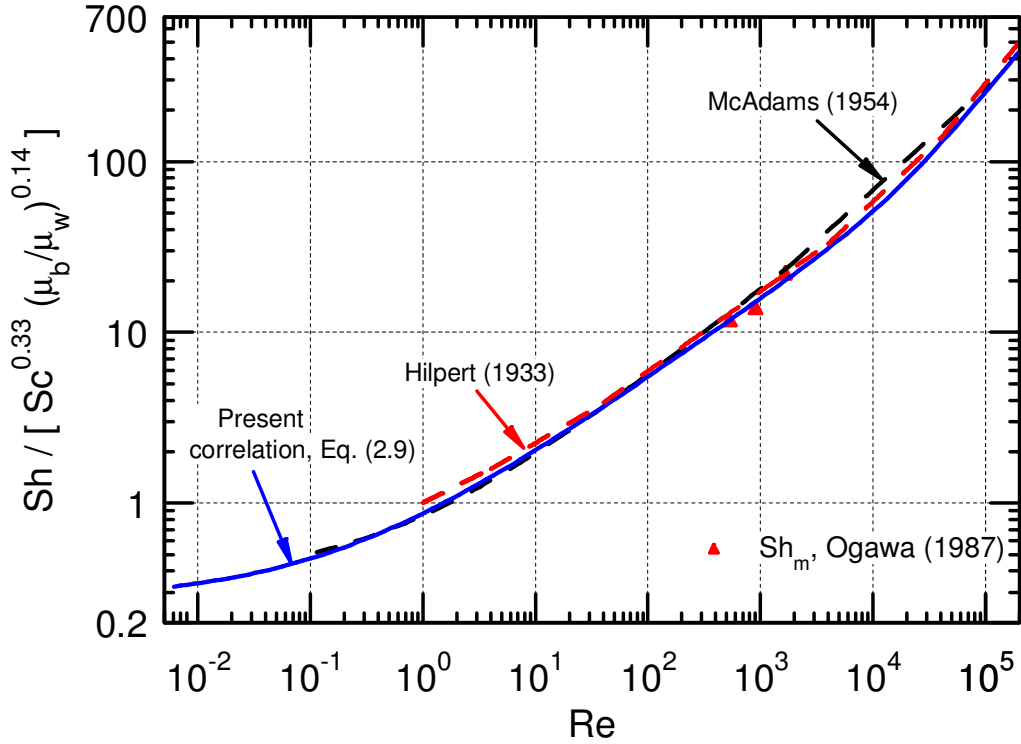


Figure 2.6. Comparison of Present Sh Correlation with those of Hilpert (1933) and McAdams (1954).

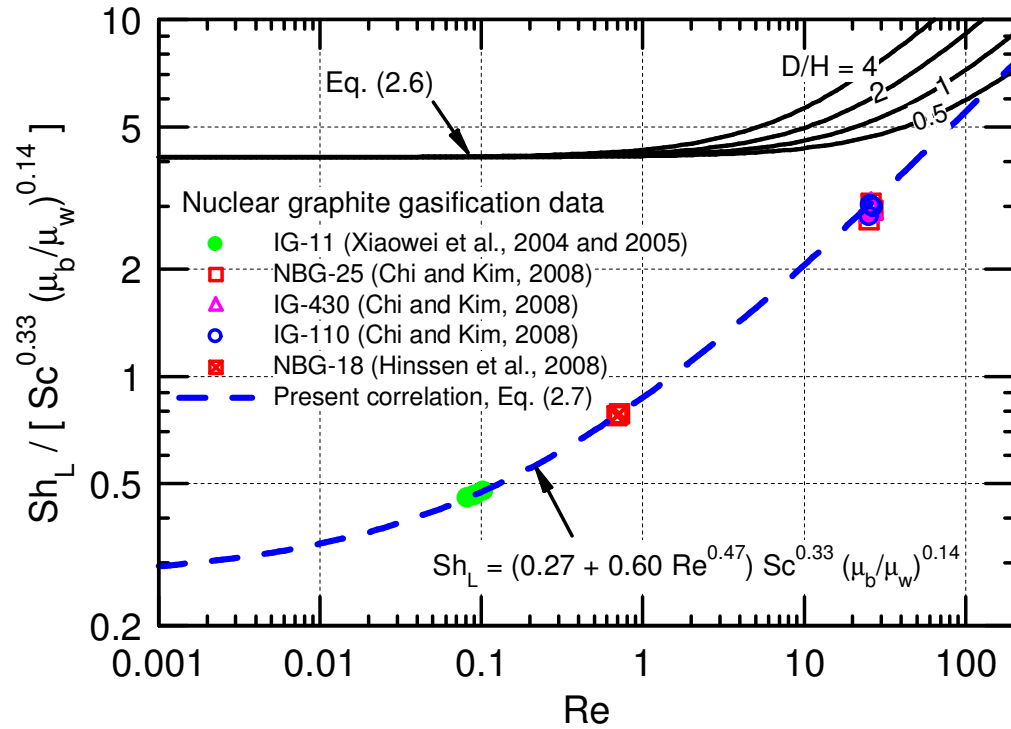


Figure 2.7. Comparison of Present Sh Correlation with Graetz Solution for Laminar Flow.

This equation is the same as that of Hilpert (1933), Eq. (2.10) for $40 \leq Re_f < 4000$, after substituting a $Sc = 0.71$ for air (Ogawa, 1987).

2.2.2 Application to nuclear graphite gasification

Figure 2.7 compares the present convection correlation of Sh_L (Eq. (2.7)) with the Graetz expression (Kakaç and Yener, 1995), Eq. (2.6), used by Kim and No (2006) to calculate the oxygen diffusion velocity in their experiments with IG-110 nuclear graphite at high temperatures in mode (c) (Fig. 2.1).

Figure 2.7 compares the correlations in Eqs. (2.6) and (2.7) for $0.001 < Re < 200$. Equation (2.6) indicates that, depending on the aspect ratio of the graphite test specimen in the experiment, D/H , Sh_L decreases with decreasing Re approaching a constant value of 3.66 when $Re \leq 1.0$. Conversely, the present correlation (Eq. (2.7)) shows that for $Re < 200$, Sh is not only significantly lower than 3.66 but also decreases monotonically with decreasing Re . It is ~ 0.23 of that given by the Graetz solution (Eq. (2.6)) at $Re = 1.0$ and more than an order of magnitude lower at $Re = 0.06$. This explains the earlier findings of the inadequacy of Eq. (2.6) to calculate an oxygen diffusion velocity that is consistent with the total gasification rate measurements for the different grades of nuclear graphite at high temperatures in mode (c) (Table 2.2) (Xiaowei et al., 2004 and 2005; Hinssen et al., 2008; Chi and Kim, 2008).

In the gasification experiments of Chi and Kim (2008), wires attached the nuclear graphite specimens, placed inside a quartz tube, to an overhead micro-scale balance. The balance measures the decreases in their masses, due to gasification, with time in the experiments (Table 2.2). The balance had a maximum capacity of 200 g and a resolution of ± 1 mg. A non-contact, vertical infrared thermometer having an accuracy of ± 2 K at 750°C measured the bottom temperature of the graphite specimens (Chi and Kim, 2008). The graphite specimens in these experiments are heated using an external vertical furnace, and a continuous atmospheric airflow is introduced into the test tube from the bottom at 10 SLPM. Transient weight loss measurements from 5% to 10% for the nuclear graphite test specimens are reported at 4 temperatures (876, 975, 1081 and 1184 K). The reported total gasification rates at these temperatures are for a 7.5% weight loss. The reported gasification rate measurements at these and higher temperatures of 1127 and 1226 K are determined from the slope of the transient weight loss measurements of the nuclear graphite specimens in the experiments. The ~ 20 g nuclear graphite specimens in the experiments of Chi and Kim (2008) were 25.4 mm right cylinders machined using a computerized numerical control lathe with a polycrystalline diamond bit at 1200 rpm. No surface treatment was applied following machining.

The less reactive NBG-18 nuclear graphite specimens in the gasification experiments of Hinssen et al. (2008) were much smaller, dime-sized cylinders, 8.0 mm in diameter and 2.69 mm high, weighing only 0.25 g (Table 2.2). Such a small size was a compromise between ensuring specimen material homogeneity and attempting to ensure in-pore diffusion in mode (a) of gasification (Fig. 2.1). To examine the homogeneity of the NBG-18 material, the 3 specimens used in the gasification experiments of Hinssen et al. (2008) were cut out from different graphite cylinders. The NBG-18 graphite specimens were placed on a small alumina crucible supported by a balance below with a hollow alumina rod. The rod houses a thermocouple for measuring the specimens' temperatures in the experiments (Table 2.2). The dry air introduced in the test section flowed downward over the graphite specimen at a low rate of 0.125 SLPM.

Table 2.2. Test Conditions and Setups of the Gasification Experiments that Used Test Specimens of Different Grades of Nuclear Graphite.

Reference	Chi and Kim (2008)	Hinssen et al. (2008)	Xiaowei et al. (2004 and 2005)
Cylindrical Test Sample			
Dimensions (mm)	$D = 25.4$, $H = 25.4$	$D = 8.0$, $H = 2.69$	$D = 10.0$, $H = 10.0$
Volume (cm ³)	12.87	0.1351	0.7854
A_w (cm ²)	27.87	1.179	1.3509
Test Conditions			
Gas type	Dry air	Dry air	Dry air
Flow direction	Up flow	Down flow	Down flow
Total P (kPa)	101.3	100.0	101.3
P_{O_2} (mole%)	21.0	21.0	21.0
Flow (SLPM)	10.0	0.125	0.020
Test Conduct			
Heating	Furnace	Furnace	Furnace
Mounting method	Dangled	On alumina plate	In alumina crucible
Tube material	Quartz	–	–
Tube D (mm)	76.2	30.0	34.5
T_w , K (°C)	876 – 1,226 (603 – 953)	923 – 1023 (650 – 750)	673 – 1473 (400–1200)
Test Setup			
			<p>TA2000C thermo-balancer (Mettler Co).</p> <p>Specimen seated inside deep crucible of slightly larger diameter (10.7 mm), limiting oxygen access to lateral and bottom surfaces of test sample.</p>

The gasification experiments of Xiaowei et al. (2004 and 2005) used the TA2000C thermogravimetric analytic apparatus. The bottom and most of the external side surface of the 1.0 cm straight cylindrical IG-11 test specimens did not have direct access to oxygen. The graphite specimens were placed in a tight fitting crucible with an inner diameter of 10.7 mm and the experiments performed for a duration of 4 hours at 673 – 1473 K in airflow of 0.020 SLPM.

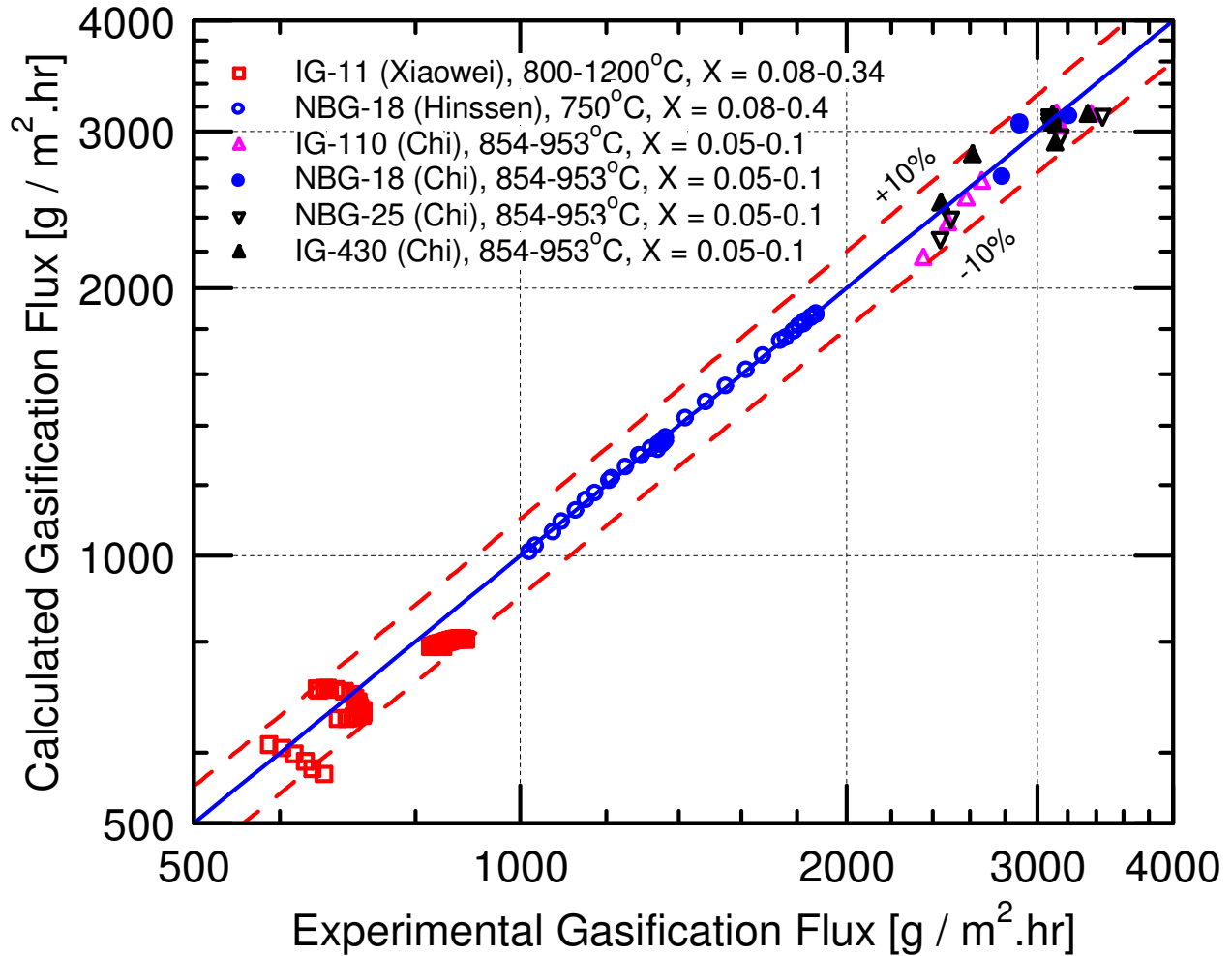


Figure 2.8. Comparison of the Calculated and Measured Diffusion-limited Gasification Fluxes for Different Grades of Nuclear Graphite.

The total gasification rates in the experiments of Chi and Kim (2008), Hinssen et al. (2008) and Xiaowei et al. (2004 and 2005) were successfully compared with the calculations of the chemical-reaction kinetics oxidation model developed by the authors (El-Genk and Tournier, 2011 and 2012a) at the reported test conditions. At high temperatures in mode (c), the model used Eq. (2.7) to calculate the oxygen diffusion velocity through the boundary layer. More details on the development of the chemical-reaction kinetics model for the gasification of nuclear graphite and on the oxidation kinetics parameters obtained by the model for the different grades of nuclear graphite can be found elsewhere (El-Genk and Tournier, 2011 and 2012a), and thus are not repeated herein.

As shown in Figs. 2.7 and 2.8, the estimates of the oxygen diffusion velocity using the developed correlation (Eq. (2.9) or (2.7)) at $Re < 1,000$) match well the reported total gasification rate measurements for the different grades of nuclear graphite in the experiments in mode (c) (Xiaowei et al., 2004 and 2005; Hinssen et al., 2008; Chi and Kim, 2008). The inferred Sh values for matching the total gasification rate measurements in the experiments of Chi and Kim

(2008) with specimens of nuclear graphite grades of NBG-25, IG-430 and IG-110 are within $\pm 8\%$ of the present correlation (Eq. (2.7)). Similar results are obtained for the total gasification rate measurements in the experiments of Hinssen et al. (2008) with specimens of nuclear graphite grade of NBG-18 and those of Xiaowei et al. (2004 and 2005) for IG-11 nuclear graphite (Fig. 2.7). In the gasification experiments of Hinssen et al. (2008), $0.69 < Re < 0.72$, which corresponds to a Sh number of ~ 0.78 . At the lowest Re values of 0.08 to 0.11 in the experiments of Xiaowei et al. (2004 and 2005), Sh is ~ 0.46 (Fig. 2.7).

Figure 2.8 compares the predictions of the chemical-reaction kinetics model (El-Genk and Tournier, 2011 and 2012a) in the diffusion-limited gasification mode (c) (Fig. 2.1) with the reported experimental measurements of the total gasification flux in the experiments (Xiaowei et al., 2004 and 2005; Hinssen et al., 2008; Chi and Kim, 2008). The gasification flux measurements in Fig. 2.8 include those reported by:

- (a) Xiaowei et al. (2004 and 2005) for IG-11 nuclear graphite at 1073 – 1473 K and for weight loss fractions of 0.08 – 0.34;
- (b) Hinssen et al. (2008) for NBG-18 nuclear graphite at 1023 K and weight loss fractions of 0.08 – 0.4; and
- (c) Chi and Kim (2008) for NBG-18, NBG-25, IG-110 and IG-430 nuclear graphite grades at 1127 – 1226 K and for weight loss fractions of 0.05 – 0.1.

Even though the experiments of Hinssen et al. (2008) were performed at 1023 K, the gasification mode (c) was encountered at a weight loss fraction as low as 8%. This is because the lower airflow rate in the experiments results in a lower oxygen diffusion velocity in the boundary layer. In addition, the much smaller NBG-18 specimens of Hinssen et al. (2008) have high surface-to-volume ratio (8.73 versus 2.16 cm^{-1}) and specific active surface area ($21.62 \text{ } \mu\text{mole/g}$), and are therefore effectively much more reactive than the NBG-18 test samples of Chi and Kim (2008).

As shown in Fig. 2.8, the calculated total gasification fluxes in the diffusion-limited mode (c) based on Eq. (2.7) are within $\pm 10\%$ of the reported experimental measurements by Xiaowei et al. (2004 and 2005), Hinssen et al. (2008) and Chi and Kim (2008) for different nuclear graphite grades. The lowest gasification fluxes of $< 1,000 \text{ g/m}^2\cdot\text{hr}$ are those reported in the experiments of Xiaowei et al. (2004 and 2005). The experiments used an airflow rate of 0.02 SLPM, which corresponds to Re of 0.08 - 0.103, depending of the test temperature (Fig. 2.7).

The intermediate gasification fluxes of $1,000$ to $2,000 \text{ g/m}^2\cdot\text{hr}$ are those reported in the experiments of Hinssen et al. (2008) that used an airflow rate of 0.125 SLPM, corresponding to a Re of 0.69 – 0.72, depending on the test specimens' temperatures (Figs. 2.7 and 2.8). In the experiments of Chi and Kim (2008) the airflow rate was 10 SLPM (or $25.3 \leq Re \leq 26.8$) and the reported measurements of the diffusion-limited gasification fluxes are $> 2,000 \text{ g/m}^2\cdot\text{hr}$ (Fig. 2.8). In this figure, the excellent agreement of the calculated gasification fluxes with the reported measurements confirms the suitability of the present Sh correlation (Eqs. (2.7) to (2.9)) for calculating the diffusion velocity of oxygen through the boundary layer in the diffusion-limited gasification mode (c) of nuclear graphite at high temperatures. It is worth noting that the developed Sh correlations are practically limited to below 1400 K, when the contributions of the Boudouard reaction and the CO/O_2 homogeneous reaction in the boundary layer are negligible.

2.3 SUMMARY

The gasification of graphite in the core, reflector and support columns in the lower plenum of VHTRs and HTGRs is a primary safety analysis concern in the unlikely event of an air ingress accident. At or below 673 K, graphite gasification is negligible. Up to 900 K, graphite gasification occurs within the open volume pores and its rate increases exponentially with increased temperature, solely driven by the kinetics of the oxidation chemical reactions. As the graphite temperature increases to 1123 K, the limited penetration of oxygen into the open volume pores, due to the counter-current diffusion of the gasification products of CO and CO₂, decreases the increase in graphite gasification rate with increasing temperature. Further increase in temperature gradually shifts graphite gasification from the volume pores to the external surface of the graphite structure with increased temperature. At high temperatures > 1123 K graphite gasification in the volume pores ceases and occurs solely at the external surface. Despite the increase in the chemical oxidation kinetics of graphite at such high temperatures, the diffusion of oxygen from the bulk gas mixture through the boundary layer to the external surface of the graphite structure limits its gasification.

In reality, since modes (a) and (b) and modes (b) and (c) partially overlap, the gasification rate of nuclear graphite increases, but follows a smooth transition with increased temperature (Fig. 2.1). While in modes (a) and (c), graphite gasification is limited by the chemical-reactions kinetics and the oxygen diffusion through the surface boundary layer, respectively, mode (b) of gasification is limited by the in pores diffusion of oxygen. Thus, calculating the gasification rate of nuclear graphite in mode (c) and in the transition from mode (b) (Fig. 2.1) requires accurate determination of the oxygen velocity through the boundary layer. In addition to the total flow rate and pressure, or Re of the bulk gas mixture, this velocity depends on the dimensions and temperatures of the graphite test specimens.

This work compiled an extensive database of 807 experiments measurements of forced-convection heat and mass transfer coefficients at $0.006 \leq Re \leq 2.42 \times 10^5$ and $0.68 < Sc < 2,000$ (Table 2.1), and Sh_m for gasification of a cylinder of V483T nuclear grade graphite (300 mm long and 200 mm in diameter) at 1141 to 1393 K in ascending cross-flow of nitrogen gas containing 5 vol. % oxygen at $533 \leq Re \leq 1660$. Based on this database, the developed Sh correlation calculates the oxygen diffusion velocity in the boundary layer during the gasification of nuclear graphite at high temperatures, and is within $\pm 8\%$ of the compiled experimental database that covers laminar, turbulent and combined convection regimes.

The calculated total gasification fluxes based on the developed Sh correlation are within $\pm 10\%$ of the reported measurements in the experiments with different size specimens of nuclear graphite grades NBG-18, NBG-25, IG-11, IG-110, and IG-430. The results favorably suggest that the developed Sh correlation in this paper (Eqs. (2.7) – (2.9)) for laminar, turbulent and combined convection ($0.006 < Re < 2.42 \times 10^5$) is suitable for calculating the nuclear graphite gasification rates in mode (c) at intermediate and high temperatures (900 – 1400 K) in experiments and in future safety analysis of VHTRs and HTGRs in the unlikely event of an air ingress accident. In such an analysis, since reported graphite gasification measurements are for relatively small size specimens, the applicability of the developed Sh correlation to calculating the gasification rate for large nuclear graphite structures using the authors' chemical-reactions kinetics model needs further verification. This would require generating transient gasification and weight loss measurements in well controlled and adequately instrumented experiments. The

measurements may also include the actual local surface temperatures of the graphite structure, the production rates of CO and CO₂ gases and the local weight loss in the direction of the entering or crossing airflow or the bulk gas mixture.

In such experiments, the heat generation by the exothermic chemical reactions generating the CO and CO₂ gaseous products would increase the local surface temperature, while the progressive consumption of oxygen in the bulk gas would limit the local oxidation rate. The combined effect of these two processes and of the corresponding changes in the properties, Re and temperature of the bulk gas flow would undoubtedly influence the local gasification rate in the large nuclear graphite components in the nuclear reactor core, reflector and of the massive graphite support columns in the lower plenum.

The next Chapter 3 compares the calculations of the previously developed chemical-reactions kinetics model with reported measurements of weight loss and total gasification rate for different NBG-18 nuclear graphite specimens in experiments performed at 876 K to 1226 K. Results show that the gasification rate is chemical-kinetics limited at low and intermediate temperatures and diffusion-limited at high temperatures. At high temperatures, the model calculates the diffusion velocity of oxygen through the boundary layer using the correlation developed in this Chapter 2.

2.4 NOMENCLATURE

A	Gas flow area (m^2)
A_w	Effective surface area (m^2)
D	Diameter (m)
$D_{A,B}$	Binary diffusion coefficient for gas mixture of A and B components (m^2/s), Eq. (2.5)
$D_{O_2,m}$	Effective diffusion coefficient of oxygen in boundary layer (m^2/s), Eq. (2.4)
H	Total tube length (m), Eq. (2.6)
k	Gas thermal conductivity at wall temperature (W/m K)
k_m	Effective diffusion velocity of oxygen in boundary layer (m/s), Eq. (2.3)
\dot{m}	Gas mass flow rate (kg/s)
M_j	Molecular weight of gas species j in a mixture (kg/mole)
N_a	Avogadro number, $6.0225 \times 10^{23} \text{ mole}^{-1}$
$[\hat{O}_2]_b$	Oxygen concentration in bulk gas mixture (mole/m^3)
$[\hat{O}_2]_w$	Oxygen concentration at graphite surface (mole/m^3)
P_{tot}	Total pressure of gas mixture (Pa)
\dot{R}	Reaction rate (mole/s)
Re	Reynolds number at wall surface temperature, $\dot{m}D/(\mu A)$
Re_f	Reynolds number at average film temperature, $\dot{m}D/(\mu_f A)$
R_{gas}	Perfect gas constant, 8.3144 J/mole.K
Sc	Schmidt number at wall surface temperature, $\nu / D_{O_2,m}$
Sh	Sherwood number at wall surface temperature, $k_m D / D_{O_2,m}$
Sh_f	Sherwood number at average film temperature, $(k_m D / D_{O_2,m})_f$
Sh_m	Surface means Sherwood number at average film temperature (Ogawa, 1987), Eq. (2.12)
T	Temperature (K)
x_j	Molar fraction of gas species j in a mixture
X	Weight loss fraction

Greek

ε	Depth of molecular potential well (J)
μ	Dynamic viscosity (kg/m.s)
ν	Kinematic viscosity (m^2/s), $\nu = \mu / \rho$
ρ	Solid or gas mixture density (kg/m^3)
σ_j	Effective molecular diameter of gaseous species j (m)
$\Omega^{(1,1)*}$	Dimensionless collision integral for self-diffusion, Eq. (2.5)

Subscript/Superscript

a	Adsorption of oxygen onto active free sites to form un-dissociated complexes
b	bulk gas
CO_2	Carbon dioxide gas

f	Evaluated at film temperature
L	Laminar
m	Mean
N_2	Nitrogen gas
O_2	Oxygen gas
T	Turbulent
W	Graphite external surface

3. VALIDATION OF GASIFICATION MODEL FOR NBG-18 NUCLEAR GRAPHITE

The challenges in developing a chemical kinetics model for the gasification of nuclear graphite are the complexity and the strong coupling among various processes taking place, the variances in the fabrication methods, volume porosity and microstructure of nuclear graphite, and insufficient information from experiments on the production rates of CO and CO₂ gases and surface area of active free sites (Essenhigh, 1981). In addition, the gasification rate of nuclear graphite depends on many other variables. These include temperature; oxygen partial pressure; total flow rate and pressure of air or the bulk gas mixture; the specific activation energies for the adsorption of oxygen and desorption of CO and CO₂ gases, and the initial value and the changes in the surface area of active free sites and complexes with weight loss. The surface area of active free sites directly relates to the crystalline structure and the fabrication method of nuclear graphite, including the degree and temperature of graphitization of the green article, and the orientation of the cutting plane of the test specimens used in experiments. The graphitization conditions of nuclear graphite affect its volume porosity, the average size of the volume pores, and the amount of impurities, such as Ca, that act as a catalyst for increased gasification.

This Chapter briefly summarizes the developed chemical-reaction kinetics model for nuclear graphite gasification and focuses on comparing the model calculations of weight loss and total gasification rate with the reported measurements in experiments with cylindrical specimens of NBG-18 nuclear graphite at 876 – 1226 K in atmospheric air flow, and weight loss fraction up to 0.90 (Chi and Kim, 2008; Hinssen et al., 2008). In addition, parametric analyses are performed for the NBG-18 nuclear graphite specimens in the experiments of Chi and Kim (2008) and Hinssen et al. (2008), using the determined values of the chemical kinetics parameters and rate constants, values and Gaussian-like distributions of the specific activation energies for adsorption and desorption, and surface area of active sites. The parametric analysis investigated the effects of increasing temperature up to 1250 K and oxygen partial pressures from 0.5 to 21 kPa on the total gasification rate, the transient weight loss and the production rates of CO and CO₂ gases.

3.1 NUCLEAR GRAPHITE OXIDATION MODEL

The many grades of nuclear graphite may be classified based on the size of the filler particles and microstructure. In medium-grain nuclear graphite, the filler particles range in sizes from 100 to 4 mm, compared to ~ 10 μm and 2 μm in fine-grain and ultra-fine grain graphite, respectively. The porous graphite structure with open and closed volume pores has volume porosities of 20% to 30%, compared to < 1% for a single graphite crystal. The volume pores are classified into macro-pores > 50 nm, transitional pores of 2 – 50 nm, and small micro-pores < 2 nm in size. The volume pores provide the internal surface area for graphite oxidation at low and intermediate temperatures (Fig. 2.1). The NBG-18 nuclear graphite grade, the subject of this Chapter, uses coal tar pitch coke particles, is vibration molded and has nearly isotropic properties (Vreeling et al., 2008). The medium-grain (300 μm mean) NBG-18 nuclear graphite has very low ash content < 10 ppm and relatively low volume porosity, ~18.3% (Chi and Kim, 2008). It exhibits one of the highest mass density of all modern grades of nuclear graphite (1.85 g/cm³).

Graphite gasification primarily depends on the Active sites Surface Area (ASA), in contrast to the geometrical Total Surface Area (TSA). The former is the fraction of TSA that is chemically

active. Graphite test specimens cut parallel to the extrusion direction are far more reactive than those cut perpendicular to the extrusion plane (Xiaowei et al., 2005). In addition, graphite irradiation in nuclear reactors changes its crystal structure, density, and decreases both the ASA and the average size of volume pores; thus, irradiated graphite would be less reactive than unirradiated graphite (Nonal, 2001).

The ASA can be measured directly as a function of weight loss in temperature-controlled adsorption and desorption experiments, along with the values and distributions of the specific activation energies for the adsorption of oxygen and desorption of gaseous products (Ahmed and Back, 1985; Laine et al., 1963; Du et al., 1990 and 1991). In the absence of direct measurements, estimates of these parameters can be obtained from the reported experimental measurements of the total gasification rate and transient weight loss at different temperatures, using a multi-parameters optimization algorithm (El-Genk and Tournier, 2011 and 2012a). The following section briefly describes the three basic modes of graphite gasification with increasing temperatures.

The gasification of nuclear graphite proceeds through a number of successive processes (Essenhigh, 1981; Moulijn and Kapteijn, 1995; Campbell and Mitchell, 2008): (a) *Diffusion of oxygen* to the surface, and/or into the open volume pores; (b) *Adsorption of oxygen atoms* onto the ASA and the simultaneous formation of C-O bonds and breaking of the C-C bonds; and (c) *Desorption of CO and CO₂* gaseous products and transport to the bulk gas. The direct route for the production of CO gas is desorption of stable complexes, possibly ethers and carbonyl groups. Due to the stability of these complexes, CO production is not observed at low temperatures (< 400 °C), but its rate increases exponentially with increasing temperature (Moulijn and Kapteijn, 1995). On the other hand, the main venue for the simultaneous production of CO₂ gas is by the bonding of oxygen atom to a saturated carbon atom adjacent to an edge carbon atom already bonded to an oxygen atom (Chen et al., 1993; El-Genk and Tournier, 2011).

Since the total gasification rate as well as the production rates of CO and CO₂ gases are characteristics of the type of graphite, they could be used to determine the values and the Gaussian-like distributions of the specific activation energies and the kinetics parameters for the elementary chemical reactions for gasification. During graphite gasification, the effective ASA is solely dependent on weight loss. However, the time it takes to reach a specific weight loss depends on temperature, and hence the mode of oxidation (Fig. 2.1), the oxygen partial pressure, and the type of graphite. The next Section presents and briefly discusses the elementary reactions in the developed chemical kinetics model of nuclear graphite (El-Genk and Tournier, 2011 and 2012a).

3.1.1 Elementary reactions in chemical kinetics model

Despite the complexity of graphite oxidation, the following 4 adsorption and desorption reactions in the present chemical kinetics model are adequate (Ahmed et al., 1987; Du et al., 1990 and 1991; Minh et al., 1997; Moulijn and Kapteijn, 1995; Campbell and Mitchell, 2008):

(a) *Adsorption of oxygen molecules to form un-dissociated C(O₂) surface complexes:*



The rate constants for these reactions are given by the Arrhenius relation:

$$k_{a,i} = k_a^o \cdot e^{-\varepsilon_{i,a}/(R_g T)} . \quad (3.1b)$$

(b) Breakup of un-dissociated C(O₂) oxygen radicals to form stable (CO) complexes:



The rate constant for this reaction is expressed by the following Arrhenius relation as:

$$k_b = k_b^o \cdot e^{-\varepsilon_b/(R_g T)} . \quad (3.2b)$$

(c) Desorption of stable (CO) surface complexes to produce CO gas:

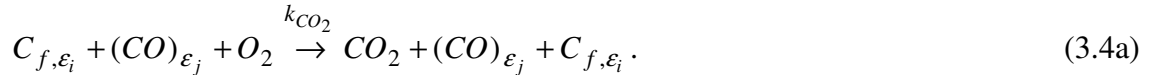


The rate constants for these reactions are given by the following Arrhenius relation as:

$$k_{d,j} = k_d^o \cdot e^{-\varepsilon_{j,d}/(R_g T)} . \quad (3.3b)$$

Note that besides the change in ASA with weight loss, the desorption reactions of Eq. (3.3a) are the only venue in the model for “regenerating” new surface active sites.

(d) Desorption of CO₂ gas:



The rate constant for this reaction is given by the following Arrhenius relation as:

$$k_{CO_2} = k_d^* \cdot e^{-\varepsilon_d^*/(R_g T)} . \quad (3.4b)$$

The surface complexes and the neighboring free active sites act as a catalyst for the production of CO₂ gas (Moulijn and Kapteijn, 1995). Although active sites are freed by desorption of CO₂ molecules, the reactions in Eq. (3.4a) remove carbon atoms from the surface and consume only oxygen molecules; they do not consume active sites nor surface complexes. Nonetheless, the rates of these reactions are limited by the availability of both surface active free sites and (CO) complexes. The desorption reactions of CO₂ (Eq. 3.4a) are first order in oxygen partial pressure, even at high pressures (Ahmed et al., 1987; Zhuang et al, 1995). The specific desorption energy for a CO₂ gas molecule (Eq. 3.4a) is considerably less than that for desorption of a (CO) complex to generate a CO gas molecule (Eq. 3.3a). Thus, based on these closely coupled desorption reactions, the total rate and the production rates of CO and CO₂ gases during

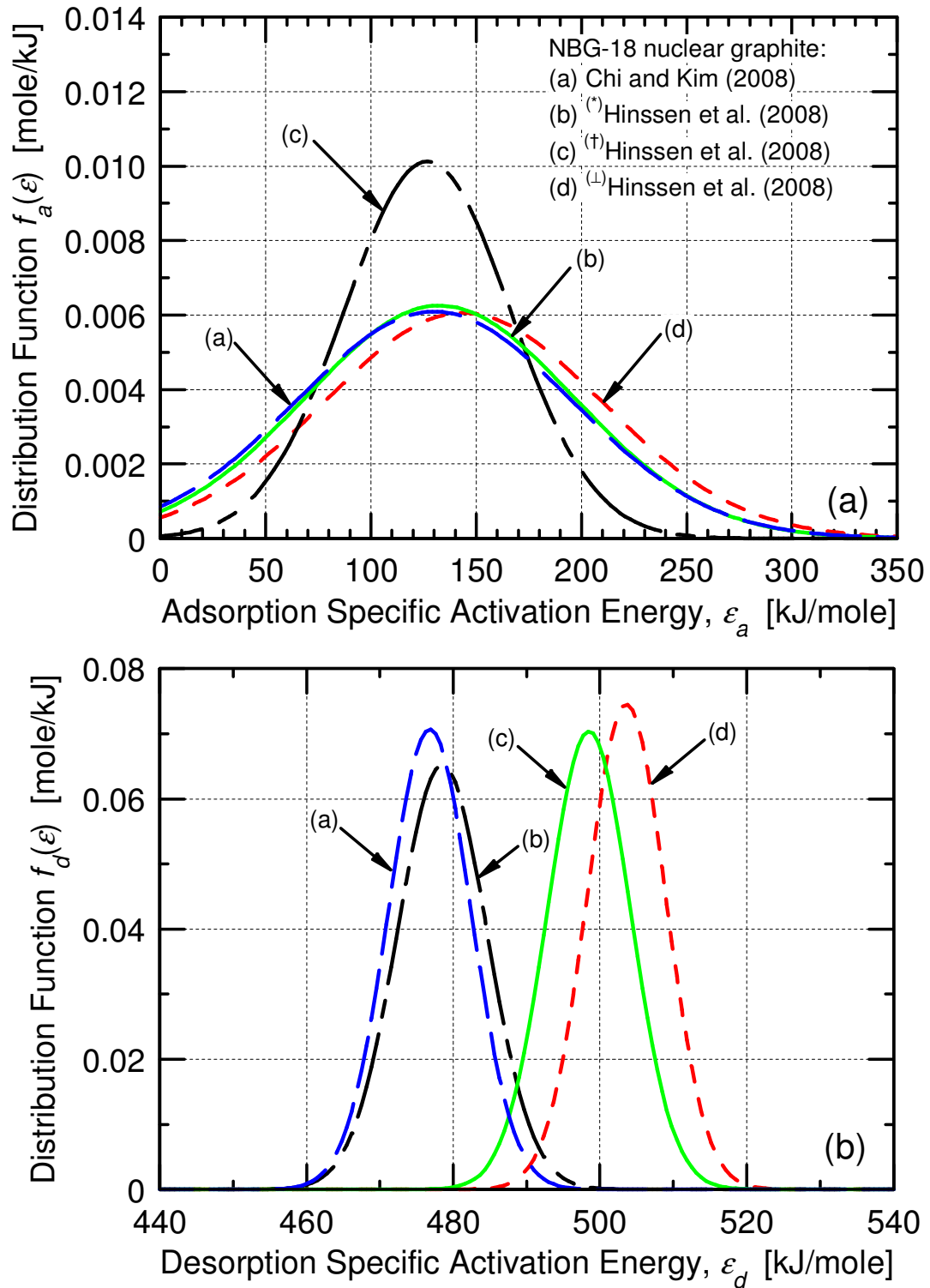


Figure 3.1. Determined Specific Activation Energy Distributions for NBG-18 Nuclear Graphite Test Specimens. (a) Adsorption; (b) Desorption.

graphite gasification would strongly depend on the specific activation energies for the adsorption of oxygen and desorption of CO and CO₂ gases. The determined specific activation energies and their Gaussian-like distributions for NBG-18 nuclear graphite are discussed next.

3.1.2 Specific activation energies

The specific activation energies for the adsorption of oxygen and desorption of CO gas during the gasification of graphite are not constant but have Gaussian-like distributions. In the absence of direct measurements, the values and Gaussian-like distributions of the specific activation energies for adsorption and desorption and corresponding pre-exponential rate constants for different grades of nuclear graphite are obtained from the reported experimental measurements of the total gasification rate and transient weight loss, using a multi-parameter optimization algorithm (El-Genk and Tournier, 2011 and 2012a). The obtained distribution of the specific activation energies of NBG-18 nuclear graphite for the adsorption of oxygen is characterized by a most probable specific energy, $\bar{\epsilon}_a$ and a standard deviation, σ_a (Fig. 3.1a). Similarly, the Gaussian-like distribution of the specific activation energies for desorption of stable complexes, produced by the reactions in Eq. (3.2a), in the energy bins i and j , has a most probable specific energy, $\bar{\epsilon}_d > \bar{\epsilon}_a$ and a standard deviation, $\sigma_d < \sigma_a$ (Fig. 3.1b).

The constituent equations for calculating the molar reaction rates for the 4 elementary reactions in the present chemical-reactions kinetics model (Eqs. (3.1) – (3.4)) are detailed elsewhere (El-Genk and Tournier, 2011) and will not be repeated here. The model, assuming that the graphite surface is initially devoid of adsorbed oxygen radicals, solves the constituent equations describing the kinetics of the elementary chemical reactions given by Eqs. (3.1) – (3.4), in Mode (a) and Mode (b) (Fig. 2.1) at low and intermediate temperatures. At high temperatures, graphite gasification (Mode (c)) is limited by the diffusion of oxygen from the bulk gas mixture to the surface through the boundary layer, and the diffusion velocity of oxygen through the boundary layer is calculated as detailed next.

3.1.3 Oxygen diffusion velocity

In Mode (c) (Fig. 2.1c), the total gasification rate is expressed as:

$$\dot{R}_{O_2} = (A_w \sqrt{1-X}) k_m \times ([\hat{O}_2]_b - [\hat{O}_2]_w) . \quad (3.5)$$

The term $\sqrt{1-X}$ accounts for the change in the external surface area with weight loss fraction, X , k_m is the effective diffusion velocity of oxygen through the boundary layer, and $[\hat{O}_2]_b$ and $[\hat{O}_2]_w$ are the average concentrations of oxygen in the bulk gas mixture and at the graphite surface. The rate of oxygen consumption on the left-hand-side of Eq. (3.5) is related to those of the elementary reactions (Eqs. (3.1a) and (3.4a)), as:

$$\dot{R}_{O_2} = \sum_i \dot{R}_{a,i} + \sum_{ij} \dot{R}_{CO_2,ij} . \quad (3.6)$$

The effective diffusion velocity of oxygen in Eq. (3.5) is calculated as:

$$k_m = Sh \times D_{O_2,m} / D . \quad (3.7)$$

The values of Sh and $D_{O_2,m}$ depend on the flow conditions and total pressure of the bulk gas mixture, the oxygen partial pressure, and the geometry and dimensions of the graphite specimens and the setup used in the gasification experiments. A semi-empirical correlation for calculating the Sherwood number in Eq. (3.7) is developed based on reported experimental measurements of laminar-convection heat transfer for heated wires and cylinders of different diameters and air at different flow rates corresponding to Reynolds numbers from 0.01 to 1000 (Collis and Williams, 1959; Hatton et al., 1970; Hilpert, 1933; Kennelly and Sanborn, 1914; El-Genk and Tournier, 2012a). The developed Sh correlation is given as (see Chapter 2 of this report):

$$Sh = [0.27 + 0.60 Re^{0.47}] Sc^{0.33} (\mu_b / \mu_w)^{0.14} . \quad (3.8)$$

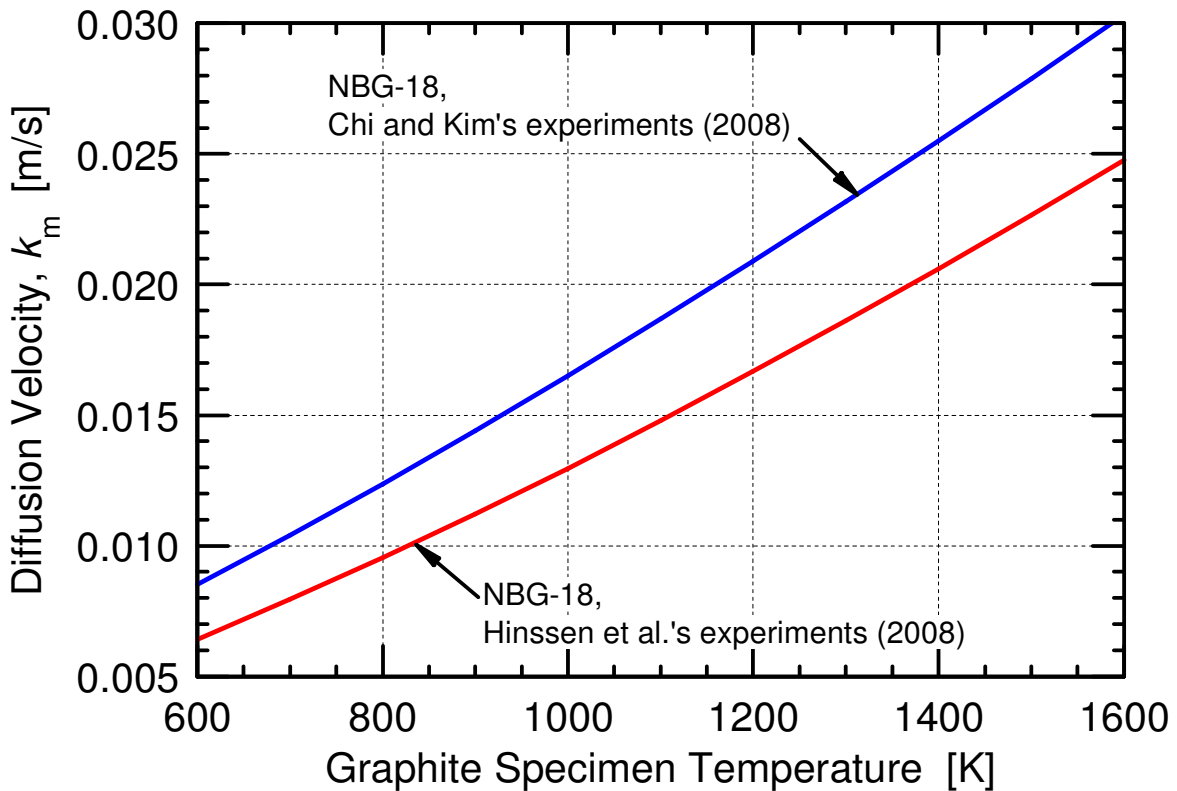


Figure 3.2. Estimates of Oxygen Diffusion Velocities in NBG-18 Nuclear Graphite Experiments.

This correlation, in which the fluid properties in Sh , Sc , and Re are evaluated at the surface temperature, is applicable to nuclear graphite gasification experiments with $Re < 100$ (Chi and Kim, 2008; Hinssen et al., 2008; Xiaowei et al., 2004 and 2005) and to the safety analysis of VHTRs and HTGRs in the unlikely event of an air ingress accident, in which Re could be < 1000 . In such an accident, Eq. (3.8) is more applicable to graphite gasification than the Graetz solution (Kakaç and Yener, 1995) used by others (Kim and No, 2006). The Graetz solution for laminar flow condition expresses Sh as:

$$\text{Sh} = 3.66 + \frac{0.0668 \times (D/H) \text{Re Sc}}{1 + 0.04 \times [(D/H) \text{Re Sc}]^{2/3}} \quad (3.9)$$

This expression (Fig. 2.7) gives the average Sherwood number over a uniformly heated pipe length H . At $\text{Re} < \sim 100$, the second term on the right hand side of Eq. (3.9) is negligible and Sh becomes constant and equal to 3.66. Such value is significantly higher than that given by Eq. (3.8), showing that Sh decreases monotonically well below 3.66 with decreasing Reynolds number.

The effective diffusion coefficient of oxygen in the boundary layer, $D_{O_2,m}$ is calculated using the first-approximation of the molecular theory of gases at low pressure (Hirschfelder et al., 1954) for a 3-component gas mixture (O_2 , N_2 and CO), as:

$$D_{O_2,m} = \frac{1 - x_{O_2}}{x_{N_2} / D_{O_2,N_2} + x_{CO} / D_{O_2,CO}} \quad (3.10)$$

Recently, the present chemical-reaction kinetics model has been used successfully to calculate the total gasification rates for IG-110, IG-430 and NBG-25 nuclear graphite cylindrical specimens in the experiments by Chi and Kim (2008). The obtained values of the oxygen diffusion velocity, k_m , for matching the reported gasification rate measurements at 1127 K, 1184 K and 1226 K in standard air flow of 10 SLPM (Standard Liters Per Minute) are calculated and compared with those from Eq. (3.8) in Fig. 2.7. The Sh values inferred from the reported total gasification rate measurements by Chi and Kim (2008) for the 3 grades of nuclear graphite (IG-110, IG-430 and NBG-25) and Re of 25.3 to 26.8 are within $\pm 8\%$ of the correlation in Eq. (3.8), confirming its applicability to nuclear graphite gasification at low Re values (Fig. 2.7). Besides the oxygen diffusion velocity, other input parameters to the present chemical-reaction kinetics model are discussed next.

3.1.4 Oxidation model input parameters

The constituent equations in the present chemical-reaction kinetics model for graphite gasification are solved using the MATLAB®/SIMULINK® platform (Simulink, 2008) and the *ode15s* solver (Shampine et al., 1999). The input to the graphite's chemical-reaction kinetics model includes the values of 10 parameters, namely: (a) the most probable specific activation energies for the adsorption of O_2 and desorption of CO ($\bar{\varepsilon}_a$ and $\bar{\varepsilon}_d$) and the standard deviations (σ_a and σ_d) characterizing their Gaussian-like distributions; (b) the specific activation energies ε_b and ε_d^* for elementary reactions in Eqs. (3.2a) and (3.4a); and (c) the pre-exponential rate constants, k_a^o , k_b^o , k_d^o and k_d^* for the four elementary reactions (Eqs. (3.1a), (3.2a), (3.3a) and (3.4a)). These parameters characterize the type of nuclear graphite used in the experiments (Table 3.1), while the initial value of the surface active free sites (ASA_o) and the change of the ASA with weight loss characterize the reactivity of the graphite specimens.

Table 3.1. Setups and Conditions in the Experiments of NBG-18 Nuclear Graphite Gasification (Chi and Kim, 2008; Hinssen et al., 2008).

Reference	Chi and Kim (2008)	Hinssen et al. (2008)
Geometry	Cylinder	Cylinder
Dimensions (mm)	$D = 25.4, H = 25.4$	$D = 8.0, H = 2.69$
Volume (cm ³)	12.87	0.1351
Effective side area (cm ²)	27.87	1.179
Gas type / Flow direction	Dry air / Up flow	Dry air / Down flow
Total pressure (kPa)	101.3	100.0
P_{O_2} (mole%)	21.0	21.0
Flow rate (SLPM)	10.0	0.125
Heating method	Furnace	Furnace
Mounting method	Dangled	On alumina plate
Tube material	Quartz	Not reported
Tube dia. (mm)	76.2	30.0
Surface T , K (°C)	876 – 1226 (603 – 953)	923 – 1023 (650 – 750)
Test Setup (all dimensions in mm)		
Calculated Flow fields (dry air at 300 K, 101.3 kPa)		

The 10 input parameters and ASA_o are determined using a multi-parameter optimization from the reported measurements of the total gasification rate and the transient weight loss in the experiments. The production rates of the CO and CO₂ gases, when measured in the experiments, could be substituted for the transient weight loss measurements. The obtained characteristic distributions of the specific activation energies for adsorption and desorption for the NBG-18 nuclear graphite specimens (Tables 3.1) are shown in Fig. 3.1 and the values of ASA_o , the activation energies and the pre-exponential rate constants of the elementary reactions, (Eqs. (3.1) – (3.4)) are listed in Table 3.2.

3.2 OXIDATION EXPERIMENTS OF NBG-18 NUCLEAR GRAPHITE

The NBG-18 graphite specimens used in the gasification experiments of Chi and Kim (2008) and Hinssen et al. (2008) have different microstructures and are right cylinders with different dimensions (Table 3.1). A constant oxygen partial pressure is maintained in the experiments by flowing atmospheric dry air through the test section (Table 3.1). The graphite specimens used in the experiments of Chi and Kim (2008) and Hinssen et al. (2008) are described next.

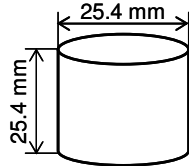
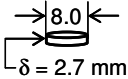
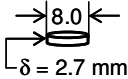
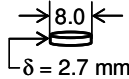
3.2.1 Test specimens

The degree of graphitization, G , of the NBG-18 graphite test samples is determined from measurement of the crystal dimension c using an X-ray diffraction, and $c/2 = 3.354 \text{ \AA}$ for a fully-graphitized graphite ($G = 1$), and $c/2 = 3.44 \text{ \AA}$ for the green article ($G = 0$). Chi and Kim (2008) reported $G = 0.835$ for the NBG-18 specimens in their experiments, which is comparable to those reported for other specimens of nuclear graphite grades: IG-110 ($G = 0.848$), IG-430 ($G = 0.845$) and NBG-25 ($G = 0.789$) (Chi and Kim, 2008).

The NBG-18 graphite specimens used in the experiments of Chi and Kim (2008) (Table 3.1) are machined using a computerized numerical control lathe with a polycrystalline diamond bit at 1200 rpm. No surface treatment is performed following machining. The NBG-18 test specimens of Hinssen et al. (2008) are much smaller, dime-sized cylinders weighing only 0.250 g (Table 3.1). This specimen size is selected as a compromise between ensuring microstructure homogeneity and suppressing in-pore diffusion in Mode (a) of gasification at $\sim 600 \text{ K}$. To verify the homogeneity of the NBG-18 nuclear graphite used in the experiments of Hinssen et al. (2008), 3 specimens were cut out from different cylinders. The reported results showed that the specimens exhibited large differences in reactivity. Specimen 3 (\perp) is the most reactive, with a gasification rate more than double that of the least reactive specimen 2 (\dagger). Hinssen et al. (2008) attributed such large differences in reactivity to variances in the microstructure and impurities.

The surface areas of the active free sites (ASA or S_m) for the NBG-18 nuclear graphite specimens are not measured in the gasification experiments of Chi and Kim (2008) and Hinssen et al. (2008). The values of ASA_o listed in Table 3.2 are obtained from the reported total gasification rates in the experiments at different temperatures using the multi-parameter optimization algorithm for the chemical-reactions kinetics model (El-Genk and Tournier, 2011 and 2012a). This algorithm also calculates the variation in ASA with weight loss, based on the reported measurements of the transient weight loss in the experiments at low and intermediate temperatures, at which graphite gasification is not diffusion, but chemical-kinetics limited.

Table 3.2. Determined Kinetics and Micro-Structural Parameters for NBG-18 Nuclear Graphite Specimens in Gasification Experiments (Chi and Kim, 2008; Hinssen et al., 2008).

Test Specimens	Chi and Kim (2008)	(*)Hinssen et al. (2008)	(†)Hinssen et al. (2008)	(^L)Hinssen et al. (2008)
Graphite type	NBG-18	NBG-18	NBG-18	NBG-18
Density (g/cm ³)	1.85	1.85	1.85	1.85
Mass (g)	23.81	0.250	0.250	0.250
[C] _o (mole)	1.984	0.020833	0.020833	0.020833
Test specimens dimensions (mm)				
Characteristic Micro-Structural Parameters				
Ψ	80 ^(a)	35 ^(b)	35 ^(b)	35 ^(b)
ASA _o (μmole)	14.286 ^(a,c,e)	4.238 ^(d,e)	2.912 ^(d,e)	5.405 ^(d,e)
S_m^o (μmole/g)	0.600	16.95	11.65	21.62
Oxidation Kinetics Parameters				
$\bar{\epsilon}_a$ (kJ/mole)	130.0	132.6	126.8	143.8
σ_a (kJ/mole)	65.49	63.80	39.41	65.87
k_a^o (mole ⁻¹ .s ⁻¹)	11,853.	11,325.	11,843.	10,810.
k_b^o (mole ⁻¹ .s ⁻¹)	9.558 x 10 ¹⁴	9.754 x 10 ¹⁴	12.50 x 10 ¹⁴	9.802 x 10 ¹⁴
ϵ_b (kJ/mole)	196.3	196.2	194.3	191.8
$\bar{\epsilon}_d$ (kJ/mole)	476.8	498.5	478.5	503.6
σ_d (kJ/mole)	5.647	5.669	6.114	5.353
k_d^o (s ⁻¹)	5.673 x 10 ²⁶	5.864 x 10 ²⁶	6.052 x 10 ²⁶	5.333 x 10 ²⁶
k_d^* (mole ⁻² .s ⁻¹)	4.217 x 10 ¹²	4.298 x 10 ¹²	3.964 x 10 ¹²	4.597 x 10 ¹²
ϵ_d^* (kJ/mole)	152.0	154.9	168.8	157.5

(a) Based on reported transient weight loss measurements.

(b) Based on reported measurements of total gasification rate versus weight loss up to 15%.

(c) Based on reported measurements of total gasification rate at a weight loss of 7.5%.

(d) Based on reported measurements of total gasification rate versus weight loss up to 60%.

(e) From the multi-parameter optimization algorithm.

To account for the change in chemical reactivity of nuclear graphite with weight loss, due to widening and random overlap of reacting surfaces (or coalescence) of the volume pores, the present chemical-reaction kinetics model employs the approach of Bathia and Perlmutter (1980). It helps in determining the change in the effective surface area of active sites in the volume pores during gasification at low and intermediate temperatures. Bathia and Perlmutter (1980) assume

that the graphite microstructure is comprised of infinitely-long overlapping random cylinders. The solid graphite microstructure is characterized using a structural parameter, Ψ given by:

$$\Psi = (4\pi L_v^o(1-\varepsilon_o)) / (S_v^o)^2 . \quad (3.11)$$

In Mode (a) of graphite gasification (Fig. 2.1a), the gasification rate within the volume pores is uniform and ASA is proportional to the internal surface of these open and interconnected pores. The fractional change in ASA with weight loss fraction, X , during gasification is expressed (Bathia and Perlmutter, 1980; Su and Perlmutter, 1985) as:

$$Y(X) = (1 - X) \sqrt{1 - \Psi \ln(1 - X)} . \quad (3.12)$$

Note that the approach of Su and Perlmutter (1985) does not account for the opening of initially closed volume pores, and would not be applicable to volume porosities > 60% and/or weight loss > 40%, when graphite fragmentation likely occurs. Results of the NBG-18 nuclear graphite gasification experiments of Hinssen et al. (2008) and those of Fuller and Okoh (1997) for nuclear graphite grades of K018, K022 and IG-110 confirmed that the maximum ASA typically occurs at a weight loss of ~ 35%. In the next section, the present chemical-reaction kinetics model, with the input parameters determined by the multi-parameter optimization algorithm, is applied to the gasification of the NBG-18 nuclear graphite specimens in the experiments of Chi and Kim (2008) and Hinssen et al. (2008) (Tables 3.1 and 3.2).

3.2.2 Effective surface area in experiments

In the diffusion-limited Mode (c), the input to the present chemical-reaction kinetics model includes the effective surface area of the nuclear graphite specimen in the experiment. This is the total geometrical surface area minus the portions of the surface experiencing either flow stagnation or not directly exposed to the air flow through the test section in the experiments. To identify the portions of the surface of the nuclear graphite specimens experiencing flow stagnation in the experiments (Table 3.1), 3-D Computational Fluid Dynamics (CFD) simulations are performed to calculate the flow fields in the tests using the STAR-CCM+ commercial software package (STAR-CCM+, 2012).

The obtained images of the flow fields are presented in Table 3.1. They show that the downstream end faces of the specimens in the gasification experiments of Chi and Kim (2008) could have partially contributed to the reported total gasification rates. The results of the present chemical-reaction kinetics model show that accounting for 50% of the downstream end face of the NBG-18 cylindrical specimen provides good agreement with the high-temperature gasification rate measurements reported by Chi and Kim (2008). In the experiments by Hinssen et al. (2008), the nuclear graphite specimens were seated on an alumina plate and the air flowed downward over the specimens, thus the bottom end face would not have contributed to the measured total gasification rates (Table 3.1). The calculations of the chemical-reaction kinetics model are compared next with the reported gasification measurements of NBG-18 nuclear graphite (Chi and Kim, 2008; Hinssen et al., 2008).

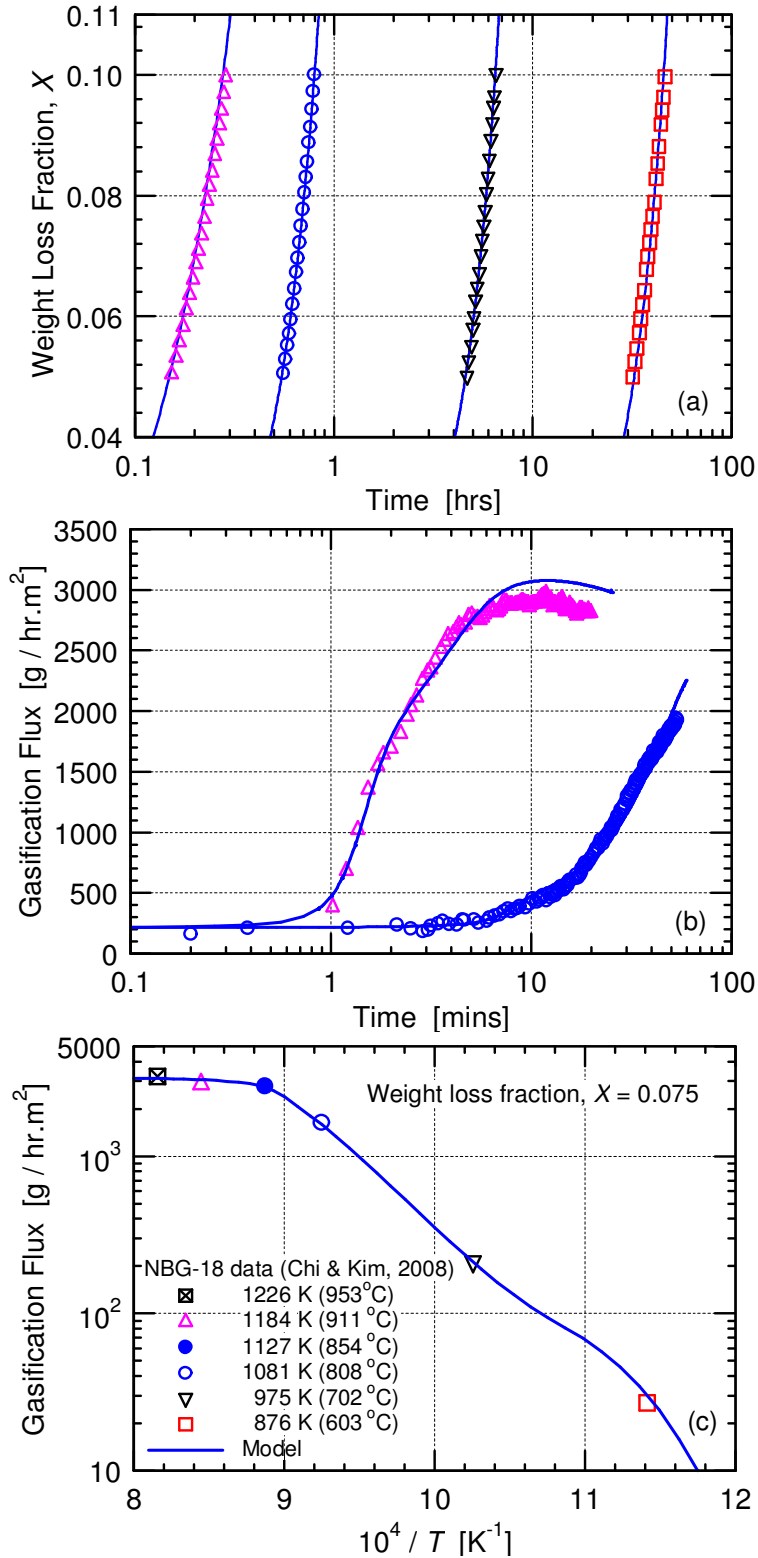


Figure 3.3. Comparison of Model Results with Reported Measurements for NBG-18 in the Experiments of Chi and Kim (2008): (a) Transient Weight Loss; (b) Transient Gasification Rate; (c) Arrhenius Curve of Total Gasification Rate.

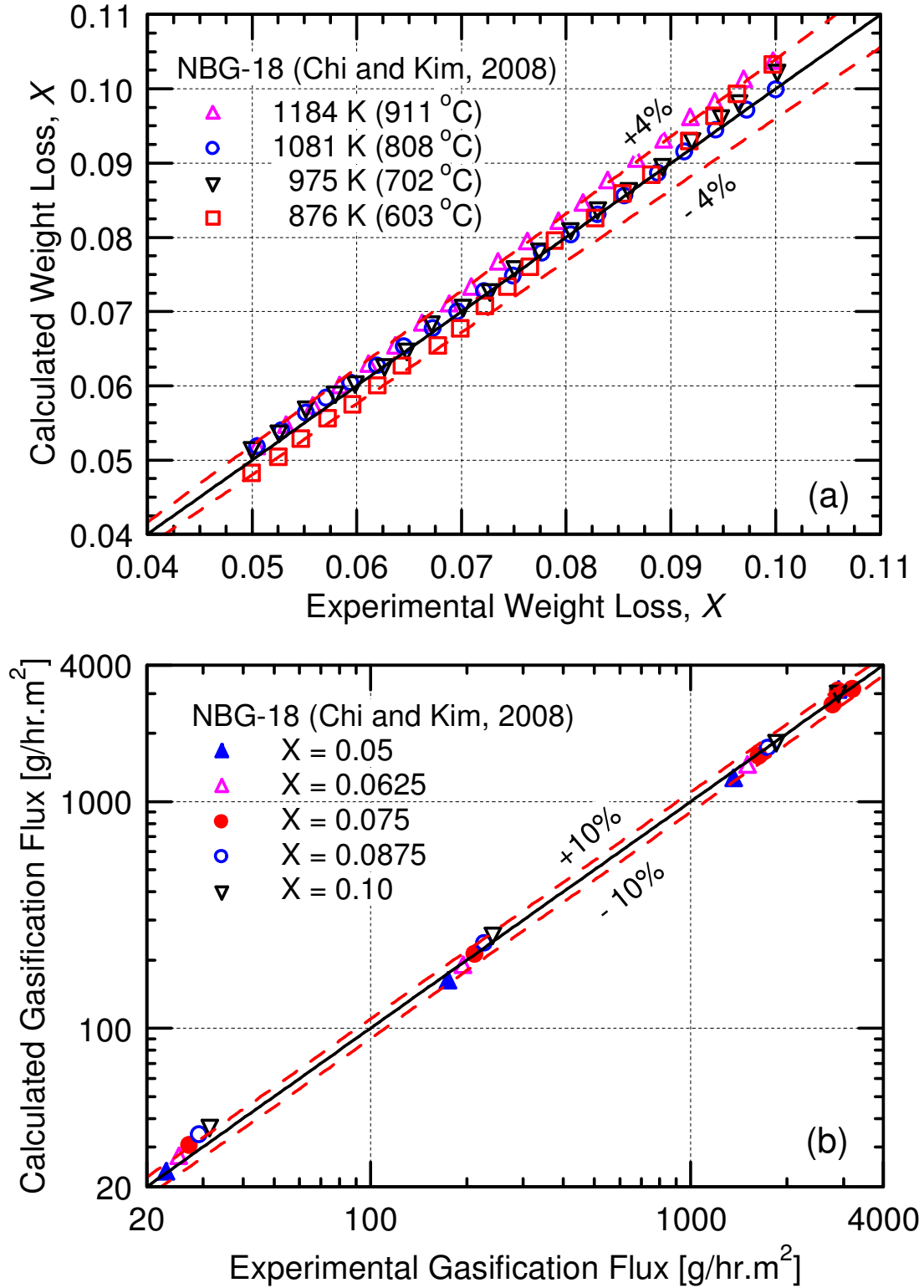


Figure 3.4. Comparison of Model Results with Reported Measurements for NBG-18 in the Experiments of Chi and Kim (2008); (a) Weight Loss Fraction; (b) Total Gasification Rate.

3.3 MODEL VALIDATION FOR NBG-18 NUCLEAR GRAPHITE

The reported total gasification rates and transient weight loss in the experiments by Chi and Kim (2008) and Hinssen et al. (2008) with NBG-18 nuclear graphite specimens are compared in this section with the calculations of the present chemical-reaction kinetics model. In these calculations, the used values of the microstructural parameters Ψ , defining the variation of active surface area for the test specimens with weight loss fraction (Eq. (3.12)), are obtained using a parametric analysis and best fit of the reported transient weight loss measurements. The determined values of Ψ for the NBG-18 specimens in the experiments of Hinssen et al. (2008) and Chi and Kim (2008) are listed in Table 3.2, along with the determined chemical kinetics parameters.

The reported transient weight loss measurements for the NBG-18 specimens in the experiments of Chi and Kim (2008) are accurately calculated using a structural parameter, $\Psi = 80$ (Table 3.2 and Figs. 3.3 and 3.4). The same value is used successfully in the present graphite oxidation model to predict the reported total gasification rate and transient weight loss measurements in experiments performed using identical test conditions and IG-110, IG-430 and NBG-25 nuclear graphite cylinders identical in size (Chi and Kim, 2008; El-Genk and Tournier, 2012). By contrast, the transient weight loss and total gasification measurements for the three NBG-18 cylindrical specimens, 1 (*), 2 (†) and 3 (⊥) in the experiments of Hinssen et al. (2008) are best predicted by the present model using a smaller Ψ of 35 (Table 3.2 and Figs. 3.5 and 3.6). The different values of the microstructural parameter Ψ are attributed to the differences in the size and shape of the NBG-18 specimens in the experiments. The specimens of Hinssen et al. (2008) are 2 orders of magnitude smaller and lighter than those of Chi and Kim (2008) (Table 3.1), and have higher total surface-to-volume ratio (8.73 versus 2.16 cm⁻¹).

The values of the 10 chemical kinetics parameters determined for each of the NBG-18 test specimens in Table 3.2 appear to be comparable and vary within a narrow range, except for the least reactive test specimens 2 (†) of Hinssen et al. (Table 3.2). These parameters include: (a) the most probable specific activation energy for the chemisorption of oxygen ($130.0 \leq \bar{\epsilon}_a \leq 143.8$ kJ/mole), standard deviation ($63.8 \leq \sigma_a \leq 65.9$ kJ/mole) and pre-exponential coefficient ($10,810. \leq k_a^o \leq 11,853. \text{ mole}^{-1} \cdot \text{s}^{-1}$); (b) the mean specific activation energy for the dissociation of oxygen radicals to form stable (CO) complexes ($191.8 \leq \epsilon_b \leq 196.3$ kJ/mole) and the pre-exponential coefficient ($9.56 \times 10^{14} \leq k_b^o \leq 9.80 \times 10^{14} \text{ mole}^{-1} \cdot \text{s}^{-1}$); (c) the most probable specific activation energy for the desorption of CO gas ($476.8 \leq \bar{\epsilon}_d \leq 503.6$ kJ/mole), and the standard deviation ($5.35 \leq \sigma_d \leq 5.67$ kJ/mole) and pre-exponential coefficient ($5.33 \times 10^{26} \leq k_d^o \leq 5.86 \times 10^{26} \text{ s}^{-1}$); and (d) the specific activation energy ($152.0 \leq \epsilon_d^* \leq 157.5$ kJ/mole) and pre-exponential coefficient ($4.22 \times 10^{12} \leq k_d^* \leq 4.60 \times 10^{12} \text{ mole}^{-2} \cdot \text{s}^{-1}$) for the desorption of CO₂ gas.

Conversely, the determined values of ASA_o and S_m^o for the four NBG-18 nuclear graphite specimens in the gasification experiments (Chi and Kim, 2008; Hinssen et al., 2008) are quite different (Table 3.2). These differences can be attributed to variations in the size, surface-to-volume ratio, microstructure and impurities of the graphite specimens in the experiments.

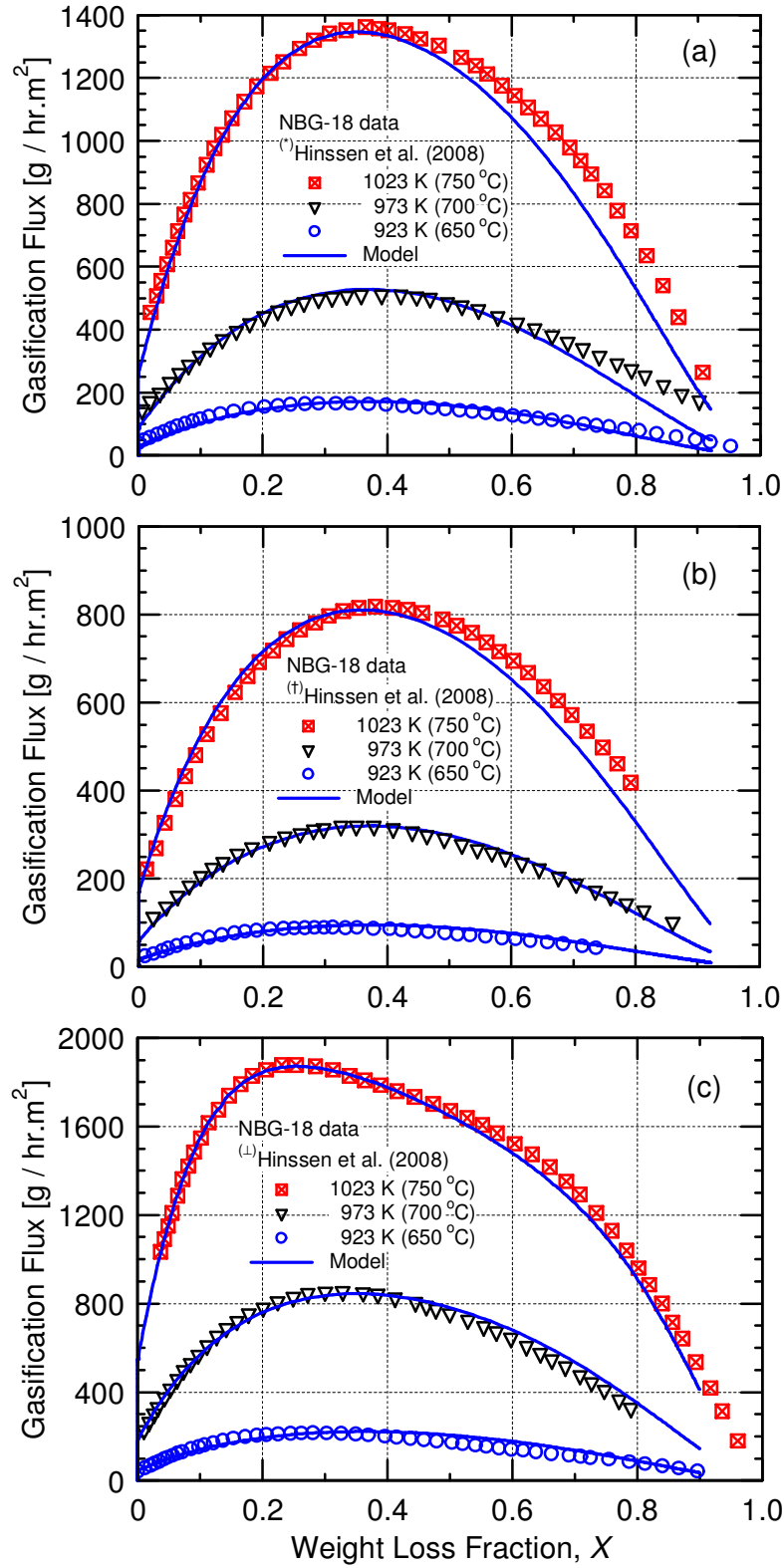


Figure 3.5. Comparison of Model Results of the Total Gasification Rate with Reported Measurements for NBG-18 in the Experiments of Hinssen et al. (2008): (a) Specimen 1 (*); (b) Specimen 2 (†); (c) Specimen 3 (⊥).

The determined chemical kinetics and microstructure parameters (Table 3.2), along with the estimates of the diffusion velocity, k_m in Fig. 3.2 are used to calculate the total gasification rate and transient weight loss for the NBG-18 specimens in the experiments of Chi and Kim (2008) and Hinssen et al. (2008). The comparisons of the model calculations with the reported measurements are for a wide range of temperatures, encompassing all three modes of graphite oxidation (Fig. 2.1).

3.3.1 Reported measurements by Chi and Kim (2008)

Figures 3.3a and 3.4a compare the calculated transient weight loss fractions for the NBG-18 specimens in the experiments of Chi and Kim (2008) (Table 3.1) with the reported measurements at 876 K, 975 K, 1081 K and 1184 K. At these temperatures, a weight loss fraction of 0.10 is reached in the experiments after 46 hrs, 6.6 hrs, 48 minutes and 17 minutes, respectively (Fig. 3.3a). Results in Figs. 3.3a and 3.4a show good agreement between calculated and measured transient values of the weight loss fraction, X in the experiments (Chi and Kim, 2008).

The calculations of the total gasification rate are also in good agreement with the measured rates in the experiments at 1081 K (808°C) and 1184 K (911°C) (Fig. 3.3b). The oxygen concentration in the volume pores is assumed to increase with time as a hyperbolic tangent at early times. Figure 3.3c compares the model calculations of the total gasification rate with the reported measurements for the NBG-18 specimens in the experiments of Chi and Kim (2008) (Table 3.2), at different temperatures and a weight loss fraction of 0.075. Figures 3.3c and 3.4b demonstrate excellent agreement between the calculations and the reported measurements, spanning more than 2 decades (Fig. 3.3c). The inflexion point in the calculations at 900 K corresponds to the condition when the CO and CO₂ production rates are equal. At low temperatures, graphite gasification produces mostly CO₂ gas, but above 980 K, graphite oxidation essentially produces CO gas and the contribution of the CO₂ gas to the total gasification rate becomes negligible.

As shown in Figs. 3.4a and 3.4b, the calculated weight loss fractions and total gasification rates for the NBG-18 specimens in the experiments of Chi and Kim are within $\pm 4\%$ and $\pm 10\%$ of the reported measurements, respectively. The good agreement between the calculations and the reported measurements in Figs. 3.3 and 3.4 confirms the effectiveness of the used multi-parameter optimization algorithm and the present chemical-reaction kinetics model. The model calculations show smooth Arrhenius curves (Fig. 3.3c) of the total gasification rate for the NBG-18 test specimens of Chi and Kim (2008). Similar calculations have recently been reported for IG-110, IG-430 and NBG-25 nuclear graphite specimens in experiments by Chi and Kim (2008) (El-Genk and Tournier, 2012a).

3.3.2 Reported measurements by Hinssen et al. (2008)

The reported gasification rate measurements for the dime-sized NBG-18 cylindrical specimens of Hinssen et al. (2008) [1 represented by the superscript (*), 2 represented by the superscript (†), and 3 represented by the superscript (⊥)] in Table 3.2 are compared with the calculations of the present model in Figs. 3.5 and 3.6, at three different temperatures, 923 K, 973 K and 1023 K. The chemical kinetics parameters and rate coefficients obtained for test specimens 1 (*) and 3 (⊥) in Figs. 3.5a and 3.5c are nearly identical to those of the NBG-18 specimens in the experiments of

Chi and Kim (2008), except for the values of the micro-structural parameters, Ψ and ASA_o (Table 3.2).

As shown in Fig. 3.5, the model calculations are in good agreement with the reported experimental measurements at 923 – 1023 K. At the highest temperature, the total gasification rates for the test specimens 1 (*) and 3 (\perp) are partially limited by the oxygen diffusion through the boundary layer. The results delineated in Fig. 3.5 show that the NBG-18 specimens in the experiments of Hinssen et al. (2008) exhibit large differences in reactivity, as indicated by their different ASA_o values in Table 3.2. The measured total gasification rate in the experiments for the most reactive specimen 3 (\perp) is 2.3 times that of the least reactive specimen 2 (\dagger), while the gasification rate for specimen 1 (*) is 65% higher than that of specimen 2 (\dagger). The determined values of ASA_o are 4.238 μmole ($S_m^o = 16.95 \mu\text{mole/g}$), 2.912 μmole ($S_m^o = 11.65 \mu\text{mole/g}$) and 5.405 μmole ($S_m^o = 21.62 \mu\text{mole/g}$) respectively (Table 3.2).

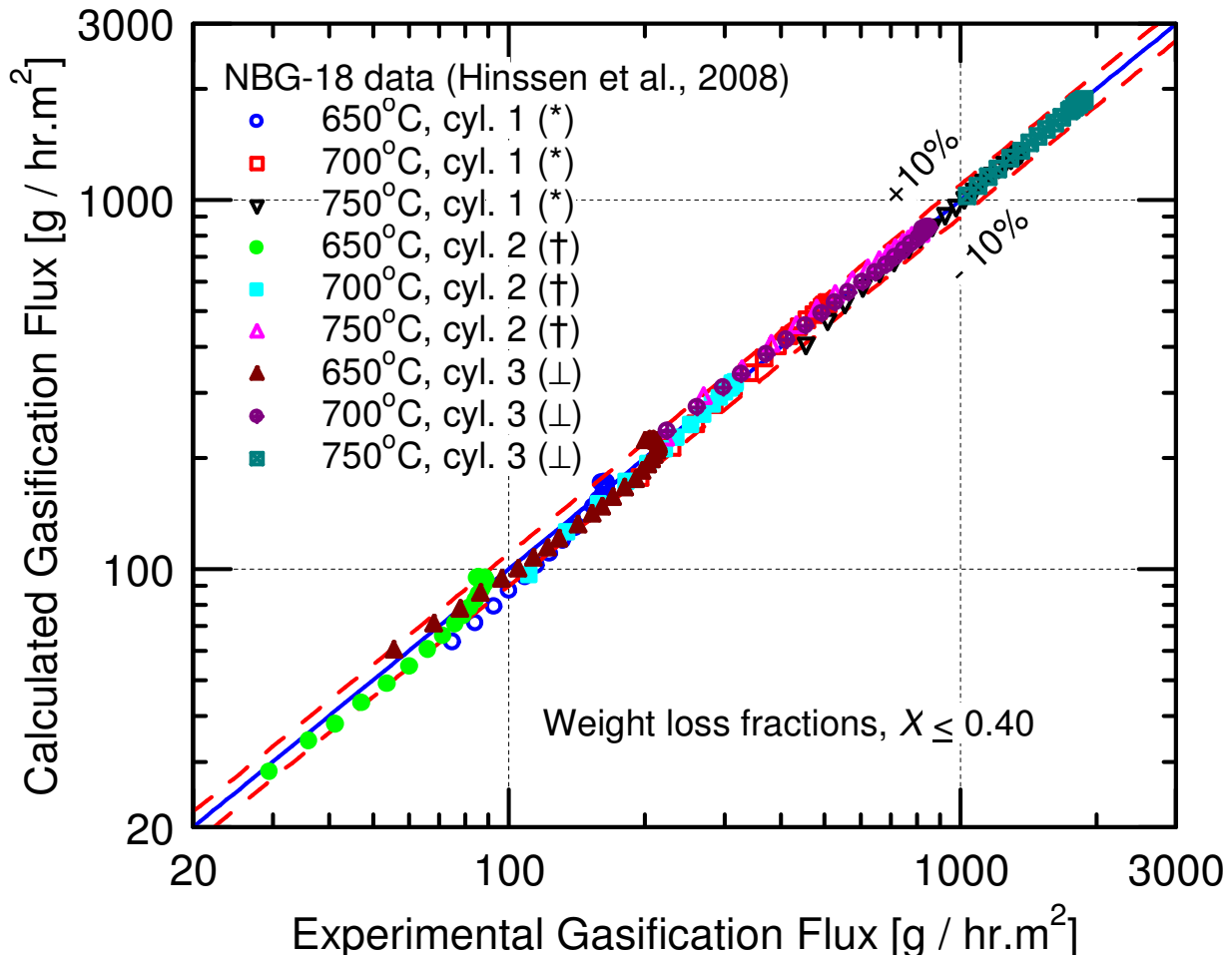


Figure 3.6. Comparison of Model Results with Reported Total Gasification Rates for NBG-18 Test Specimens in the Experiments of Hinssen et al. (2008) in Dry Air.

The model calculations and the reported measurements of the total gasification rates for specimens 1 and 2 of Hinssen et al (2008) peak at a weight loss fraction, $X \simeq 0.35$ (Figs. 3.5a and

3.5b). This value is representative of the variation in the surface area of the free active sites for these specimens with weight loss ($\Psi = 35$). By contrast, the total gasification rate at 1023 K for the most reactive specimen 3 peaks earlier at a weight loss of ~ 0.25 , apparently due to limited oxygen diffusion through the boundary layer (Mode (c)). The total gasification rate then decreases slowly with further increase in weight loss, due to the decrease in the external surface area of the specimen in the experiments (Fig. 3,5c).

The present model is not expected to be valid for weight loss fractions > 0.40 and/or volume porosities $> 60\%$, even though the comparison in Figs. 3.5a – 3.5c is generally good over the full range of weight loss. At weight loss fractions > 0.40 , nuclear graphite is expected to undergo a loss of structural strength and fragmentation. This may explain why the measured gasification rates at $X > 0.40$ are higher than the values calculated by the model (Fig. 3.5). As shown in Fig. 3.6, for weight loss fractions ≤ 0.40 , the calculated total gasification rates for all 3 NBG-18 specimens in the experiments of Hinssen et al. (2008) are within $\pm 10\%$ of the reported measurements, except for a few run-away data points at the lowest temperature of 923 K and low weight loss fractions.

The good agreements of the calculations with the experimental measurements reported by Chi and Kim (2008) and Hinssen et al. (2008) in Figs. 3.3 to 3.6 validate the present graphite gasification model. They also confirm the effectiveness of the multi-parameter optimization algorithm and procedure used to determine the values and distributions of the specific activation energies and other chemical kinetics parameters for NBG-18 specimens (Table 3.2).

3.4 PARAMETRIC ANALYSES

In this Section, parametric analyses are performed to examine the effects of both temperature and oxygen partial pressure on the production rates of CO and CO₂ gases and the total gasification rate as functions of weight loss, for the NBG-18 nuclear graphite specimens in the experiments of both Chi and Kim (2008) and Hinssen et al (2008). The results presented in this section include estimates of the times to reach weight loss fractions of 0.05, 0.10 and 0.40 and of the changes in the transient weight loss with both temperature and oxygen partial pressure. The performed parametric analyses use the diffusion velocities calculated using Eq. (3.7) and the developed correlation in Eq. (3.8) and Fig. 3.2 and the determined values and distributions of the specific activation energies (Figs. 3.1a and 3.1b), ASA_o , S_m^o , Ψ , and the chemical kinetics parameters (Table 3.2) for the NBG-18 cylindrical specimens in the gasification experiments of Chi and Kim (2008) and for specimens 1 (*) of Hinssen et al. (2008). The analyses are performed at atmospheric pressure, constant oxygen partial pressures of 0.5 – 21 kPa, and constant temperatures of 773 K to 1273 K. These temperatures cover all three oxidation modes of graphite (Fig. 2.1), with the total gasification rate spanning more than 4 decades.

3.4.1 Effects of temperature and oxygen partial pressure

The calculated results showing the effect of temperature on the total gasification rate of the NBG-18 specimen in the experiments of Chi and Kim (Tables 3.1 and 3.2) in air ($P_{O_2} = 21$ kPa) are shown in Fig. 3.7 as functions of the weight loss fraction, X . Below ~ 1050 K, the total gasification rate, driven by the changes in the graphite microstructure and ASA with weight loss, increases exponentially with increasing temperature. At higher temperatures (> 1050 K), graphite

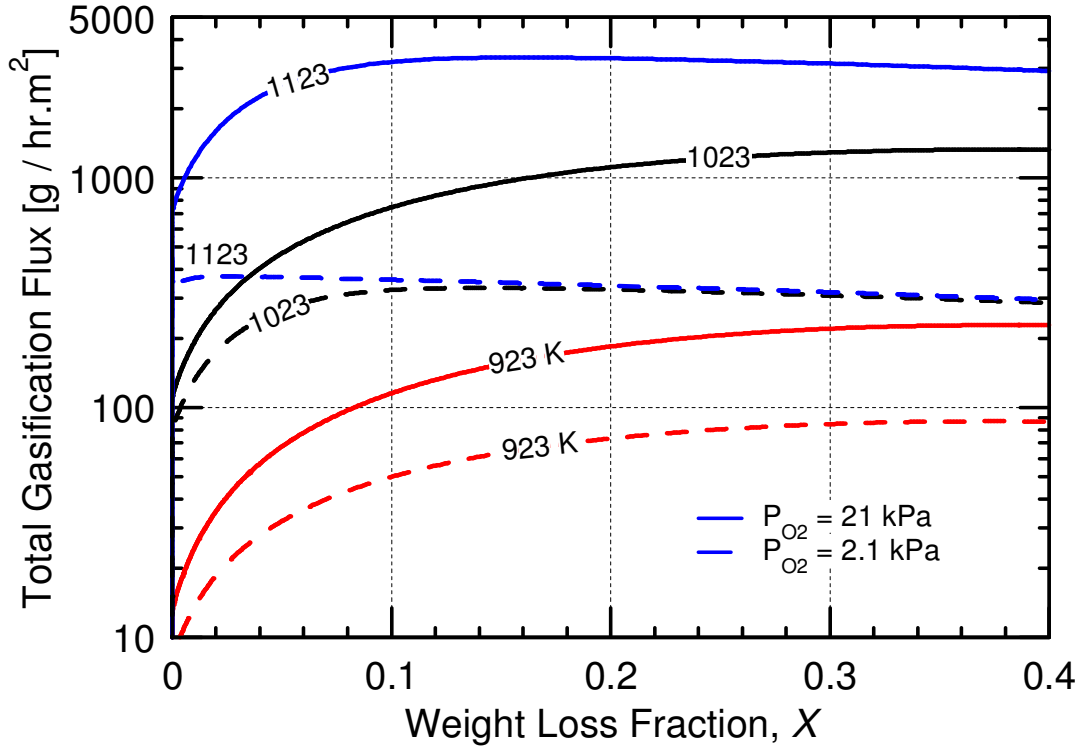


Figure 3.7. Model Predictions of Gasification Rate for NBG-18 Test Specimens of Chi and Kim (2008).

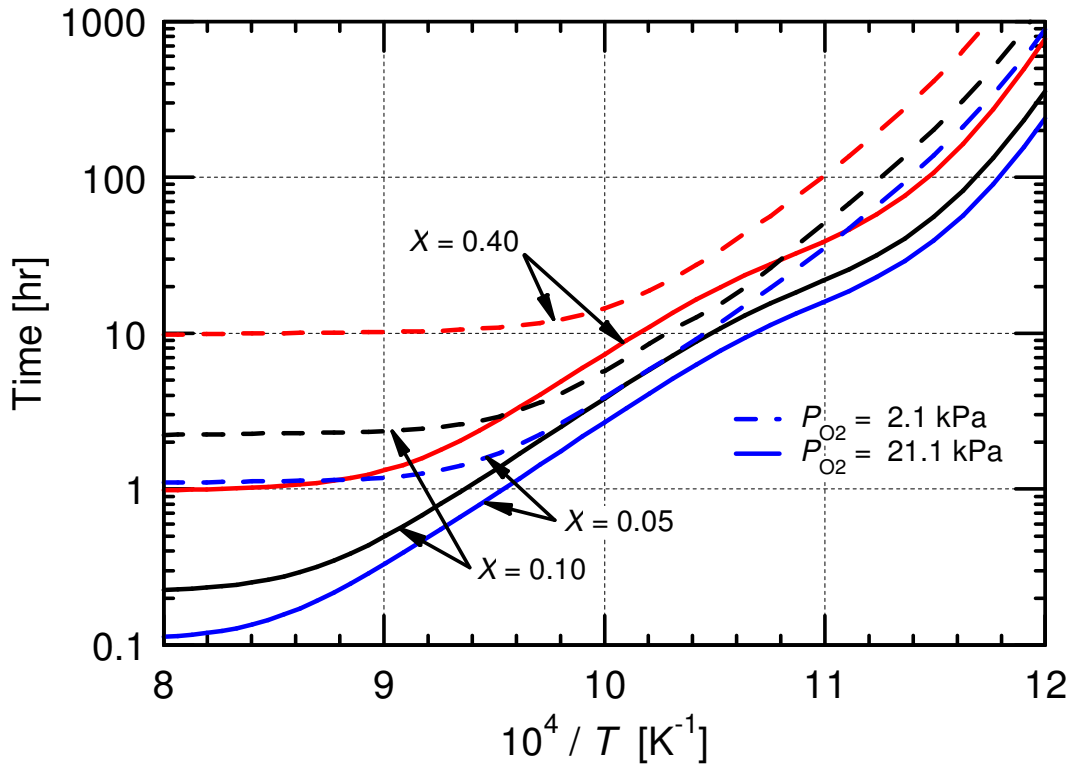


Figure 3.8. Calculated Time to Reach a Given Weight Loss for NBG-18 Test Specimens of Chi and Kim (2008).

gasification is diffusion-limited, and the total gasification rate is almost constant for weight loss fractions > 0.10 and nearly independent of temperature (Fig. 3.7). In this diffusion-limited Mode (c), the total gasification rate is proportional to the oxygen partial pressure in the bulk gas flow, P_{O_2} . It is encountered at 1023 K when $P_{O_2} = 2.1$ kPa, and at 1123 K when $P_{O_2} = 21$ kPa (Fig. 3.7). The slight decrease in the total gasification rate in Mode (c) with increasing weight loss fraction is due to the gradual decrease in the external surface area of the NBG-18 test specimen with time.

The time to reach a specific weight loss fraction strongly depends on both temperature and oxygen partial pressure (Fig. 3.8). In the diffusion-limited Mode (c), this time increases inversely proportional to P_{O_2} , and is almost independent of temperature. Conversely, at lower temperatures, when graphite gasification is driven by in-pores diffusion and/or chemical kinetics, the time to reach a specific weight loss fraction increases rapidly with decreasing temperature (Fig. 3.8). Decreasing the oxygen partial pressure also increases the time to reach a specific weight loss fraction over the entire range of temperatures, but significantly less when graphite gasification is not diffusion-, but chemical-kinetics limited (< 1050 K).

For example, at an oxygen partial pressure of 21 kPa, the time to reach a 0.40 weight loss fraction, $t_{0.4}$ at 873 K, 923 K, 973 K and 1023 K is 4.0 days, 31 hrs, 12.7 hrs and 4.6 hrs respectively (Fig. 3.9). For the same temperatures and oxygen partial pressure, a 0.10 weight loss fraction is reached after only 50 hrs, 17.4 hrs, 6.9 hrs and 2.4 hrs, respectively (Fig. 3.9). These are nearly half the times to reach a weight loss fraction of 0.40.

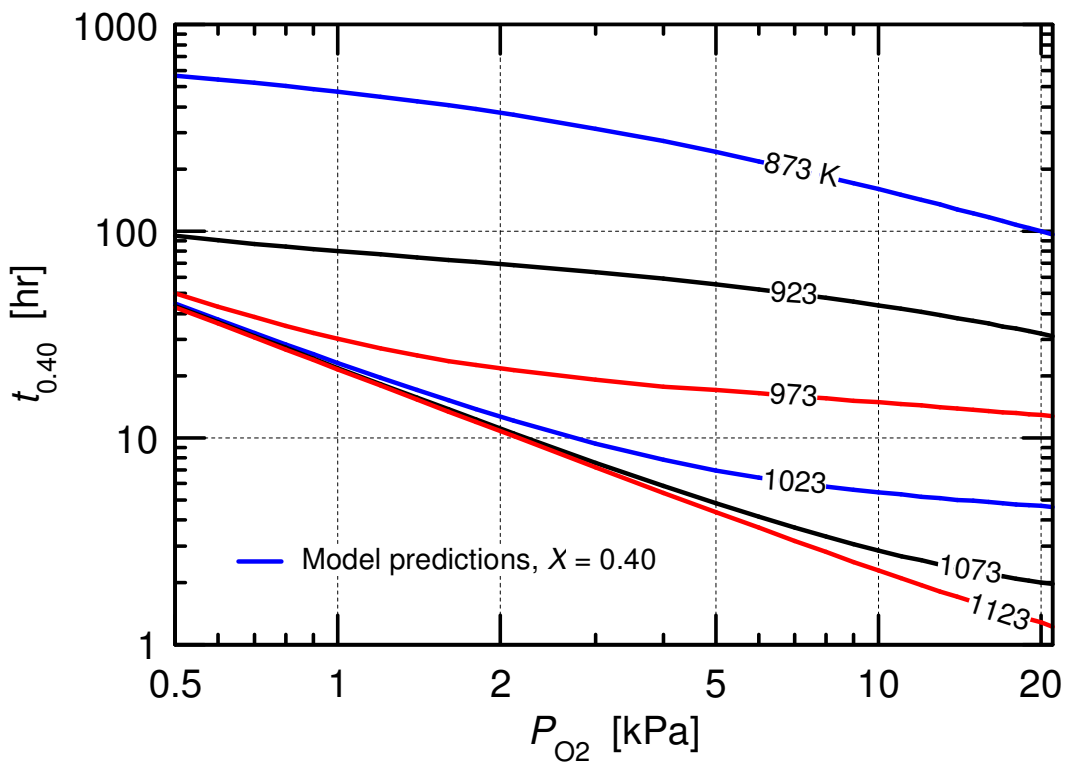


Figure 3.9. Calculated Time to Reach 40% Weight Loss for the NBG-18 Test Specimens of Chi and Kim (2008).

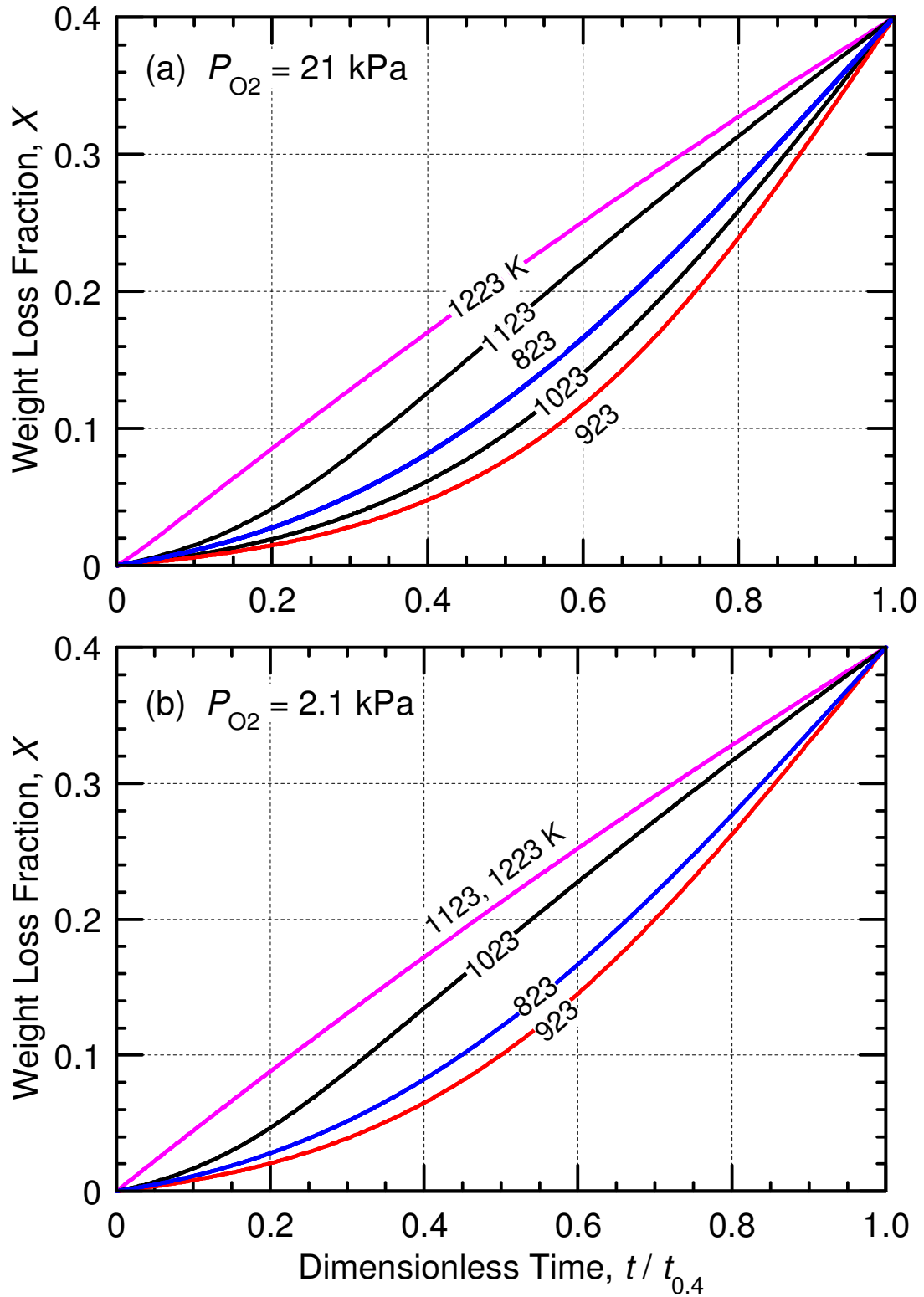


Figure 3.10. Results of Effect of Temperature on Weight Loss of NBG-18 Test Specimens of Chi and Kim (2008): (a) $P_{O_2} = 21$ kPa; (b) $P_{O_2} = 2.1$ kPa.

The time to reach a weight loss fraction of 0.40, $t_{0.4}$, is an interesting quantity that depends on both temperature and oxygen partial pressure (Fig. 3.9). This time spans more than 4 decades over the range of temperatures investigated and is inversely proportional to the oxygen partial pressure raised to a power n that varies from 0.3 to 1.0, depending on temperature. The value of $t_{0.4}$ decreases rapidly with increasing temperature up to 1050 K, and then becomes almost independent of temperature at low oxygen partial pressures (Fig. 3.9). At temperatures > 1050 K, when graphite gasification is limited by the oxygen diffusion through the boundary layer, $t_{0.4}$ decreases with increasing oxygen partial pressure with an order of unity, $n = 1.0$ (Fig. 3.9).

Figures 3.10a and 3.10b present the calculated weight loss fractions versus the dimensionless time, $\tau_{0.4} = t/t_{0.4}$ at different temperatures that span all three oxidation modes of graphite (Fig. 2.1). At temperatures < 1000 K, the profile of the weight loss fraction, X , versus $\tau_{0.4}$ exhibits a well-known sigmoid shape that is independent of the oxygen partial pressure. The inflexion at a weight loss fraction of 0.40 corresponds to the peak ASA for the NBG-18 nuclear graphite (Fig. 3.5). At temperatures > 1000 K, graphite gasification is diffusion-limited (Mode (c) in Fig. 2.1), and the weight loss fraction, X increases linearly with time (Figs. 3.10a and 3.10b).

For example, at an oxygen partial pressure of 2.1 kPa and 1023 K, graphite gasification becomes diffusion-limited after reaching a weight loss fraction of 0.05. At a higher temperature of 1123 K, graphite gasification is fully diffusion-limited (Fig. 3.10b). By contrast, at a higher P_{O_2} of 21 kPa and 1123 K, graphite gasification is partially diffusion-limited until $X = 0.06$ (Fig. 3.10a). This is because oxygen diffusion through the boundary layer is proportional to P_{O_2} .

3.4.2 CO and CO₂ production rates

The production rates of CO₂ and CO gases in the oxidation experiments of the NBG-18 nuclear graphite specimens of Chi and Kim (2008) and of ^(*)Hinssen et al. (2008) at different temperatures and oxygen partial pressures are calculated for a weight loss fraction of 0.10 (Figs. 3.11 and 3.12). In Fig. 3.11, the Arrhenius curves for the production rate of CO₂ gas span more than 9 decades, and those for the CO gas in Fig. 3.12 span nearly 4 decades. The temperatures in these figures span all three modes of graphite oxidation (Fig. 2.1).

Figure 3.11 shows that at temperatures $< 800 - 925$ K and oxygen partial pressures of 0.5 – 21 kPa, the production rates of CO₂ are comparable to or higher than those of CO. At higher temperatures, however, the production rates of CO are significantly higher than those of CO₂. At lower temperatures (< 900 K), the production rates of CO gas are lower and essentially independent of the oxygen partial pressure (Fig. 3.12). The effect of oxygen partial pressure becomes more pronounced at higher temperatures, when the diffusion-limited gasification of the NBG-18 nuclear graphite is proportional to P_{O_2} raised to a power of unity. The temperatures, beyond which the production rate of CO gas becomes constant, decrease with decreasing P_{O_2} (Fig. 3.12). In the diffusion-limited Mode (c), the CO production fluxes for the NBG-18 specimens in the experiments of ^(*)Hinssen et al. (2008) (Table 3.1) are 20% lower than those for the larger NBG-18 specimens of Chi and Kim (2008). This difference is caused by a 20% lower oxygen diffusion velocity in the boundary layer than in Chi and Kim experiments (Table 3.1 and Fig. 3.2).

At temperatures < 850 K, the surface active sites become essentially saturated with adsorbed oxide complexes and the rates of adsorption reactions (Eqs. (3.1a) and (3.2a)) are higher than those of the desorption reactions (Eqs. (3.3a) and (3.4a) and Table 3.2). On the other hand, at

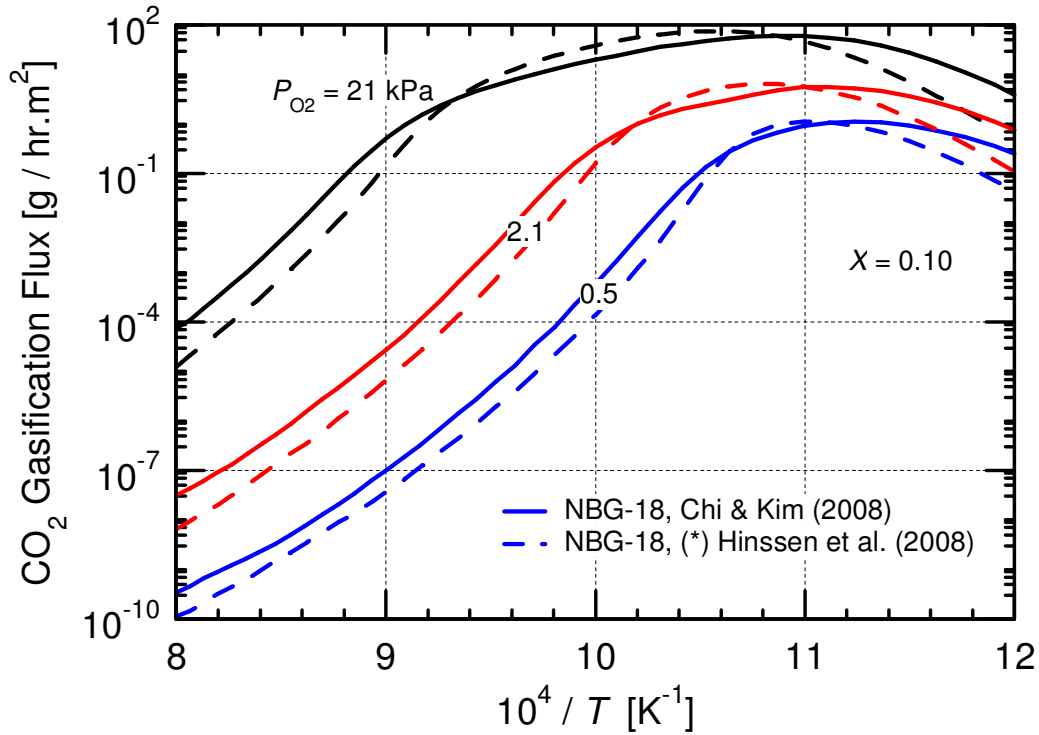


Figure 3.11. Results of Effects of Temperature and P_{O_2} on the CO_2 Production Rate for NBG-18 Nuclear Graphite Specimens.

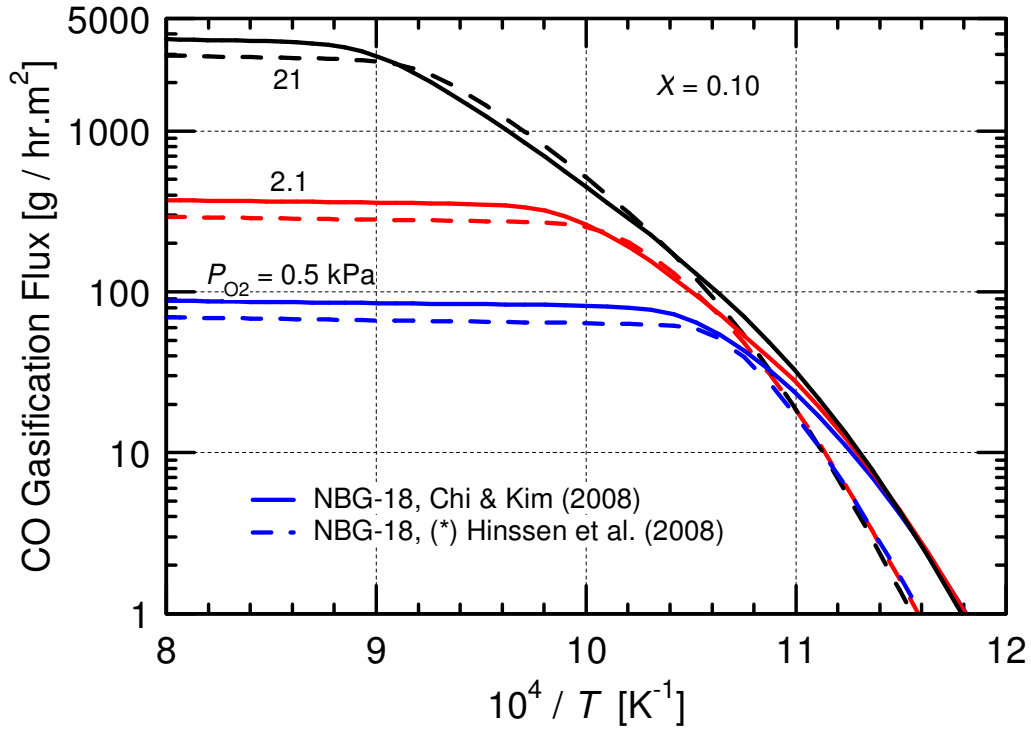


Figure 3.12. Results of Effects of Temperature and P_{O_2} on the CO Production Rate for NBG-18 Nuclear Graphite Specimens.

temperatures > 1050 K, the surface coverage with oxide complexes decreases and the rate of the CO desorption by the reactions in Eq. (3.3a) increases due to its higher effective activation energy (\bar{E}_d) (Table 3.2). At these temperatures, the desorption rate of the surface complexes is as fast as their rate of formation and the fractional coverage of the ASA is low, $< 20\%$ depending on oxygen partial pressure, thus the ASA is made up mostly of free active sites.

In the intermediate temperature range of $850 - 1050$ K, the ASA coverage with oxygen complexes is only partial and increases with increasing oxygen partial pressure. Also, in the chemical reactions given by Eq. (3.1a), the bonding of oxygen molecules to form un-dissociated oxygen complexes is first-order in oxygen pressure, increasing the gasification rate with increasing oxygen partial pressure. The results in Fig. 3.11 for the NBG-18 specimens of Chi and Kim (2008) show that the production rate of CO_2 gas initially increases exponentially with temperature, reaches a peak and then decreases steadily with further increase in temperature. This trend reflects the dependence of the CO_2 desorption reaction in Eq. (3.4a) on the availability of both surface free sites and stable (CO) complexes in close proximity to act as catalysts for the formation and desorption of CO_2 . The CO_2 production rate peaks when the ASA fractional coverage with surface complexes reaches $\sim 45\%$ to 55% , at $870 - 910$ K and oxygen partial pressures of 0.5 and 21 kPa (Fig. 3.11).

At temperatures < 900 K, the desorption rate of CO is much lower than for CO_2 gas molecules and hence, the latter becomes the primary contributor to the graphite total gasification. Also, the number of available surface free sites is low because many sites are occupied with stable oxide complexes. As the temperature increases, the contribution of CO production increases at the expense of decreasing that of CO_2 gas due to the decrease in surface coverage with stable (CO) complexes. At temperatures > 1050 K, graphite gasification is diffusion-limited and the CO_2 production rate decreases exponentially with increasing temperature, but increases with oxygen partial pressure to an effective order of ~ 4 (Fig. 3.11). The combination of decreasing surface coverage and exponential increase in the rates of the chemical reactions with temperature causes the CO desorption rate to increase faster than that of CO_2 , with effective activation energy of $400 - 450$ kJ/mole for NBG-18 specimens in the experiments of both Chi and Kim and Hinssen et al. (Table 3.1 and Fig. 3.12).

3.4.3 Total gasification rate

The total gasification rate is the sum of the production rates of CO and CO_2 gases. As discussed earlier, the latter prevails at low temperatures when graphite gasification is driven by the chemical kinetics and/or in-pores diffusion, and the former prevails at high temperatures when graphite gasification is diffusion-limited. For the NBG-18 specimens of Chi and Kim (2008), the calculated CO_2 gas production rate exceeds that of CO below 800 K, 860 K, 910 K and 930 K, when the oxygen partial pressure is 0.5 , 2.1 , 10 and 21 kPa, respectively (Fig. 3.11). For the NBG-18 specimens of Hinssen et al. (2008), these temperatures are 30 to 40 K lower (Fig. 3.11).

Figure 3.13 compares the calculated Arrhenius curves of the total gasification fluxes for the NBG-18 specimens in the experiments of Chi and Kim (2008) and Hinssen et al. (2008), at oxygen partial pressures of 0.5 , 2.1 and 21 kPa. The results clearly show that at high temperatures, when graphite gasification is diffusion-limited (Mode (c) in Fig. 2.1), the total gasification rate is almost independent of temperature, but increases with increasing P_{O_2} with an effective order of unity (Fig. 3.13). At low and intermediate temperatures (< 950 K), the total

gasification rate increases exponentially with increasing temperature (Fig. 3.13). The effect of the oxygen partial pressure on the total gasification rate at these temperatures is essentially due to the contribution of the CO₂ production (Figs. 3.12 and 3.13, and Eq. (3.4a)). In the experiments of Hinssen et al., the temperatures for Mode (c) of gasification to prevail are slightly lower than those in the experiments of Chi and Kim (Fig. 3.13).

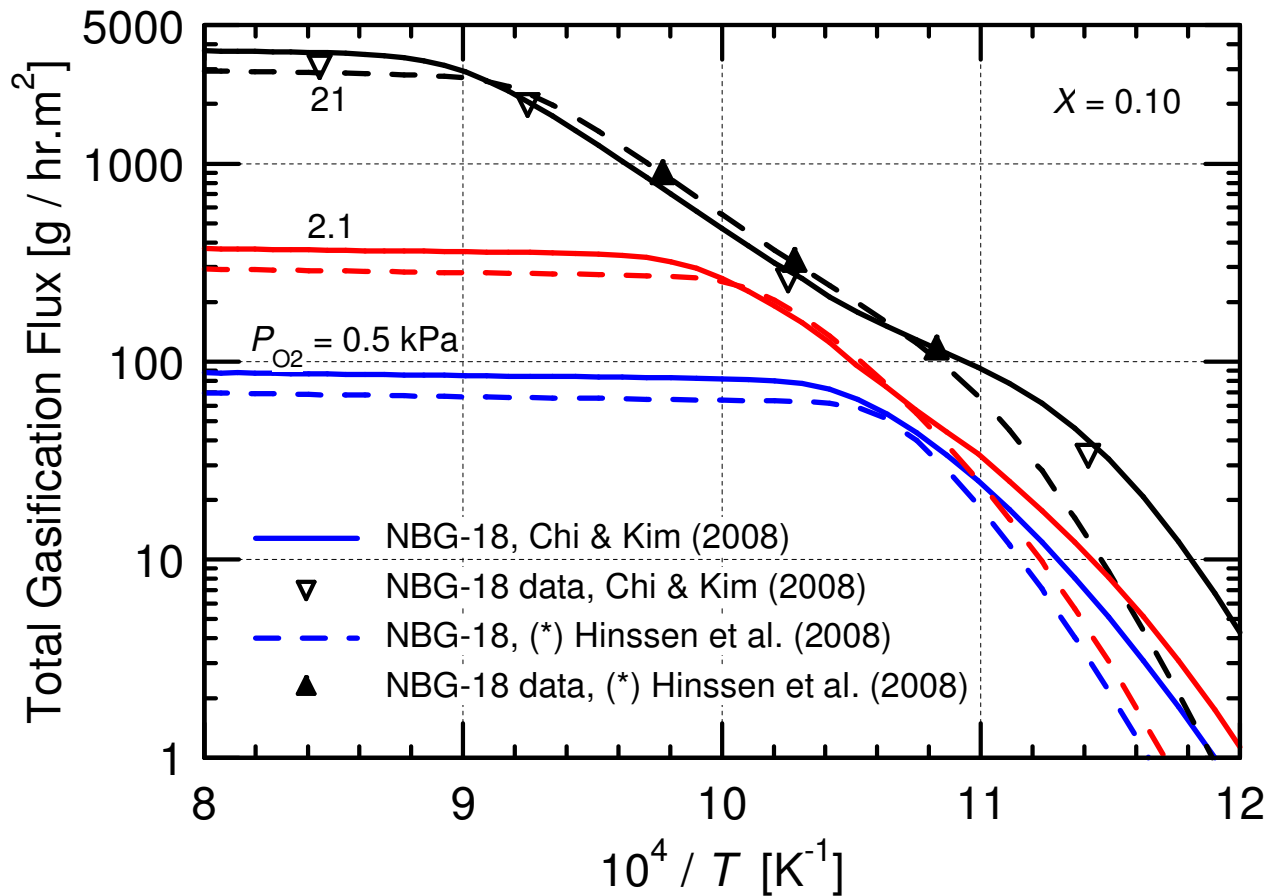


Figure 3.13. Results of Effects of Temperature and P_{O_2} on the Total Gasification Rate for NBG-18 Nuclear Graphite Specimens.

3.5 SUMMARY

The work in this chapter used a systematic methodology and applied a developed chemical-reaction kinetics model for predicting the reported gasification rates and transient weight loss for NBG-18 nuclear graphite specimens in experiments by different investigators. The chemical-reaction kinetics model also calculates the production rates of CO and CO₂ gases. The model employs 4 elementary reactions for the chemisorption of oxygen molecules to form un-dissociated oxygen radicals, the dissociation and adsorption of oxygen radicals to form stable surface complexes, the desorption of stable surface complexes to produce CO gas, and the desorption of CO₂ gas.

The specific activation energies for the adsorption of oxygen and desorption of CO gas in the model have Gaussian-like distributions. The model accounts for the change in the surface area of active sites (ASA) with weight loss using the Random Cylinders model, valid for weight loss fractions ≤ 0.40 . At high temperatures, when graphite gasification is diffusion limited, the model calculates the oxygen diffusion velocity in the boundary layer using a semi-empirical correlation developed for air flows at Reynolds numbers < 1000 . The model also accounts for the changes in the external surface area, the oxygen partial pressure in the bulk gas mixture and the effective diffusion coefficient in the boundary layer with weight loss.

The Gaussian-like distributions of the specific activation energies for adsorption of oxygen and desorption CO gas and the values of ASA_o , the pre-exponential rate constants and the kinetics parameters for the elementary chemical reactions are obtained using a multi-parameter optimization algorithm from the reported measurements of the total gasification rate and transient weight loss in the experiments. The obtained kinetics parameters and the values and Gaussian-like distributions of the specific activation energies for all NBG-18 test specimens, but one, are nearly identical (Table 3.2). However, the specific S_m^o values for the much smaller test specimens of Hinssen et al. (2008) are much higher than for the larger straight cylinders of Chi and Kim (2008).

The model calculations are compared favorably with the reported measurements for NBG-18 nuclear graphite specimens at different temperatures in flowing atmospheric air in the experiments of Hinssen et al. (2008) and Chi and Kim (2008) at various temperatures and weight loss fractions. Such good agreements validate the present model and confirm that the chemical-kinetics approach for graphite gasification is more realistic than the empirical approach, with predictably important consequences to the safety analysis of VHTRs and HTGRs in the unlikely event of an air ingress accident. The developed chemical-kinetics model provides thermodynamic information and chemical kinetics properties of nuclear graphite not obtainable otherwise.

A parametric analysis is performed, which investigated the effects of temperature and oxygen partial pressure on the total gasification and CO and CO₂ production rates, and on the transient weight loss for the NBG-18 cylindrical specimens used in the experiments of Chi and Kim (2080) and Hinssen et al. (2008). The results covered temperatures from 773 K to 1273 K and oxygen partial pressures of 0.5 – 21 kPa. The calculated continuous Arrhenius curves of the total gasification rate show that at low temperatures the total rate increases exponentially with temperature, and oxygen pressure with an order ≤ 1.0 . At these temperatures, graphite gasification is driven by the chemical kinetics of the elementary reactions. Conversely, at high temperatures when graphite gasification is diffusion limited, the total rate is almost independent of

temperature, but increases proportionally to the oxygen partial pressure raised to a power of unity.

The next Chapter 4 provides recommended values of the chemical kinetics parameters for the gasification of nuclear graphite grades of IG-110, IG-430, NBG-18 and NBG-25 and presents empirical correlations of the surface area of free active sites as a function of mass and type of graphite.

3.6 NOMENCLATURE

A_{flow}	Gas flow area (m^2)
A_w	Effective external surface area of graphite cylinder before oxidation (m^2)
ASA	Active surface area (mole)
C_{f,E_i}	Active free sites with activation energies in bin i
$C(O_2)_{E_i}$	Un-dissociated oxygen complexes in energy bin i
$(CO)_{E_i}$	Surface stable oxides complexes in energy bin i
D	Diameter of nuclear graphite test cylinder (m)
$D_{A,B}$	Binary diffusion coefficient for gas mixture of A and B components (m^2/s)
$D_{O_2,m}$	Effective diffusion coefficient of oxygen in experiments (m^2/s), Eq. (3.10)
$f(\mathcal{E})$	Normal probability function
H	Height of nuclear graphite test cylinder (m)
k_m	Effective diffusion velocity of oxygen in boundary layer (m/s), Eq. (3.7)
k^o, k^*	Pre-exponential rate constant ($\text{mole}^{-n} \cdot \text{s}^{-1}$)
L_v^o	Effective pore length per unit volume (m/m^3)
\dot{m}	Test gas mass flow rate (kg/s)
$[\hat{O}_2]_b$	Oxygen bulk gas concentration (mole/m^3)
$[\hat{O}_2]_w$	Oxygen concentration at graphite external surface (mole/m^3)
P_{O_2}	Partial pressure of oxygen (Pa)
R_g	Perfect gas constant ($8.3144 \text{ J}/\text{mole} \cdot \text{K}$)
\dot{R}	Reaction rate (mole/s)
Re	Reynolds number, $\dot{m}D / (\mu A_{\text{flow}})$
Sc	Schmidt number, $\nu / D_{O_2,m}$
Sh	Sherwood number, $k_m D / D_{O_2,m}$
S_m	Specific active surface area (mole/kg)
S_v^o	Pores volumetric surface area (m^2/m^3)
t	Time (s)
$t_{0.4}$	Time to 0.40 weight loss (s)
T	Temperature (K)
x_j	Molar fraction of gas species j in a mixture
X	Weight loss fraction
Y	Normalized active surface area, ASA/ASA_o
<i>Greek</i>	
\mathcal{E}	Specific activation energy (J/mole)
$\bar{\mathcal{E}}$	Gaussian most probable specific activation energy (J/mole)
\mathcal{E}_o	Initial volume porosity of nuclear graphite

μ	Gas dynamic viscosity (kg/m.s)
ν	Gas kinematic viscosity (m ² /s)
σ	Gaussian standard deviation (J/mole)
Ψ	Dimensionless structural parameter, Eq. (3.12)
$\tau_{0.4}$	Dimensionless time, $t / t_{0.4}$

Subscript/Superscript

a	Adsorption of oxygen onto active free sites to form un-dissociated complexes
b	Breakup of un-dissociated surface complexes to form stable complexes
CO	Carbon monoxide gas
d	Desorption of CO gas
i, j	Energy bin numbers
N_2	Nitrogen gas
o	Initial value
O_2	Oxygen gas
*	Desorption of CO ₂ gas

4. CHEMICAL KINETICS PARAMETERS OF NUCLEAR GRAPHITE GASIFICATION

The variables that affect the total gasification rate and transient weight loss of nuclear graphite in the unlikely event of an air ingress accident are operational and intrinsic. Operation variables include the total flow rate and total pressure of air or bulk gas mixture, the oxygen partial pressure and the graphite temperature. The intrinsic variables, which depend on the grade of nuclear graphite, include the specific activation energies for adsorption of oxygen and desorption of CO and CO₂ gaseous products; the surface area of active free sites and stable complexes; the graphite microstructure; and the volume porosity and the size and fraction of open volume pores. The impurities that could act as catalysts for oxidation also increase the reactivity and the total gasification rate of nuclear graphite.

Numerous experiments have been carried out with relatively small specimens of different grades of nuclear graphite to measure the total gasification rate and the transient weight loss at different flow conditions, compositions of the inlet gas, and specimen temperatures (Chi and Kim, 2008; Fuller and Okoh, 1997; Hinssen *et al.*, 2008; Kim and No, 2006; Xiaowei, Jean-Charles and Suyuan, 2004 and 2005). Experimental results have also shown that the orientation of the cutting plane of the relatively small specimens affects the oxidation reactivity (Xiaowei, Jean-Charles and Suyuan, 2005).

A practical and consistent alternative to calculating the total gasification rate of nuclear graphite is that based on the chemical kinetics of the elementary reactions involved. In addition to the predictably important consequences in the safety analysis of VHTRs and HTGRs, the chemical kinetics approach could calculate not only the total gasification rate and transient weight loss, but also the production rates of CO and CO₂ gases as functions of temperature, total pressure and flow rate of the bulk gas mixture, and oxygen partial pressure. It could also provide estimates of these quantities beyond the range of the experimental measurements, and of other quantities that are not measured in the experiments (El-Genk and Tournier, 2011 and 2012a). Examples include the surface active free sites and stable complexes as functions of weight loss, the progressive transition among the three principal modes of graphite gasification with increasing temperature (Figure 2.1), and the effects of changing the total flow rate and pressure of the bulk gas mixture and the oxygen partial pressure on graphite gasification.

The chemical-reaction kinetics model of nuclear graphite recently developed by the authors has been successfully validated with reported experimental measurements for different size specimens of NBG-18, NBG-25, IG-110 and IG-430 (El-Genk and Tournier, 2011 and 2012a; also Chapter 3 of this report). As explained earlier, the model employs only 4 elementary reactions and the applicable chemical kinetics parameters. These parameters include the values and Gaussian-like distributions of the specific activation energies and rate constants for the adsorption of oxygen and desorption of CO and CO₂ gaseous products, and the surface area of active free sites. The chemical kinetics parameters for IG-110, IG-430, NBG-18 and NBG-25 are obtained from the reported measurements of the total gasification rate and transient weight loss in the experiments with small specimens. The values of these parameters are determined using a multi-parameter optimization algorithm. However, for consistency and future application to the safety analysis of VHTR and HTGR in the unlikely event of an air ingress accident, this work also examines the applicability of the determined chemical kinetics parameters to large graphite

structures. In particular, the dependence of the surface active free sites on the mass or volume of the graphite structure is examined.

This Chapter compares the values of recently determined chemical kinetics parameters for the gasification of nuclear graphite grades of NBG-18, NBG-25, IG-11, IG-110 and IG-430 and makes recommendations of values for future safety analyses of VHTR and HTGR with massive graphite structures. Also presented are the results of an analysis investigating the effects of the graphite grade and mass on the total gasification rate as function of temperature. The analysis used the recently developed and validated chemical-reaction kinetics model for the gasification of different grades of nuclear graphite, and the recommended chemical kinetics parameters. The next Section briefly reviews the chemical kinetics and micro-structural parameters of the model.

4.1 CHEMICAL-REACTION KINETICS MODEL PARAMETERS

As explained earlier (see Section 3.1), the chemical-reaction kinetics model for graphite gasification incorporates the following successive processes: (a) adsorption of oxygen onto surface active free sites; (b) simultaneous formation of C-O bonds and break up of C-C bonds to form stable surface complexes; and (c) the desorption of CO and CO₂ gaseous products (El-Genk and Tournier, 2011 and 2012a).

The specific activation energies for the adsorption of oxygen onto surface active free sites (Eq. (3.1a)) have a Gaussian-like distribution (Figure 4.1), with a most-probable specific energy, $\bar{\epsilon}_a$ and a standard deviation, σ_a . Similarly, the specific activation energies for desorption of CO gas have a Gaussian distribution with a most-probable specific energy, $\bar{\epsilon}_d > \bar{\epsilon}_a$ and a standard deviation $\sigma_d < \sigma_a$ (Figure 4.2).

The input to the graphite gasification model includes 10 parameters: (a) the most-probable specific activation energies for adsorption of oxygen and desorption of CO ($\bar{\epsilon}_a$ and $\bar{\epsilon}_d$) and standard deviations (σ_a and σ_d) characterizing their Gaussian distributions; (b) the specific activation energies ϵ_b and ϵ_d^* for elementary reactions in Eqs. (3.2a) and (3.4a); and (c) the pre-exponential rate coefficients, k_a^o , k_b^o , k_d^o and k_d^* for the rate constants of the four elementary reactions, Eqs. (3.1b), (3.2b), (3.3b) and (3.4b).

The values of the chemical kinetics parameters are specific to the type of nuclear graphite, and the initial Active Surface Area (ASA_o) depends on the type of graphite and the size of the specimen. The change in the surface area of active sites (ASA) with weight loss indicates the reactivity of graphite and depends on its microstructure and the amounts of reactive impurities. The ASA changes with weight loss due to the widening and random overlap of reacting surfaces (or coalescence) within the volume pores during gasification in Modes (a) and (b) (Fuller and Okoh, 1997; Su and Perlmutter, 1985). To determine the change in ASA with weight loss, the model employs an approach that characterizes the graphite microstructure as comprised of infinitely-long overlapping random cylinders (Su and Perlmutter, 1985). This approach uses the volume pores distribution function, the initial volume porosity, total surface area and the effective pore length per unit volume to determine a structural parameter, Ψ . The fractional change in ASA with weight loss fraction, X , during gasification is expressed as (Su and Perlmutter, 1985):

$$Y(X) = \text{ASA}/\text{ASA}_o = (1 - X) \sqrt{1 - \Psi \ln(1 - X)} . \quad (4.1)$$

This approach does not account for the effect of opening previously closed volume pores and is not applicable to volume porosities > 60% and weight losses > 40%. The ASA increases initially with increasing weight loss to a maximum, then decreases with further increase in weight loss as the widening pores coalesce. Results of gasification experiments of nuclear graphite grades of NBG-18 (Hinssen *et al.*, 2008), K018, K022 and IG-110 (Fuller and Okoh, 1997) have confirmed that the maximum gasification rate typically occurs at a weight loss of ~ 35%. However, the rate and the maximum change in ASA with weight loss depend on the grade of nuclear graphite and the size and shape of specimens used in the experiments.

The values of the 10 chemical kinetics parameters, and of ASA_o and Ψ for individual grades of nuclear graphite are obtained using a multi-parameter optimization algorithm from the reported experimental measurements. These are the total gasification rate and the transient weight loss as a function of temperature (El-Genk and Tournier, 2011 and 2012a). As indicated earlier, the performed gasification experiments used small size specimens of IG-110, IG-430, NBG-25 and NBG-18 (Chi and Kim, 2008; Fuller and Okoh, 1997; Hinssen *et al.*, 2008) (Tables 4.1 and 4.2). These experiments are briefly described next.

4.2 GASIFICATION EXPERIMENTS

Table 4.1 summarizes the setups and conditions used in the gasification experiments of Chi and Kim (2008), Fuller and Okoh (1997) and Hinssen *et al.* (2008). These experiments employed small size specimens of IG-110, IG-430, NBG-25 and NBG-18 nuclear graphite. In the experiments of Chi and Kim (2008), the cylindrical graphite specimen is placed inside a quartz tube and attached, with wire, to an overhead micro-scale balance. The balance measures the graphite weight loss with time in the experiments. A non-contact infrared thermometer measured the bottom temperature of the specimen (Table 4.1). The graphite specimen is heated using an external vertical furnace. A continuous flow of atmospheric air enters through the bottom of the quartz tube (Table 4.1). Transient weight loss measurements from 5% to 10% are reported at 876, 975, 1081 and 1184 K, and total gasification rate measurements at a 7.5% weight loss are also reported at 1127 and 1226 K.

In the experiments of Fuller and Okoh (1997), the IG-110 cylindrical specimen was seated onto an alumina crucible. The crucible is connected to a weight-scale below by a small-diameter alumina support rod. A Pt-10%Rh thermo-couple, inserted through the rod to the base of the crucible, measured the temperature of the specimen (Table 4.1). The graphite specimen is heated using an electric furnace. Fuller and Okoh (1997) reported transient weight loss data up to 86% in atmospheric air flow at a specimen temperature of 750 °C (1023 K). They also reported total gasification rates for 13.3% weight loss at 723 to 1023 K.

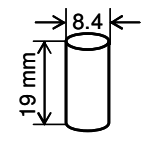
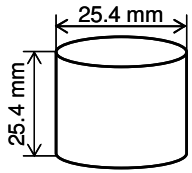
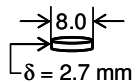
The total gasification measurements reported by Fuller and Okoh (1997) are only applicable to Modes (a) and (b) (Figure 2.1). In their experiments, Hinssen *et al.* (2008) used three very small graphite specimens cut from different cylinders. The specimen was seated onto an alumina plate, and the introduced air flowed downward over the specimens (Table 4.1).

The IG-110 cylindrical specimens used in the experiments of Fuller and Okoh (1997) (1.756 g) are an order of magnitude smaller than the IG-110, IG-430, NBG-25 and NBG-18 specimens in the experiments of Chi and Kim (2008), weighing between 22.52 and 23.81 g (Table 4.2).

Table 4.1. Test Conditions and Setups in Reported Gasification Experiments of Nuclear Graphite (Chi and Kim, 2008; Fuller and Okoh, 1997; Hinssen *et al.*, 2008).

Reference	Chi and Kim (2008)	Hinssen <i>et al.</i> (2008)	Fuller & Okoh (2008)
Specimen dimensions (mm)	$D = 25.4, H = 25.4$	$D = 8.0, H = 2.69$	$D = 8.41, H = 19.05$
Specimen volume (cm ³)	12.87	0.1351	1.058
Effective side area (cm ²)	27.87	1.179	5.589
Bulk Gas	Dry air	Dry air	Dry air
Flow direction	Up	Down	Down
Total pressure, P (kPa)	101.3	100.0	101.3
P_{O_2} (mole%)	21.0	21.0	21.0
Flow (SLPM)	10.0	0.125	0.50
Heating method	Furnace	Furnace	Furnace
Mounting method	Dangled	On alumina plate	On alumina plate
Test tube	Quartz	–	–
Tube diameter (mm)	76.2	30.0	76.2
Specimen temperature, K (°C)	876 – 1,226 (603 – 953)	923 – 1023 (650 – 750)	723 – 1023 (450–750)
Test Setup			

Table 4.2. Kinetics and Micro-Structural Parameters for Different Grades of Nuclear Graphite.

Parameters	Fuller and Okoh (1997)	Chi and Kim (2008)				Hinssen <i>et al.</i> (2008)		
Graphite type	IG-110	IG-110	IG-430	NBG-25	NBG-18	NBG-18 ^(*)	NBG-18 ^(†)	NBG-18 ^(⊥)
Density (g/cm ³)	1.66	1.75	1.82	1.82	1.85	1.85	1.85	1.85
Mass (g)	1.756	22.52	23.42	23.42	23.81	0.25	0.25	0.25
Specimen	#17	#18a	#18b	#18c	#18d	#19a	#19b	#19c
Specimen dimensions								
Microstructural Parameters								
Ψ	80 ^(c)	80 ^(a)	80 ^(a)	80 ^(a)	80 ^(a)	35 ^(a)	35 ^(a)	35 ^(a)
ASA _o (μmole)	8.91 ^(d,e)	29.28 ^(b,e)	15.75 ^(b,e)	29.81 ^(b,e)	14.29 ^(b,e)	4.24 ^(b,e)	2.91 ^(b,e)	5.41 ^(b,e)
S _m ^o (μmole/g)	5.07	1.30	0.673	1.27	0.60	16.95	11.65	21.62
Oxidation Kinetics Parameters								
$\bar{\epsilon}_a$ (kJ/mole)	124.6	117.0	115.0	119.7	130.0	132.6	126.8	143.8
σ_a (kJ/mole)	50.70	64.35	63.25	59.85	65.49	63.80	39.41	65.87
k _a ^o (mole ⁻¹ .s ⁻¹)	13,199.	13,014.	12,842.	12,776.	11,853.	11,325.	11,843.	10,810.
k _b ^o (mole ⁻¹ .s ⁻¹)	8.844 x 10 ¹⁴	7.568 x 10 ¹⁴	10.60 x 10 ¹⁴	7.351 x 10 ¹⁴	9.558 x 10 ¹⁴	9.754 x 10 ¹⁴	12.50 x 10 ¹⁴	9.802 x 10 ¹⁴
ϵ_b (kJ/mole)	203.1	205.3	199.5	205.7	196.3	196.2	194.3	191.8
$\bar{\epsilon}_d$ (kJ/mole)	416.3	484.5	475.6	486.3	476.8	498.5	478.5	503.6
σ_d (kJ/mole)	5.645	4.96	6.153	5.118	5.647	5.669	6.114	5.353
k _d ^o (s ⁻¹)	7.08 x 10 ²⁶	4.234 x 10 ²⁶	5.462 x 10 ²⁶	4.333 x 10 ²⁶	5.673 x 10 ²⁶	5.864 x 10 ²⁶	6.052 x 10 ²⁶	5.333 x 10 ²⁶
k _d [*] (mole ⁻² .s ⁻¹)	4.477 x 10 ¹²	5.112 x 10 ¹²	3.712 x 10 ¹²	5.091 x 10 ¹²	4.217 x 10 ¹²	4.298 x 10 ¹²	3.964 x 10 ¹²	4.597 x 10 ¹²
ϵ_d^* (kJ/mole)	159.1	158.4	149.4	158.0	152.0	154.9	168.8	157.5

(a) Based on reported transient weight loss measurements; (b) Based on reported measurements of the transient weight loss and total gasification rate; (c) Assumed as in (a) for same IG-110 graphite type; (d) Based on reported total gasification rate measurements versus weight loss up to 86%; (e) From multi-parameter optimization algorithm (El-Genk and Tournier, 2011 and 2012a); and *, † and ⊥ are specimens cut from different cylinders.

The IG-110 specimens of Chi and Kim are also 5.4% denser than those of Fuller and Okoh (1997) (1.75 g/cm^3 versus 1.66 g/cm^3). The IG-430 and NBG-25 specimens used in the experiments by Chi and Kim (2008) are 4% denser than IG-110 (1.82 g/cm^3 versus 1.75 g/cm^3). Although the experiments were performed with dry air at atmospheric pressure (inlet oxygen partial pressure of 21.4 kPa), the standard air inlet flow rate in the experiments of Chi and Kim (2008) (10 SLPM) was 20 times that used in the experiments by Fuller and Okoh (1997) (0.50 SLPM).

The NBG-18 dime-sized cylindrical specimens in the experiments of Hinssen *et al.* (2008) are much smaller (0.25 g) (Table 4.1), with markedly different reactivity. Since the specific surface areas of active free sites for the specimens in these experiments are not reported, the values listed in Table 4.2 are obtained from the total gasification rate measurements using a multi-parameter optimization algorithm, in conjunction with the chemical-reaction kinetics model (El-Genk and Tournier, 2012a). Table 4.2 compares the obtained values of Ψ , ASA_0 and S_m^o for the nuclear graphite specimens of IG-110, IG-430, NBG-18 and NBG-25 in the gasification experiments (Chi and Kim, 2008; Fuller and Okoh, 1997; Hinssen *et al.*, 2008; see Table 4.1).

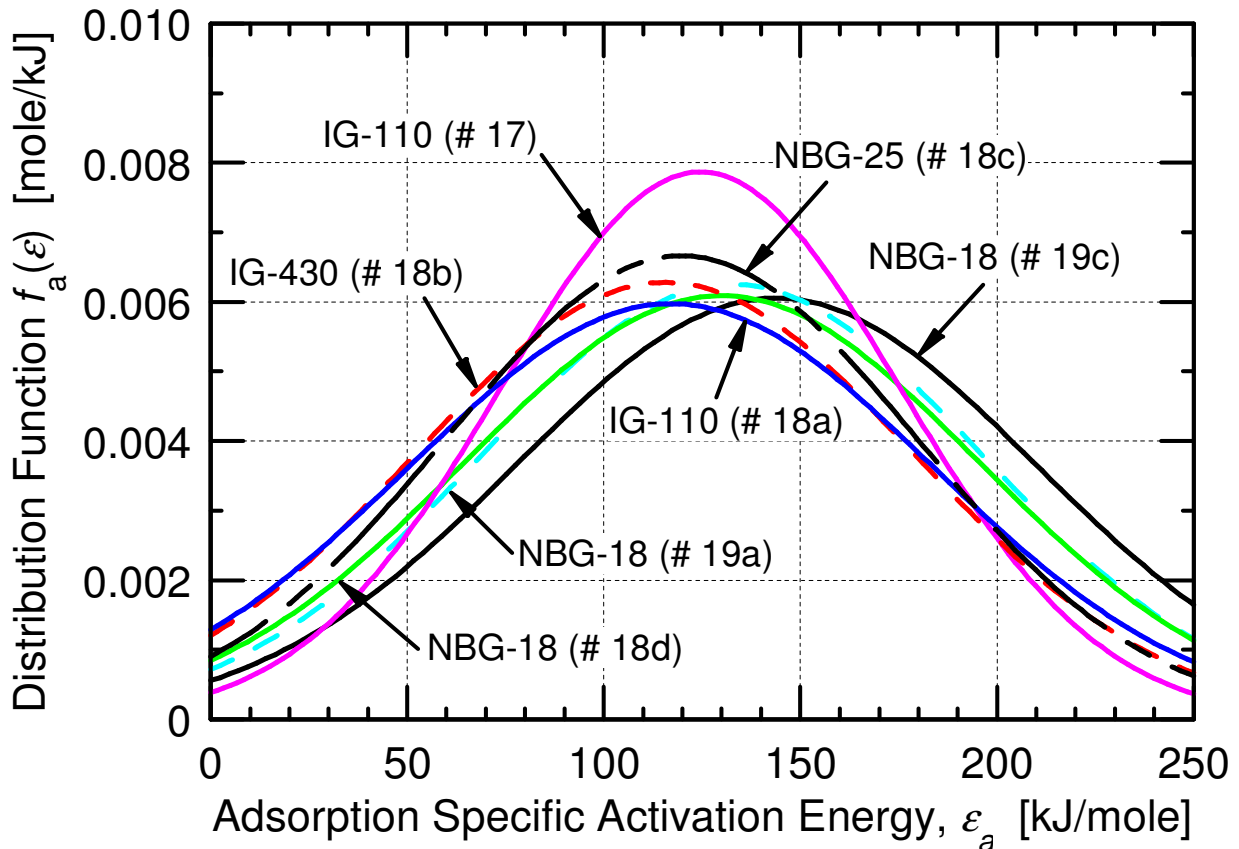


Figure 4.1. Gaussian-like Distributions of the Specific Activation Energies for Adsorption of Oxygen for Different Grades of Nuclear Graphite (*Numbers in Parentheses Refer to the Specimen Numbers Listed in Table 4.2*).

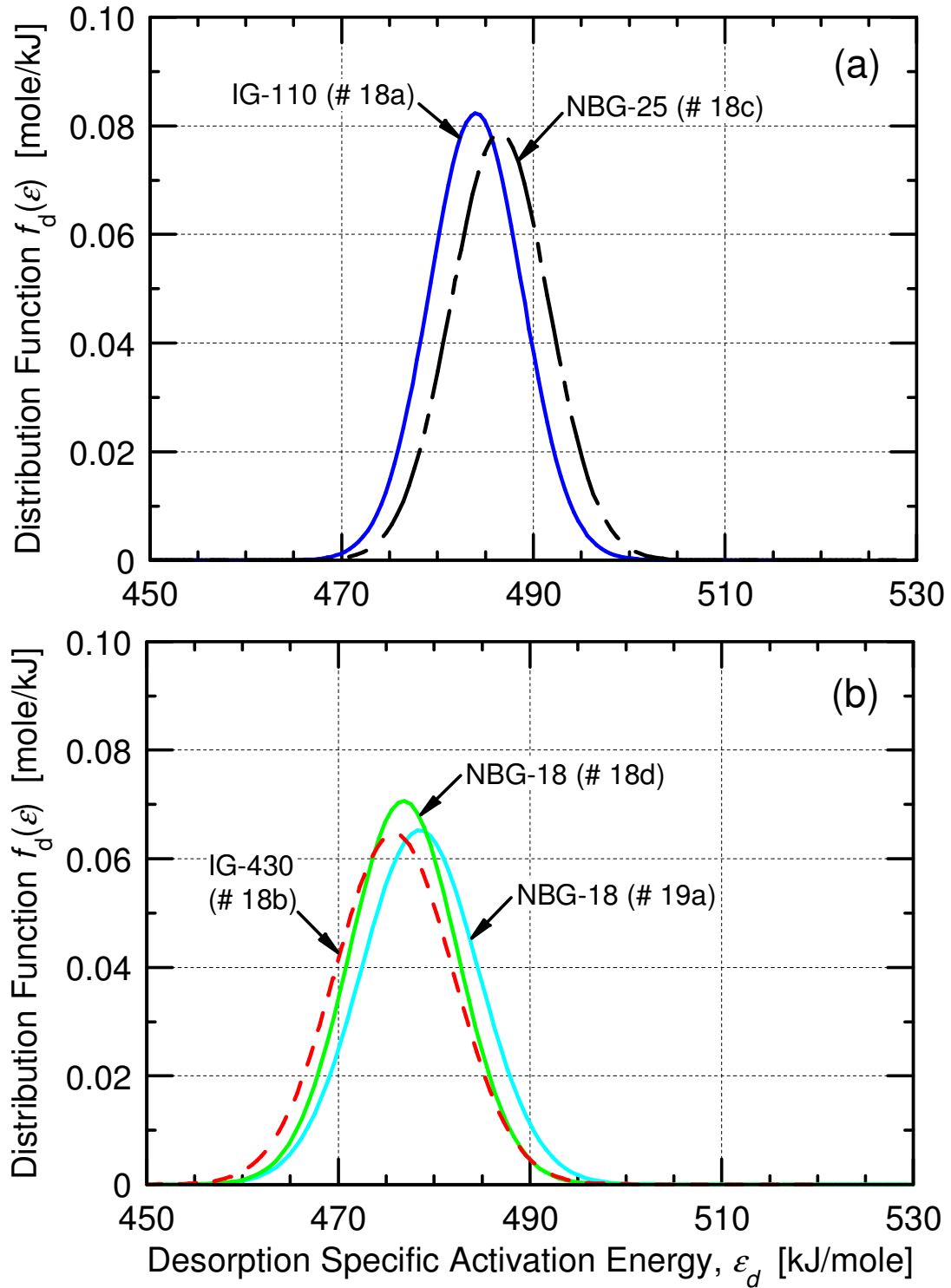


Figure 4.2. Gaussian-like Distributions of Specific Activation Energies for Desorption of CO Gas for Different Grades of Nuclear Graphite. (a) IG-110 and NBG-25; (b) IG-430 and NBG-18 (*Numbers in Parentheses Refer to the Specimen Numbers Listed in Table 4.2*).

4.3 CHEMICAL KINETICS PARAMETERS

The chemical kinetics parameters obtained for the different grades of nuclear graphite used in the aforementioned gasification experiments include:

- (a) The Gaussian-like distributions of the specific activation energies (Figures 4.1 and 4.2) for adsorption of oxygen and desorption of CO gas, ε_a and ε_d , and the corresponding pre-exponential rate coefficients, k_a^o and k_d^o (Figures 4.6 and 4.8) for the reactions in Eqs. (3.1) and (3.3). These distributions (Figures 4.1 and 4.2) are fully described using the most probable activation energies $\bar{\varepsilon}_a$ and $\bar{\varepsilon}_d$ (Figures 4.3a and 4.3b), and the standard deviations σ_a and σ_d (Figures 4.4a and 4.4b).
- (b) The specific activation energy for desorption of CO₂ gas, ε_d^* (Figure 4.5), and corresponding pre-exponential coefficient, k_d^* (Figure 4.7) for the reactions in Eqs. (3.4a) and (3.4b).
- (c) The specific activation energy for un-dissociated surface oxides to form stable complexes, ε_b and pre-exponential coefficient, k_b^o (Eqs. (3.2a) and (3.2b)) in Figures 4.5 and 4.6.

The Gaussian-like distributions of the specific activation energies for adsorption of oxygen and desorption of CO gas, obtained from the gasification rate measurements in the experiments (Chi and Kim, 2008; Fuller and Okoh, 1997; Hinssen *et al.*, 2008), are compared in Figures 4.1 and 4.2. The distributions for the specific activation energies of the different graphite grades for oxygen adsorption are quite similar and the values of the most-probable specific activation energy ($\bar{\varepsilon}_a$) and the characteristic standard deviation (σ_a) are very close (Figures 4.3a and 4.4a). The values of $\bar{\varepsilon}_a$ for different grades of nuclear graphite vary from 115 – 144 kJ/mole (Figure 4.3a) and the corresponding Gaussian standard deviations, σ_a vary from 51 – 66 kJ/mole (Figure 4.4a).

The distributions of the specific activation energies for desorption of CO gas during gasification of different grades of nuclear graphite in the experiments are similar with a most-probable value, $\bar{\varepsilon}_d = 416 – 504$ kJ/mole (Figure 4.2 and Table 4.2) and standard deviation of 5 – 6.1 kJ/mole (Figure 4.4b). The distributions for the IG-110 specimens #17 of Fuller and Okoh (1997) and NBG-18 specimens #19c of Hinssen *et al.* (2008) are different from those of the others. The Gaussian distributions of the specific energies of CO desorption for the IG-110 specimens #18a and NBG-25 specimens #18c (Chi and Kim 2008) are nearly identical (Figure 4.2a). Similarly, the IG-430 specimens #18b and NBG-18 specimens #18d of Chi and Kim (2008), and the NBG-18 specimens #19a of Hinssen *et al.* (2008) exhibit nearly identical Gaussian distributions (Figure 4.2b).

Figures 4.3a and 4.3b present the recommended values of the specific activation energies for adsorption of oxygen ($\bar{\varepsilon}_a$) and desorption of CO gas ($\bar{\varepsilon}_d$) for nuclear graphite grades of IG-110 and NBG-25. These values are $\bar{\varepsilon}_a = 120.4 \pm 4$ kJ/mole and $\bar{\varepsilon}_d = 485.4 \pm 3$ kJ/mole (Figures 4.3a and 4.3b). They are slightly different from those recommended in this work for IG-430 and NBG-18: $\bar{\varepsilon}_a = 131.7 \pm 16$ kJ/mole and $\bar{\varepsilon}_d = 476 \pm 24$ kJ/mole (Figures 4.3a and 4.3b).

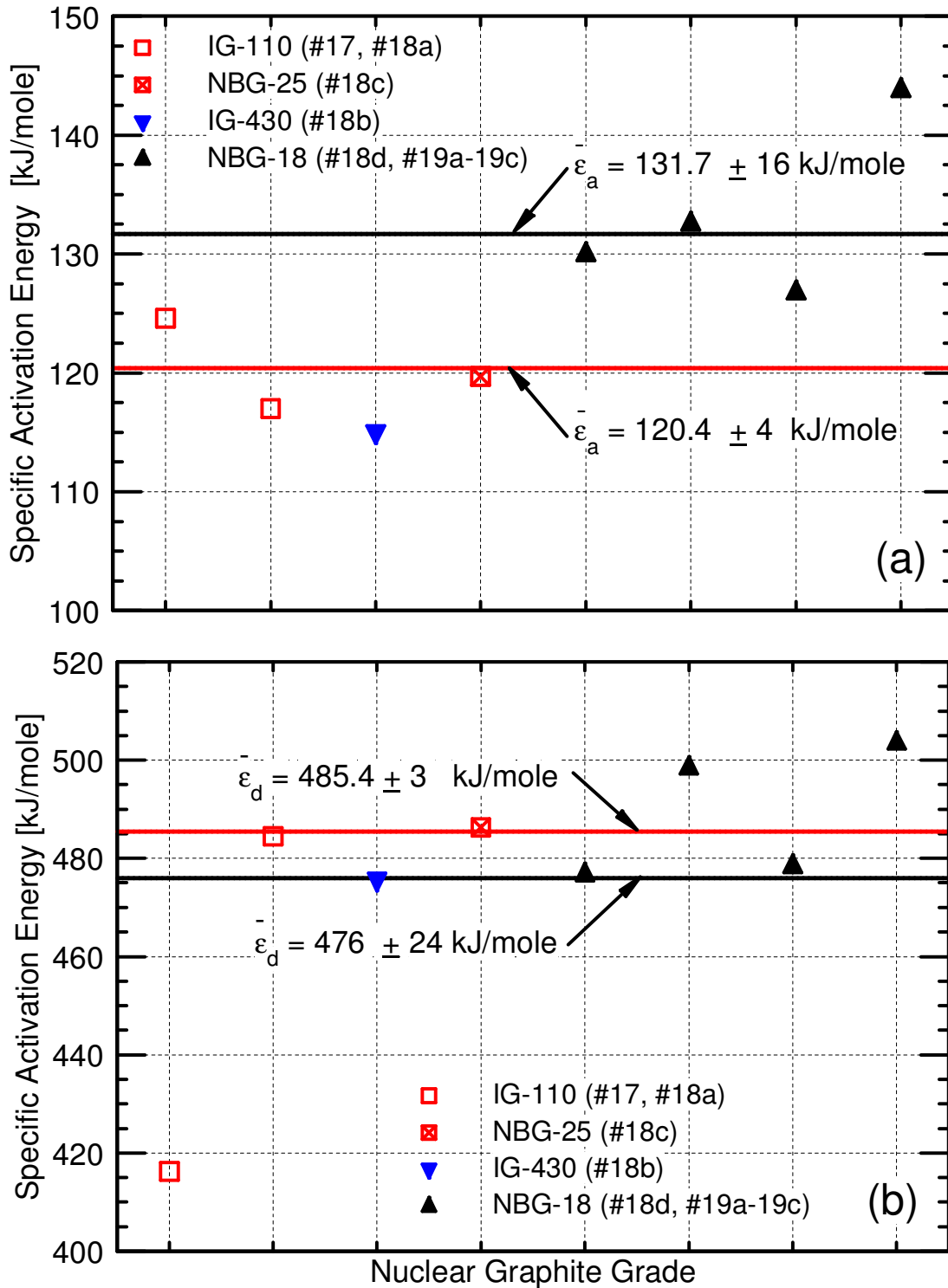


Figure 4.3. Gaussian-Distribution Most Probable Specific Activation Energies. (a) For Adsorption of Oxygen; (b) For Desorption of CO Gas (*Numbers in Parentheses Refer to the Specimen Numbers Listed in Table 4.2*).

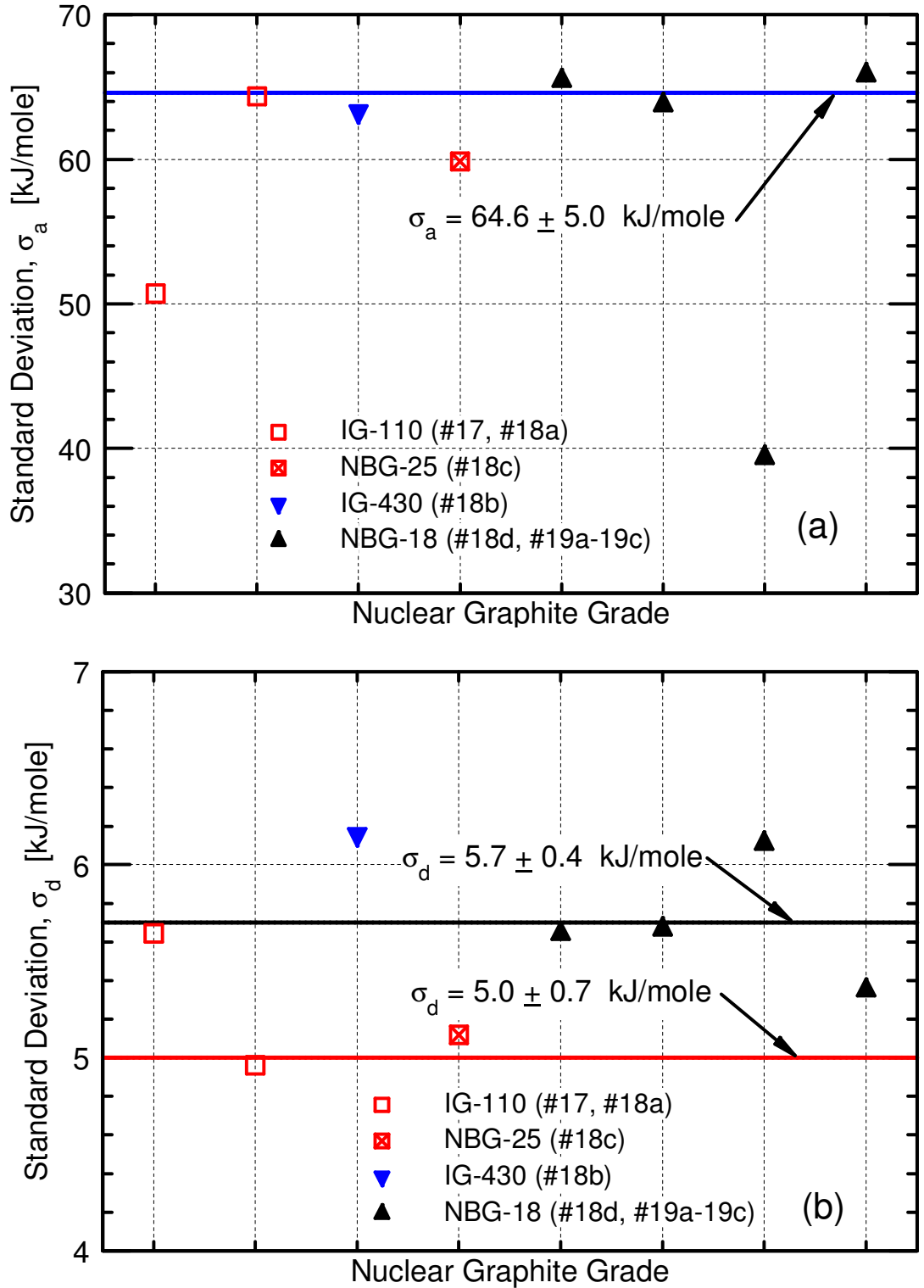


Figure 4.4. Standard Deviations of Specific Activation Energies for the Gasification of Different Grades of Nuclear Graphite. (a) Adsorption of Oxygen; (b) Desorption of CO Gas (Numbers in Parentheses Refer to the Specimen Numbers Listed in Table 4.2).

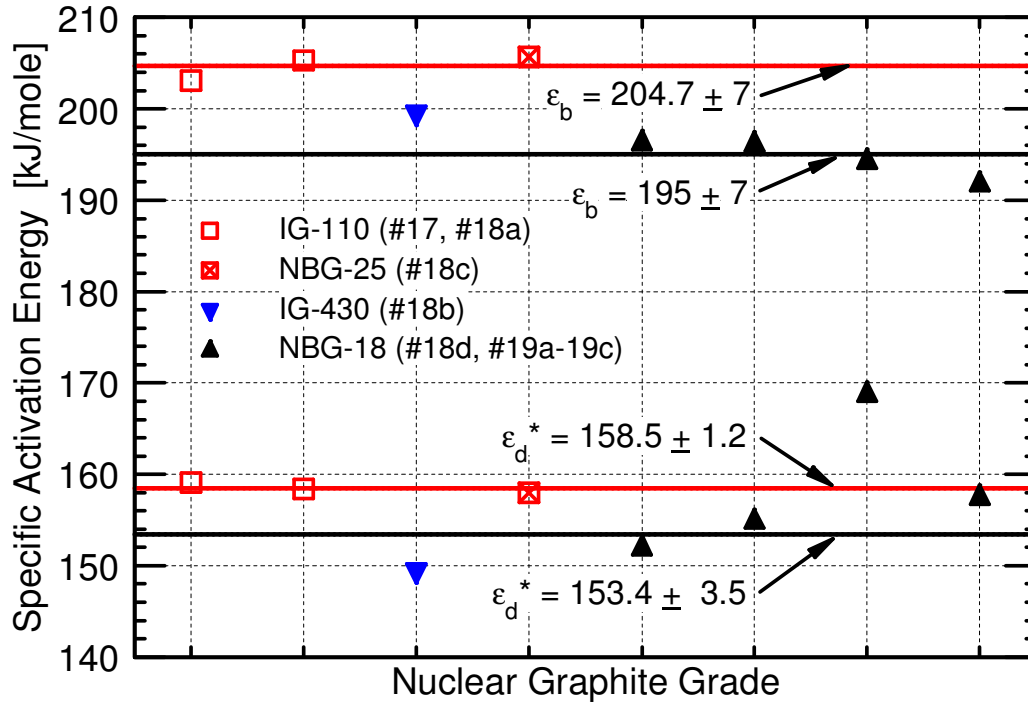


Figure 4.5. Specific Activation Energies for Forming Stable (CO) complexes and for Desorption of CO₂ for Different Nuclear Graphite Grades (*Numbers in Parentheses Refer to the Specimen Numbers Listed in Table 4.2*).

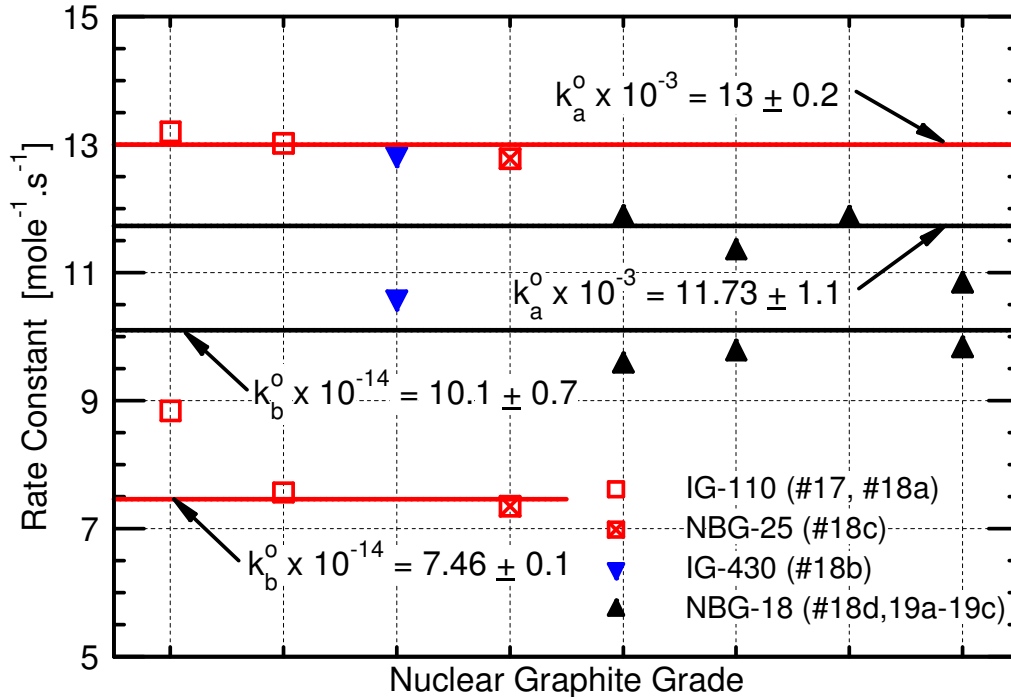


Figure 4.6. Chemical Kinetics Rate Constants k_a^o for Adsorption of Oxygen and k_b^o for Forming Stable (CO) Complexes (*Numbers in Parentheses Refer to the Specimen Numbers Listed in Table 4.2*).

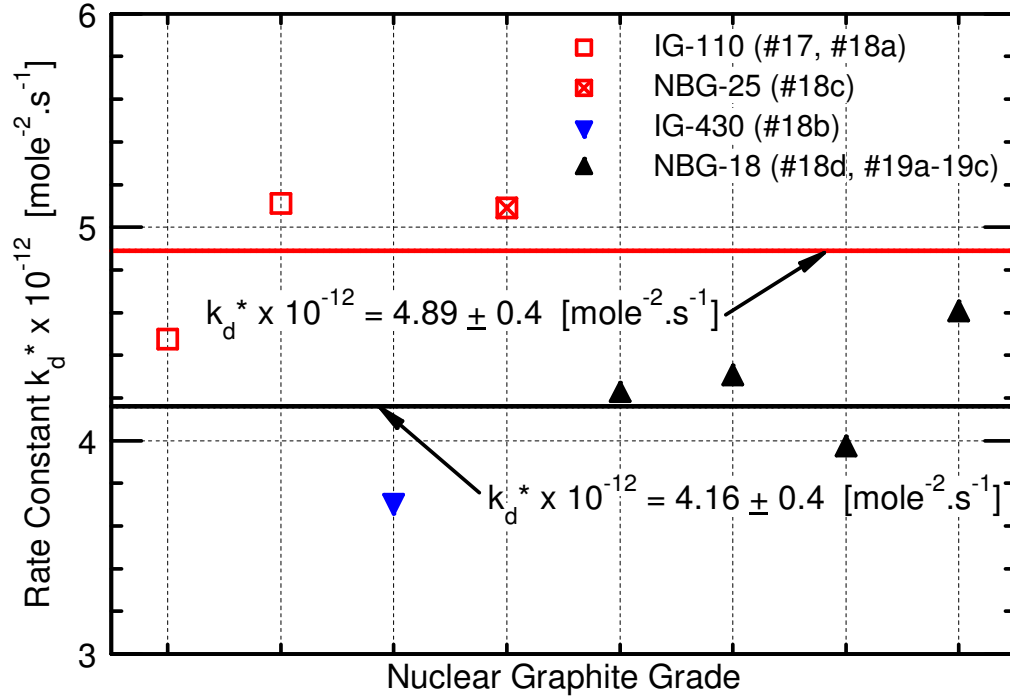


Figure 4.7. Chemical Kinetics Rate Constant k_d^* for Desorption of CO₂ (Numbers in Parentheses Refer to the Specimen Numbers Listed in Table 4.2).

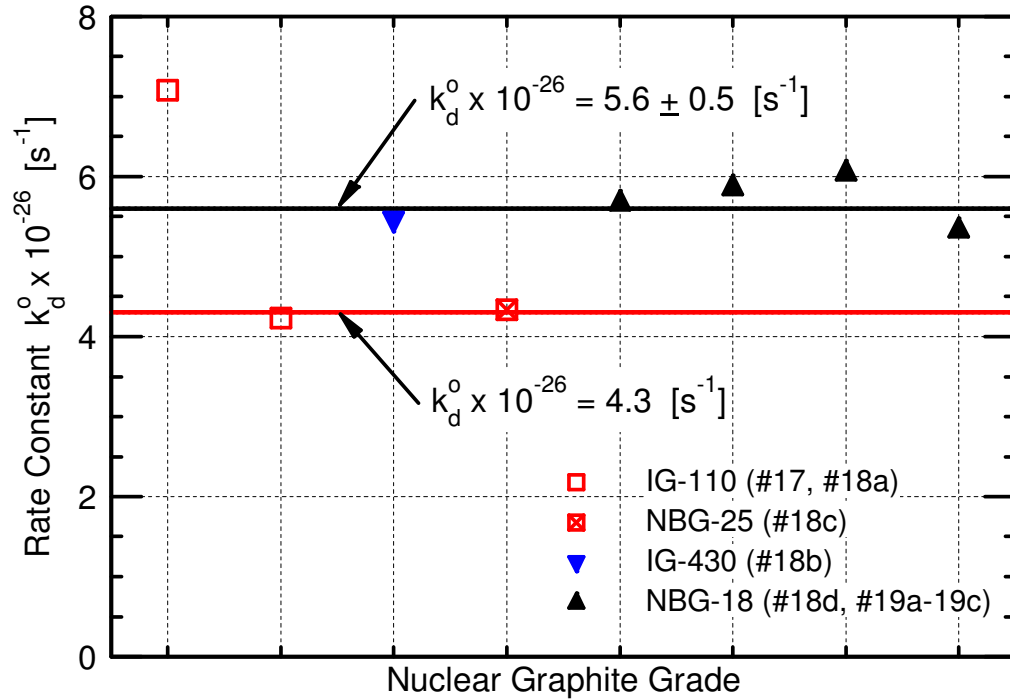


Figure 4.8. Chemical Kinetics Rate Constant for Desorption of CO Gas during Gasification of Different Grades of Nuclear Graphite (Numbers in Parentheses Refer to the Specimen Numbers Listed in Table 4.2).

For all four grades of nuclear graphite in Table 4.2, the standard deviations of the Gaussian distributions for the specific energy of adsorption of oxygen are nearly the same, $\sigma_a = 64.6 \pm 5$ kJ/mole (Figure 4.4a). On the other hand, for nuclear graphite grades IG-110 and NBG-25, the recommended standard deviation of the Gaussian distribution of the specific activation energy for desorption of CO gas is $\sigma_d = 5.0 \pm 0.7$ kJ/mole, and $\sigma_d = 5.7 \pm 0.4$ kJ/mole for IG-430 and NBG-18 (Figure 4.4b).

Figure 4.5 presents the recommended values for the specific activation energy for the breakup of the un-dissociated C(O₂) radicals to form stable (CO) complexes (ε_b). These values are $\varepsilon_b = 204.7 \pm 7$ kJ/mole for nuclear graphite grades of IG-110 and NBG-25, and $\varepsilon_b = 195 \pm 7$ kJ/mole for IG-430 and NBG-18 (Figure 4.5). Figure 4.5 also presents the recommended values of the specific activation energy for desorption of CO₂ gas for different grades of nuclear graphite. For IG-110 and NBG-25, $\varepsilon_d^* = 158.5 \pm 1.2$ kJ/mole, compared to a slightly lower value of 153.4 ± 3.5 kJ/mole for nuclear graphite grades of IG-430 and NBG-18.

Figure 4.6 compares the values of the pre-exponential rate coefficients for the adsorption of oxygen. The recommended value of the rate constant, $k_a^o = 13,000. \pm 200$ mole⁻¹.s⁻¹ for nuclear graphite grades IG-110 and NBG-25, is slightly larger than that recommended for IG-430 and NBG-18, $k_a^o = 11,730. \pm 1,100.$ mole⁻¹.s⁻¹ (Figure 4.6).

Similar results are obtained of the chemical kinetics rate constant for the breakup of un-dissociated C(O₂) oxygen radicals to form stable (CO) complexes (Eqs. (3.2a) and (3.2b)). As shown in Figure 4.6, the recommended rate constant for the nuclear graphite grades IG-110 and NBG-25 is $k_b^o = (7.46 \pm 0.1) \times 10^{14}$ mole⁻¹.s⁻¹, and $(10.1 \pm 0.7) \times 10^{14}$ mole⁻¹.s⁻¹ for graphite grades of IG-430 and NBG-18.

Figure 4.7 shows the values of the pre-exponential rate coefficient for the desorption of CO₂ gas. The recommended value, $k_d^* = (4.89 \pm 0.4) \times 10^{12}$ mole⁻².s⁻¹ for nuclear graphite grades IG-110 and NBG-25 is 17% larger than that recommended for the IG-430 and NBG-18 grades, $k_d^* = (4.16 \pm 0.4) \times 10^{12}$ mole⁻².s⁻¹ (Figure 4.7).

Finally, Figure 4.8 compares the chemical kinetics rate constants for desorption of CO during graphite gasification (Eqs. (3.3a) and (3.3b)). The recommended value for nuclear graphite grades IG-110 and NBG-25 is $k_d^o = 4.3 \times 10^{26}$ s⁻¹, and $5.6 \pm 0.5 \times 10^{26}$ s⁻¹ for the IG-430 and NBG-18 grades. The recommended values of the kinetics parameters for the different grades of nuclear graphite examined in this work (i.e. IG-110, NBG-25, IG-430 and NBG-18) are listed in Table 4.3. Other parameters that describe the changes in the microstructure of nuclear graphite during gasification are discussed next.

4.4 MICRO-STRUCTURAL PARAMETERS

A key parameter for estimating the gasification rate of nuclear graphite is the initial surface area of free active sites, ASA_o. It depends not only on the graphite microstructure, but also on the mass or volume of the graphite block or test specimen in the experiments (Chi and Kim, 2008; Fuller and Okoh, 1997; Hinssen *et al.*, 2008). The cutting plane and size of the test specimens both

Table 4.3. Recommended Oxidation Kinetics Parameters for Different Grades of Nuclear Graphite.

Parameters	IG-110 and NBG-25	IG-430 and NBG-18
$\bar{\epsilon}_a$ (kJ/mole)	120.4 ± 4	131.7 ± 16
σ_a (kJ/mole)	64.6 ± 5	64.6 ± 5
k_a^o (mole ⁻¹ .s ⁻¹)	$13,000. \pm 200$	$11,730. \pm 1,100.$
k_b^o (mole ⁻¹ .s ⁻¹)	$(7.46 \pm 0.1) \times 10^{14}$	$(10.1 \pm 0.7) \times 10^{14}$
ϵ_b (kJ/mole)	204.7 ± 7	195.0 ± 7
$\bar{\epsilon}_d$ (kJ/mole)	485.4 ± 3	476.0 ± 24
σ_d (kJ/mole)	5.00 ± 0.7	5.70 ± 0.4
k_d^o (s ⁻¹)	$(4.3 \pm 0.1) \times 10^{26}$	$(5.6 \pm 0.5) \times 10^{26}$
k_d^* (mole ⁻² .s ⁻¹)	$(4.89 \pm 0.4) \times 10^{12}$	$(4.16 \pm 0.4) \times 10^{12}$
ϵ_d^* (kJ/mole)	158.5 ± 1.2	153.4 ± 3.5

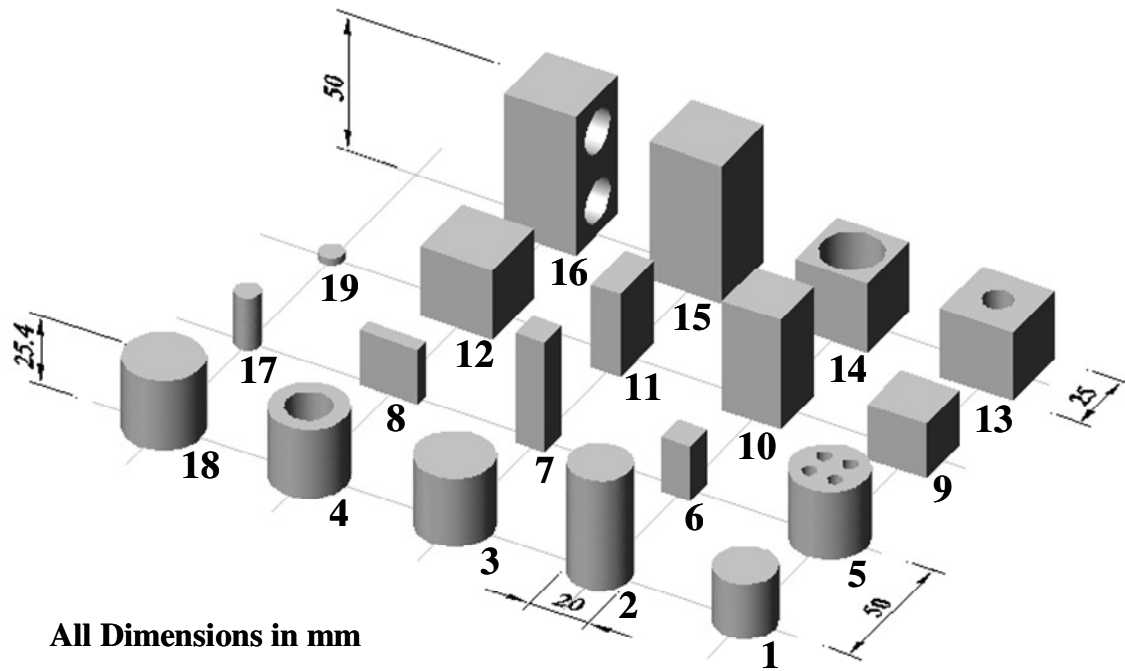


Figure 4.9. Size and Shape of Nuclear Graphite Specimens in Gasification Experiments of Kim, Lee and No (2006), Fuller and Okoh (1997), Chi and Kim (2008) and Hinssen *et al.* (2008).

affect ASA_0 and the corresponding specific area for free active sites, S_m^o ($\mu\text{mole/g}$) (Table 4.2 and Figure 4.11). The change in ASA with weight loss in Modes (a) and (b) of gasification (Figure 2.1) is calculated using the structural parameter, Ψ (Table 4.2), introduced by the Random Cylinders model of Su and Perlmutter (1985) (Eq. (4.1)).

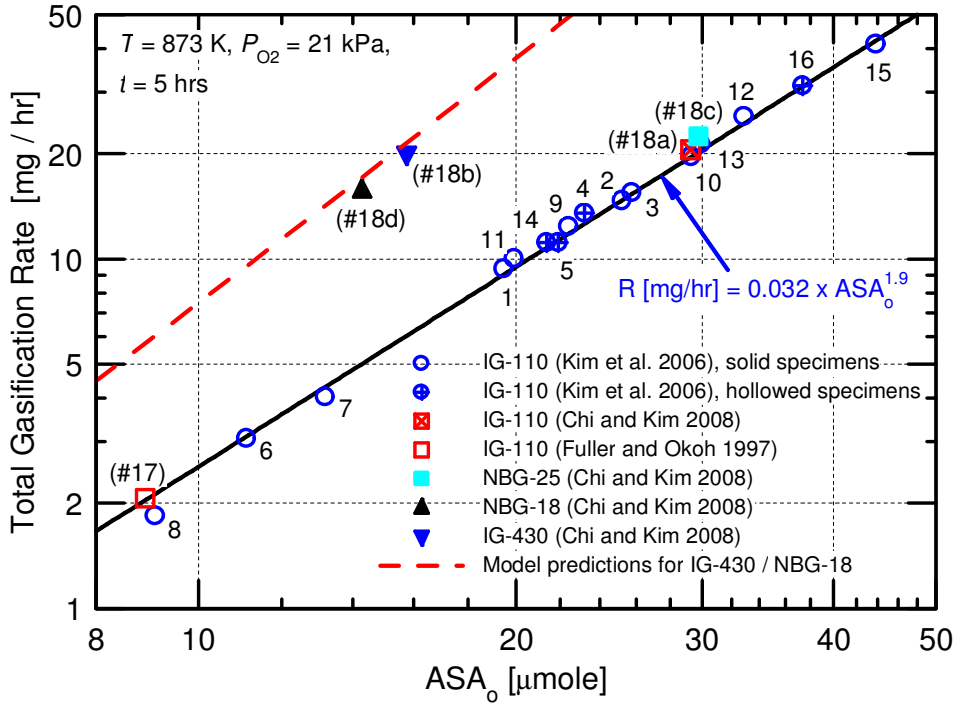


Figure 4.10. Effect of ASA_0 on Gasification Rate after 5 Hours at 873 K for Different Grades of Nuclear Graphite (Numbers in Parentheses Refer to the Specimen Numbers Listed in Table 4.2, and Other Numbers Refer to the Graphite Specimens in Figure 4.9).

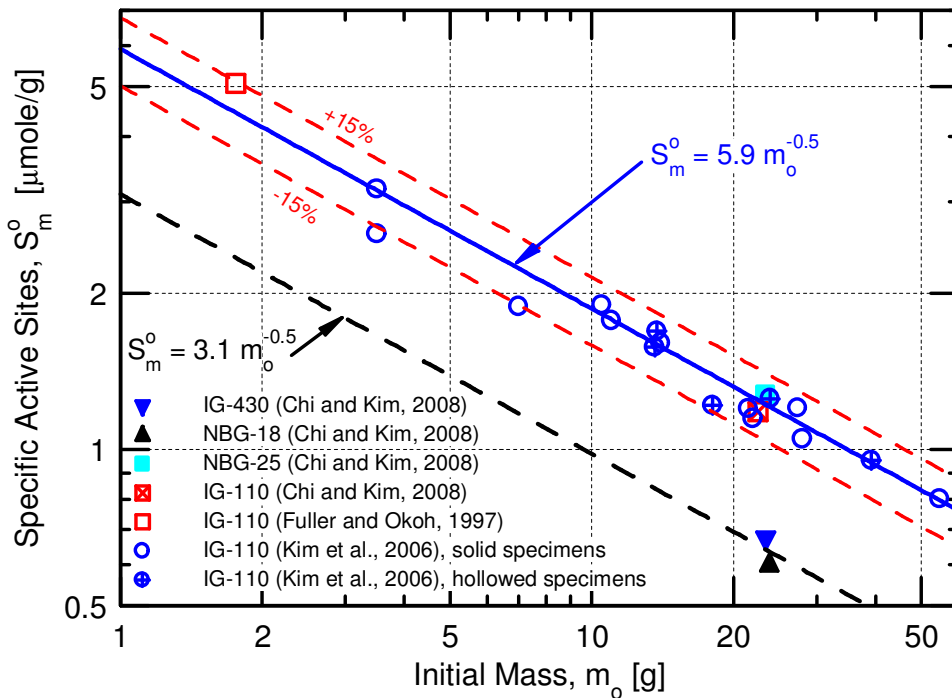


Figure 4.11. Specific Area of Free Active Sites, S_m^0 as a Function of Specimen Mass, for Different Grades of Nuclear Graphite.

Transient weight loss measurements have been reported for IG-110 in the experiments of Fuller and Okoh (1997) and Chi and Kim (2008) and for IG-430, NBG-25 and NBG-18 in the experiments of Chi and Kim (2008). For these measurements, the change in ASA with weight loss is best described by $\Psi = 80$. By contrast, for the NBG-18 specimens in the experiments of Hinssen *et al.* (2008), the change in ASA with weight loss is best predicted using $\Psi = 35$. This lower value is attributed to the fact that the specimens in the experiments of Hinssen *et al.* (2008) are 2 orders of magnitude smaller than those of Chi and Kim (2008) and have a much higher surface-to-volume ratio (8.73 versus 2.16 cm⁻¹) (Table 4.2). The results of the gasification experiments of Hinssen *et al.* (2008) showed that the specimens used exhibited large differences in reactivity; specimen #19c was the most reactive, with a gasification rate more than double that of the least reactive specimen #19b (Table 4.2). Hinssen *et al.* attributed such large differences in reactivity to local variances in both the microstructure and impurities.

The determined values of S_m^o using a multi-parameter optimization algorithm, from the gasification measurements reported by Chi and Kim (2008) and Fuller and Okoh (1997) are presented in Figure 4.11. The results for the NBG-18 specimens #19a, 19b and 19c of Hinssen *et al.* (2008) in Table 4.2 are omitted due to their extremely small size (0.25 g) and large variances in reactivity. As expected from the results obtained for the chemical kinetics parameters, the identical-size right cylinders of IG-110 and NBG-25 (specimens #18a and #18c of Chi and Kim, 2008), have nearly identical S_m^o values of 1.30 and 1.273 $\mu\text{mole/g}$ (Table 4.2 and Figure 4.11). Similarly, the IG-430 and NBG-18 test specimens #18b and #18d in Table 4.2, also of same size and shape, have close S_m^o values, 0.673 and 0.60 $\mu\text{mole/g}$ (Figure 4.11).

4.5 EFFECT OF GRAPHITE MASS

To investigate the effect of nuclear graphite mass on the specific ASA, the experimental measurements of the total gasification rate by Kim, Lee and No (2006) for IG-110 specimens of different sizes and configuration are used. These investigators tested sixteen IG-110 specimens of different shapes and masses ranging from 3.5 g (#6 in Figure 4.9) to 54.7 g (#15 in Figure 4.9). The specimens in the experiments of Kim, Lee and No (2006) are shown in Figure 4.9 (#1 to #16), along with those of Chi and Kim (2008) (#18), Fuller and Okoh (1997) (#17) and Hinssen *et al.* (2008) (#19). Kim, Lee and No (2006) tested the IG-110 specimens at a fixed temperature of 873 K (600 °C) in flowing dry atmospheric air, and reported the measured total gasification rates after 5 hours. The final weight loss achieved at those conditions was < 0.8%. The specimen temperature used in the experiments was low enough for the gasification to be solely controlled by the chemical reaction kinetics.

Although the reported total gasification measurements by Kim, Lee and No (2006) are very limited, the present graphite oxidation kinetics model is used to infer the ASA_o values of all IG-110 specimens in the experiments. The model used the kinetics parameters recommended in this work for IG-110 (Table 4.3) and $\Psi = 80$. The ASA_o value is chosen to match the model calculation to the reported gasification rate after 5 hours at 873 K in the experiments. The reported total gasification rate measurements are plotted in Figure 4.10 versus the calculated ASA_o values for the different IG-110 specimens in Figure 4.9. Figure 4.10 also includes the results for the IG-110 specimens of Fuller and Okoh (1997) and Chi and Kim (2008), and of Chi and Kim (2008) of nuclear graphite grades of NBG-25, NBG-18 and IG-430.

The results presented in Figure 4.10 are very consistent. The total gasification rate increases proportionally to ASA_o raised to the power 1.9. This exponent is indicative of the dominance of the desorption of CO_2 gas, by the chemical reactions of Eq. (3.4a), at the experimental conditions in Figure 4.10. Figure 4.10 also shows that the dependence of the total gasification rate on ASA_o is consistent for the different shapes and configurations of the graphite specimens used in the experiments. It is worth noting, however, that the results for the NBG-25 specimen #18c in Table 4.2 of Chi and Kim (2008) are consistent with those of the IG-110 specimens. On the other hand, the results for the NBG-18 and IG-430 specimens of Chi and Kim (2008), #18d and #18b in Table 4.2, fall on a different curve, confirming again the present classification of the nuclear graphite grades in terms of their gasification reactivity into two distinct groups: (a) IG-110 and NBG-25 grades manufactured with petroleum coke filler particles; and (b) NBG-18 and IG-430 grades manufactured from coal tar pitch filler particles (Figure 4.10 and Table 4.3).

Figure 4.11 plots the obtained values of the specific ASA_o (S_m^o) for the different grades of nuclear graphite versus the initial mass of the graphite specimens in the experiments, spanning nearly 2 orders of magnitude, from 1.7 to 55 grams. The results in this figure show that the dependence of S_m^o on the mass of graphite is not the same for all grades. For IG-110 and NBG-25, S_m^o can be expressed in terms of the initial mass of the graphite, m_o in grams, as (Figure 4.11):

$$S_m^o (\mu mole / g) = 5.9 m_o^{-0.5}. \quad (4.2)$$

This correlation is consistent to within $\pm 15\%$ of the determined S_m^o values. The area of free active sites ($ASA_o = S_m^o \times m_o$) increases proportionally to the square root of the initial mass. Pending further qualification with specimens of larger masses, this correlation, along with the recommended values of kinetics parameters in Table 4.3, may be used in future safety analyses of VHTRs and HTGRs for calculating the gasification rate for nuclear graphite blocks of large sizes. For the nuclear graphite grades of NBG-18 and IG-430, the following expression for S_m^o is proposed, pending further qualification with additional experimental data (Figure 4.11):

$$S_m^o (\mu mole / g) = 3.1 m_o^{-0.5}. \quad (4.3)$$

The recommended chemical kinetics parameters in Table 4.3, along with Eqs, (4.2) and (4.3) are used in the analysis presented next to examine the effect of the graphite mass on the total gasification rate for IG-110 and NBG-18, as representative of the two precursor groups in Table 4.3, as function of temperatures covering all three modes of gasification in Figure 2.1.

4.6 EFFECT OF GRAPHITE MASS ON TOTAL GASIFICATION RATE

The recommended values of the specific activation energies and pre-exponential rate coefficients for the chemical-reaction kinetics of the different grades of nuclear graphite (Figures 4.3 to 4.8 and Table 4.3), along with Eqs. (4.2) and (4.3)), are incorporated in the model. The calculated gasification rates are compared to those reported in the experiments of Chi and Kim (2008), Fuller and Okoh (1997) and Hinssen *et al.* (2008). The results in Fig. 4.12 show that the model calculations of the total gasification rate are in excellent agreement with the reported

measurements for IG-110 (Chi and Kim, 2008; Fuller and Okoh, 1997), NBG-25 (Chi and Kim, 2008), IG-430 (Chi and Kim, 2008) and NBG-18 (Chi and Kim, 2008; Hinssen *et al.*, 2008). The agreement is for different temperatures, from 876 to 1226 K and weight loss fractions from 0.05 to 0.81 (Figure 4.12).

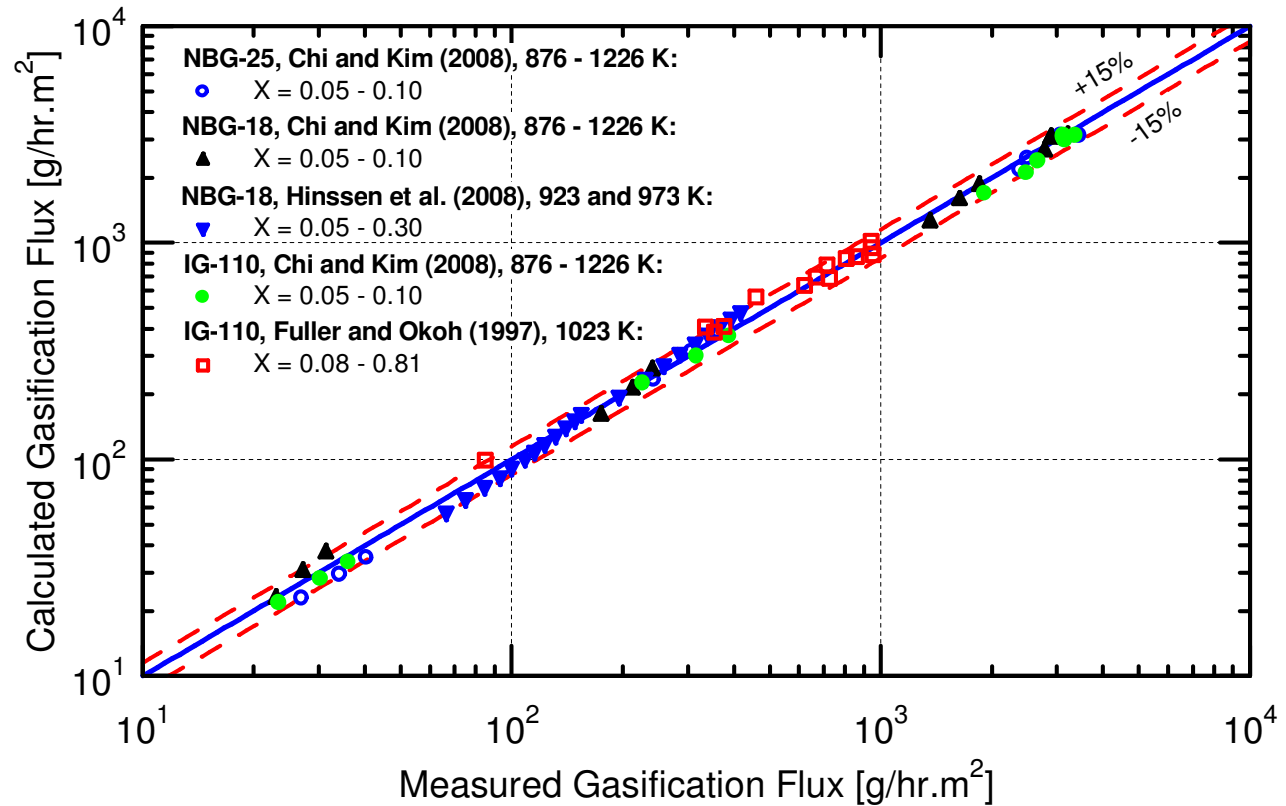


Figure 4.12. Comparison of Reported Measurements with Present Calculations of the Total Gasification Rates from Different Grades of Nuclear Graphite. Calculations Use Recommended Chemical-Reaction Kinetics Parameters in Table 4.3 and Eqs. (4.2) and (4.3) for s_m^o .

The calculated total gasification rates in Figure 4.12 span nearly 3 orders of magnitude and are within $\pm 15\%$ of the reported measurements for small-size specimens. Such good agreement confirms the effectiveness of the present chemical kinetics model and the soundness of the recommended values of the chemical kinetics parameters in Figures 4.3 – 4.8 and Table 4.3, and of Eqs. (4.2) and (4.3). In the remainder of this section, analyses are performed using the chemical kinetics model to examine the effects of temperature and initial graphite mass on the gasification rate of IG-110 and NBG-18.

The analysis used right cylinders of graphite weighting 1 kg, 10 kg and 100 kg. The top and bottom surfaces of the cylinders are isolated such that gasification only occurs at the lateral surface exposed to atmospheric ambient airflow at a velocity of 1 cm/s. At 800 K, the

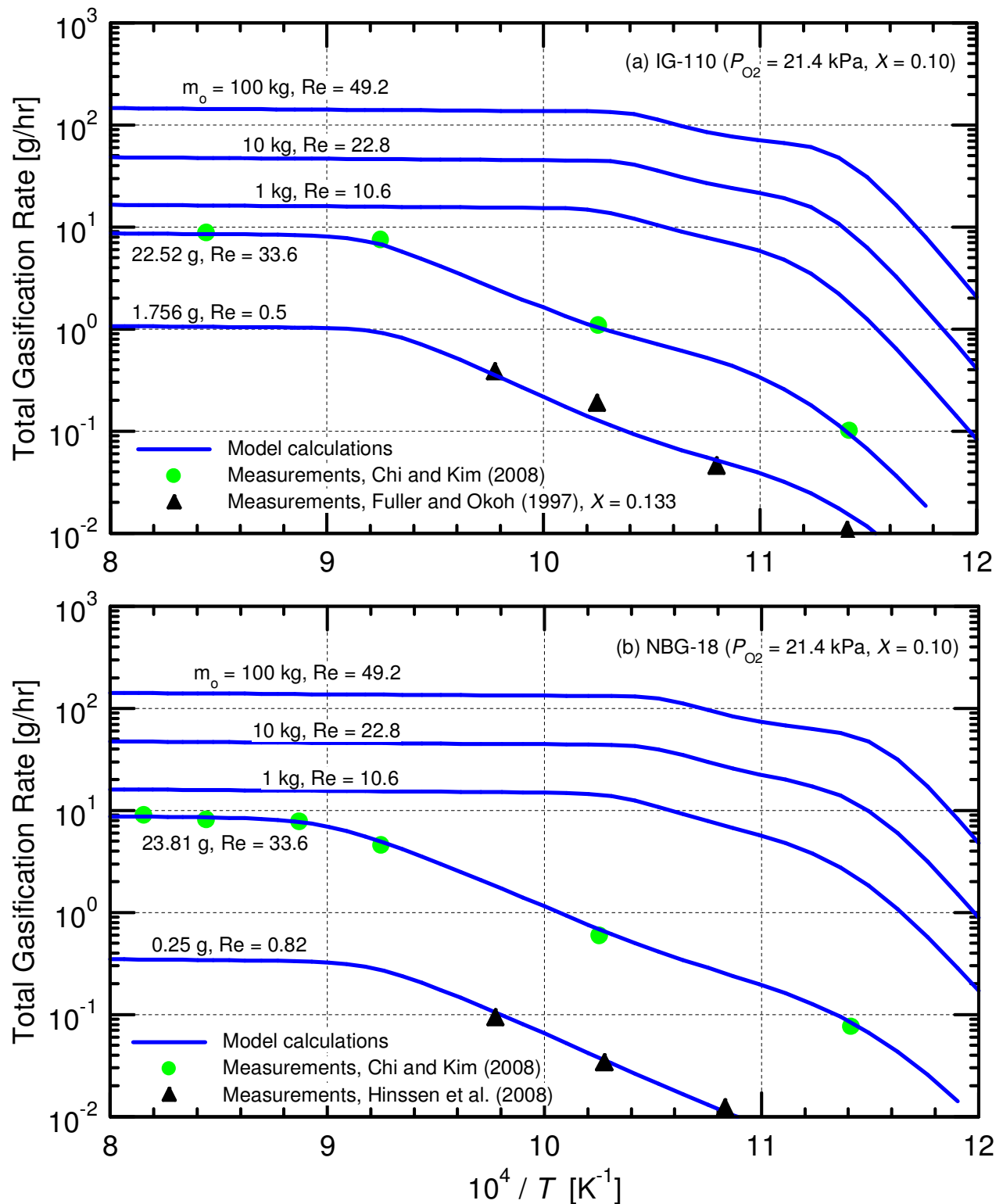


Figure 4.13. Calculated Arrhenius Curves of the Total Gasification Rate in Flowing Atmospheric Air for Different Graphite Grades and Initial Masses. (a) IG-110 Nuclear Graphite; (b) NBG-18 Nuclear Graphite.

corresponding Reynolds numbers, based on the diameter of these graphite cylinders, are 10.6, 22.8 and 49.2, and the values of the Sherwood number (El-Genk and Tournier, 2012a) are 1.72, 2.35 and 3.31, respectively. The performed parametric analyses for IG-110 and NBG-18 use the recommended values of the chemical kinetics parameters in Table 4.3, and the specific areas of active sites, S_m^o calculated using Eqs. (4.2) and (4.3).

Figures 4.13a and 4.13b show the calculated Arrhenius curves of the total gasification rate for IG-110 and NBG-18 at an oxygen partial pressure of 21.4 kPa and a weight loss of 10%. The temperature range investigated (830 K to 1250 K) covers all three oxidation modes of graphite (Figure 2.1), with the total gasification rate spanning more than 3 orders of magnitude.

At high temperatures > 950 K, when graphite gasification is diffusion-limited (Mode (c) in Figure 2.1), the total gasification rate is weakly dependent on temperature. It is proportional to the product of the oxygen diffusion velocity through the boundary layer and the lateral surface area of the nuclear graphite cylinder (Figure 4.13). As a result, in the diffusion-limited mode of gasification, the rate increases proportionally to the diameter of the right graphite cylinder raised to the power ~ 1.40 . The 1 kg, 10 kg and 100 kg IG-110 right cylinders have diameters of 9 cm, 19.38 cm and 41.75 cm, respectively. The corresponding NBG-18 cylinders of the same initial masses have slightly smaller diameters of 8.83 cm, 19 cm and 41 cm, due to the higher density of NBG-18 (1.85 versus 1.75 g/cm³ for IG-110). At lower temperatures < 950 K, the total gasification rate in Modes (a) and (b) is chemical-kinetics limited, and increases exponentially with temperature (Figures 4.13a and 4.13b).

The total gasification rate of the nuclear graphite cylinders is the sum of the production rates of CO and CO₂ gases. At low temperatures $< \sim 900$ K, when graphite gasification is controlled by the chemical kinetics and in-pores diffusion, the gasification is dominated by the production of CO₂. At these temperatures, the production rate of CO gas is negligibly small because of its higher desorption specific energy. The production rate of CO gas, however, increases rapidly with increasing temperature, at the expense of decreasing that of CO₂ gas. Thus, at intermediate temperatures (Mode (b) in Figure 2.1) and high temperatures in the diffusion-limited Mode (c), the gasification of nuclear graphite is almost entirely by CO gas desorption.

This trend reflects the dependence of the CO₂ desorption reaction in Eq. (3.4a) on the availability of both surface free sites and stable (CO) complexes in close proximity to act as catalysts for the formation and desorption of CO₂ (Moulijn and Kapteijn, 1995). The CO₂ production rate peaks at ~ 900 K, when the ASA fractional coverage with surface complexes reaches $\sim 50\%$ (Figures 4.13a and 4.13b). These figures also compare the calculated total gasification rates with the reported measurements for the small size specimens of IG-110 and NBG-18 in the experiments (Chi and Kim, 2008; Fuller and Okoh, 1997; Hinssen *et al.*, 2008).

The calculated gasification rates for the smaller IG-110 specimens of Chi and Kim (2008) (#18a in Table 4.2, weighting 22.52 g) and Fuller and Okoh (1997) (#17 in Table 4.2, weighting only 1.756 g) using the kinetics parameters in Table 4.3 are also shown in Figure 4.–13a for comparison, along with the reported experimental data. As shown in this Figure, the model calculations compare well with the measurements.

For the IG-110 specimen of Chi and Kim (2008), the diffusion-limited Mode (c) of gasification begins at much higher temperature (> 1073 K) than for the larger mass right cylinders, and the corresponding rate is relatively high for such a smaller specimen. This is because of the

larger air velocity used (10 cm/s) in the experiments of Chi and Kim (2008), corresponding to $Re = 33.6$ (Figures 4.13a and 4.13b).

Similar results are obtained in Figure 4.13b for the small NBG-18 specimens in the experiments of Chi and Kim (2008) (#18d in Table 4.2, weighting 23.81 g) and Hinssen *et al.* (2008) (#19 in Table 4.2, weighting only 0.25 g). Again, the comparison shows good agreement between the model calculations and reported measurements of the total gasification rate for NBG-18.

4.7 SUMMARY

Recommendations of the chemical kinetics parameters for the gasification of nuclear graphite grades IG-110, IG-430, NBG-18 and NBG-25 are developed based on the reported gasification rate and transient weight loss measurements by various investigators. These parameters, along with the reported total gasification rate measurements of Kim, Lee and No (2006) for IG-110, are used to develop empirical correlations of the surface area of free active sites as functions of the initial mass and type of nuclear graphite.

The kinetics parameters for the 4 elementary chemical reactions in the graphite oxidation model include the values and Gaussian distributions of the specific activation energies and the values of the pre-exponential rate coefficients for the adsorption of oxygen and desorption of CO and CO₂ gases. Results show that the chemical kinetics parameters and the surface area of free active sites for IG-110 and NBG-25 are similar, but slightly different from those of NBG-18 and IG-430. The values of these parameters are almost independent of the size of the filler particles, but strongly depend on the type of those particles. The IG-110 and NBG-25 grades are manufactured with petroleum coke filler particles, while the NBG-18 and IG-430 grades are manufactured from coal tar pitch.

The developed empirical expressions of the initial specific area of free active sites, S_m^o as a function of mass of the different grades of nuclear graphite may be used and applied, in conjunction with the recommended chemical kinetics parameters, to the gasification of large graphite structures in VHTRs and HTGRs. For nuclear graphite specimens of varied shapes, results show that S_m^o decreases inversely proportionally to the square root of the initial graphite mass. Conversely, the initial surface area of free active sites, ASA, increases proportionally to the square root of the initial mass.

Estimates of the gasification rates for IG-110 and NBG-18, using the recommended chemical-reaction kinetics parameters and the developed empirical correlations for calculating S_m^o , are given as functions of graphite mass and temperature. Estimates for right cylinders weighing 1, 10 and 100 kg show that increasing the initial mass rapidly increases the total gasification rate. This rate also increases with increasing temperatures. For the small specimens of IG-110 and NBG-18 (0.25g – 23.81g) used in experiments, the calculations are in good agreement to within $\pm 15\%$ of the total gasification rate measurements. The reported measurements cover a wide range of temperatures spanning all three modes of graphite gasification (Figure 2.1). The calculated Arrhenius curves of the total gasification rate smoothly progress from one mode to the next with increasing temperature.

The results presented in this work are the first to compare the gasification kinetics of the different grades of nuclear graphite, and to make recommendations of the specific activation energies and pre-exponential rate coefficients of the primary chemical processes of gasification. In addition, the results on the effects of the initial mass of graphite on the specific area of active free sites and the total gasification rate as a function of temperature are a welcome new contribution, with practical implication to future design and analysis of VHTRs and HTGRs. The recommended chemical kinetics parameters and the developed empirical correlations for S_m^o would be useful in the safety analysis of these reactors in the unlikely event of a massive air ingress accident.

The chemical kinetics approach, based on a solid understanding of the primary processes taking place, provides valuable insight into the gasification of different grades of nuclear graphite. Unlike the empirically developed Arrhenius correlations for predicting the total gasification rate, the chemical kinetics approach provides smooth and gradual transitions in the total rate of gasification through the prevailing modes with increasing temperature. The chemical kinetics approach can also predict the effect of various important variables on the total gasification rate and transient weight loss. These variables include the oxygen partial pressure, the total pressure and flow velocity of the oxidizing gas mixture and the initial mass of the graphite structure. Furthermore, the chemical kinetics approach tracks the changes in ASA and oxides fractional coverage with time and weight loss, and calculates the production rates of CO and CO₂ gases and their relative contributions to the total gasification rate for different grades of nuclear graphite.

The next chapter investigates the transient gasification of NBG-18 nuclear graphite with atmospheric air ingress in a 0.8-m long flow channel of a VHTR prismatic fuel assembly. Varied are the initial graphite and air inlet temperature, T_o , from 800 to 1100 K at air $Re_{in} = 5, 10$ and 20. A Generic Interface couples a multi-species diffusion and flow model developed on the Matlab®/Simulink® platform to readout tables of the CO and CO₂ production fluxes. These fluxes are calculated as functions of temperature, oxygen partial pressure and weight loss fraction using the chemical-reactions kinetics model previously developed for the gasification of nuclear graphite. In addition, the practical implementation of the gasification Generic Interface into a commercial Finite-Element CFD code is successfully demonstrated using CD-Adapco STAR-CCM+.

4.8 NOMENCLATURE

ASA	Active surface area (mole)
C_{f,E_i}	Active free sites with activation energies in bin i
$C(O_2)_{E_i}$	Un-dissociated oxygen complexes in energy bin i
$(CO)_{E_i}$	Surface stable oxide complexes in energy bin i
D	Diameter of nuclear graphite test cylinder (m)
$f(\varepsilon)$	Normal probability function (mole/J)
H	Height of nuclear graphite test cylinder (m)
k^o, k^*	Pre-exponential rate constants ($\text{mole}^{-n} \cdot \text{s}^{-1}$)
m	Mass of nuclear graphite specimen (g)
P_{O_2}	Partial pressure of oxygen (Pa)
R_g	Perfect gas constant (8.3144 J/mole.K)
S_m	Specific active surface area (mole/g)
T	Temperature (K)
X	Weight loss fraction
Y	Normalized active surface area (ASA/ASA_o).

Greek

ε	Specific activation energy (J/mole)
$\bar{\varepsilon}$	Gaussian most-probable specific activation energy (J/mole)
σ	Gaussian standard deviation (J/mole)
Ψ	Dimensionless structural parameter, Eq. (4.1)

Subscript/Superscript

a	Adsorption of oxygen onto active free sites to form un-dissociated complexes
b	Breakup of un-dissociated surface oxides to form stable complexes
CO	Carbon monoxide gas
CO_2	Carbon dioxide gas
d	Desorption of CO gas
i, j	Energy bin numbers
o	Initial value
O_2	Oxygen gas
*	Desorption of CO_2 gas

5. TRANSIENT GASIFICATION OF NBG-18 NUCLEAR GRAPHITE IN A VHTR FLOW CHANNEL

A massive air ingress following a pipe break and a steam ingress caused by a leak in the steam generator tubes are among the design basis accidents for Very-High Temperature and High-Temperature gas-cooled Reactors (VHTRs and HTRs). In such accidents, gasification could compromise the structure integrity of the reactor core's graphite support columns in the lower plenum and release the fission products entrapped in the graphite matrix of the coated particles fuel compacts in the core. The rate and mode of graphite gasification depend on temperature, as well as the total and oxygen partial pressures, the nuclear graphite's micro-structure and the surface area of free sites and adsorbed stable oxide complexes (Maruyama et al., 1995; Takeda, 2004; Xiaowei et al., 2004; Yu et al., 2008; Kim et al., 2008).

A prismatic core HTR or VHTR (Fig. 5.1) could be comprised of 102 hexagonal fuel assemblies or elements loaded with cylindrical fuel compacts and stacked 8 m high in 3 concentric rings (IAEA, 2001; MacDonald et al., 2004; Baxi et al., 2006; INL, 2007). The hexagonal fuel elements are 0.36 m flat-to-flat and 0.80 m tall (Fig. 5.2). The annular reactor core is surrounded on both sides by hexagonal graphite reflector assemblies in five inner and 2-3 outer rings (Fig. 5.1). In addition, graphite reflector assemblies are stacked (1.2 m) on the top and (0.8 m) at the bottom of the radially reflected core (Fig. 5.1). The fuel compacts consist of Tristructural-isotropic (TRISO) fuel particles dispersed in graphite (Froschauer et al., 2008). The TRISO particles, ~1 mm in diameter, are uranium oxy-carbide spherical kernels surrounded by PyC and SiC coatings (Fig. 5.3a). The fuel compacts, typically 1.245 cm in diameter and 4.95 cm tall (Fig. 5.3b), are loaded into vertical channels in a triangular lattice within the hexagonal fuel assemblies (Figs. 5.2 and 5.3c). On average, six fuel compacts surround a helium coolant flow channel (Fig. 5.3c) that carries approximately the fission heat generated in two fuel compacts. The coolant channels in the fuel assemblies are 8.0 m long and most are 1.5875 cm in diameter.

The chemical-reactions kinetics model recently developed by the authors for the gasification of nuclear graphite has been validated successfully using the reported measurements of the total gasification rate and transient weight loss for graphite grades of NBG-18, IG-430, NBG-25 and IG-110 (El-Genk and Tournier, 2011, 2012a and 2012b; see Chapters 3 and 4 of this report). These measurements are used in a multi-parameter optimization algorithm to determine the chemical kinetics parameters for the 4 elementary chemical reactions in the model (see Eqs. (3.1) to (3.4)).

The input to the chemical-reactions kinetics model (El-Genk and Tournier, 2011, 2012a, 2012b and 2012c) for gasification includes 10 parameters whose values depend on the grade of nuclear graphite. These parameters are: (a) the most-probable specific activation energies for the adsorption of oxygen and desorption of CO ($\bar{\varepsilon}_a$ and $\bar{\varepsilon}_d$) and the standard deviations (σ_a and σ_d); (b) the specific activation energies ε_b and ε_d^* for elementary reactions in Equations (3.2a) and (3.4a); and (c) the pre-exponential rate coefficients k_a^o , k_b^o , k_d^o and k_d^* for the rate constants in Equations (3.1b), (3.2b), (3.3b) and (3.4b). The model also accounts for the change in the surface area of free active sites with weight loss and the oxygen's effective diffusion velocity in the boundary layer and the effect of surface erosion in Mode (c) on graphite gasification see Chapters 2 and 3). The results provide continuous Arrhenius curves of the total gasification rate of nuclear

graphite versus the reciprocal of its temperature and of the production rates of CO and CO₂ gases. In addition to the temperature, the results include the effects of the total and oxygen partial pressures of the bulk gas mixture on the graphite weight loss.

Figure 5.4 presents some of the results of the authors' chemical-reactions kinetics model with reported experimental measurements by Chi and Kim (2008) at different test temperatures in atmospheric air. The NBG-18 specimens used in the experiments of Chi and Kim were right cylinders measuring 2.54 x 2.54 mm.

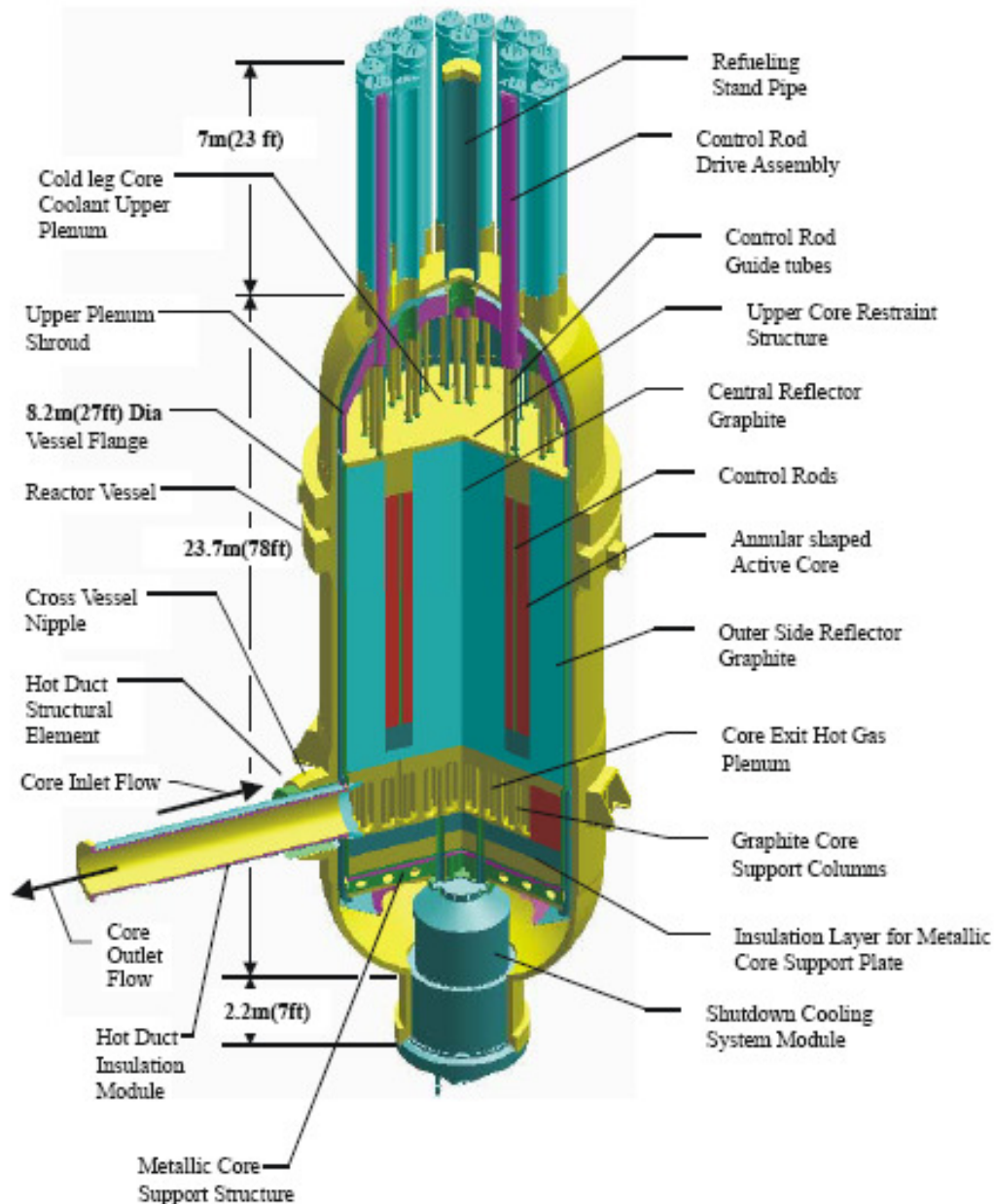


Figure 5.1. A Cut-away View in a Prismatic Core VHTR (McDonald et al., 2004).

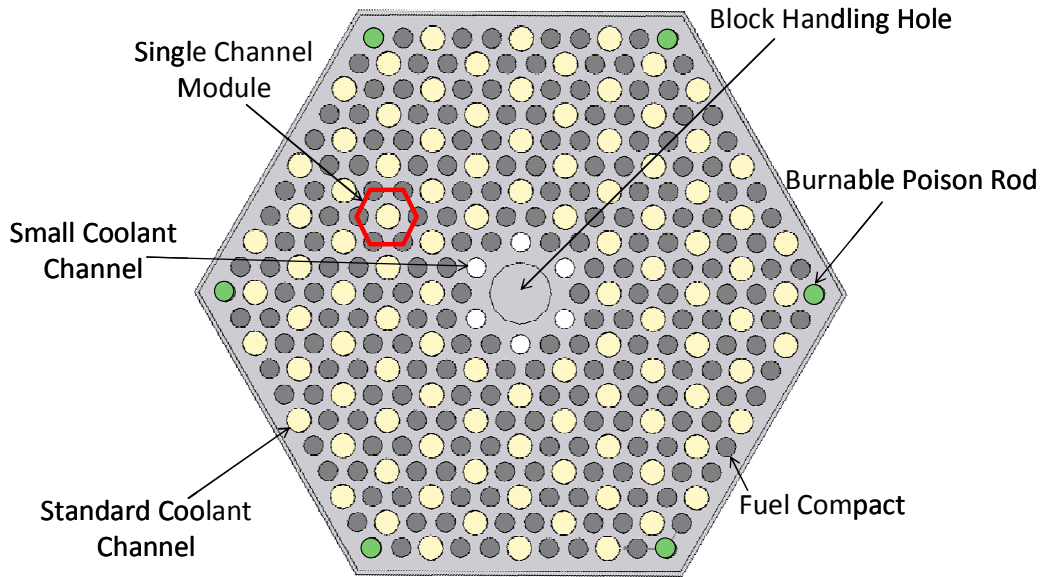
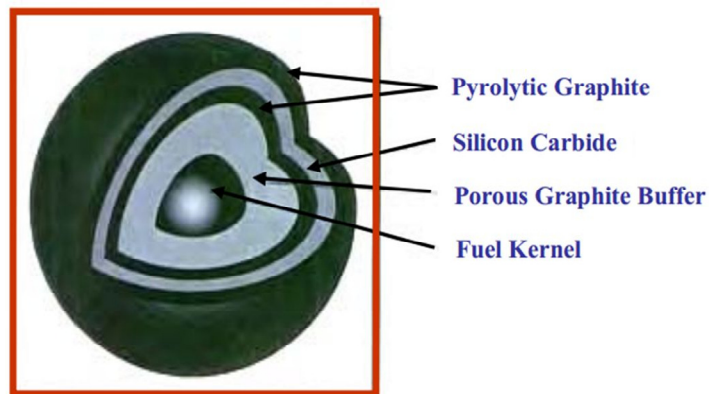
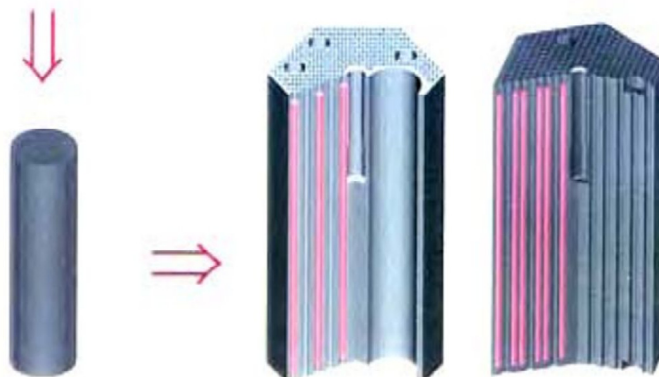


Figure 5.2. Transverse Cross-sectional View of a Prismatic Fuel Assembly or Element.



(a) TRISO-Coated Fuel Particle



(b) Graphite Coated Particles Compact

(c) Prismatic Fuel Elements or Assemblies

Figure 5.3. VTHR or HTR TRISO Fuel Particle, Fuel Compact and Prismatic Assemblies (INL, 2007).

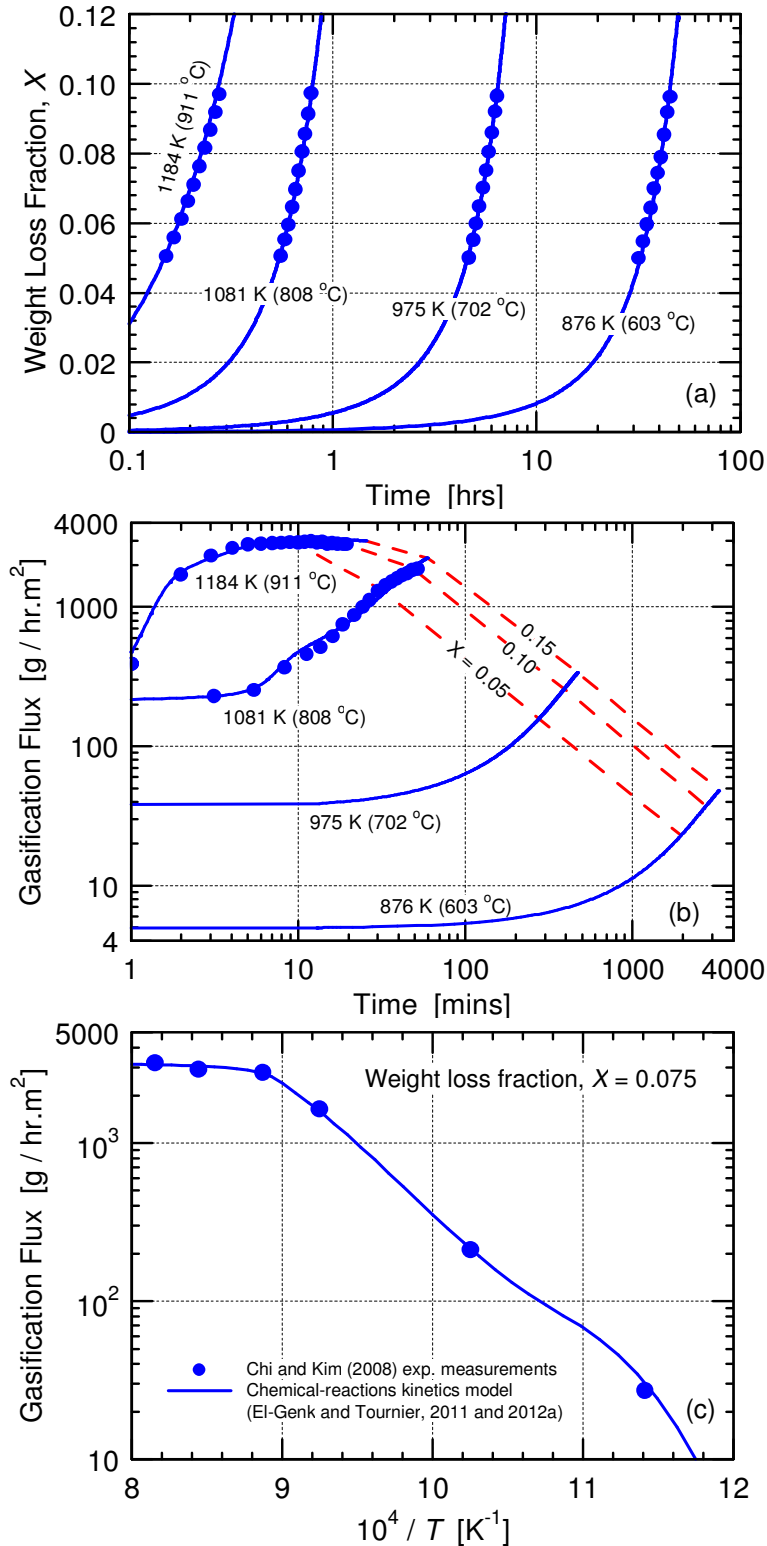


Figure 5.4. Comparison of Model Results with Reported Measurements for NBG-18 in the Experiments of Chi and Kim (2008): (a) Transient Weight Loss; (b) Transient Gasification Rate; (c) Arrhenius Curve of Total Gasification Rate.

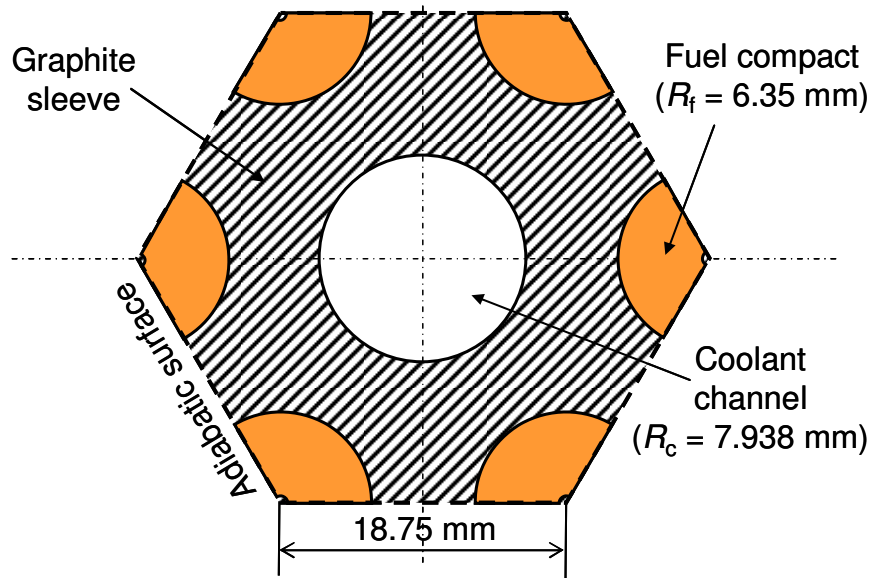
In the safety analysis of a VHTR or HTR, in the unlikely event of massive air ingress, coupling a 3-D Computational Fluid Dynamics (CFD) code to the chemical-reactions kinetics model of gasification would be computationally intensive. An alternative approach is to compile the results from the gasification model into two-dimensional readout tables or arrays. These tables will then be coupled using a User Interface to the CFD codes for performing the reactor safety analysis. The readout tables list the molar fluxes of CO and CO₂ gases as functions of temperature, oxygen partial pressure in the bulk gas flow and local graphite weight loss.

To demonstrate the fidelity and implementation of this approach, this Chapter presents the results of a transient gasification analysis of NBG-18 nuclear graphite in a typical flow channel in a VHTR or HTR fuel assembly (Fig. 5.3). A transient, multi-species diffusion and flow model for the flow channel is developed and coupled, using a Generic Interface, to the compiled readout tables of the gasification results for NBG-18 nuclear graphite. The model is implemented on the Matlab®/Simulink® platform (Simulink, 2008). It handles a bulk gas flow comprised of up to 5 species (He, N₂, O₂, CO and CO₂) and accounts for the heat released in the exothermic production reactions of CO and CO₂ gases. When coupled to the readout tables, the results include the transient values of the local production fluxes (mole/m².s) of CO and CO₂ gases, the local oxygen partial pressure in the bulk gas mixture, and the local graphite loss as functions of graphite temperature and temperature and Reynolds number of the atmospheric air entering the channel. The transient gasification analysis is carried out until reaching a 10% graphite weight loss at the entrance of the flow channel. In addition, the practical implementation of the gasification Generic Interface into a commercial Finite-Element CFD code is demonstrated using CD-Adapco STAR-CCM+. The gasification results of the NBG-18 nuclear graphite flow channel obtained using STAR-CCM+ are successfully compared with those obtained using the multi-species diffusion and flow model developed on the Matlab®/Simulink® platform. The next Section provides details of the problem statement and conditions.

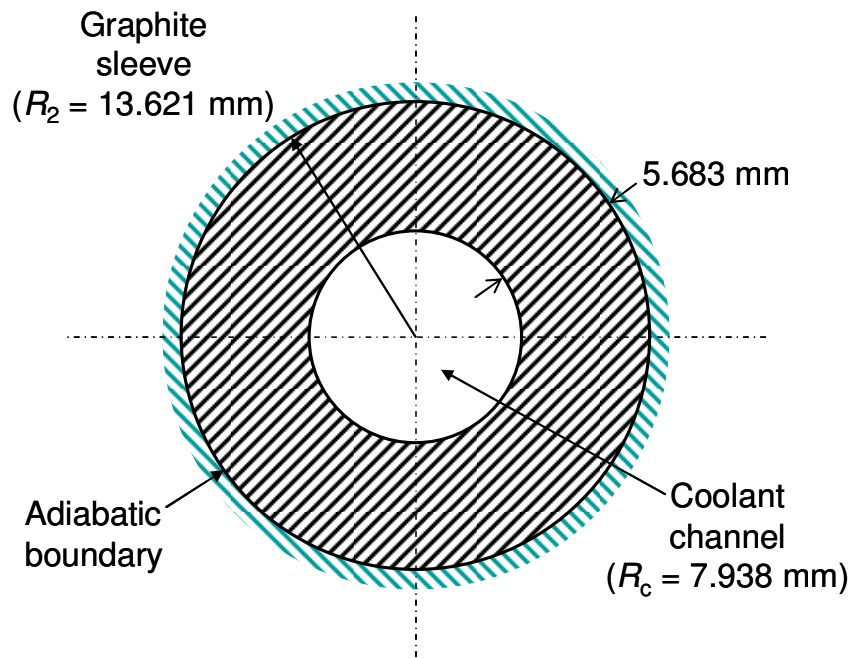
5.1 GEOMETRY AND PROBLEM STATEMENT

A hexagonal fuel assembly in a typical prismatic core VHTR or HTR is ~ 80 cm-high and 36 cm flat-to-flat (Figs. 5.2 and 5.3) (IAEA, 2001; MacDonald et al., 2004; Baxi et al., 2006; INL, 2007). It comprises 210 channels for loading the TRISO fuel compacts and 108 helium coolant flow channels in a triangular lattice with a pitch of 18.75 mm (Figs. 5.3 and 5.5a). Most coolant channels are 15.876 mm in diameter and the fuel channels are 12.7 mm in diameter, slightly larger than that (12.5 mm) of the fuel compacts. The minimum thickness of the graphite structure between adjacent coolant and fuel compact channels is 4.462 mm (Figs. 5.2 and 5.5a). This figure presents schematics of the geometry for implementing and testing the Generic Interface for coupling the readout tables for the gasification of NBG-18 nuclear graphite in the flow channel to the multi-species, bulk gas flow and diffusion model. The channel is surrounded by a 5.683 mm thick NBG-18 graphite sleeve (Fig. 5.5b) that preserves the amount of NBG-18 graphite for a single channel in a prismatic fuel assembly. For symmetry, the outer, top and bottom surfaces of the graphite sleeve are thermally insulated. The height of the flow channel (0.80 m) is the same as that of a typical prismatic fuel assembly (Fig. 5.3).

Initially, the graphite sleeve (Fig. 5.6) is at a uniform temperature, T_o , and the flow channel is filled with helium gas at atmospheric pressure and T_o . At the start of the transient, $t = 0$, atmospheric air enters through the bottom of the channel at T_o and Re_{in} (Fig. 5.6b). The transient



(a) A Single Flow Channel Module



(b) An Equivalent Graphite Sleeve Annulus

Figure 5.5. Single-Channel Fuel Module and Equivalent Graphite Annulus in a Prismatic VHTR or HTR Fuel Assembly.

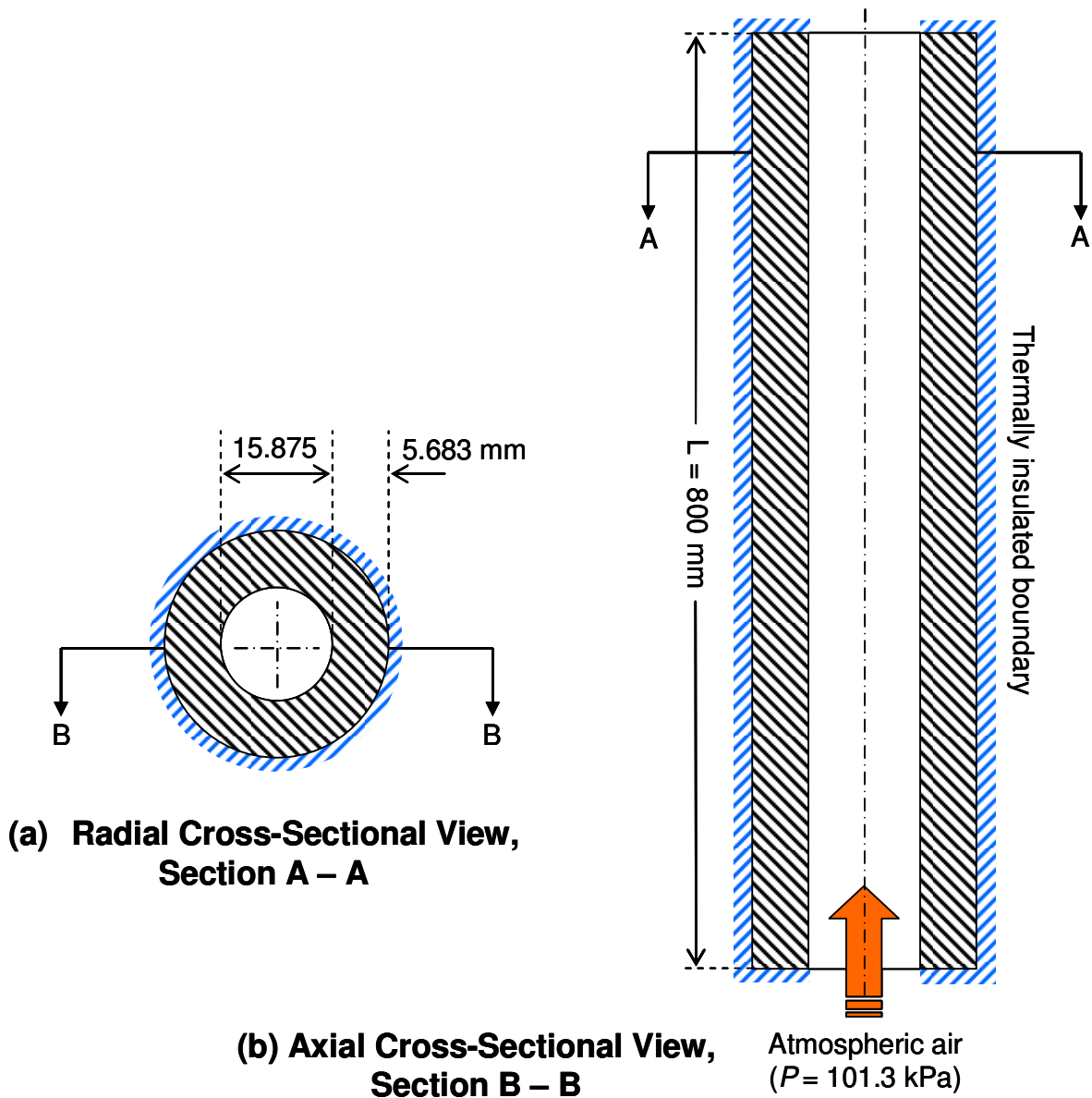


Figure 5.6. Cross-Sectional Views of a Flow Channel and Equivalent NBG-18 Graphite Sleeve.

gasification analysis varies T_0 from 800 K to 1100 K at $Re_{in} = 5, 10$ and 20. Calculated are the spatial temperature distributions in the graphite sleeve, the local temperature and composition of the bulk gas flow, and the oxygen partial pressure along the flow channel. Also calculated are the local productions of CO and CO₂ gases and the local and total gasification of NBG-18 graphite in the channel. The gasification transient continues until the graphite weight loss fraction at the inlet of the flow channel reaches 0.10, $t = t_{10}$. The developed multi-species diffusion and flow model and the readout gasification tables for NBG-18 nuclear graphite are discussed in the next sections.

5.2 READOUT TABLES OF NBG-18 GASIFICATION

The gasification and weight loss of the NBG-18 nuclear graphite are calculated as functions of temperature and oxygen partial pressure using the chemical-reactions kinetics models with the parameters listed in Table 5.1. These parameters are consistent with the reported measurements of the total gasification rate and transient weight loss for NBG-18 in experiments by various investigators (Chi and Kim, 2008; Hinssen et al., 2008). The gasification results listed in the readout tables are for every 10 K, from 800 K to 1250 K, and oxygen partial pressure every decade, from 10^{-3} Pa to 10^4 Pa, with additional values of 300 Pa, 3 kPa and 21.4 kPa, for seven weight loss fractions, $X = 0.0001, 0.01, 0.02, 0.04, 0.06, 0.08$ and 0.10 . The values of the CO and CO₂ molar fluxes [mole/m².s] are compiled into seven, 2-D readout tables of 46 x 11 elements, one for each weight loss fraction. These 2-D tables are then loaded into a 3-D table block in Simulink® (2008) with an index i corresponding to temperature [K], index j corresponding to $\log_{10}(P_{O_2})$ in [Pa], and index k corresponding to the local weight loss fraction, X . Accurate linear interpolation and extrapolation in the 3-D readout table are obtained when using the logarithmic values of the oxygen partial pressure and of the CO and CO₂ molar fluxes.

Table 5.1. Recommended Oxidation Kinetics Parameters for Different Grades of Nuclear Graphite (El-Genk and Tournier, 2012c).

Parameters	IG-110 and NBG-25	IG-430 and NBG-18
$\bar{\epsilon}_a$ (kJ/mole)	120.4 ± 4	131.7 ± 16
σ_a (kJ/mole)	64.6 ± 5	64.6 ± 5
k_a^o (mole ⁻¹ .s ⁻¹)	$13,000. \pm 200$	$11,730. \pm 1,100.$
k_b^o (mole ⁻¹ .s ⁻¹)	$(7.46 \pm 0.1) \times 10^{14}$	$(10.1 \pm 0.7) \times 10^{14}$
ϵ_b (kJ/mole)	204.7 ± 7	195.0 ± 7
$\bar{\epsilon}_d$ (kJ/mole)	485.4 ± 3	476.0 ± 24
σ_d (kJ/mole)	5.00 ± 0.7	5.70 ± 0.4
k_d^o (s ⁻¹)	$(4.3 \pm 0.1) \times 10^{26}$	$(5.6 \pm 0.5) \times 10^{26}$
k_d^* (mole ⁻² .s ⁻¹)	$(4.89 \pm 0.4) \times 10^{12}$	$(4.16 \pm 0.4) \times 10^{12}$
ϵ_d^* (kJ/mole)	158.5 ± 1.2	153.4 ± 3.5

Because some CFD codes such as STAR-CCM+ (2012) are not compatible with the 3-D readout table, a different approach that would work is also tested. A subroutine is developed in C-programming language to perform the linear interpolation and extrapolation on the weight loss fraction in seven individual 2-D readout tables. The subroutine also performs linear interpolations and extrapolations on temperature and oxygen partial pressure in each of the seven 2-D readout tables, one for a different weight loss fraction. The subroutine could be loaded as a User Code

Field Function in CFD codes such as STAR-CCM+ (2012) for performing future safety analysis of a VHTR or HTR in the unlikely event of a massive air ingress accident. Such an approach is also successfully tested in this work (see Section 5.5).

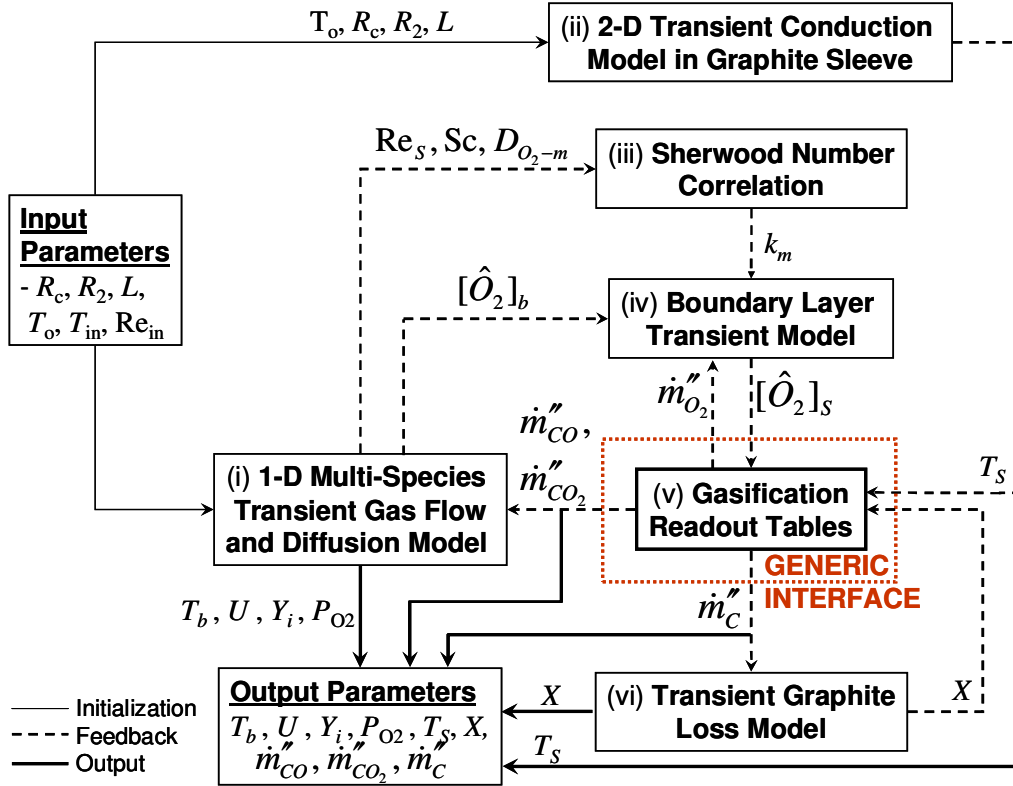


Figure 5.7. Block-Diagram of Multi-Species Transient Flow and Diffusion Model Developed Using the Matlab/Simulink® Platform.

5.3 MULTI-SPECIES DIFFUSION AND FLOW MODEL

A multi-nodal, multi-species transient flow and diffusion model of the bulk gas mixture in the NBG-18 graphite channel in Fig. 5.6 is developed and implemented on the Matlab/Simulink® platform using a control-volume approach (Fig. 5.7). The bulk gas mixture in the channel comprises up to 5 species (He, CO, CO₂, O₂ and N₂, $n = 5$). The model calculates the local gas temperature, pressure and mass-averaged velocity as well as the fractions of the 5 gaseous species in the bulk flow along the channel. It solves the transient mass balance equations of the different species in the bulk gas flow mixture, and the momentum and energy balance equations of the flow along the channel (Fig. 5.7 block (i)). The accuracy of the model is successfully verified by comparing its results with those of a 3-D analysis of the helium gas flow through a 8-m long channel in a VHTR core using the STAR-CCM+ code (Travis and El-Genk, 2013).

The multi-species flow and diffusion model is coupled to a two-dimensional transient conduction model in the graphite sleeve of the 0.80 m long flow channel (Figs. 5.6 and 5.7 block

(ii)). It accounts for the heat released in the production of CO and CO₂ gases as well as the convective heat transfer at the graphite surface and counter-current diffusion in the boundary layer. The diffusion velocity of oxygen in the boundary layer, from the bulk gas to the graphite surface, is calculated using a recently developed Sherwood number correlation (El-Genk and Tournier, 2012d; Fig. 5.7 block (iii)). The diffusion of oxygen from the bulk gas and the counter-current diffusion of the CO and CO₂ gaseous products from the graphite surface are incorporated into the mass balance equations. The energy balance at the graphite surface in the channel determines the local graphite temperature, including the effect of the heat released in the formation reactions of the CO and CO₂ gases. The governing equations in the multi-species diffusion and flow model are presented and discussed next.

5.3.1 Governing equations

The bulk gas flow in the channel (Fig. 5.6) is modeled using one-dimensional, transient mass, momentum and energy balance equations. The gas mixture consists of 5 components ($n = 5$), He ($i = 1$), CO ($i = 2$), CO₂ ($i = 3$), O₂ ($i = 4$) and N₂ ($i = 5$).

5.3.1a Mass balance

The mass balance for the gas species, i , in the bulk gas flow accounts for the consumption and production during gasification (e.g., O₂ and both CO and CO₂ gases) as well as the mass-averaged flow and inter-diffusion (Bird, Stewart and Lightfoot, 1960). Thus, the transient mass balance equation for the bulk gas species is written as:

$$\frac{\partial(\rho Y_i)}{\partial t} + \frac{\partial(\rho \bar{U} Y_i)}{\partial z} = \frac{\partial}{\partial z} \left(\rho D_{i-m} \frac{\partial Y_i}{\partial z} \right) + \dot{m}_i''' , \quad (i = 1 \text{ to } 5). \quad (5.1a)$$

These equations are subject to the overall conservation of mass:

$$\sum_{i=1}^n Y_i = 1 . \quad (5.1b)$$

The 6 mass balance equations (5.1a) and (5.1b) are solved for the density of the bulk gas mixture, ρ and the mass fractions, Y_i , of the five species in the mixture. In practice, the bulk density is obtained from the solution of the gas flow overall mass balance, given by the summation for the five species in Equations (5.1a), as:

$$\frac{\partial \rho}{\partial t} + \frac{\partial(\rho \bar{U})}{\partial z} = \sum_{i=1}^n \dot{m}_i''' . \quad (5.2)$$

The multi-component diffusion coefficients in Equations (5.1a) are calculated assuming dilute concentrations in a homogeneous bulk gas mixture (Bird, Stewart and Lightfoot, 1960). For the species i , the diffusion coefficient is expressed as:

$$D_{i-m} = (1 - X_i) \left/ \sum_{k=1, k \neq i}^n (X_k / D_{ik}) \right. . \quad (5.3)$$

The binary diffusion coefficients are calculated using Eq. (2.4b). The values of the binary diffusion coefficients (Eq. 2.4b) are within $\pm 15\%$ of the measured values for all binary mixtures of interest (Landolt and Börnstein 1962). The mass source/sink terms on the right hand side of Equations (5.1a) and (5.2) account for the depletion of oxygen and the addition of gasification products CO and CO₂ to the bulk gas mixture, thus:

$$\dot{m}_1''' = 0, \text{ for helium,} \quad (5.4a)$$

$$\dot{m}_{2,j}''' = 4M_2 \dot{N}_{CO,j}'' / D, \text{ for CO gas,} \quad (5.4b)$$

$$\dot{m}_{3,j}''' = 4M_3 \dot{N}_{CO_2,j}'' / D, \text{ for CO}_2 \text{ gas,} \quad (5.4c)$$

$$\dot{m}_4''' = -M_4 (0.5 \dot{m}_2''' / M_2 + \dot{m}_3''' / M_3) < 0, \text{ for oxygen,} \quad (5.4d)$$

$$\dot{m}_5''' = 0, \text{ for nitrogen.} \quad (5.4e)$$

The mass source terms for the CO and CO₂ gaseous species are determined from their rates of production at the graphite surface in the flow channel (Fig. 5.7 block (v)). The mass sink term of oxygen depletion by diffusion from the bulk gas to the graphite surface in the channel (Fig. 5.7 block (iv)) is given as:

$$\dot{m}_4''' = - (4/D) M_4 k_m \left([\hat{O}_2]_b - [\hat{O}_2]_s \right). \quad (5.5)$$

This equation can be re-arranged to explicitly express the oxygen partial pressure at the graphite surface as:

$$(P_{O_2})_s = R_g T_s [\hat{O}_2]_s = R_g T_s \left([\hat{O}_2]_b + \frac{\dot{m}_4''' D}{4M_4 k_m} \right). \quad (5.6)$$

In these equations, $[\hat{O}_2]_b$ and $[\hat{O}_2]_s$ are the local concentrations of oxygen in the bulk gas mixture and at the graphite surface, respectively, and k_m is the oxygen's effective diffusion velocity through the boundary layer. It is expressed in terms of Sherwood number, Sh, of the bulk gas mixture as:

$$k_m = \text{Sh } D_{O_2-m} / D. \quad (5.7)$$

The local values of Sh and D_{O_2-m} depend on the local flow conditions and the properties and composition of the bulk gas. The recently developed Sh correlation for laminar flow condition ($0.006 \leq \text{Re}_s \leq 1,000$) is given as (El-Genk and Tournier, 2012d):

$$\text{Sh} = [0.27 + 0.60 \text{Re}_s^{0.47}] \text{Sc}^{0.33} (\mu_b / \mu_s)^{0.14}. \quad (5.8)$$

The values of k_m are consistent with the reported total gasification rate measurements in experiments with relatively small specimens, 0.25 g to 25 g of nuclear graphite grades of NBG-18, NBG-25, IG-11, IG-110 and IG-430 in atmospheric air at $0.08 \leq \text{Re}_s \leq 30$ (see Section 2.2

and Fig. 2.7). These measurements include those reported by: (a) Xiaowei et al. (2004) for IG-11 nuclear graphite at 1073 – 1473 K and weight loss fraction of 0.08 – 0.34; (b) Hinssen et al. (2008) for NBG-18 graphite at 1023 K and weight loss fraction of 0.08 – 0.4; and (c) Chi and Kim (2008) for NBG-18, NBG-25, IG-110 and IG-430 nuclear graphite at 1127 – 1226 K and weight loss fraction of 0.05 – 0.1.

The Sh correlations of Hilpert (1933) and McAdams (1954) in Fig. 2.6 are within –5% to +10% of Equation (5.8). It is worth noting that Equation (5.8) is practically limited to below 1400 K, when the contributions of the Boudouard reaction and the CO/O₂ homogeneous reaction in the boundary layer are negligible. These reactions are not considered in the present model.

The local graphite loss rate (Fig. 5.7 block (vi)) is expressed in terms of the rate of removal of carbon atoms from its surface as:

$$(d[C'']/dt) = -(\dot{N}''_{CO_2} + \dot{N}''_{CO}). \quad (5.9)$$

The moles of carbon atoms per unit surface of the graphite sleeve (Fig. 5.6) is given by:

$$[C''](z,t) = [C'']_o + \int_0^t \frac{d[C'']}{dt} dt = [C'']_o - \int_0^t [\dot{N}''_{CO_2}(z,t) + \dot{N}''_{CO}(z,t)] dt. \quad (5.10)$$

The corresponding transient local weight loss fraction of graphite at an axial local, z , from the channel entrance (Fig. 5.7 block (vi)) is given by:

$$X(z,t) = 1 - ([C''](z,t)/[C'']_o). \quad (5.11)$$

For the flow channel initially filled with helium ($t < 0$), atmospheric air is introduced at $t = 0$ through the bottom at a specified temperature and Reynolds number. Equation (5.2) is solved subject to the initial and boundary conditions:

$$\rho(z, 0) = \rho_{He}, \quad \text{and} \quad \rho(0, t) = \rho_{air}. \quad (5.12)$$

Air is simulated as a binary gas mixture of oxygen and nitrogen, and the mass balances of the gaseous species in the bulk gas flow (Eq. 5.1a) are solved subject to the following initial and boundary conditions:

$$Y_1(z, 0) = 1.0, \quad Y_1(0, t) = 0.0 \quad (\text{helium}), \quad (5.13a)$$

$$Y_2(z, 0) = 0.0, \quad Y_2(0, t) = 0.0 \quad (\text{CO gas}), \quad (5.13b)$$

$$Y_3(z, 0) = 0.0, \quad Y_3(0, t) = 0.0 \quad (\text{CO}_2 \text{ gas}), \quad (5.13c)$$

$$Y_4(z, 0) = 0.0, \quad Y_4(0, t) = 0.2345 \quad (\text{oxygen}), \quad (5.13d)$$

$$Y_5(z, 0) = 0.0, \quad \text{and} \quad Y_5(0, t) = 0.7655 \quad (\text{nitrogen}). \quad (5.13e)$$

5.3.1b Momentum balance

The momentum balance equation for the bulk gas flow in the channel, expressed in terms of the mass-averaged flow velocity, \bar{U} , is written as:

$$\frac{\partial(\rho\bar{U})}{\partial t} + \frac{\partial(\rho\bar{U}^2)}{\partial z} = -\frac{\partial P}{\partial z} - \frac{f}{2D}\rho|\bar{U}|\bar{U}, \quad (5.14)$$

The pressure of the bulk gas mixture is expressed using the equation of state for an ideal gas, as:

$$P = \rho R_g T_b \times \sum_{i=1}^n (Y_i / M_i). \quad (5.15)$$

Equation (5.14) is solved subject to the following initial and boundary conditions:

$$\bar{U}(z, t = 0) = 0.0, \quad \bar{U}(z = 0, t) = v_{air}^o \text{Re}_{in} / D, \quad \text{and} \quad P(z, 0) = P(0, 0) = P_o. \quad (5.16)$$

5.3.1c Energy balance

The energy balance equation for the bulk gas flow in the channel is written as:

$$\frac{\partial(\rho C_p T_b)}{\partial t} + \frac{\partial(\rho\bar{U} C_p T_b)}{\partial z} = \frac{\partial}{\partial z} \left(\lambda_m \frac{\partial T_b}{\partial z} \right) - \sum_{i=1}^n (\Delta H_i^f \dot{m}_i^m) + \frac{4}{D} h (T_{G,s} - T_b). \quad (5.17)$$

This equation accounts for the convective heat transfer at the inner surface of the graphite sleeve and for the released heats of production of CO and CO₂ during graphite gasification. The friction factor, f and the heat transfer coefficient, h , are those for a fully-developed laminar flow. The viscosity and thermal conductivity of the bulk gas mixture are calculated using the mean average of the simple and reciprocal mixing rules (Gandhi and Saxena, 1966; Mathur, Tondon and Saxena, 1967), as:

$$\mu_m = \frac{1}{2} \left\{ \sum_{i=1}^n (X_i \mu_i) + \left(\sum_{i=1}^n (X_i / \mu_i) \right)^{-1} \right\}, \quad (5.18a)$$

$$\lambda_m = \frac{1}{2} \left\{ \sum_{i=1}^n (X_i \lambda_i) + \left(\sum_{i=1}^n (X_i / \lambda_i) \right)^{-1} \right\}. \quad (5.18b)$$

The molar fraction of species, X_i , is calculated in terms of the mass fractions, Y_i as:

$$X_i = \frac{Y_i}{M_i} \times \left(\sum_{k=1}^n (Y_k / M_k) \right)^{-1}. \quad (5.19)$$

The molecular weight of the multi-component gas mixture is given by:

$$M_m = \sum_{i=1}^n (X_i M_i) = \left(\sum_{i=1}^n (Y_i / M_i) \right)^{-1} \quad (5.20)$$

The energy balance Equation (5.17) is solved for the bulk gas temperature, T_b , subject to the following initial and boundary conditions:

$$T_b(z, 0) = T_o, \quad T_b(0, t) = T_o \quad \text{and} \quad T_b(L, t) = T_{b,ex} \quad (5.21)$$

The temperature of the exiting gas mixture, $T_{b,ex}$, is calculated from the overall energy balance in the flow channel.

5.3.1d Energy balance in graphite sleeve

The transient two-dimensional temperature distribution in the graphite sleeve (Fig. 5.5) is calculated from the energy balance equation (Fig. 5.7 block (ii)):

$$\frac{\partial(\rho_G C_{p,G} T_G)}{\partial t} = \frac{1}{r} \frac{\partial}{\partial r} \left(r \lambda_G \frac{\partial T_G}{\partial r} \right) + \frac{\partial}{\partial z} \left(\lambda_G \frac{\partial T_G}{\partial z} \right) \quad (5.22)$$

This equation is solved subject to the following initial and boundary conditions:

$$\begin{aligned} T_G(r, z, t = 0) &= T_o, \quad T_G(R_c, z, t) = T_{G,s}, \quad \text{and} \\ \frac{\partial T_G}{\partial z}(r, 0, t) &= \frac{\partial T_G}{\partial z}(r, L, t) = \frac{\partial T_G}{\partial r}(R_2, z, t) = 0. \end{aligned} \quad (5.23)$$

The graphite surface temperature, $T_{G,s}$, is determined from the energy balance:

$$\left(-\lambda_G \frac{\partial T_G}{\partial r} \right) = \sum_{i=1}^n (\Delta H_i^f \dot{m}_i''') - \frac{4}{D} h (T_{G,s} - T_b) \quad (5.24)$$

5.3.2 Solution implementation

The transient diffusion and flow model of the bulk gas mixture in the graphite channel in Fig. 5.5 (Equations (5.1) – (5.24)) is implemented in Matlab/Simulink® and coupled to the readout tables of the gasification of NBG-18 nuclear graphite (Fig. 5.7 block (v)). Calculated are the local productions of CO and CO₂ gases, graphite local and total losses, oxygen partial pressure and composition and temperature of bulk gas mixture flow along the channel.

The implemented model in Matlab/Simulink® (Simulink, 2008) uses the control-volume approach and conventional computational staggered grid in cylindrical coordinates to solve the governing equations (Fig. 5.8). The local temperature and pressure of the bulk gas are calculated

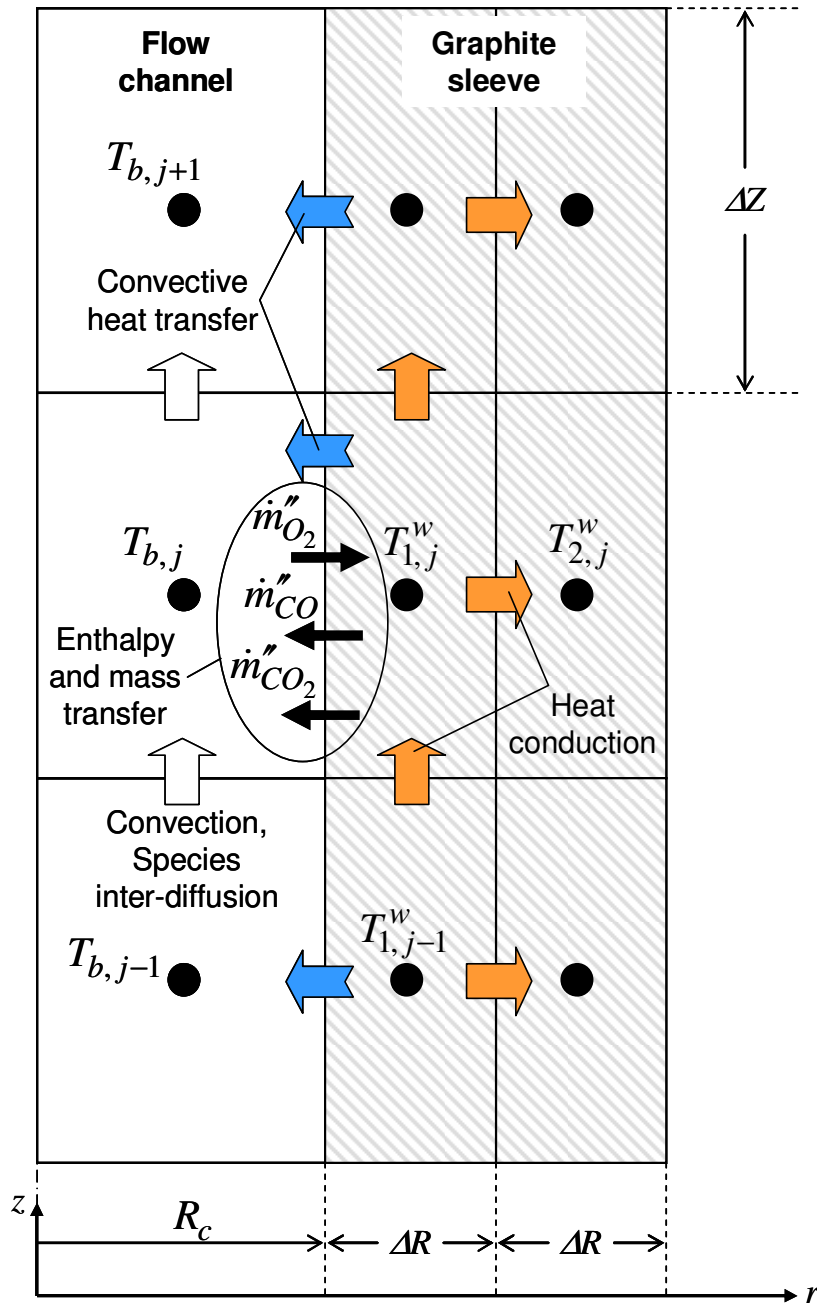


Figure 5.8. Computational Grid for the Gasification of NBG-18 Nuclear Graphite in a Single Channel of a VHTR or HTR Prismatic Fuel Assembly.

at the center of the numerical mesh elements in the flow channel, while the velocity and mass flux are evaluated at the interfaces of the mesh elements. The gas flow domain in the channel comprises one radial control volume or mesh element and N_z identical axial mesh elements. The nuclear graphite sleeve is discretized radially into N_r mesh elements of identical width, ΔR , and N_z

axial mesh elements (Fig. 5.8). The results of the graphite gasification and temperature in the channel (Figs. 5.6 and 5.8) are not affected by increasing the number of radial numerical mesh elements in the graphite sleeve, N_r , from 2 to 9.

Owing to the flow channel's large height-to-diameter ratio and the relatively high thermal conductivity of nuclear graphite, results show that despite the release of the heats of formation of CO and CO₂ gases at the surface of the graphite in the channel, the radial temperature differential across the graphite sleeve is very small (< 1 K). The axial change in the graphite temperature is much larger and depends on the time of gasification and the values of T_o and Re_{in} .

5.4 GASIFICATION RESULTS AND DISCUSSION

The results of the transient gasification of NBG-18 nuclear graphite in a 0.8 m long circular channel with atmospheric air (Fig. 5.6) are presented and discussed in this section. The analysis varies the initial graphite temperature, T_o , which is the same as that of the air entering the channel, from 800 K to 1100 K at air Re_{in} of 5, 10 and 20. With time into the transient, the axial profile of the local gasification rate changes along the flow channel. This is because of the rise in the graphite surface temperature by the released heats in the exothermic production reactions of CO and CO₂ gases. The rates of these reactions depend on the local partial pressure of oxygen in the bulk gas as well as the surface temperature. Graphite gasification in the channel ceases where the oxygen in the bulk gas flow is fully depleted. Depending on the values of T_o and Re_{in} , this could occur somewhere in the flow channel.

In addition to the local graphite and bulk gas temperatures along the channel, transient calculations include the local composition of the bulk gas, the local production of CO and CO₂ gases and the total graphite loss in the channel. The gasification transient continues until reaching a weight loss fraction of 0.10 at the channel entrance, $t = t_{10}$. At the start of the gasification transient, $t = 0$, purging the helium gas initially present in the channel with the atmospheric air introduced through the bottom (Fig. 5.6) generates a sonic pressure wave. It is simulated using the ODE23s numerical solution technique of Matlab®/Simulink® (Shampine et al., 1999), but increases the CPU time for completing the calculations. To accelerate the calculations, a reflective impedance introduced at the exit of the channel nearly eliminated or effectively damped the sonic wave in less than 200 ms of transient time. Beyond this time, the reflective impedance is no longer needed, and was turned off.

The time to fully purge the helium from the flow channel and replace it with air is tens of seconds long, depending on the values of T_o and Re_{in} . At $T_o = 900$ K and $Re_{in} = 20$ (or air average inlet velocity = 13 cm/s) purging the helium gas from the 80 cm-long flow channel by the atmospheric air takes < 7 s of real time, increasing to ~ 30 s at $Re_{in} = 5$. During this relatively short time, the air flow is established along the channel with insignificant effect on graphite gasification. This is because t_{10} is much longer, varying from ~ 0.5 hr (1,800 s) to ~ 200 hrs, depending on the values of T_o and Re_{in} used in the analysis.

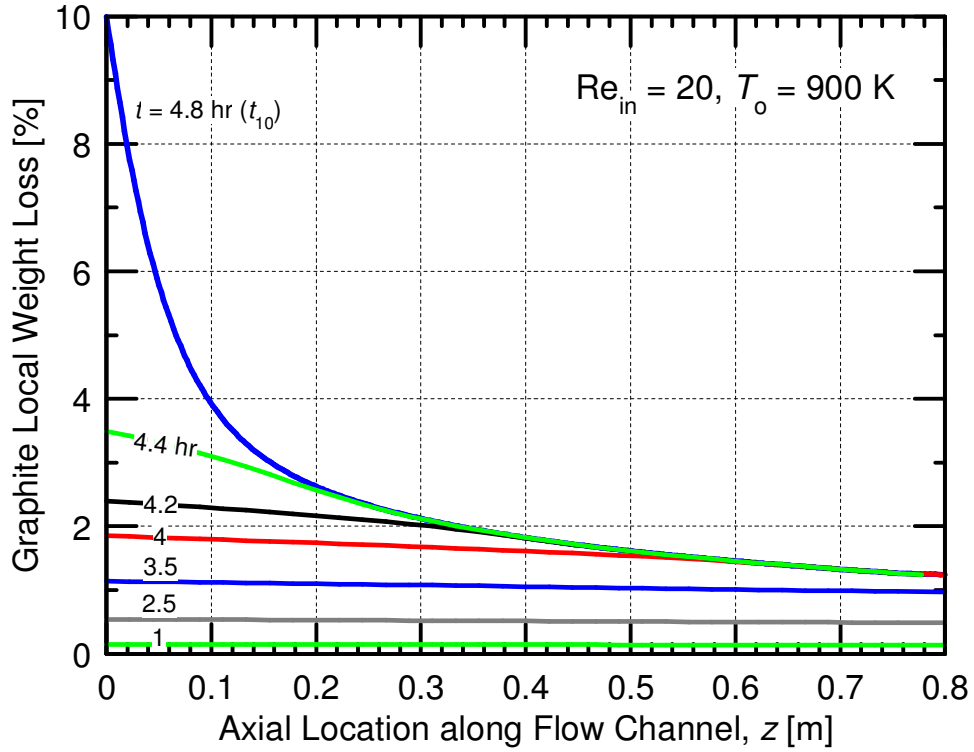


Figure 5.9. Calculated Graphite Local Loss along the Flow Channel at Different Times in the Gasification Transient.

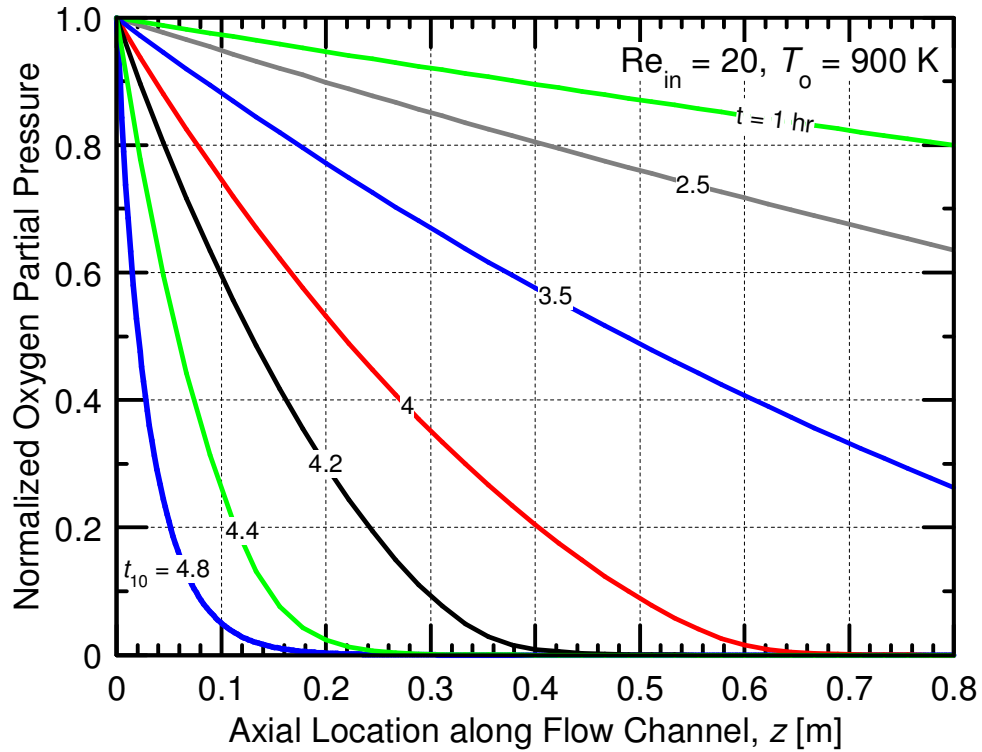


Figure 5.10. Axial Distribution of Oxygen Partial Pressure in Flow Channel in the Gasification Transient.

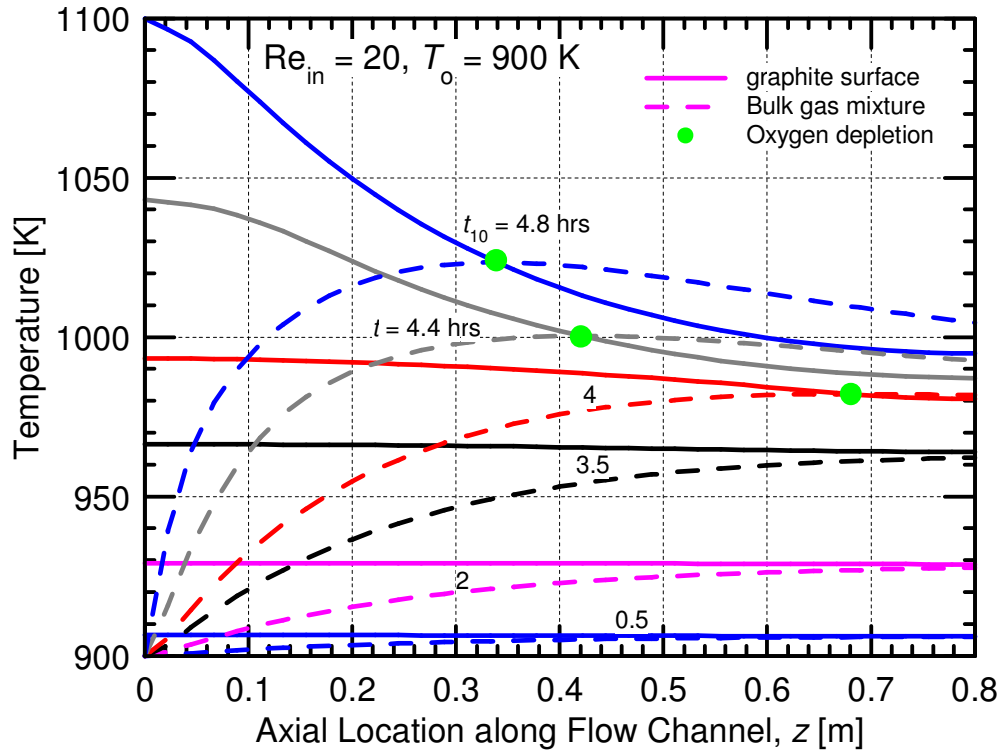


Figure 5.11. Axial Distributions of Graphite Surface Temperature and Bulk Gas Temperature in the Gasification Transient.

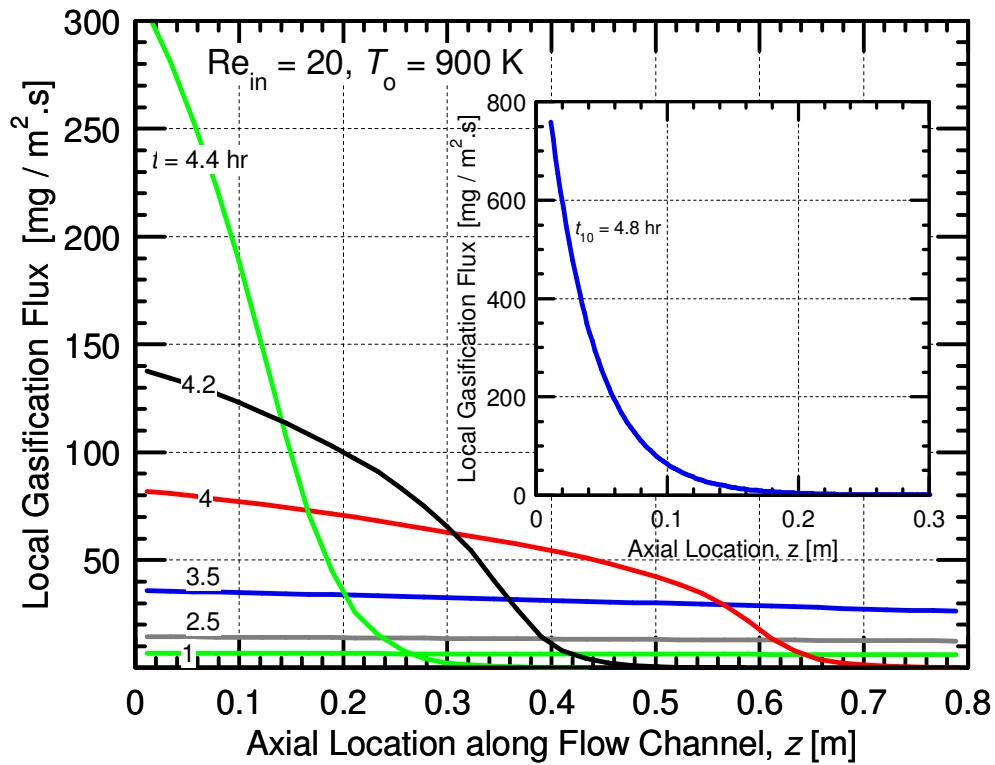


Figure 5.12. Axial Distribution of Gasification Flux in Flow Channel in the Gasification Transient.

5.4.1 Graphite gasification

The calculated axial profiles of the graphite local weight loss at different times during the gasification transient are compared in Fig. 5.9, for $Re_{in} = 20$ and $T_o = 900$ K. During the first 3.5 hrs, the local gasification rate is relatively low and the graphite weight loss is nearly uniform along the channel. This is because of the availability of oxygen in the bulk gas flow (Fig. 5.10) and the uniform rise in graphite temperature due to gasification along the channel (Fig. 5.11). The oxygen mole fraction in the bulk gas flow exiting the channel is as much as 27% of its value at the channel entrance (0.2115) (Fig. 5.10). After 3.5 hrs of gasification transient, the local weight loss of NBG-18 graphite along the channel is nearly uniform and equals $\sim 1\%$ (Fig. 5.9). Owing to the uniform graphite gasification, the increase in surface temperature due to the exothermic reactions that produce CO and CO₂ gases (Eqs. (5.25) and 5.26), is also uniform along the channel (Fig. 5.11). The uniform increase in the local gasification rate is the combined contribution of a number of effects:

- (a) The increase in graphite surface temperature caused by the release of the heats of formation of the CO and CO₂ gases, whose rates increase exponentially with increasing temperature;
- (b) The increase in the Active Surface Area (ASA) of free sites with weight loss increases the CO production, and to a lesser extent, that of CO₂ (El-Genk and Tournier, 2012a); and
- (c) Though the decrease in the oxygen partial pressure along the flow channel decreases the local gasification rate, its effect seems to be much smaller than those of (a) and (b) above, but becomes increasingly important with longer times in the gasification transient.

At larger times in the transient, $t > 3.5$ hrs, the gasification rate along the channel becomes non-uniform (Fig. 5.12); with the local weight loss increasing faster near the entrance (Fig. 5.9) and decreasing with distance into the channel. This is due to the increase in the surface temperature by the release of the heats of formation of CO and CO₂ gases, whose rates are highest near the entrance of the channel (Fig. 5.11). This is where the oxygen partial pressure is also the highest. The local graphite gasification decreases with axial distance into the channel due to the decrease in the oxygen partial pressure in the bulk gas flow. After 4 and 4.2 hrs into the transient at $Re_{in} = 20$ and $T_o = 900$ K, the oxygen in the bulk gas flow is fully depleted at ~ 70 and 50 cm into the channel, respectively (Figs 5.9, 5.10 and 5.12). The graphite temperature in the part of the channel with no oxygen in the bulk gas continues to increase slowly due to the axial conduction in the graphite sleeve (Fig. 5.11). After 4.8 hrs into the gasification transient, the graphite weight loss at the entrance of the channel reaches 10%, while that at the exit of the channel is only 1.2% (Fig. 5.9). At that time ($t = t_{10}$), the oxygen partial pressure is fully depleted all along the flow channel, except in the 30 cm section near the entrance (Fig. 5.10).

Figure 5.11 shows the calculated axial distributions of the graphite surface and bulk gas flow temperatures during the gasification transient. During the first 3.5 hrs, the graphite local surface temperature rises uniformly along the channel, and the convective heat transfer to the bulk gas increases its temperature with increasing axial distance in the channel. At longer times, oxygen is depleted near the exit of the channel, and the rapid rise in the graphite surface temperature near the entrance due to the heats of formation of CO and CO₂ gases increases that of the bulk gas flow (Fig. 5.11). The following sub-section presents and discusses the results of the total, or cumulative production of CO and CO₂ gases in the flow channel during the simulated transient, up to t_{10} , at $T_o = 900$ K and $Re_{in} = 20$.

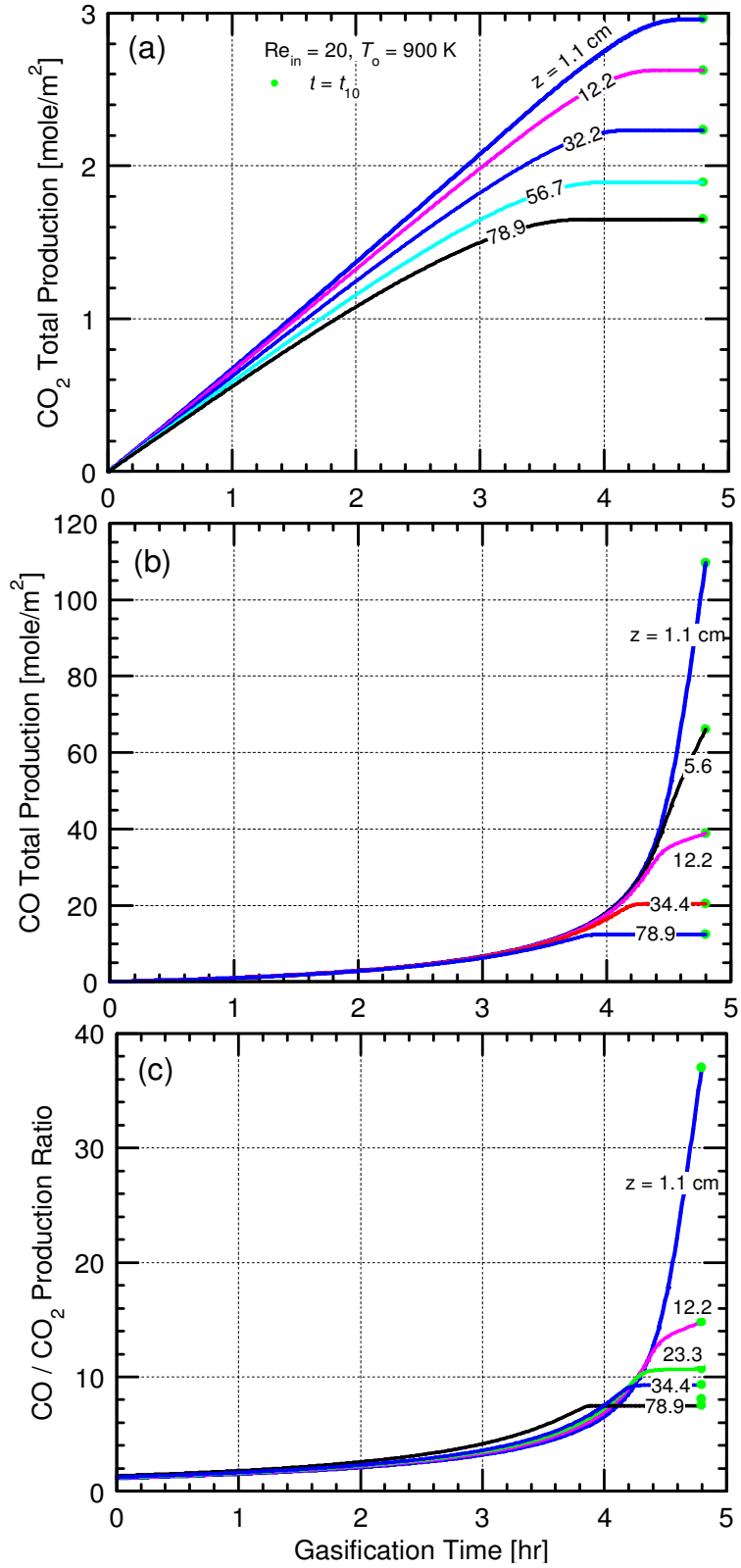


Figure 5.13. Transient CO₂ and CO Total Productions and Production Ratio in Gasification Transient.

5.4.2 Production of CO and CO₂ gases

The production of CO and CO₂ during graphite gasification strongly depends on temperature. At low temperatures ($\leq \sim 950$ K), gasification occurs mostly in the volume pores and the production of CO₂ is typically higher than or comparable to that of CO gas. This is because the specific activation energy for desorption of CO gas molecules is larger than that for CO₂ gas molecules (El-Genk and Tournier, 2012b and 2012c). As the graphite temperature increases, the corresponding increase in the pre-exponential rate constant for the CO desorption increases its production, exceeding that of the CO₂ gas. At high temperatures, the production of CO is significantly higher than that of CO₂, and the primary contributor to graphite loss in the channel.

The calculated local values and ratios of the cumulative productions of CO and CO₂ gases within the flow channel are compared in Figs. 5.13a to 5.13c. These figures present the results up to the time of reaching 10% weight loss at the entrance of the channel ($t = t_{10}$). Initially and for a short period into the gasification transient, the cumulative local production of CO₂ decreases slightly with axial distance in the channel, though comparable to that of CO (Figs. 5.13a and 5.13b). The local cumulative production of CO₂ at the various axial locations in the channel increases linearly with time and ceases to increase when the oxygen in the bulk gas flow is fully depleted. This is indicated by the plateaus of the various curves in Fig. 5.13a.

The local cumulative production of CO in the flow channel increases exponentially with time, exceeding that of CO₂, but remains independent of axial location up to ~ 3.5 hrs of the transient (Fig. 5.13b). Beyond this time, CO production ceases to increase near the exit the flow channel, indicating the depletion of oxygen in the bulk gas flow. Near the entrance of the channel (e.g., $z = 1.1$ and 5.6 cm), where the increases in the graphite temperature are the highest (Fig. 5.11), the local cumulative production of CO continues to increase exponentially with time (Fig. 5.13b). Conversely, at these and other locations along the flow channel the production of CO₂ ceases, even before the end of the transient ($t < t_{10}$) (Fig. 5.13a).

Figure 5.13c compares the ratio of the local cumulative productions of CO and CO₂ gases within the flow channel. This ratio is initially little more than unity, but increases exponentially with time due to the local increase in the graphite surface temperature. This continues until oxygen in the bulk gas is depleted, which is indicated by the plateaus of the curves for the axial locations near the exit of the flow channel ($z > 23.3$ cm). Closer to the entrance of the channel, the ratio of the cumulative productions of CO and CO₂ continue to increase with time (Fig. 5.13c).

The gasification results of the NBG-18 nuclear graphite in a single flow channel of a prismatic fuel assembly in a VHTR or HTR at $T_o = 900$ and $Re_{in} = 20$ (Figs. 5.9 to 5.13) clearly show that the weight loss is not uniform along the flow channel. Such non-uniformity is caused primarily by the increase in the graphite local surface temperature due to the release of the heats of formation of CO and CO₂ gases. The graphite weight loss is significantly higher near the channel entrance. In that section of the flow channel, the oxygen partial pressure in the bulk gas flow sustains gasification. In the remainder of the channel, however, the local gasification and graphite weight loss could be significantly lower owing to the lower production rates of CO and CO₂ due to the limited availability of oxygen in the bulk gas. Results also show that the local graphite weight loss near the channel entrance exceeds 8 times that at the exit of the channel, with most of the difference occurring in the last 50 minutes of the 4.8 hrs long gasification transient (Figs. 5.9 to 5.13). This is when the local graphite temperature and the productions of CO and CO₂ gases

increase rapidly. The next subsection presents the results of a parametric analysis, which investigates the effects of Re_{in} and T_o on the NBG-18 graphite gasification in the simulated flow channel (Fig. 5.6).

5.4.3 Effects of Re_{in} and T_o

The parametric analysis quantifies the effects of changing the initial graphite and air inlet temperatures, T_o , from 800 K to 1100 K and the air inlet Reynolds number, Re_{in} , from 5 to 20 on graphite gasification. The results are presented in Figs. 5.14 to 5.18. The transient values of the total graphite loss in grams, until reaching a 10% weight loss at the channel entrance (t_{10}), are compared in Fig. 5.14. When $T_o = 900$ K and $Re_{in} = 20$, $t_{10} = 4.8$ hrs and the total graphite loss in the channel is 14 g. This loss increases with increasing Re_{in} (or oxygen supply), but decreases with increasing T_o due to the exponential effect of temperature on the gasification rate. The results in Fig. 5.14 also show that t_{10} decreases with increasing Re_{in} and/or increasing T_o . Because of the higher gasification rate at the channel entrance, a local weight loss of 10% is reached rapidly. For the same Re_{in} , the graphite total loss in the flow channel increases with decreasing T_o , due to the increases in t_{10} and the extent of gasification to the entire or the majority of the channel. Increasing T_o not only decreases t_{10} , but also limits graphite gasification to a shorter section near the entrance. This effectively decreases the total graphite loss in the channel, as well as stimulates the production of mostly CO gas. Thus, the higher the initial graphite temperature, the smaller is the total graphite loss and the shorter the time to reach a 10% weight loss at the channel entrance, t_{10} .

The values of t_{10} are given in Fig. 5.15 as functions of T_o and Re_{in} . When $T_o = 800$ K, increasing Re_{in} from 5 to 20 decreases t_{10} from 158 hrs to 100 hrs, respectively. The values of t_{10} decrease almost exponentially with increasing T_o , but relatively much less with increasing Re_{in} . At Re_{in} of 20, t_{10} is ~ 10 hrs when $T_o = 850$ K, and only 30 mins at 1100 K. When $T_o = 1000$ K, t_{10} is 1.1, 1.5 and 2 hrs at $Re_{in} = 20, 10$ and 5, respectively. When $T_o < 840$ K, graphite gasification is more uniform along the channel and t_{10} is almost independent of Re_{in} . The effect of Re_{in} on t_{10} becomes increasingly more pronounced at high temperatures (Fig. 5.15). At these temperatures, increasing Re_{in} increases the oxygen supply with the air entering the channel, causing the graphite temperature to rise faster near the entrance of the channel due to the higher productions of CO and CO₂ gases. The increase in the gasification rate significantly shortens t_{10} . Conversely, decreasing Re_{in} decreases the oxygen supply to the channel and both the rise in local surface temperature and the gasification rate near the channel entrance, increasing t_{10} (Fig. 5.15). The same explains why decreasing Re_{in} decreases the total graphite loss in the flow channel at t_{10} (Fig. 5.16). When $T_o = 900$ K, the calculated total loss of graphite in the channel up to t_{10} increases from 9.2 g to 11.2 g and 13.9 g when Re_{in} increases from 5 to 10 and 20, respectively.

To quantify the importance of including the heats of formation of CO and CO₂ gases in the calculations, Fig. 5.15 also presents the results when they are neglected. The values of t_{10} increase with decreasing T_o and are almost independent of Re_{in} . At $Re_{in} = 5$ and $T_o = 1100$ K, the value of t_{10} is nearly identical to that when the heats of reactions are included in the calculations. This is because at such high temperature, graphite gasification is limited by the diffusion of oxygen through the boundary layer (Mode (c)), and its high rate decreases the duration of the gasification transient. At $T_o = 1000$ K and $Re_{in} = 20$, $t_{10} = 2.9$ hrs for the isothermal condition (neglecting the heats of production of CO and CO₂ gases), compared to only 1.1 hr when the heats of reactions are included. When $T_o = 900$ K and $Re_{in} = 20$, $t_{10} = 23$ hrs for the isothermal condition, compared to 10 hrs with the heats of reactions included in the graphite gasification calculations.

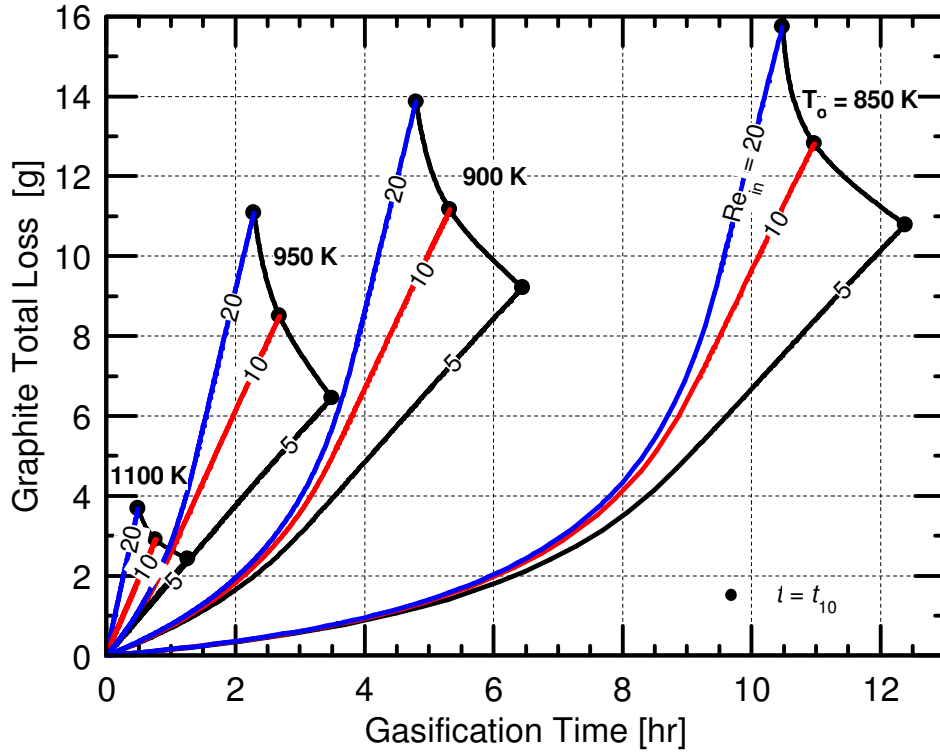


Figure 5.14. Effects of T_o and Re_{in} on Graphite Total Loss versus Gasification Time in a Flow Channel of a Prismatic VHTR or HTR Fuel Assembly.

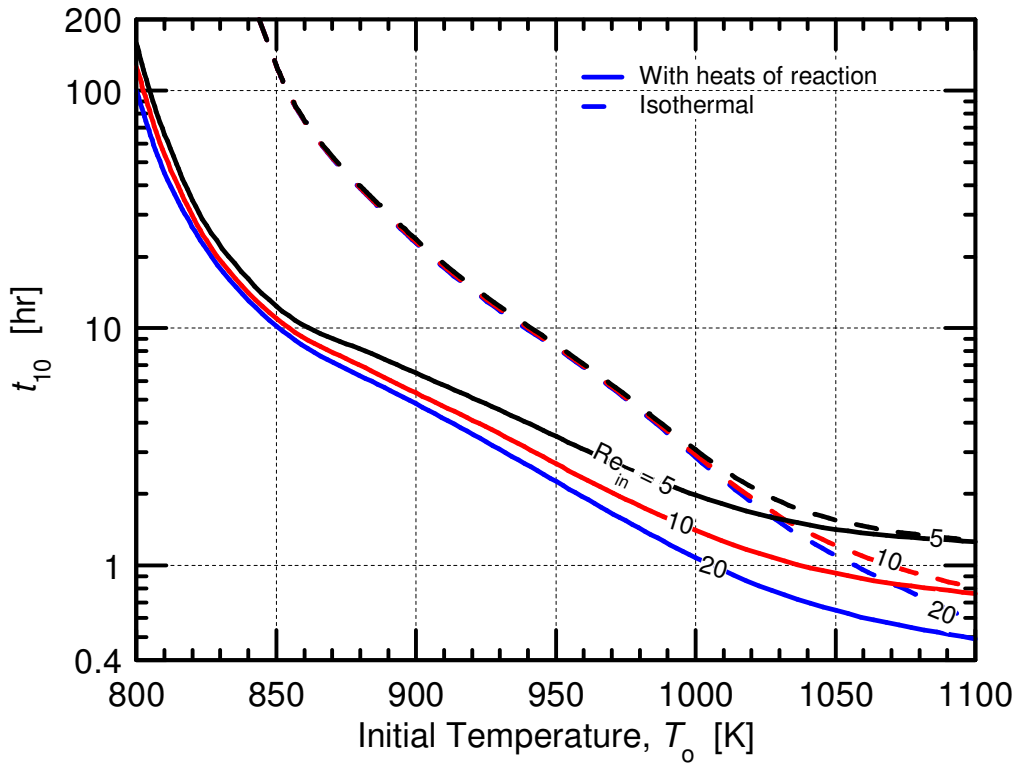
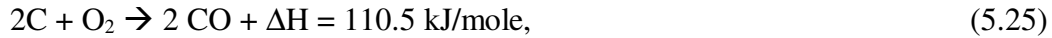


Figure 5.15. Dependence of Gasification Time to Reach 10% Weight Loss at Channel Entrance, t_{10} , on both T_o and Re_{in} .

The surface in Fig. 5.16 of the NBG-18 graphite total loss in the flow channel is a grid of constant Re_{in} curves and intersecting curves of constant initial temperature, T_o . This surface clearly shows that decreasing the initial graphite temperature, T_o , increases t_{10} as well as the total graphite loss in the channel. The results illustrate the complex interplays between the initial temperature and oxygen supply in the air and the rise in the local temperature and both the local and the extent of graphite loss along the flow channel.

As indicated earlier, the heats released in the exothermic chemical reactions producing CO and CO₂ gases raise the surface temperature and, hence, the local graphite gasification and the productions of CO and CO₂ gases along the flow channel. These exothermic reactions are:



The effects of neglecting the heats of reactions in the calculations are well illustrated in Figs 5.15 and 5.17. For $T_o = 1000 \text{ K}$, t_{10} for the isothermal condition is 2.6 times higher, and more than one order of magnitude higher when $T_o = 850 \text{ K}$ (Fig. 5.17). At $T_o = 1000 \text{ K}$ and $Re_{in} = 20$, the total graphite loss in the channel is 19.7 g for the isothermal condition, compared to only 7.4 g when the heats of reactions are included in the calculations. When $T_o = 900 \text{ K}$ and $Re_{in} = 20$, the total graphite loss in the flow channel is 40 g for the isothermal condition, compared to only 14 g when the heats of reactions are included in the calculations (Fig. 5.17).

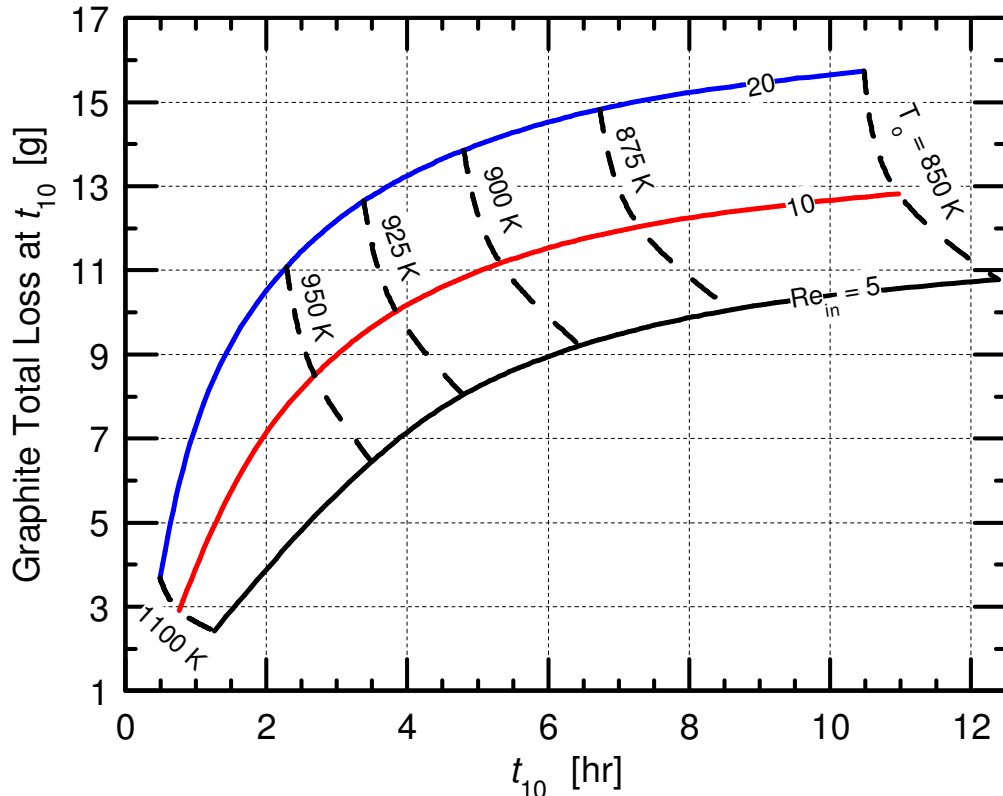


Figure 5.16. Effects of T_o and Re_{in} on Graphite Total Loss and Gasification Time, t_{10} .

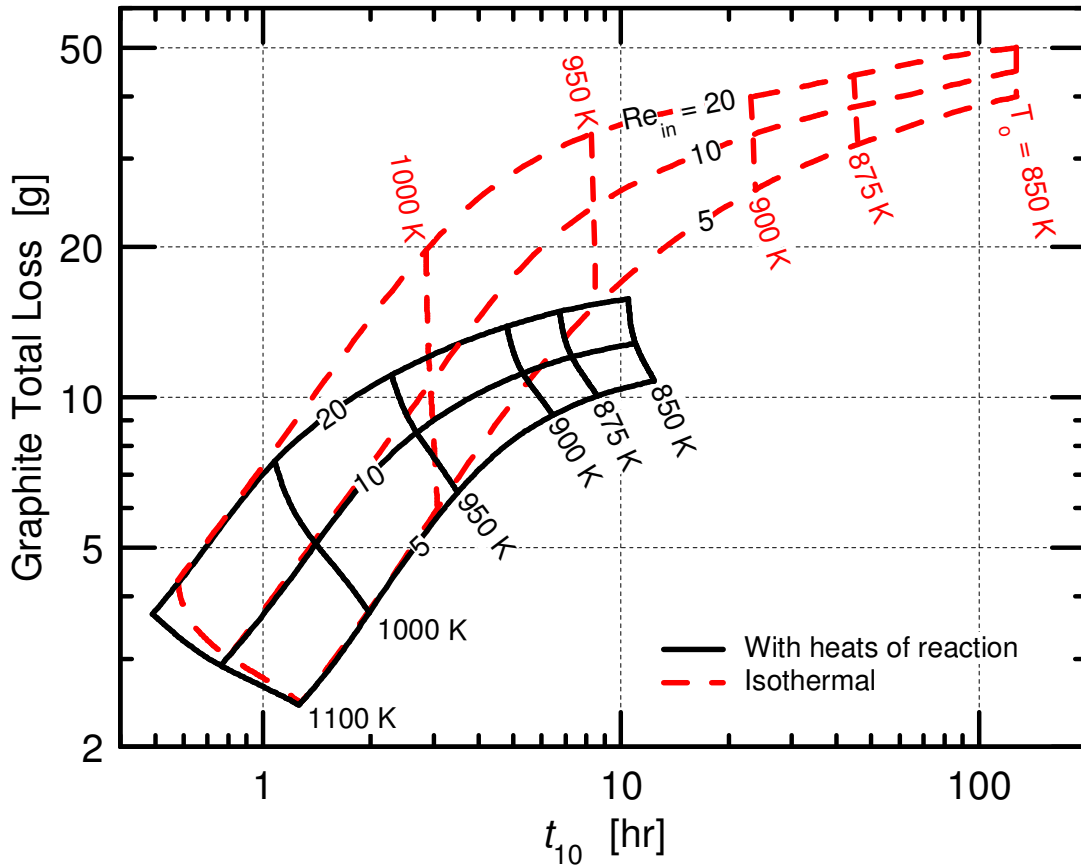


Figure 5.17. Effects of Heats of Formation of CO and CO₂ Gases on the Graphite Total Loss and Gasification Time, t_{10} .

The calculated rise in the graphite local surface temperature due to gasification and the graphite local weight loss along the flow channel depend on the initial temperatures of graphite and inlet air, T_o , and the air Re_{in} (Figs. 5.18a and 5.18b). The results in these figures at the end of the simulated gasification transient, $t = t_{10}$, depict the effects of changing T_o and Re_{in} . When $T_o = 1100$ K, the high local gasification rate near the channel entrance depletes the oxygen in the bulk gas flow within 30 cm from the entrance. This decreases t_{10} from ~ 1.25 to only 0.5 hr when Re_{in} increases from 5 to 20 (Figs. 5.14 and 5.15). At t_{10} , when $T_o = 1100$ K the calculated total rise in the graphite surface temperature at the entrance of the channel is 45, 65 and 95 K when $Re_{in} = 5, 10$ and 20, respectively (Fig. 5.18b). At this high graphite temperature, the high local gasification fully depletes the oxygen in the bulk gas flow within a short distance from the channel entrance, $z = 20$ cm. A weight loss of 10% at the channel entrance is reached after only 29 mins and 76 mins when $Re_{in} = 20$ and 5. The axial extent of graphite gasification in the channel increases as T_o decreases, increasing the total graphite loss and t_{10} (Figs. 5.16 and 5.18a). At lower T_o , the rise in the graphite surface temperature along the flow channel increases as Re_{in} increases.

At $T_o = 800$ K, t_{10} is as much as 100 hrs and the graphite gasification occurs all along the channel (Fig. 5.18a). The rise in the graphite temperature at the channel entrance is 200 K and 275 K, when Re_{in} increases for 5 to 20 (Fig. 5.18b). The corresponding rise in the local graphite temperature at the exit of the channel is lower, but still appreciable, ranging from 162 K to 180 K.

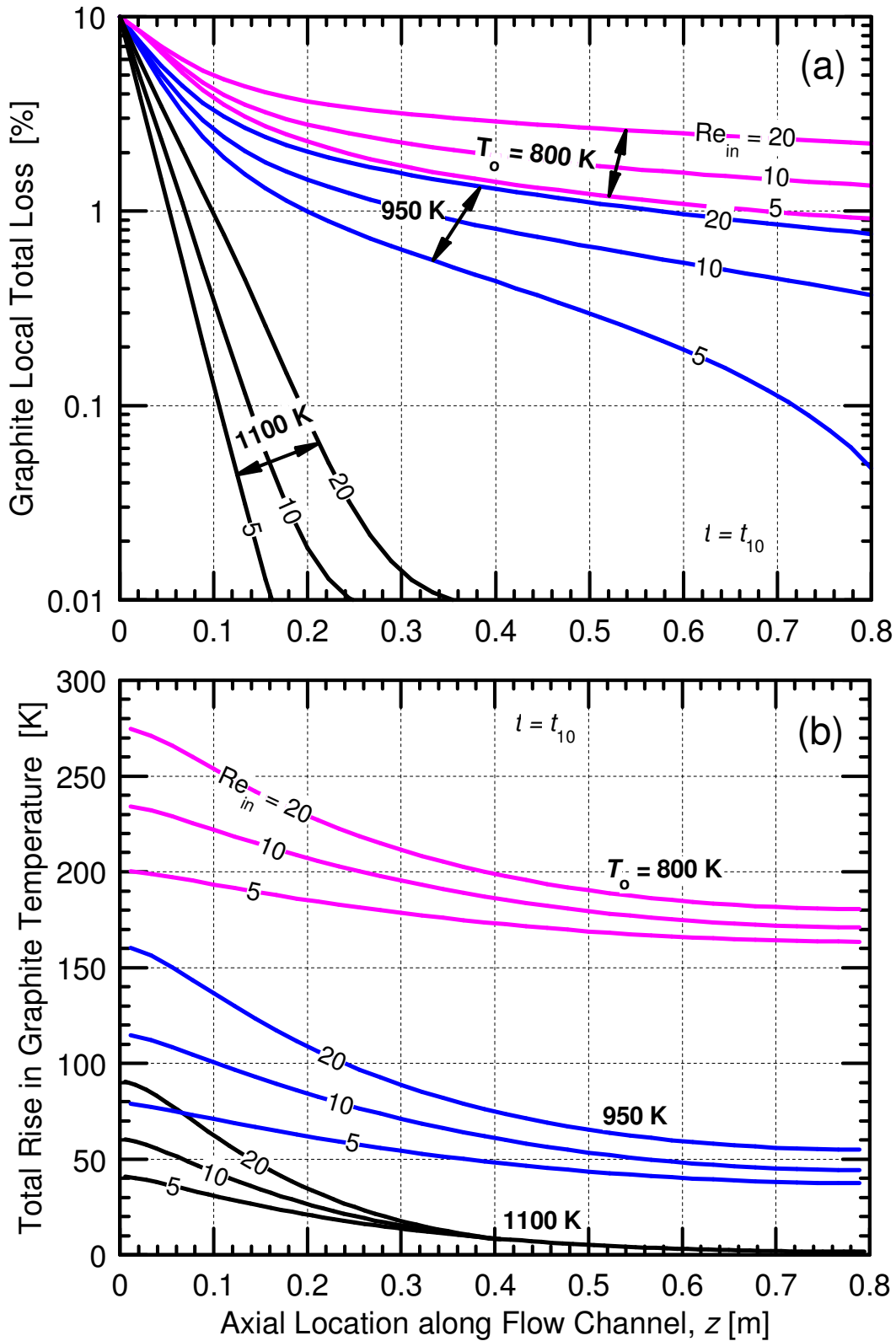


Figure 5.18. Effects of T_o and Re_{in} on Axial Distributions of Graphite Loss and Temperature Rise along the Flow Channel.

At an intermediate initial temperature, $T_o = 950$ K, graphite gasification occurs all along the channel when $Re_{in} = 10$ and 20 , but it is limited to the ~ 74 cm from the entrance of the channel when $Re_{in} = 5$ (Fig. 5.18a). The total rise in the graphite temperature at the entrance of the channel increases from 80 to 160 K as Re_{in} increases from 5 to 20 (Fig. 5.18b). The corresponding total rise in the local graphite temperature at the exit of the channel is only 38 K when $Re_{in} = 5$ and 55 K when $Re_{in} = 20$. The decline in the local temperature rise with distance from the entrance of the flow channel due to gasification correlates directly with the total and local loss of graphite at the end of the gasification transient, $t = t_{10}$ (Figs. 5.16 and 5.18a).

In the next Section, the practical implementation of the gasification Generic Interface into a commercial Finite-Element CFD code is demonstrated using CD-Adapco STAR-CCM+. The gasification results of the NBG-18 nuclear graphite flow channel obtained using STAR-CCM+ are then successfully compared with those obtained using the multi-species diffusion and flow model developed on the Matlab®/Simulink® platform.

5.5 COUPLING OF GASIFICATION MODEL WITH STAR-CCM+ CFD CODE

In this Section, the commercial Finite-Element CFD code (STAR-CCM+) developed by CD-Adapco is used to model the transient gasification of NBG-18 nuclear graphite in a 0.8 m long circular channel with atmospheric air (Fig. 5.6). Because STAR-CCM+ does not accept multi-dimensional data tables, it was not possible to directly implement the developed gasification tables of the CO and CO₂ gas mass fluxes as functions of local temperature, oxygen partial pressure and graphite weight loss (see Section 5.2), as was done on the Matlab®/Simulink® platform. Instead, a specific Generic Interface was developed in STAR-CCM+ to implement the gasification fluxes. The Interface works in STAR-CCM+ version 7.0.4.006 and higher on Windows 64-bit computers or parallel machines. Those versions offer/support the primitive Field Functions of the mass fluxes of gas species at the graphite inner surface, such as *BoundarySpeciesFluxCO* for the mass flux of CO gas in [kg / m².s] for example. The developed Generic Interface makes use of this capability. The next subsection describes the numerical mesh grid used in STAR-CCM+ for the gasification of the NBG-18 graphite channel.

5.5.1 3-D and 2-D numerical mesh grids considered in STAR-CCM+

The initial 3-D mesh developed in STAR-CCM+ to model the multi-species gas flow channel and nuclear graphite sleeve (Fig. 5.6) used a conventional tetrahedral mesh of one quarter (90° azimuthal angle) of the channel and graphite sleeve. Three different regions are modeled: (a) a 40 cm-long adiabatic entrance section to establish the axial velocity profile transversely, without mass nor heat transfer; (b) the 80 cm-long coolant channel; and (c) the surrounding graphite sleeve (Fig. 5.6). The original tetrahedral mesh used had over $62,000$ cells or control volumes, and the calculations required a very long computational time to complete.

To remedy this limitation, the 3-D Directed Mesh Tool of STAR-CCM+ is used to generate a high-quality structural mesh aligned with the flow direction. This increased the accuracy of the solver while reducing the number of numerical mesh elements. The axial end faces of the coolant and graphite regions are meshed first, then the mesh is extruded in the axial direction with a uniform mesh size. A quarter radial section of the flow channel is meshed with 64 cells, with a

geometric progression from the outer radius, using a first prism element 0.1 mm thick. This prism is thin enough to provide the required accuracy for modeling the boundary layer in the coolant region. The graphite sleeve cross-section is meshed from its inner radius, also using a first prism thickness of 0.1 mm at the coolant interface. Finally, 50 equally-spaced axial nodes are used in the coolant entrance region, and 100 nodes along the coolant channel and graphite sleeve regions. This high-quality 3-D Directed numerical Mesh grid has 3,200 cells in the entrance region, 6,400 in the flow channel and 4,000 in the graphite sleeve, for a total of 13,600 cells. Calculations using this Directed Mesh are nearly 5 times faster than those using the original tetrahedral mesh. However, maintaining the accuracy of the transient results over 6 hours of actual time required using a relatively small time step (< 0.2 s), and took over 150 hours of CPU time on a PC with Intel i5-2500 quad-core at 3.3GHz and 8 GB of RAM.

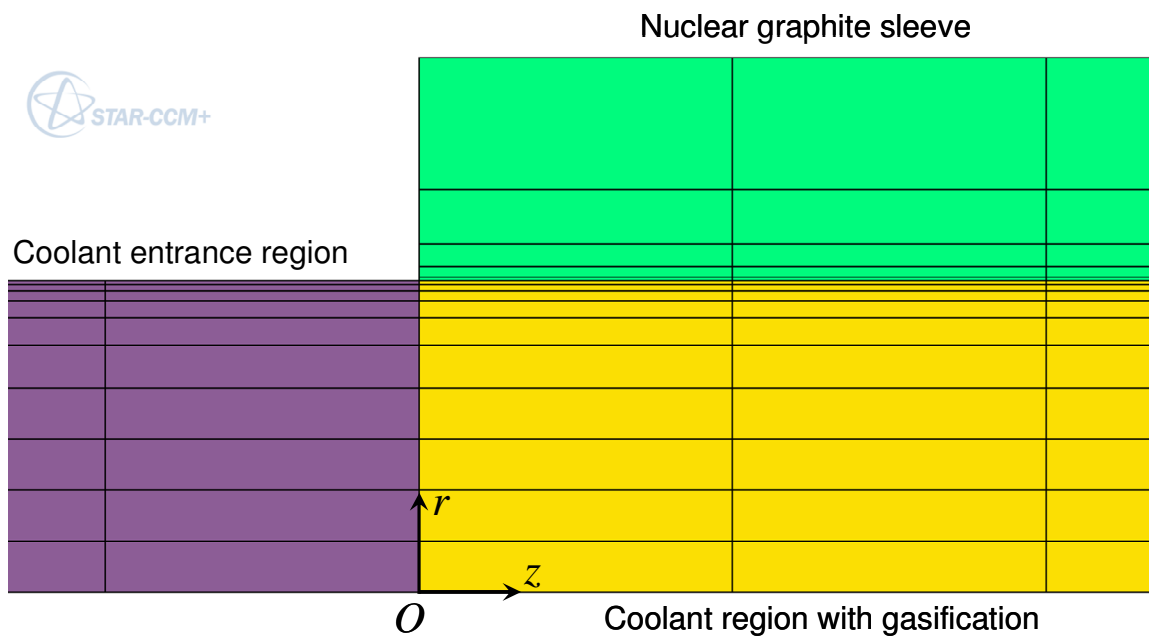


Figure 5.19. View of 2-D Numerical Mesh Grid Used in the Transient Analysis of the Gasification of an Axi-Symmetric NBG-18 Graphite Sleeve in CD-Adapco STAR-CCM+.

The third approach used to accelerate the numerical calculations took advantage of the axi-symmetry of the problem. Since flow and gradients in the azimuthal direction (θ in cylindrical coordinates) are nil, the projection of the high-quality 3-D Directed Mesh on the ($y = 0$) plane is used to generate a two-dimensional mesh (Fig. 5.19), and a 2-D axi-symmetric model of the problem is developed in STAR-CCM+. The flow region uses 10 numerical mesh cells in the radial direction, with a minimum prism thickness of 0.1 mm at the interface with the surrounding graphite sleeve. In the graphite sleeve, only 5 radial cells are used, with a minimum prism thickness of 0.1 mm at the graphite-gas flow interface (Fig. 5.19). The mesh nodes are evenly spaced in the axial direction, with 50 nodes in the coolant entrance region, and 100 nodes along the coolant channel and graphite sleeve regions. This 2-D axi-symmetric mesh uses 500 cells in

the entrance flow region, 1,000 cells in the channel section undergoing gasification, and 500 in the graphite sleeve region, for a total of only 2,000 cells (Fig. 5.19). The 2-D axi-symmetric mesh accelerates the calculations nearly 5 times compared to those using the previous high-quality 3-D Directed Mesh.

5.5.2 Implementation of gasification model in STAR-CCM+

A block-diagram of the 2-D STAR-CCM+ model of the gasification of the NBG-18 graphite channel by atmospheric air (depicted in Fig. 5.6) is shown in Fig. 5.20. The 2-D multi-species transient gas flow and diffusion model (block (i)) is activated in the coolant entrance region and coolant channel, while the 2-D transient conduction model is activated in the graphite sleeve region (block (ii)). The 2-D mesh in those regions (Fig. 5.19) is developed based on the geometrical parameters R_c , R_2 and L , and all temperatures are initialized at T_o . Air is introduced at the inlet section ($z = -L/2$) of the entrance region at constant temperature T_{in} and constant mass flow rate specified by the Reynolds number, Re_{in} . At the exit of the coolant channel ($z = L$), the multi-component gas pressure is specified and equal to 10^5 Pa.

One major difference between the STAR-CCM+ 2-D (or 3-D) flow model (Fig. 5.20) and the 1-D flow model developed on the Matlab/Simulink platform (El-Genk and Tournier, 2013) (Fig. 5.7) is the need to use a Sherwood number correlation (El-Genk and Tournier, 2012d) and a transient boundary layer model in the latter. In STAR-CCM+, the boundary layer is “naturally” calculated by the radial component of the transient gas flow and diffusion model; in this case, care must be taken to ensure that the discretization mesh grid near the graphite sleeve interface is thin enough.

The implementation of the gasification processes in the STAR-CCM+ CFD required developing 2 procedures: (a) the gasification Generic Interface (block (iii) in Fig. 5.20) using a User Coded C Library; and (b) predicting the local graphite weight loss using the Passive Scalar Model option (block (iv) in Fig. 5.20). Those 2 sub-models are described in more details next.

5.5.2a User coded C Library for gasification

The role of the Generic Interface (block (iii) in Fig. 5.20) is to calculate the gasification mass fluxes of CO and CO₂ (and the corresponding consumption of O₂) at the coolant/graphite interface. Those mass fluxes are functions of local wall temperature, T_s , oxygen partial pressure or concentration at the wall, $[\hat{O}_2]_s$, and local graphite weight loss fraction, X (Fig. 5.20). A subroutine is developed in C-programming language to perform the linear interpolation and extrapolation on the weight loss fraction between seven individual 2-D readout tables. The subroutine also performs linear interpolations and extrapolations on temperature and oxygen partial pressure in each of the seven readout tables, one for a different weight loss fraction. The subroutines, one for CO gas and the other for CO₂ gas, are loaded as User Code Field Functions in STAR-CCM+.

The Microsoft Visual C++ Express 2008 freeware edition was used for compiling the STAR-CCM+ User Code Library. Although this edition only comes with support for 32-bit libraries, it was possible to link against the *UserFunctions.lib* library file supplied with the 64-bit installation of STAR-CCM+ and create a 64-bit library on Windows. The following steps are necessary in order to create this C library:

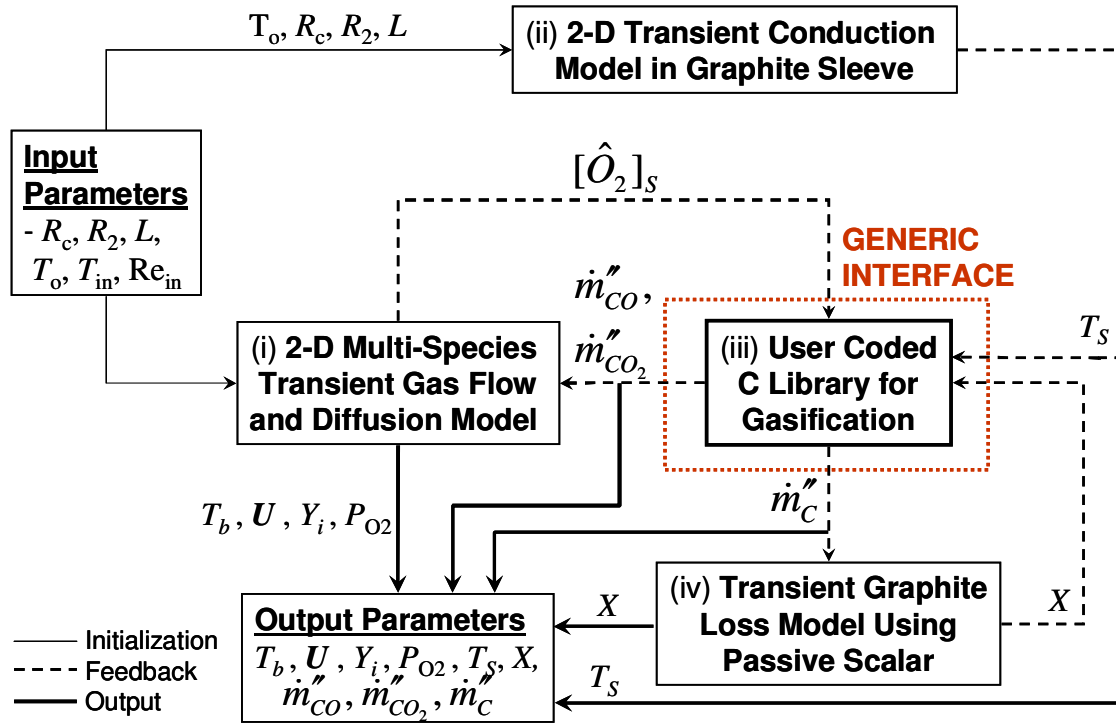


Figure 5.20. Block-Diagram of Multi-Species Transient Flow and Diffusion Model and Gasification Generic Interface Developed on CD-Adapco STAR-CCM+.

(a) In the [C:\Program Files (x86)\Microsoft Visual Studio 9.0\VC\bin] folder, open the Visual Studio 2008 x64 Cross Tools Command Prompt;

(b) Move to the appropriate folder (using the command “change directory” > *cd*) and compile the provided C source codes (the *uclib* registration function, and the CO and CO₂ gasification functions) into object files using the commands:

```
> cl /MD /D_WINDOWS -c EXTERNAL4X_uclib.c
> cl /MD /D_WINDOWS -c EXTERNAL_UC4X_gasificationCO.c
> cl /MD /D_WINDOWS -c EXTERNAL_UC4X_gasificationCO2.c
```

(c) Link the generated *object* files, along with the 64-bit *UserFunctions.lib* library file from the STAR-CCM+ installation, into a Dynamic Link Library (DLL):

```
> link -dll /out:libuser.dll *.obj UserFunctions.lib
```

(d) Check that you have a function called *uclib* exported from the DLL. STAR-CCM+ looks for this function in the DLL:

```
> dumpbin/exports libuser.dll
```

(e) Attach the *manifest* so that it moves with the DLL file when the DLL library file is moved to another directory:

```
> mt -manifest libuser.dll.manifest -outputresource:libuser.dll;2
```

The User Library file *libuser.DLL* is then loaded into the Tools > User Code section of STAR-CCM+ and used to specify the mass fluxes of CO and CO₂ gases at the coolant channel wall surface. A User Field Function is developed to calculate the mass flux of oxygen at this interface, in terms of the primitive Field Functions *BoundarySpeciesFluxCO* and *BoundarySpeciesFluxCO2* for the mass fluxes of CO and CO₂ gases in [kg / m².s]. Note that those primitive Field Functions only exist in STAR-CCM+ version 7.0.4.006 and higher.

5.5.2b Transient graphite loss model using Passive Scalar

The Transient Graphite Loss Model (block (iv) in Fig 5.20) tracks the local graphite weight loss, *X* along the flow channel overtime. The local weight loss is used by the gasification Generic Interface (block (iii) in Fig. 5.20) to calculate the local mass fluxes of CO and CO₂ gases. The calculations of the graphite local weight loss are done in STAR-CCM+ using the Passive Scalar Model.

The Passive Scalar Model solves one or more transport equations for user-defined variables that can be represented by arbitrary scalar values. The user sets the initial value of the scalar field, and specifies the required values at boundaries. An inherent assumption of this model is that the scalar values do not contribute to the fluid’s bulk physical properties. The Passive Scalar Model is available in STAR-CCM+ when using the Coupled Flow Model or the Segregated Flow Model (which is used in the present analyses).

The calculation of the local graphite weight loss along the coolant channel is performed using a Passive Scalar in the coolant region for which the convection and diffusion fluxes are disabled. The only source term comes from the coolant/graphite interface as a flux. In this way, the *WeightLossX* Passive Scalar values accumulate overtime in the 100 prismatic control volumes of the coolant channel region against the graphite sleeve wall (one value for each equi-distant axial location along the coolant channel), but remain nil in all other control volumes of the mesh grid. In practice, cancelling both the convection and diffusion terms in the Transport Tab does not work, but the desired effect was obtained successfully by cancelling convection only (with a Transport Tab set to “Diffusion only”), and using a diffusion coefficient equal to zero.

The Wall Passive Scalar Option can be set as a flux at the wall boundary using the appropriate Passive Scalar Flux node. The transport equation for the passive scalar component, *X*, is then:

$$VOL_k \frac{dX_k}{dt} = S_k \times (\text{Passive Scalar Flux in [m/s]}), \quad (5.27)$$

where the *WeightLossX* Passive Scalar Flux, represented by a User Field function in STAR-CCM+, is given by, in accordance with Equations (5.9) to (5.11) and (5.27):

$$(\text{Passive Scalar Flux in [m/s]}) = \frac{VOL_k}{S_k} \times \frac{dX_k}{dt} = \delta_k \times \frac{dX_k}{dt} = \frac{\delta_k}{[C_o'']} \times (\dot{N}_{CO_2}'' + \dot{N}_{CO}'')_k \cdot \quad (5.28)$$

In this Equation, the subscript k represents axial location along the channel mesh grid, δ_k is the thickness of the first radial prismatic control volume in the coolant against the graphite inner surface (equal to 0.1 mm for the mesh grid depicted in Fig. 5.19), and $[C_o'']$ is the number of moles of carbon per unit surface of graphite side wall, equal to 1,189.7 [mole / m²] for the NBG-18 graphite channel depicted in Figure 5.6. Equation (5.28) is practically implemented in STAR-CCM+ using the user-defined Field Function “User UC Weight Loss Flux” as:

$$\begin{aligned} \text{(Passive Scalar Flux in [m/s])} &= \frac{-0.1 \times 10^{-3}}{1,189.7} \\ &\times \left(\frac{\$BoundarySpeciesFluxCO2}{0.04401} + \frac{\$BoundarySpeciesFluxCO}{0.02801} \right). \end{aligned} \quad (5.29)$$

Again, we made use of the primitive Field Functions *BoundarySpeciesFluxCO* and *BoundarySpeciesFluxCO2* in [kg / m².s], which are only available in STAR-CCM+ version 7.0.4.006 and higher.

Next, the gasification results of the NBG-18 nuclear graphite flow channel obtained using STAR-CCM+ are successfully compared with those obtained using the multi-species diffusion and flow model developed on the Matlab®/Simulink® platform (see Sections 5.3 and 5.4).

5.5.3 Comparison of Matlab/Simulink and STAR-CCM+ results

Some gasification results of the NBG-18 graphite channel (see Fig. 5.6) obtained using STAR-CCM+ and the Generic Interface developed in Section 5.5.2 are presented in this section. Results were obtained for initial graphite temperatures, T_o of 925 K, 950 K and 1000 K, and for an inlet air Reynolds number, $Re_{in} = 20$. The sample results presented in this Section to illustrate and demonstrate the successful implementation of the gasification model in STAR-CCM+ are for an isothermal nuclear graphite sleeve at $T_o = 950$ K, an inlet air temperature of 950 K and inlet Reynolds number, $Re_{in} = 20$. Adequate accuracy of the results was obtained using a time step of 0.100 s, and 4 internal iterations to reduce the values of the residuals between each time step. To mitigate the generally long CPU time of those numerical analyses, the calculations were pursued until a local graphite weight loss of 10% was reached at the entrance of the coolant channel, or until oxygen depletion at the exit of the coolant channel (the oxygen concentration $[\hat{O}_2]_b \simeq 0$), whichever condition occurred first.

The results in Figs. 5.21 and 5.22 show that oxygen was depleted at the exit of the flow channel after 6.0 hours into the gasification transient. At that time, a maximum graphite weight loss of 6.0% is reached at the entrance of the flow channel, decreasing to only 3.0% at the exit of the channel (Fig. 5.22).

The graphite weight loss profiles along the flow channel at different times during the gasification transient are compared in Fig. 5.22, for $Re_{in} = 20$ and $T_o = 950$ K. During the first 2 hrs, the local gasification rate is relatively low and the graphite weight loss is nearly uniform along the channel. The oxygen molar concentration (or partial pressure) in the bulk gas flow exiting the channel is as much as 45% of its value at the channel entrance (Fig. 5.21). After 2 hrs into the gasification transient, the local weight loss of NBG-18 graphite along the channel is nearly uniform and equals ~ 0.90% (Fig. 5.22).

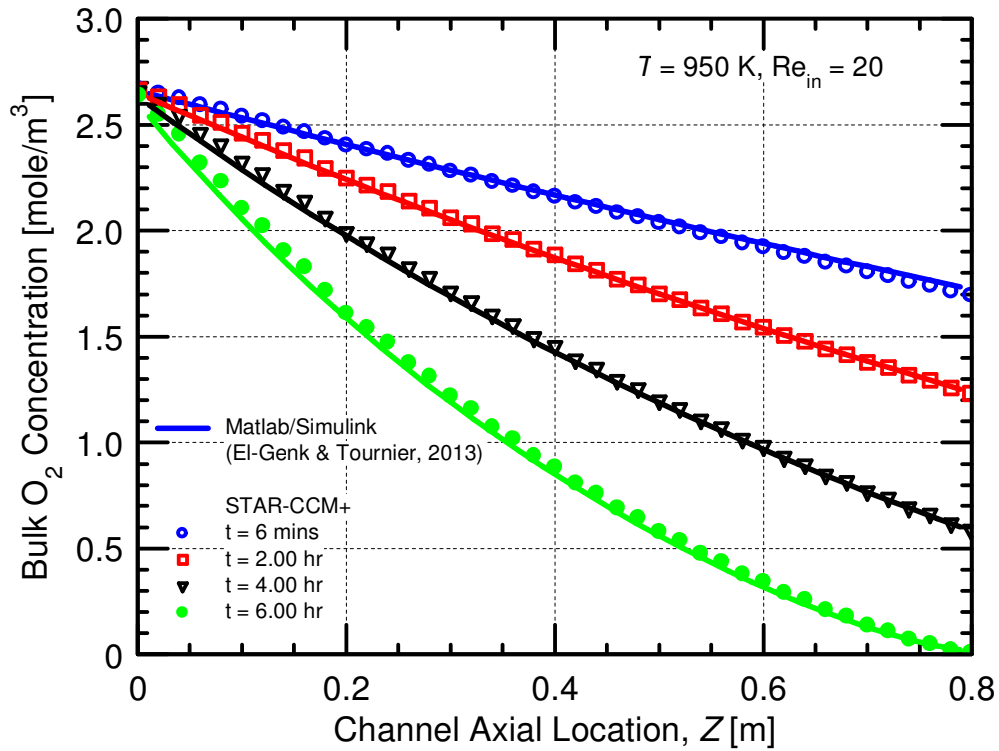


Figure 5.21. Effect of Weight Loss on Axial Distribution of Oxygen Concentration in Flow Channel during Gasification at 950 K.

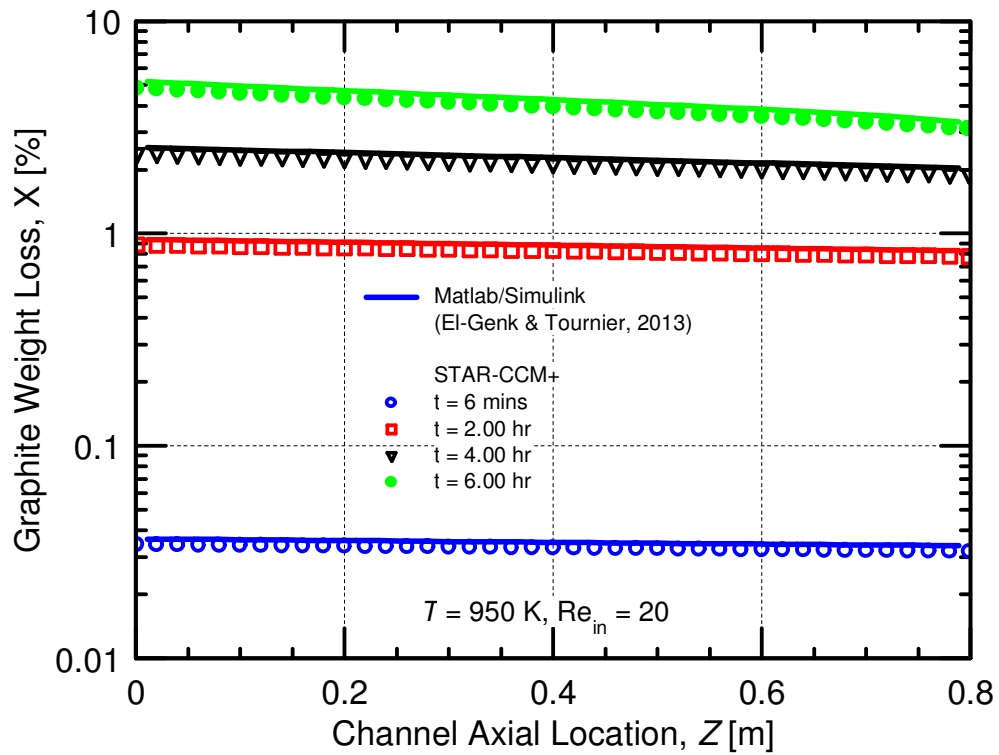


Figure 5.22. Axial Distribution of Weight Loss in Flow Channel during Gasification at 950 K.

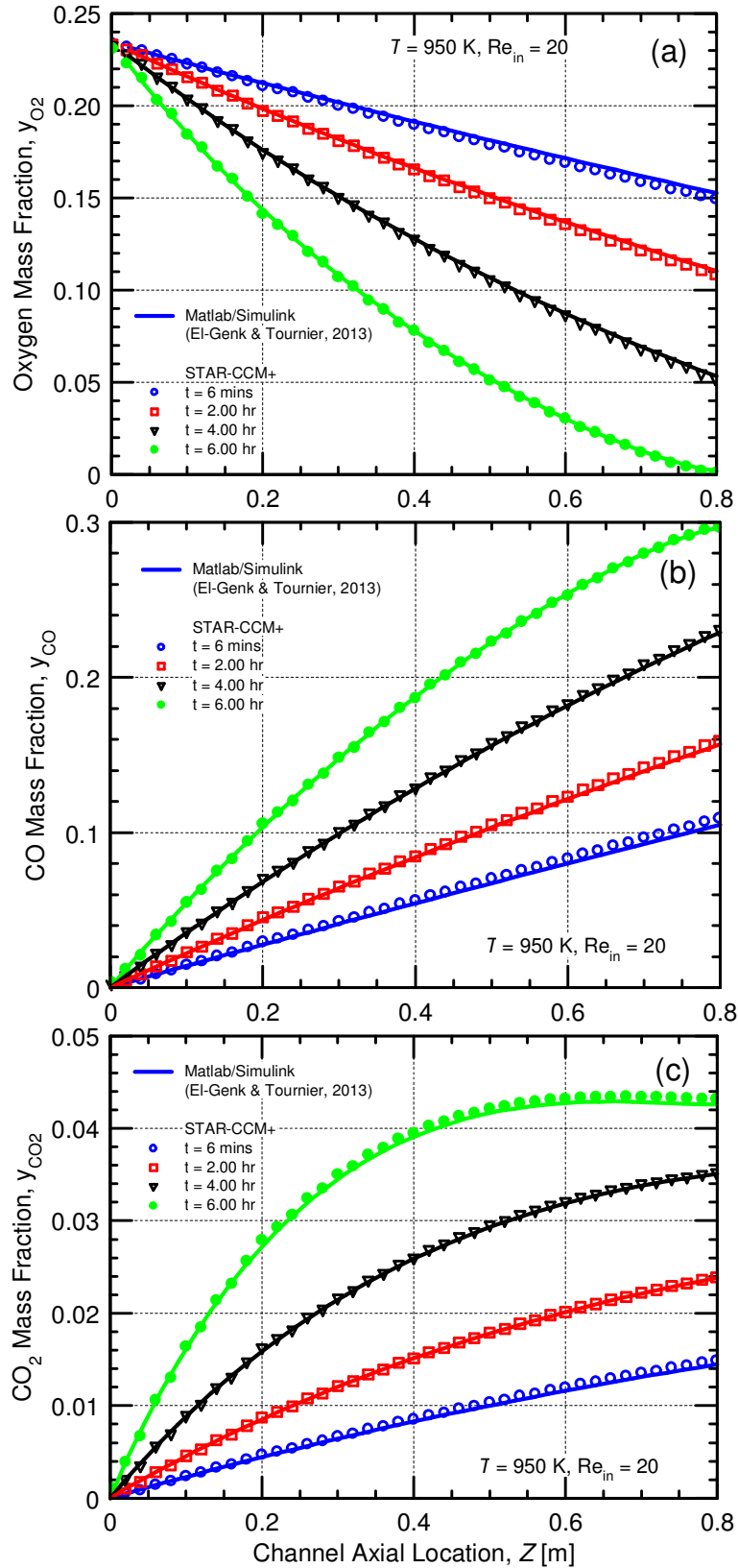


Figure 5.23. Effect of Weight Loss on Axial Distributions of Oxygen, CO and CO₂ Mass Fractions during Gasification at 950 K.

At longer times into the transient, $t > 2$ hrs, the gasification rate along the channel becomes non-uniform, with the local weight loss increasing faster near the entrance (Fig. 5.22). This is because the oxygen partial pressure is highest at the entrance of the channel (Fig. 5.21). The local graphite gasification rate decreases with axial distance into the channel due to the decrease in the oxygen partial pressure in the bulk gas flow. The oxygen partial pressure, however, affects the production rates of CO and CO₂ gases differently.

After 6.0 hrs into the transient, the oxygen in the bulk gas flow is fully depleted at the exit of the channel (Figs. 5.21 and 5.23a). At that time, the mass fraction of the produced CO gas in the bulk gas flow at the exit of the channel reaches 0.30, while that of CO₂ gas is only 0.043 (Figs. 5.23b and 5.23c). Figure 5.23c also shows that the mass fraction of CO₂ gas levels off and remains constant along the last 20 cm section of the flow channel; this is because the production rate of CO₂ vanishes with the oxygen partial pressure (Fig. 5.23a). By contrast, the mass fraction of CO gas continues to increase, albeit with a slower rate, along the flow channel (Fig. 5.23b); the rate of CO production results from the desorption of stable oxide surface complexes.

As shown in Figs. 5.21, 5.22 and 5.23, the gasification results of the NBG-18 graphite channel using STAR-CCM+ are in excellent agreement with those obtained using the transient gas flow model developed on the Matlab/Simulink platform (El-Genk and Tournier, 2013). Maintaining the accuracy of the results up to a long transient time of 6.0 hours requires the use of a relatively small time step (0.100 s) and 4 internal iterations to reduce the residuals between time steps.

5.6 SUMMARY

The safety analysis of gas-cooled VHTRs or HTRs in the unlikely event of massive air or steam ingress accident requires reliable predictions of the gasification rates of nuclear graphite of the support columns in the lower plenum and in the flow channels of the annular core fuel assemblies. Presented are the results of a transient gasification analysis of NBG-18 nuclear graphite with atmospheric air in a single channel of a VHTR or HTR prismatic fuel assembly. The analysis interfaces readout tables of graphite gasification with a transient flow and diffusion model of the bulk gas, coupled to 2-D heat conduction in the graphite sleeve, along the flow channel. The model, developed on the Matlab®/Simulink® platform, handles up to 5 gaseous species in the bulk gas flow (He, N₂, O₂, CO and CO₂) and accounts for the heats released in the exothermic chemical reactions for the production of CO and CO₂ gases, the diffusion of oxygen in the boundary layer, and the convective heat transfer at the graphite surface along the channel. Calculated results for the NBG-18 nuclear graphite, 80 cm long flow channel are of the local rise in graphite temperature, the local and total graphite weight loss and the productions of CO and CO₂ gases. The results also include the extent of graphite gasification along the flow channel as a function of the graphite initial temperature, T_o and that of the entering atmospheric air flow (800 K to 1100 K) and of the inlet Reynolds number of atmospheric air, Re_{in} (5 to 20).

Results show that the graphite local weight loss is non-uniform along the flow channel, and significantly higher near the entrance. This non-uniformity is caused primarily by the increase in the local graphite temperature due to the heat released by the exothermic chemical reactions for the productions of CO and CO₂ gases, and by the depletion of oxygen in the bulk gas flow along the channel. Near the flow channel entrance, the oxygen partial pressure in the bulk gas flow sustains graphite gasification. In the remainder of the flow channel, the local gasification and graphite weight loss could be significantly lower, owing to the lower productions of CO and CO₂ due to the limited availability of oxygen in the bulk gas flow.

Results demonstrated the fidelity of interfacing the readout tables of graphite gasification with the channel's diffusion and flow model. They show that graphite gasification is highest at the channel entrance and decreases with distance into the channel to its lowest value, either somewhere within the channel where oxygen is depleted or near the exit. The competing effects of the local oxygen partial pressure in the bulk gas flow and the rise in the graphite temperature affect the graphite weight loss along the flow channel and the total graphite loss and CO and CO₂ production at the end of the simulated transient. This is when the local graphite weight loss at the channel entrance reaches 10%, or $t = t_{10}$. This time, as well as the extent of graphite gasification along the flow channel, increases with decreasing T_o and l or Re_{in} . At a high T_o of 1100 K, graphite gasification is limited to a short section near the entrance ($z < 25$ cm) due to the high local gasification rate and the fast depletion of oxygen in the bulk gas flow. At this initial temperature, t_{10} increases from 0.5 hr to 1.25 hr as Re_{in} decreases from 20 to 5. At a lower T_o of 800 K, graphite loss occurs all along the flow channel, and t_{10} is as much as ~ 100 hrs, regardless of Re_{in} . Results demonstrated that the heats of formation of CO and CO₂ gases should not be neglected in the analysis of graphite gasification. Neglecting these heats of formation could significantly over estimate the total graphite loss and the transient gasification time.

In addition, the practical implementation of the nuclear graphite gasification model into a commercial Finite-Element CFD code was demonstrated using CD-Adapco STAR-CCM+. For

the implementation of the gasification processes in the STAR-CCM+ CFD, 2 special arrangements are made: (a) develop a Generic Interface using a User Coded C Library, for predicting the local mass fluxes of CO and CO₂ gas productions; and (b) calculate the local graphite weight loss using the Passive Scalar Model option. A subroutine is developed in C-programming language to perform the linear interpolation and extrapolation on the weight loss fraction in seven individual 2-D readout tables. The subroutine also performs linear interpolations and extrapolations on temperature and oxygen partial pressure in each of the seven 2-D readout tables, one for each weight loss fraction value. The subroutine is then loaded as a User Code Field Function in STAR-CCM+. Such an approach is successfully tested in this work. The gasification transient results for the NBG-18 nuclear graphite flow channel of STAR-CCM+ are in excellent agreement with those obtained using the multi-species diffusion and flow model developed on the Matlab®/Simulink® platform (El-Genk and Tournier, 2013).

In the next chapter, thermal-hydraulics analyses are performed of a Very High Temperature Reactor (VHTR) 1/6 prismatic core and a hexagonal fuel element with and without helium coolant bypass flow, using a highly effective technique of coupling 1-D helium flow in the channels together with a recently developed and validated convective heat transfer correlation, to a 3-D heat conduction in the graphite and fuel compacts in the core.

5.7 NOMENCLATURE

A	Flow area of channel (m^2)
$[C'']$	Moles of carbon atoms per unit surface of graphite sleeve (mole/m^2)
C_p	Specific heat capacity ($J/kg.K$)
C_{f,ε_i}	Active free sites with activation energies in bin i
$C(O_2)_{\varepsilon_i}$	Un-dissociated oxygen complexes in energy bin i
$(CO)_{\varepsilon_i}$	Surface stable oxide complexes in energy bin i
D	Diameter of flow channel (m)
$D_{A,B}$	Binary diffusion coefficient for gas mixture of A and B components (m^2/s)
D_{i-m}	Effective diffusion coefficient of gas species i in mixture (m^2/s), Eq. (5.3)
f	Darcy friction coefficient
h	Convective heat transfer coefficient ($W/m^2.K$)
k	Boltzmann constant, $k = 1.380662 \times 10^{-23}$ (J/K)
k^o, k^*	Pre-exponential rate constants ($\text{mole}^{-n}.s^{-1}$)
k_m	Effective diffusion velocity of oxygen in boundary layer (m/s), Eq. (5.7)
L	Total length of flow channel (m)
M_j	Molecular weight of gas species j (kg/mole)
\dot{m}	Gas mass flow rate (kg/s)
\dot{m}_i'''	Volumetric source of gaseous species i ($kg/m^3.s$)
n	Number of gas species in multi-component mixture
\dot{N}_i''	Interfacial molar flux of gaseous species i ($\text{mole}/m^2.s$)
N_a	Avogadro number, $N_a = 6.0225 \times 10^{23}$ (mole^{-1})
N_r	Number of radial control volumes in nuclear graphite sleeve
N_z	Number of axial control volumes in flow channel
$[\hat{O}_2]_b$	Oxygen concentration in bulk gas mixture (mole/m^3)
$[\hat{O}_2]_s$	Oxygen concentration at graphite surface (mole/m^3)
P_j	Partial pressure of gaseous species j (Pa)
P	Total pressure of gas mixture (Pa)
r	Radius (m)
R_2	Outer radius of nuclear graphite sleeve (m)
R_c	Radius of flow channel (m), $R_c = D/2$
Re_{in}	Reynolds number of inlet air evaluated at T_o
Re_s	Local Reynolds number evaluated at wall surface temperature, $\dot{m}D/(\mu_m A)$
R_f	Radius of penetrations of fuel compact rods in assembly (m)
R_g	Perfect gas constant (8.3144 J/mole.K)
Sc	Schmidt number evaluated at wall surface temperature, ν_m / D_{O_2-m}
Sh	Sherwood number evaluated at wall surface temperature, $k_m D / D_{O_2-m}$
t	Time (s)
t_{10}	Time to reach 10% weight loss at the entrance of the graphite channel (s)

T	Temperature (K)
T_o	Initial temperature and air inlet temperature (K)
\bar{U}	Mass-averaged velocity of gas mixture (m/s)
X	Local weight loss fraction of graphite ($0 \leq X \leq 1$)
X_i	Molar fraction of species i in gas mixture
Y_i	Mass fraction of species i in gas mixture
z	Axial location along flow channel (m)

Greek

ΔH^f	Enthalpy of formation (J/kg)
ΔR	Thickness of nuclear graphite control volumes (m)
ΔZ	Height of control volumes (m)
ε	Depth of molecular potential well (J)
ε	Specific activation energy (J/mole)
$\bar{\varepsilon}$	Gaussian most-probable specific activation energy (J/mole)
λ	Thermal conductivity (W/m.K)
μ	Gas viscosity (kg/m.s)
ν	Kinematic viscosity (m^2/s), $\nu = \mu / \rho$
ρ	Mass density (kg/m^3)
σ	Gaussian standard deviation (J/mole)
σ_j	Effective molecular diameter of gaseous species j (m)

Subscript/Superscript

a	Adsorption of oxygen onto active free sites to form un-dissociated complexes
b	Breakup of un-dissociated surface oxides to form stable complexes
b	bulk gas
CO	Carbon monoxide gas
CO_2	Carbon dioxide gas
d	Desorption of CO gas
G	Nuclear graphite nodes
He	Helium
i	Gaseous species i
m	Gas mixture
N_2	Nitrogen gas
o	Initial condition at time = 0
O_2	Oxygen gas
s	Inner surface of nuclear graphite sleeve
$*$	Desorption of CO_2 gas

6. THERMAL-HYDRAULICS ANALYSES OF 1/6 PRISMATIC VHTR CORE AND OF FUEL ELEMENT WITH BYPASS FLOW

The development and future deployment of generation-IV, prismatic core, Very High and High Temperature cooled Reactors (VHTRs or HTGRs) require demonstrable and effective computational tools and methodologies for design, operation and safety analysis. These reactors are graphite moderated, helium cooled, and nominally operate at thermal power of 300 – 600 MW_{th}, exit temperatures of ~ 900 – 1273 K and helium coolant pressure up to 4.0 – 7.0 MPa (Kiryushin et al., 1997; MacDonald et al., 2003; LaBar et al., 2004). The primary focus on this work is on a prismatic core VHTR (Fig. 5.1), whose annular core is comprised of 102 prismatic, hexagonal fuel elements in 3 rings, stacked 8 m high. The fuel elements are 0.36 m flat-to-flat, 0.793 m tall and loaded with graphite fuel compacts. The fuel compacts are comprised of spherical Tristructural-isotropic TRISO particles (~ 1 mm in diameter) dispersed in a graphite matrix (Kiryushin et al., 1997; MacDonald et al., 2003; LaBar et al., 2004; Schultz et al., 2004) (Fig. 6.1a). The TRISO fuel particles consist of uranium oxy-carbide fuel kernels surrounded by PyC and SiC coatings, designed for full retention of fission products and restraining fuel swelling at the reactor's nominal operating temperatures.

The core fuel elements are surrounded by graphite reflector blocks in the inner five and the outer 2–3 rings of the assembled reactor core. In addition, axial graphite reflector blocks are stacked on top and at the bottom of the active core (Fig. 5.1). The fuel compacts, ~ 1.245 cm in diameter and 4.95 cm tall (Fig. 6.1b) are loaded into vertical channels arranged in a triangular lattice within the prismatic fuel elements. On average, there are six fuel compacts surrounding a helium coolant channel (Fig. 6.1c), and each channel carries approximately the fission heat generated in two fuel compacts. The coolant channels within the stacked fuel elements in the active core region are 8.0 m long and the majority are 1.5875 cm in diameter. They extend further into the 1.2 m upper and 0.8 m lower graphite reflector blocks. Most fuel elements (Fig. 6.1c) have a uniform layout and a few have holes for control rods or reserve shutdown elements (Figs. 6.1d and 6.2). Figure 6.2 presents a radial cross-section of a prismatic VHTR core. More specifically, it is a layout of a quadrant with the 1/6th core to be simulated in this Chapter highlighted with dashed lines. In this figure, the gray hexagonal assemblies in the annular core region are the fuel elements (Fig. 6.1c) and the lighter shade hexagonal assemblies are those of the inner and outer graphite reflector.

Ideally, a full core thermal-hydraulics analysis is desired in order to optimize the performance and design of prismatic HTGRs or VHTRs. However, owing to the complexity and massive size of the core, such analysis requires extensive and massively parallelized computation capabilities and a relatively long time (weeks to months) to complete. These requirements are primarily due to the 3-D computation fluid dynamics (CFD) simulation of the helium gas flow in the 10-m long cooling channels in the 102 hexagonal fuel elements of the active core and in the top and bottom axial graphite reflector blocks. The helium bypass flow in the interstitial spaces between the fuel elements further complicates the helium flow distribution and the thermal-hydraulics analysis of the core. These spaces or small gaps are initially present because of the tolerance, in manufacturing the hexagonal fuel elements and reflector blocks. Furthermore, the width of the interstitial spaces changes in the different sections of the core with operation time due to thermal

expansion and irradiation swelling. Although the exact dimensions are not well characterized, the bypass flow interstitial spaces could be up to 5 mm wide.

Bypass flow in a prismatic VHTR core raises concerns with regards to the helium coolant flow distribution and the potential for developing hotspots in the fuel elements. Very little work has been reported on the bypass flow distribution and its effect on the thermal performance of the reactor core, thus it remains a subject for future investigations (Pointer and Thomas, 2010; Tak, Kim and Lim, 2008 and 2010). The helium bypass flow is that which does not traverse the coolant channels in the reactor core, but the interstitial spaces between the vertically stacked prismatic fuel elements. Another form of helium flow outside the coolant channels is that entering from the upper plenum through orifices to cool the control rods. It then flows through the control rod channels in the core fuel elements to the lower plenum. The control rod channel's diameter is much larger (10.16 cm) than that of a regular helium coolant channel (1.5875 cm), and although the helium inlet temperature is comparable to that entering the coolant channels, the exit temperature is significantly lower. The helium flow through the control rod channels varies with the reactor design, but is typically limited to ~ 3% of the total flow into the reactor (General Atomics, 1996).

Reported thermal-hydraulics simulations of a prismatic VHTR either neglected the helium bypass flow, or assumed an average bypass flow that is 5 to 10% of the total flow (Pointer and Thomas, 2010). To the best of the authors' knowledge, the most extensive study of the effect of bypass flow on the thermal performance of a prismatic VHTR has been that of Sato, Johnson and Schultz (2010). They analyzed a 1/12th section of a 7.93 m tall prismatic fuel element under different bypass flow conditions. Their analysis solved for the helium flow distribution in the coolant channels and the bypass flow passages. Although the method and approach used by Sato, Johnson and Schultz (2010) are fairly robust, they could not be easily expanded to the analysis of a larger section of the core due to the demanding numerical meshing and computation requirements. In addition to the massive core structure, accounting for the helium bypass flow further complicates the thermal-hydraulics analysis of the reactor core and increases the already very demanding computational and thermal-hydraulics analysis task. Thus, there is a need to develop and validate an effective approach to simplify the computational task while maintaining reasonably accuracy results.

Recent results have demonstrated the practicality of replacing a full 3-D, CFD simulation of the helium gas flow in a 10 m tall coolant channel in a prismatic VHTR core with a simplified methodology involving thermally coupling a 1-D helium flow in the channel to a 3-D heat conduction within the hexagonal fuel element. In addition to decreasing the memory requirements and the number of elements in the implemented numerical mesh grid (Pointer and Thomas, 2010), this methodology reduced the total computation time to ~ 2.5% of that required for a full 3-D analysis, without compromising the accuracy of the results (< 2% difference) (Travis and El-Genk, 2013).

The simplified methodology provides good predictions of the global parameters such as the 3-D spatial temperature distribution in the core fuel elements and the axial variation of the helium bulk temperature in the coolant channels, but not of the velocity and temperature distributions within the boundary layer. This methodology, which could be used as a surrogate of a full 3-D CFD analysis, employs a developed and validated turbulent convection heat transfer correlation to calculate the local heat transfer coefficient along the 8.0 m long heated section of the coolant

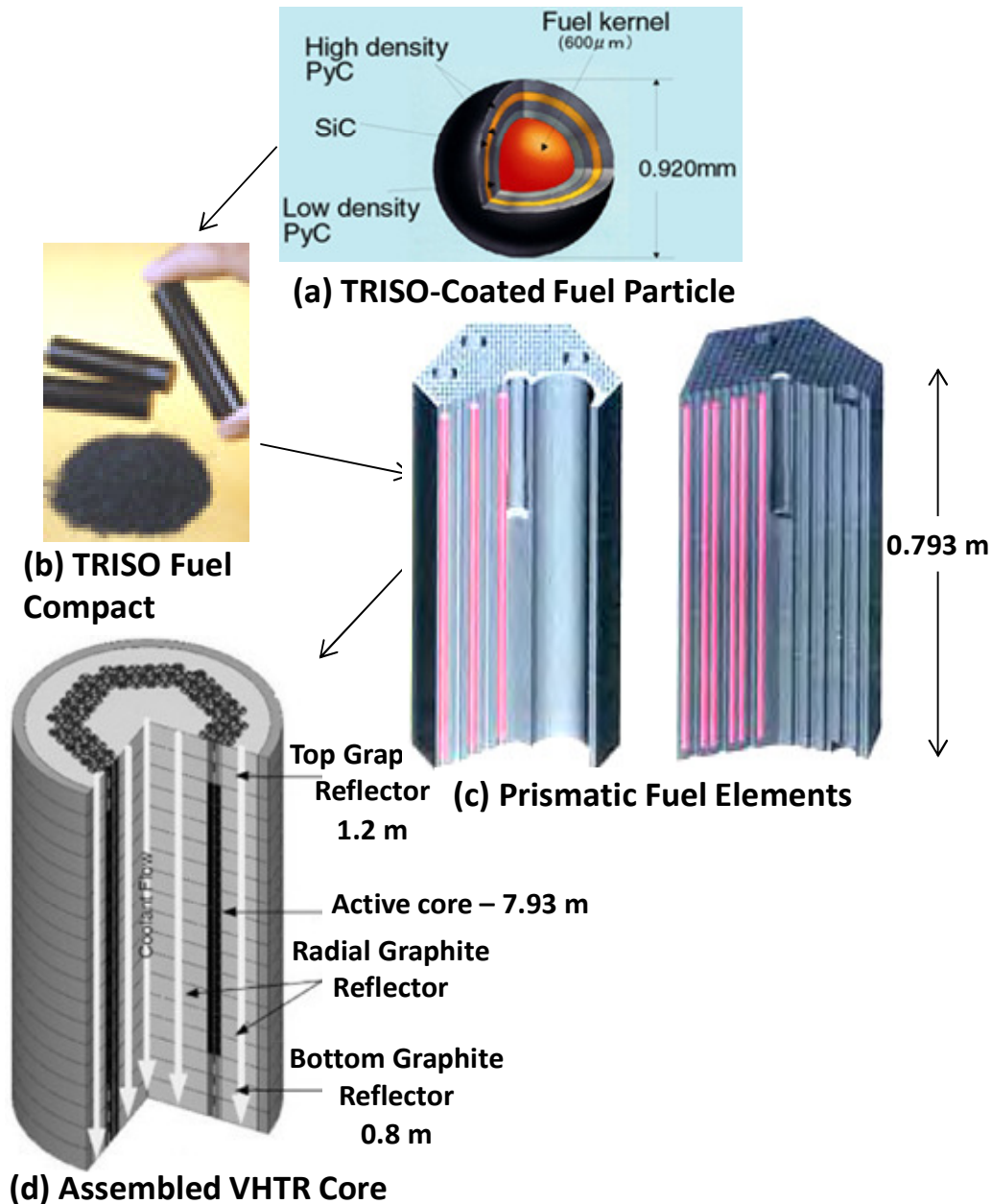


Figure 6.1. TRISO Particle, Fuel Compact, and a Prismatic Fuel Element or Assembly (Kiryushin et al., 1997; MacDonald et al., 2003; Schultz et al., 2004).

channel in the active core region (Travis and El-Genk, 2013). The correlation (Eq. (6.1)) accounts for the mixing in the entrance section of the heated helium coolant channels in the core and its effect on the local heat transfer coefficient. The correlation, applicable to both uniform and cosine axial power profiles (Travis and El-Genk, 2013), is developed based on the results of a full 3-D numerical thermal-hydraulics analysis of a single flow channel module in a typical prismatic core VHTR. The obtained values of the local heat transfer coefficient at nominal reactor operation conditions are used to develop the following Nusselt correlation, as (Travis and El-Genk, 2013):

$$Nu = Nu_{FD} \left[1 + 0.57 e^{-0.20 (z/D)} \right]. \quad (6.1)$$

The second term on the right-hand-side accounts for the effect of flow mixing in the entrance section of the heated coolant channels. The first term is the Nusselt number for fully-developed turbulent convection, Nu_{FD} , in the helium coolant channels, where $z/D \geq 25$:

$$Nu_{FD} = 0.11 Re_b^{0.653} Pr_b^{0.4}. \quad (6.2)$$

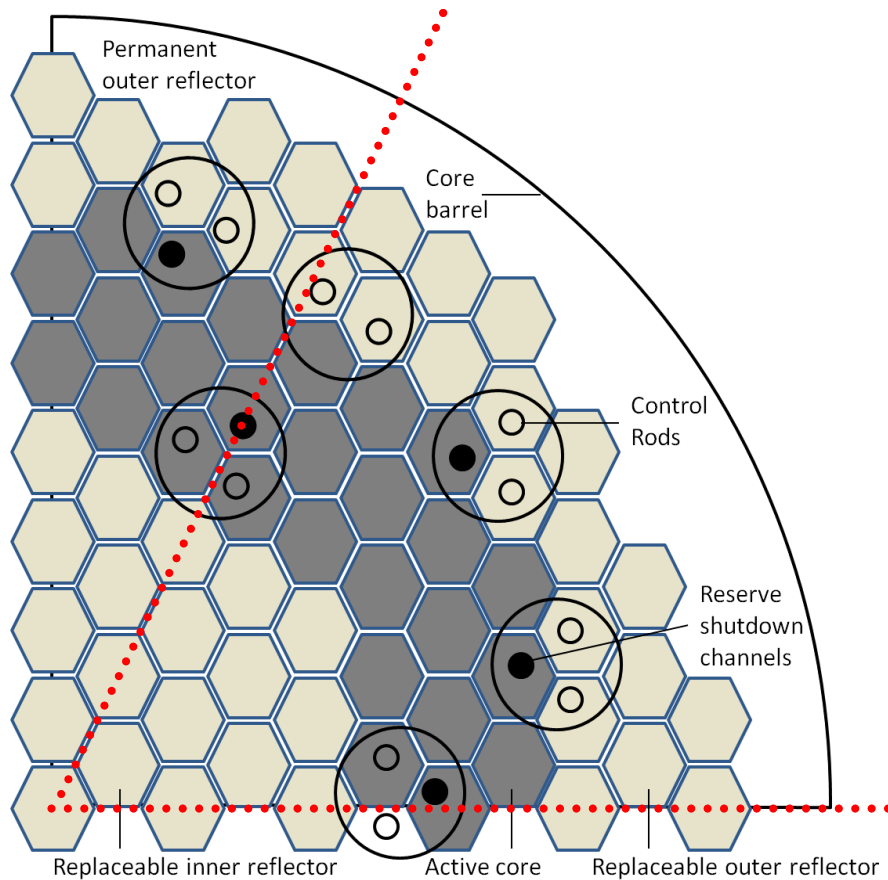


Figure 6.2. A Quadrant of a Prismatic VHTR Core (Kiryushin et al., 1997; MacDonald et al., 2003; LaBar et al., 2004; Schultz et al., 2004).

This correlation is within $\pm 2\%$ of the calculated values of Nu_{FD} using a full 3-D thermal-hydraulics numerical analysis of a 10-m tall single channel coolant (including the 1.2 and 0.80 m top and bottom axial graphite reflector blocks) (Travis and El-Genk, 2013). The results used to develop the correlations in Equations (6.1) and (6.2) are validated for $2.2 \times 10^4 \leq Re_b \leq 5.8 \times 10^4$ and $40 \text{ K} \leq \Delta T_{\text{film}} \leq 60 \text{ K}$. The thermal-hydraulics analysis results for developing the correlations in Equations (6.1) and (6.2) account for the changes in the properties of the graphite, fuel

compacts, and helium gas with temperature (Table 6.1), and are valid for both uniform and cosine axial power profiles in the heated section of the helium flow channels. The helium gas properties are evaluated at its local bulk temperature in the channel. The axial thermal power profile slightly changes the local helium bulk and channel wall temperatures, but insignificantly affects the values of the local Nusselt number. Equation (6.1) is in good agreement with Taylor’s correlation, developed based on an extensive experimental heat transfer database for different fluids in uniformly heated tubes at high temperatures (Taylor, 1967; Travis and El-Genk, 2013).

An objective of this work is to examine the effectiveness of the simplified simulation methodology validated in Travis and El-Genk (2013) to perform thermal-hydraulics analyses of a hexagonal fuel element, with and without bypass flow and of a prismatic VHTR full height 1/6 core. The fidelity and accuracy of the results for the hexagonal fuel element are verified by comparing them to those of a full 3-D numerical analysis. In addition to the temperature field, results compare the computation time and number of numerical grid elements for implementing the simplified and the full 3-D numerical simulation methods of a prismatic VHTR fuel element. Another objective of this work is to investigate the impact of the helium bypass flow through interstitial and control rod channels in the fuel elements, and of changing the heat generation in the corner burnable poison rods on the spatial temperature distribution in the prismatic fuel elements. The thermal-hydraulics analysis of the fuel element employs a uniform axial power profile and the full height 1/6 core analysis includes both uniform and cosine axial power profiles. Both analyses incorporate temperature-dependent properties of helium, graphite in the reactor core, graphite reflector blocks and TRISO fuel compacts.

Table 6.1. Material Properties Used in the Thermal-Hydraulics Analysis (Travis and El-Genk, 2013) (the Temperature, T is in Kelvin).

Property	Material	Value or Correlation
ρ (kg/m ³)	IG-110 graphite	1740
C_p (kJ/kg. K)		$C_p = 6.05 \times 10^{-4} T^3 - 2.69 T^2 + 4.19 \times 10^3 T - 2.94 \times 10^5$
r (kg/m ³)	TRISO particles fuel compact	1650
C_p (kJ/kg. K)		$C_p = 1.4 \times 10^5 - 184.4 T + 9.7 \times 10^{-2} T^2 - 1.8 \times 10^{-5} T^3$
k (kW/m.K)		$K = 8.5 \times 10^3 + 7.68 \times 10^7 / (T + 268)^{0.995}$
ρ (kg/m ³)	Helium	P/RT
C_p (kJ/kg. K)		5.197
k (kW/m.K)		$k = 103.4 + 0.258 T$
μ (Pa.s)		$\mu = 13.07 \times 10^6 + 33.2 \times 10^3 T$

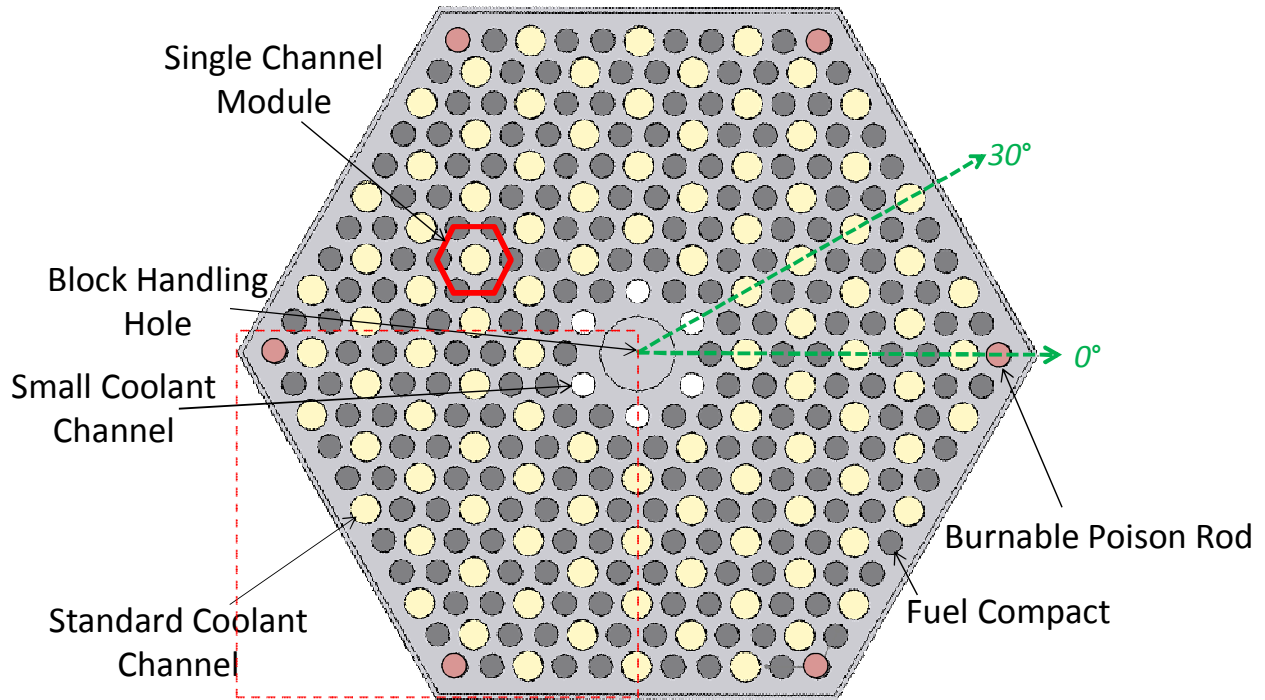
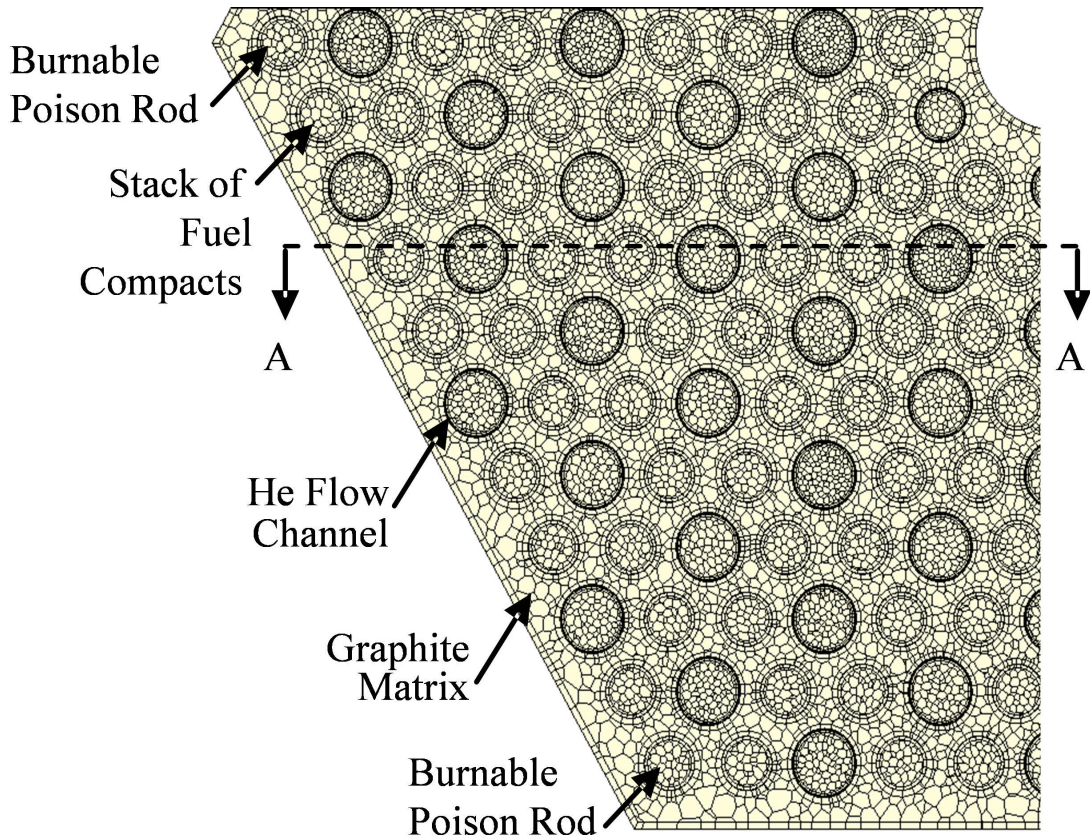


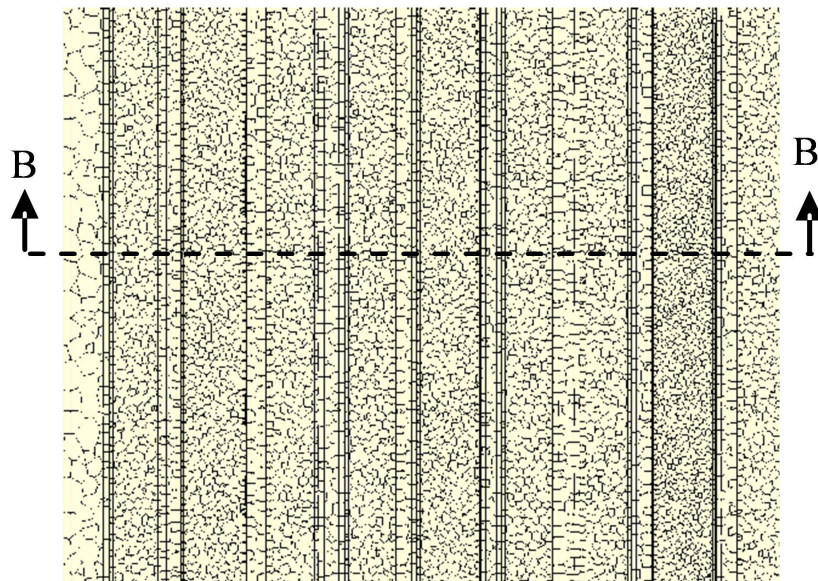
Figure 6.3. Cross-Sectional View of a VHTR Prismatic Fuel Element Showing the Burnable Poison Rods, a Single Flow Channel Model, Fuel Compacts, and Standard and Small Helium Coolant Flow Channels.

6.1 NUMERICAL ANALYSIS

There is symmetry in a prismatic VHTR or HTGR core. Thus, a full core thermal-hydraulics analysis can be carried out using a one-sixth core sector (Fig. 6.2). This approach would reduce the numerical meshing requirements and expedite calculations, without compromising accuracy (Pointer and Thomas, 2010). Even for a 1/6 VHTR core, the thermal-hydraulics analysis using the simplified methodology discussed earlier (Travis and El-Genk, 2013) is a non-trivial task. In such an analysis, considering the helium bypass flow in the interstitial spaces between the vertically stacked hexagonal fuel elements in the core region (Figs. 6.1d and 6.2) changes the inlet characteristics (velocity and temperature) of the helium flow in the coolant channels. Also, simulating the heat transfer between the helium bypass flow in the interstitial space and the solid surfaces of the hexagonal fuel elements markedly increases the number of the numerical mesh elements and the computation time. In addition, incorporating the axial and radial power profiles in the core region requires selecting an appropriate numerical meshing approach to achieve credible results without an overwhelming meshing requirement and a long computation time. The implemented numerical approach in the present analysis is discussed next.



(a) Radial Meshing Grid (Section B - B)



(b) Axial Meshing Grid (Section A - A)

Figure 6.4. Radial and Axial Cross-Sectional Views of Numerical Mesh Grid Used in the Full 3-D Thermal-Hydraulics Analysis of a Prismatic VHTR Fuel Element.

6.1.1 Numerical meshing approach

To determine the effectiveness of the numerical mesh grid for performing a larger scale VHTR core analysis, the results of the thermal-hydraulics analysis using the simplified methodology (Travis and El-Genk, 2013) are compared to those of a full 3-D analysis of a hexagonal fuel element with a 1.2-m long top graphite reflector block. Both fuel element analyses are performed using the same input and operation conditions and computer hardware. The full 3-D thermal-hydraulics analysis of the hexagonal fuel element (Figs. 6.1c and 6.3) employs a total of 43.9 million numerical mesh cells: 31.0 million cells in the flow channels, 5.7 million in the fuel compacts, 5.3 million cells in the graphite, and 1.9 million cells in the axial graphite reflector block. Figures 6.4a and 6.4b show cross-sectional views of the numerical mesh grid implemented in the helium flow channels and the solid graphite as well as in the fuel compacts in a quadrant of a VHTR prismatic fuel element. This quadrant is marked with a dashed-line square in Fig. 6.3. The size of the numerical cells or mesh elements in the graphite of the fuel element increases from 2.0 mm near the interfaces with the helium flow channels to as much as 1.2 cm far from these interfaces. In the helium flow channels, the smallest mesh element size is 1.4 mm, and is 1.6 mm in the cylindrical fuel compacts. The size of the numerical mesh elements increases up to 6.4 mm at the center of fuel compacts (Fig. 6.4b).

To accurately capture the heat flow at the interfaces between the graphite and the helium flow channels, 5 prism layers of numerical mesh elements are used near these interfaces (Fig. 6.4a). The prism layers at the interfaces between the graphite and both the fuel compacts and helium flow channels are appropriate for simulating the perpendicular heat flow at these interfaces (Figs. 6.4a and 6.4b). This meshing approach is implemented into the thermal-hydraulics analysis using the simplified thermal-hydraulics methodology (Travis and El-Genk, 2013), and also in the full 3-D analysis of the hexagonal fuel element (Fig. 6.3). Since the simplified analysis methodology eliminates meshing in the helium flow channels, the number of numerical grid elements used in the hexagonal fuel element is much smaller than for the full 3-D analysis, totaling only 12.9 million mesh elements.

A similar meshing scheme is implemented in the thermal-hydraulics analysis of the prismatic fuel element with bypass helium flow. Figure 6.5 shows the details of the meshing grid used in the bypass flow interstitial space, a corner burnable poison rod, fuel compacts and a slanted flow channel. The width of the interstitial space around the fuel elements is taken as 3 and 5 mm and the obtained results are compared to those without a bypass flow. The comparison quantifies the effects of the bypass flow as well as of the width of the interstitial space on the helium flow distribution in the coolant channels and the calculated temperature field in a prismatic VHTR fuel element. The bypass flow passages and the helium coolant channels share a top plenum region with a constant inlet mass flow rate and constant exit pressure. The prismatic fuel element (Fig. 6.3) is of a “standard” design (i.e. without control rods or reserve shutdown holes but with six burnable poison rods located at the corners). The thermal-hydraulics analysis investigates the effect of the volumetric heat generation rate in the poison rods, particularly when it is assumed the same as in the fuel compacts. In reality, the rate in the corner poison rods is only a fraction of that in the fuel compacts.

The numerical thermal-hydraulics analysis of the prismatic fuel element with a helium bypass flow employs 4.9 million numerical mesh cells in the fuel compacts and the burnable poison rods, 15.8 million cells in the graphite matrix (additional cells are added in the prism layers around the

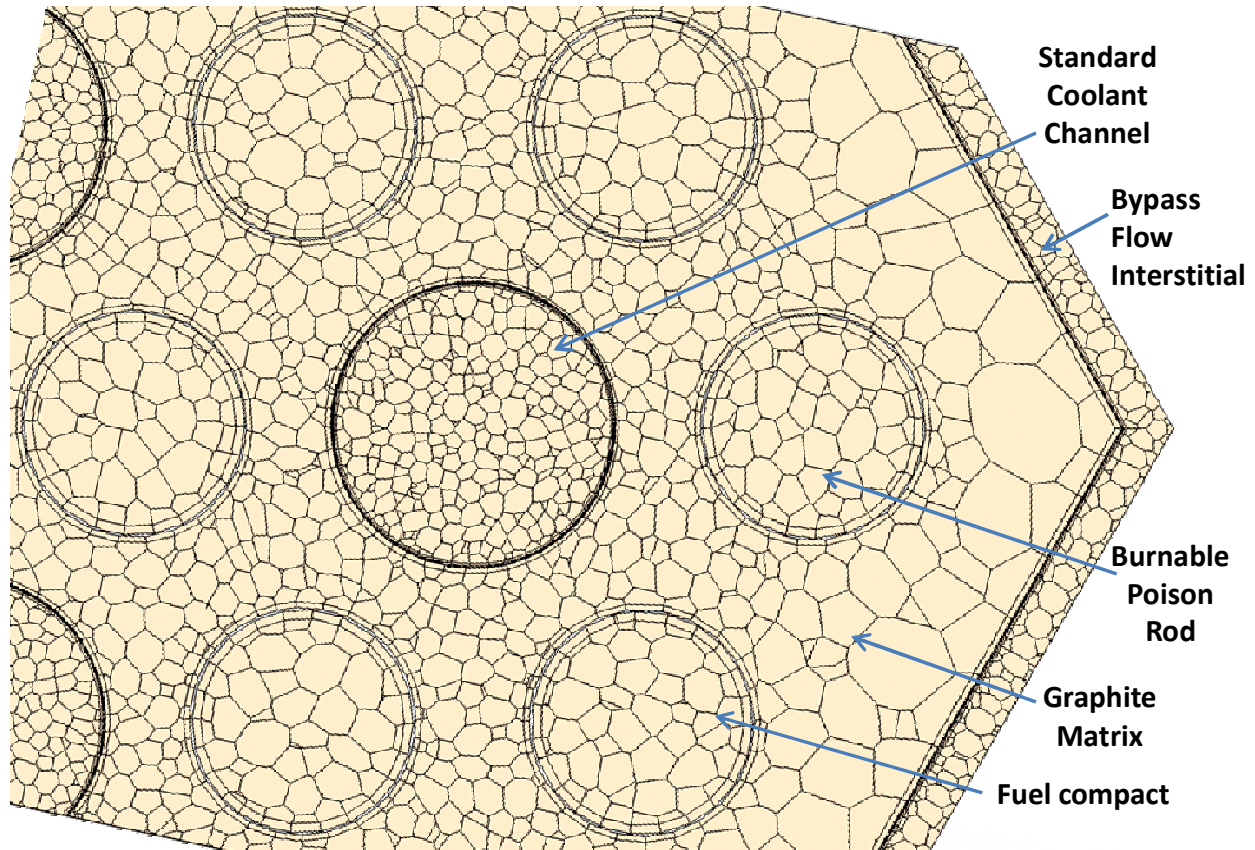


Figure 6.5. A Close-Up of the Implemented Numerical Mesh Grid in a Prismatic VHTR Fuel Element with a Helium Bypass Flow.

edges of the fuel element, the fuel compacts and the coolant channels), 2.3 million cells in the bypass flow region, 30.9 million cells in the helium coolant channels, and 1.4 million cells in the connecting top plenum region. The details of the implemented numerical mesh grid can be seen in Fig. 6.5.

The used numerical meshing approach is particularly important in modeling a prismatic VHTR full height 1/6 core. The VHTR full core is ~ 8 m tall and 10 m in outer diameter including the graphite reflector (Fig. 5.1). Although eliminating the numerical meshing in the coolant channels in the simplified analysis methodology (Travis and El-Genk, 2013) significantly decreases the numerical mesh elements, simplifies the numerical grid and markedly decreases the computational requirements, the simulation task is still extraordinarily large. The 3-D heat conduction in the graphite matrix and the fuel compacts with a few million mesh grid elements or cells is computationally taxing. The present thermal-hydraulics analysis of a VHTR full height 1/6 core uses a fine numerical mesh grid in the radial direction and a relatively coarse mesh grid in the axial direction. This two-dimensional numerical mesh grid is built upward in order to accomplish the meshing task. Although the numerical meshing in the STAR-CCM+ commercial software used to perform the thermal-hydraulics analysis could be preferentially biased toward a coarser numerical

grid in a given coordinate direction, the long computation time due to the larger number of the non-uniform numerical grid mesh elements is still undesirable.

Instead, a thin wafer (~2 cm thick) with a radial cross section identical to that of a full height 1/6 core is meshed. Then the extruder meshing model in the STAR-CCM+ code is employed to generate axial segments of specified lengths. The segment length varies with the refinement of the numerical mesh grid. For the full height 1/6 core thermal-hydraulics analysis, the length of the axial segments ranges from 2.5 to 8 cm. Figure 6.6 shows a cross-sectional view of the numerical mesh grid used in the core fuel elements and near the interfaces between these elements (darker shade) and the inner graphite reflector elements, or assemblies (lighter shade). The performed full height 1/6 core analysis used a relaxed mesh grid in the reflector assemblies (Fig. 6.6). The smallest numerical mesh cells in the reflector near the interfaces with the core fuel elements are 5 mm across, while the larger cells in the reflector elements are 1.5 cm across.

In Fig. 6.6, the numerical mesh grid is refined at the interfaces with the small features in the fuel core elements, such as the helium coolant channels and the fuel compacts. The smallest mesh size in the graphite near small features is 1.2 mm, increasing to 4.8 mm away from the small features. The mesh grid in the graphite bordering the helium coolant channels is comprised of at least one prism layer. The fuel compacts use a similar meshing scheme. Several concentric layers of prism elements are used near the wall of the coolant channels. Thus, when the 3-D heat conduction in the graphite matrix is coupled to the 1-D helium flow in the coolant channels, the calculated inner wall surface temperature and the local heat flux are calculated accurately using the heat transfer coefficient correlation in Equation (6.1).

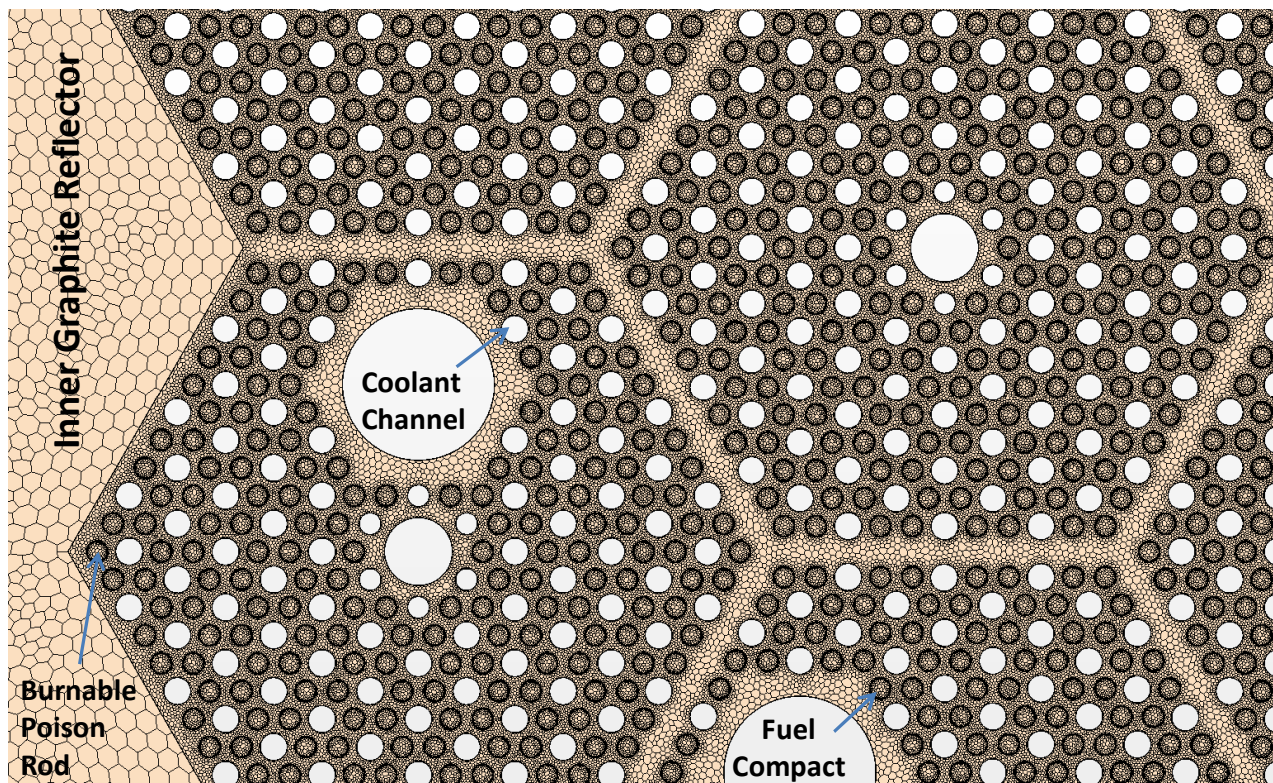


Figure 6.6. Radial Cross-Sectional View of the Numerical Mesh Grid Used in the Thermal-Hydraulics Analysis of a Full Height 1/6 Core.

Table 6.2. Parameters Used in the Thermal-Hydraulics Analysis of a Full Height 1/6 Core.

Parameter	Input Value
Coolant total mass flow rate [kg/s]	330
Volumetric heat generation rate [MW/m ³]	28.4
Coolant inlet temperature [K]	914
Coolant exit temperature [K]	1263
Reactor inlet pressure [MPa]	7.07
Reactor total power [MW _{th}]	600

A limitation to the implemented meshing approach in the full height 1/6 core thermal-hydraulics analysis is that the radial sections are of uniform composition. Thus, the non-contiguous stacks of the fuel compacts in the fuel elements are modeled as contiguous, 8.0 m long compacts. As such, the volumetric heat generation rate in the contiguous fuel compacts is lower than that in the actual shorter compacts in the active core fuel elements, but the total heat generation rate is the same. Besides simplifying the numerical grid, using contiguous fuel compacts insignificantly affect the calculated temperatures.

6.1.2 Material properties

The temperature-dependent material properties in the thermal-hydraulics analyses (Table 6.1) of the prismatic fuel element and of the full height 1/6 core are those of the helium coolant, IG-110 nuclear graphite in the core fuel elements, the TRISO fuel compacts, and the TRISO particles in the compacts. The fuel compacts, including the TRISO particles, are modeled as a homogenous medium for which the effective thermal conductivity is calculated using an expression for dispersed spheres in graphite (Travis and El-Genk, 2013). The TRISO particles in the fuel compacts are assumed to have a packing fraction of 0.28.

6.1.3 Thermal-hydraulics analysis conditions

Once the numerical mesh grid is developed and implemented, performing the thermal-hydraulics analysis is relatively straightforward. The input to the analysis includes the axial and radial power profiles in the reactor core region or the fuel element, and the inlet temperature and mass flow rate of the helium in each coolant channel. These and other input parameters used in the thermal-hydraulics analyses are listed in Table 6.2. These parameters are typical for a prismatic VHTR design (MacDonald et al., 2003; LaBar et al., 2004; Schultz et al., 2004). When assuming no bypass flow through the interstitial gaps or the channels of the reserve shutdown and control rods in the fuel elements, the total helium flow in Table 6.2 corresponds to an average mass flow rate of 0.0306 kg/s per coolant channel (Figs. 6.2, 6.3 and 6.6). The average volumetric heat generation rate in the fuel compacts in that corresponding to a reactor nominal thermal power of 600 MW_{th}. The present thermal-hydraulics analysis of a full height 1/6 core employs a uniform radial power profile and either a uniform or a cosine axial power profile. The full 3-D analyses of the prismatic fuel element and of the full height 1/6 core include a circular plenum above the top axial reflector block. They also use the helium coolant parameters listed in Table 6.2 at the inlet

plenum surface (mass flow and temperature) and assume the same total pressure at the exit of all the coolant channels.

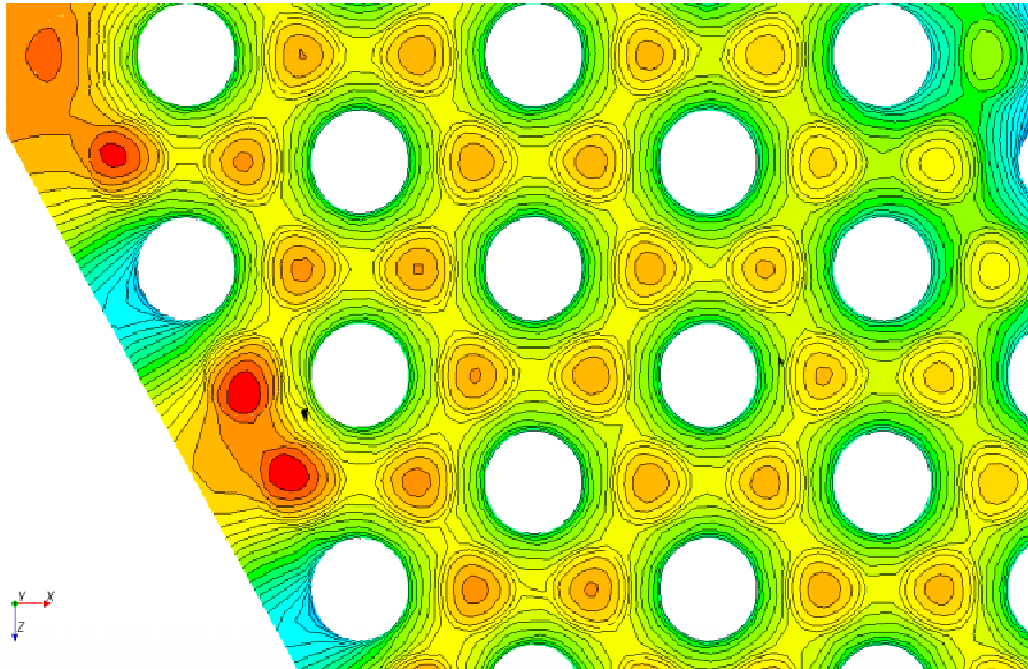
In a prismatic VHTR core fuel element, the majority of the coolant flow channels are 1.5875 cm in diameter, and a few near the center of the core fuel elements have a smaller diameter of 1.27 cm (Fig. 6.3). Thus, since the total pressure drop across the different diameter channels in the core is the same, the coolant mass fluxes in the larger and small diameter channels are different, but proportional to their respective effective cross-section areas. In the present thermal-hydraulics analyses without bypass flow, the helium flow rate in the small diameter channels is 0.0178 kg/s, which is ~ 58% of that in the large channels (0.0306 kg/s). These flow rates are incorporated into the thermal-hydraulics calculations of the prismatic fuel element, using both the simplified methodology and full 3-D analysis.

The helium bypass flow through interstitial gaps reduces the total flow rate and distribution in the coolant channels in the core. The helium flow rates in the coolant channels are a function of the width of the interstitial gap, taken as 5 mm wide in the present analysis. They are determined using a full 3-D simulation of the fuel element with no heat generation. The obtained helium flow rate estimates are then used in the thermal-hydraulics analysis of the prismatic element with a bypass flow. Although the actual helium flow rates in the coolant channels of the fuel element with fission heating could differ slightly, the results should be applicable to assessing the effect of the bypass flow on the temperature distribution within the fuel element. The thermal-hydraulics analysis of the fuel element without bypass flow is conducted using the simplified methodology (Travis and El-Genk, 2013) and the results are compared with those of the full 3-D analysis. The results of the two methods are comparable, while the savings in the computational time and meshing requirements using the former are significant. In the thermal-hydraulics analysis of the prismatic fuel element, with and without bypass flow, the total heat generation is kept constant, but the volumetric heat generation rate in the corner burnable poison rods (Fig. 6.3) is taken equal to 25%, 50% and 100% of that generated in the fuel compact. The purpose is to assess the effect of the heat rate of the poison rods on the intensity and the extent of the resulting hot spots. In reality, the volumetric heat generation rate in the poison rods (fully enriched B₄C) is expected to be ~ 25 – 30% of that of a typical fuel compact.

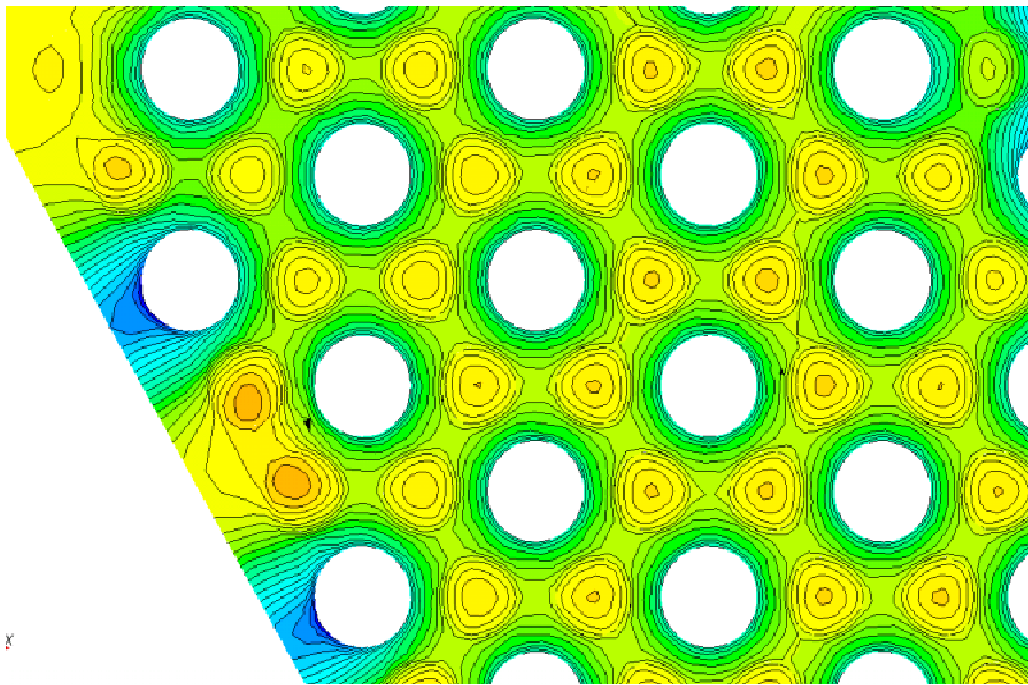
For all the performed numerical thermal-hydraulics analyses, a solution convergence is considered attained when the normalized energy residuals have dropped by at least 3 orders of magnitude and stabilized (stopped decreasing). An additional convergence requirement in the full 3-D thermal-hydraulics analysis is that the normalized residuals of the momentum variables in the coolant flow channels in the three principal coordinates are stabilized. In addition, the residuals of the turbulent dissipation and kinetic energy transport variables must fall by more than 4 orders of magnitude before stabilizing. Upon reaching a solution convergence, the error in the overall energy balance is determined by comparing the total energy input to that removed by the helium flow in the coolant channels, based on the total flow rate and inlet and exit enthalpies. The overall energy balance is typically satisfied to within $\pm 1\%$. The next section presents and discusses the results obtained.

6.2 RESULTS AND DISCUSSION

This section presents the thermal-hydraulics results for a single fuel element (Fig. 6.3) using both the simplified methodology (Travis and El-Genk, 2013) and a full 3-D analysis. The purpose of the calculations without a bypass helium flow is to account for the entrance effect in the heated



(a) Full 3-D Analysis



(b) Simplified Methodology

Figure 6.7. Calculated Temperature Contours in the Fuel Element Without Bypass Helium Flow, 4 cm above Bottom.

coolant channels as well as validate the effectiveness and fidelity of the simplified methodology in reducing the computation time and memory requirements. Also presented in this section are the thermal-hydraulics analysis results using the simplified methodology for a fuel element with helium bypass flow in a 5 mm wide interstitial gap (Fig. 6.5) and for a VHTR full height 1/6 core (Fig. 6.2). The local values of the heat transfer coefficient of the helium gas flow in the coolant channels, including the entrance mixing section ($z/D \leq 25$), are determined using Equation (6.1) based on the calculated inner wall and helium bulk temperatures in the numerical analysis (Travis and El-Genk, 2013). The results presented in this section also include those on the effect of heat generation rate in the corner burnable poison rods of a prismatic fuel element without a helium bypass flow.

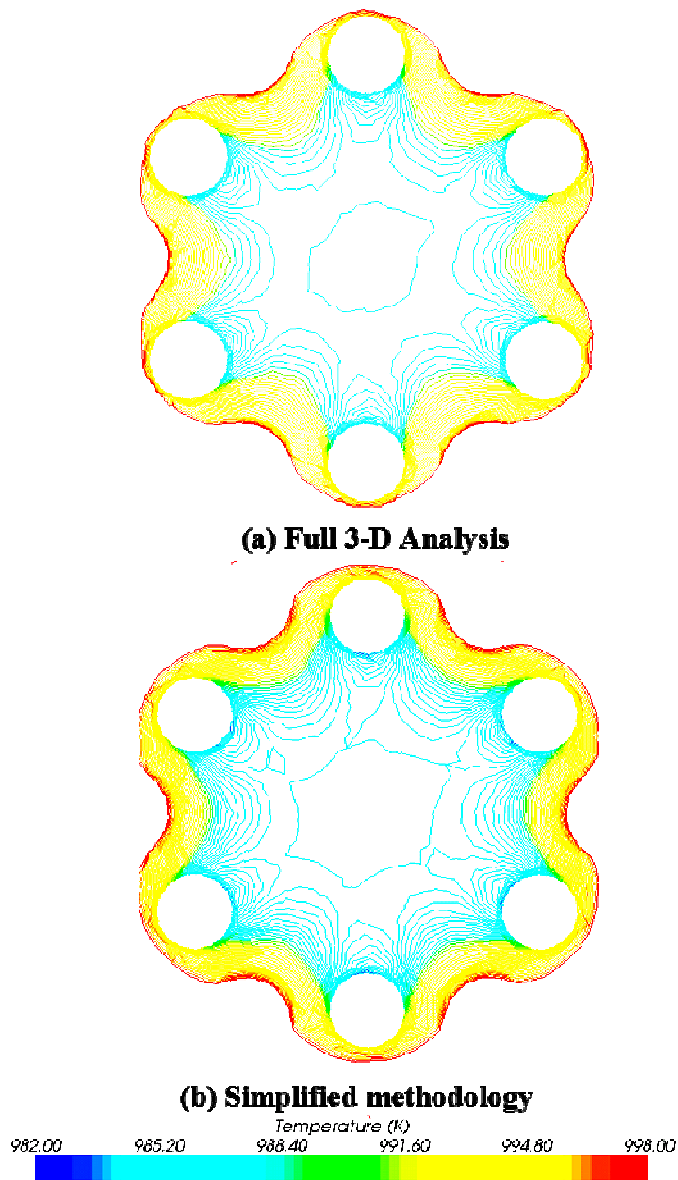


Figure 6.8. Calculated Temperature Contours in the Fuel Element without Bypass Flow, 4 cm above Bottom.

6.2.1 Fuel element analysis without a bypass flow

The thermal-hydraulics analyses of a prismatic fuel element (Fig. 6.3) using both the simplified methodology and a full 3-D numerical simulation are carried out using a node running 64-bit Windows Server 2007 with two, 2.27 GHz quad-core Intel Xeon processors and 48 GB of RAM. A full 3-D run took ~ 100 hours of real time to complete, versus only 3 hours for the simplified methodology, representing more than a 33 fold increase. The calculated temperature fields in the hexagonal fuel element using the full 3-D thermal-hydraulics analysis (Fig. 6.7a) and the simplified methodology (Fig. 6.7b) are similar and the values are within a few degrees. A more pronounced difference of up to 4 K is seen in Figs. 6.8a and 6.8b near the center of the fuel element, where there is a fuel handling hole surrounded by 6 small diameter coolant channels. These channels experience lower flow rates than the standard larger diameter channels in the fuel element. The simplified analysis methodology assumes that the small coolant channels have 57% of the mass flow of the standard channels, thus receiving ~ 5% more flow than in the full 3-D analysis. The calculated temperatures at the center of the fuel element using the simplified methodology are ~ 2 – 4 K lower than those in the full 3-D analysis (Figs. 6.8a and 6.8b).

The fuel element results presented in these figures confirm the effectiveness of the simplified methodology for performing the fuel element thermal-hydraulics analysis, with a little difference in the calculated temperatures, compared to those obtained using a full 3-D analysis. Given that the simplified methodology runs ~ 33 times faster for the single element case, it is used to perform the thermal-hydraulics analysis in the following sections.

6.2.2 Effects of helium bypass flow and heat generation in burnable poison rods

It has been recognized that the helium bypass flow in the interstitial gaps between the prismatic fuel elements of the reactor core is inevitable and should be accounted for in the thermal-hydraulics analysis of a prismatic VHTR or HTGRs. The interstitial gaps are initially present because of the manufacturing tolerance of the prismatic fuel elements, but their width changes during reactor operation because of thermal expansion and graphite swelling by neutron irradiation. Thus, the exact width of the interstitial gaps vary and could be 5 mm or larger. For the same total helium coolant flow rate, the bypass flow cools the edges of the prismatic fuel elements in the core, but effectively decreases the helium flow in the coolant channels, increasing the graphite and fuel compact temperatures in the interior regions of the fuel elements. Thus, the helium flow distribution depends on the width of the bypass flow gap.

With no bypass flow, the helium flow rate in the standard diameter coolant channels is fairly uniform, ranging from 30.1 to 30.7 g/s. This flow rate decreases to 28.3 – 29.3 g/s in a fuel element with a 3-mm wide bypass flow gap, and to 26.8 – 27.4 g/s in a fuel element with a 5-mm wide bypass flow gap. The flow area of a 3-mm wide bypass flow gap represents 5.6% of the total flow area in the fuel element and the helium bypass flow represents 5.5% of the total flow rate. With a 5-mm wide gap, the bypass flow area and rate represent 13% and 11.1% of the total, respectively. These results are obtained from the full 3-D CFD analysis of a prismatic fuel element performed without heat generation. The obtained helium flow split between the 5-mm wide bypass gap and the coolant channels is used in the performed thermal-hydraulics analysis of the fuel element. For simplicity, the helium mass flux in the coolant channels (small and standard) in the fuel element is taken constant, subject to the split in the helium flow rate determined earlier. The total helium flow rate for a prismatic fuel element of 3.24 kg/s is split into 0.36 kg/s in the 5-

mm wide bypass gap and 2.88 kg/s in the coolant channels. The total heat generation in the fuel compact of the element is 616 kW_{th}, corresponding to a nominal reactor power of 600 MW_{th}.

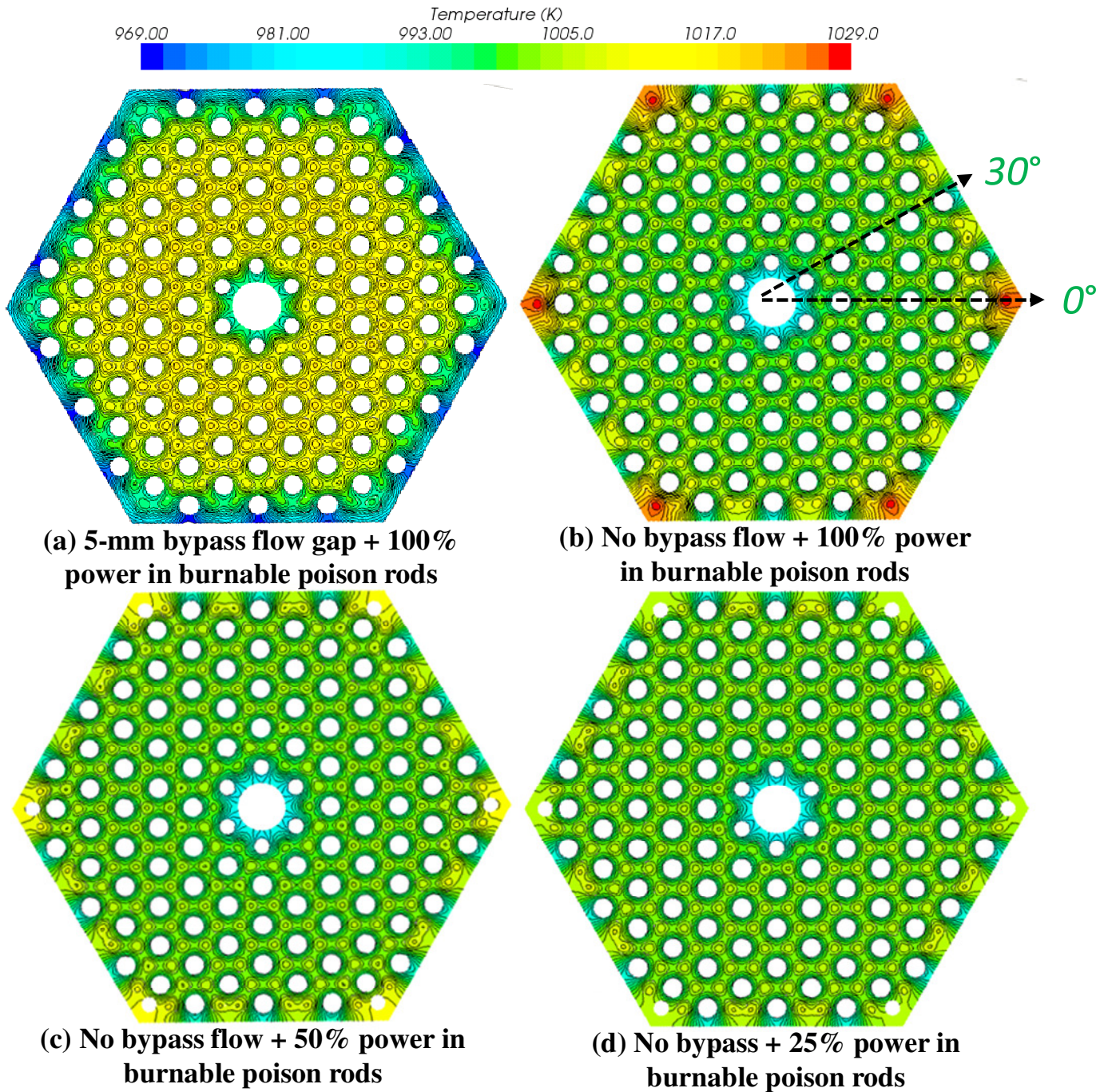


Figure 6.9. Calculated Transverse Temperature Fields, 55 cm from the Top of the Prismatic Fuel Element, with and without Bypass Flow and for Different Heating Rates of the Corner Poison Rods.

The next section presents the results of the thermal-hydraulics analysis of a prismatic VHTR fuel element with and without bypass flow and with different volumetric heating rates of the corner burnable poison rod (Fig. 6.3). The analysis is performed using the simplified methodology (Travis and El-Genk, 2013) involving a full 3-D heat conduction in the graphite and the fuel compacts, a 3-D helium flow in the interstitial bypass flow gaps, and a 1-D helium flow in the coolant channels. The helium coolant flows downward through the interstitial bypass flow gap and the coolant channels and exits through the bottom. The total length of the fuel element is the same as those of the coolant channels and the bypass flow gap (79.3 cm). Due to the symmetry in the bypass flow gap, only half the gap (2.5 mm) is included in the numerical analysis, with an adiabatic boundary at the vertical plane of symmetry. The results of the thermal-hydraulics analysis performed for the conditions listed in Table 6.2 are presented in Figs. 6.9a to 6.9d. Owing to the small height of the fuel compared to that of the full reactor core (7.93 m), the axial thermal power in fuel compacts is assumed uniform and equal to 28.4 MW/m^3 (Table 6.2).

The images of the transverse temperature fields in Figs. 6.9a to 6.9d are taken at an axial location 55 cm from the inlet (or top) of the prismatic fuel element. The results in Fig. 6.9a show that the helium bypass flow has a profound effect on cooling the edges of the fuel element, including the burnable poison rods, but increases the temperature in the rest of the fuel element. This is because the bypass flow (11% of the total) decreases the helium flow in the coolant channels of the fuel element. In the absence of a bypass flow, all the helium flows through the coolant channels in the fuel element.

The heat generation in the corner poison rods produces local hot spots, whose intensity depends on the assumed heat generation rate in these rods (Figs. 6.9b to 6.9d). The local hot spots are clearly evident in Fig. 6.9b, in which the volumetric heat generation rate in the burnable poison rods is assumed the same as that of the fuel compacts. Although unrealistic, it provides a reference case for comparison with the results in Figs. 6.9c and 6.9d. In these figures the volumetric heat generation in the burnable poison rods is 50% and 25% of that in the fuel compacts, respectively. Compared to the results in Fig. 6.9a, with no helium bypass flow and 100% power in the burnable poison rods (Fig. 6.9b), the temperatures are lower in the center but much higher near the edge of the fuel element. Decreasing the heat generation in the corner burnable poison rods to 50% and 25% of that in the fuel compacts changes the temperature in the fuel element by only a few degrees but noticeably decreases the intensity of the corner hot spots (Figs. 6.9c and 6.9d). As indicated earlier, the heat generation in the burnable poison rods during reactor nominal operation is likely to be 25% – 30% of that in the fuel compacts, for which the image in Fig. 6.9d is representative of the average fuel element in a prismatic VHTR core. To further examine the temperature fields in the fuel element with and without helium bypass flow and with different heat generation rates in the burnable poison rods, the calculated temperatures along the 0° and 30° coordinates (Figs. 6.3 and 6.9b) are compared in Figs. 6.10 to 6.12 and 6.13, respectively.

The results in Fig. 6.10 show the effect of the helium bypass flow on the temperature distribution in a fuel element with burnable poison rods generating the same amount of power as the fuel compacts (100%). The helium bypass flow (closed circle symbols) increases the temperatures in most of the fuel element by $\sim 10 - 15 \text{ K}$, while reducing the edge temperatures by as much as $\sim 32 \text{ K}$, as compared to the same simulation with no bypass flow (open circle symbols). With a helium bypass flow, the maximum temperature is 1018 K and occurs near the center of the fuel element. Without a helium bypass flow, however, the temperature is lower in

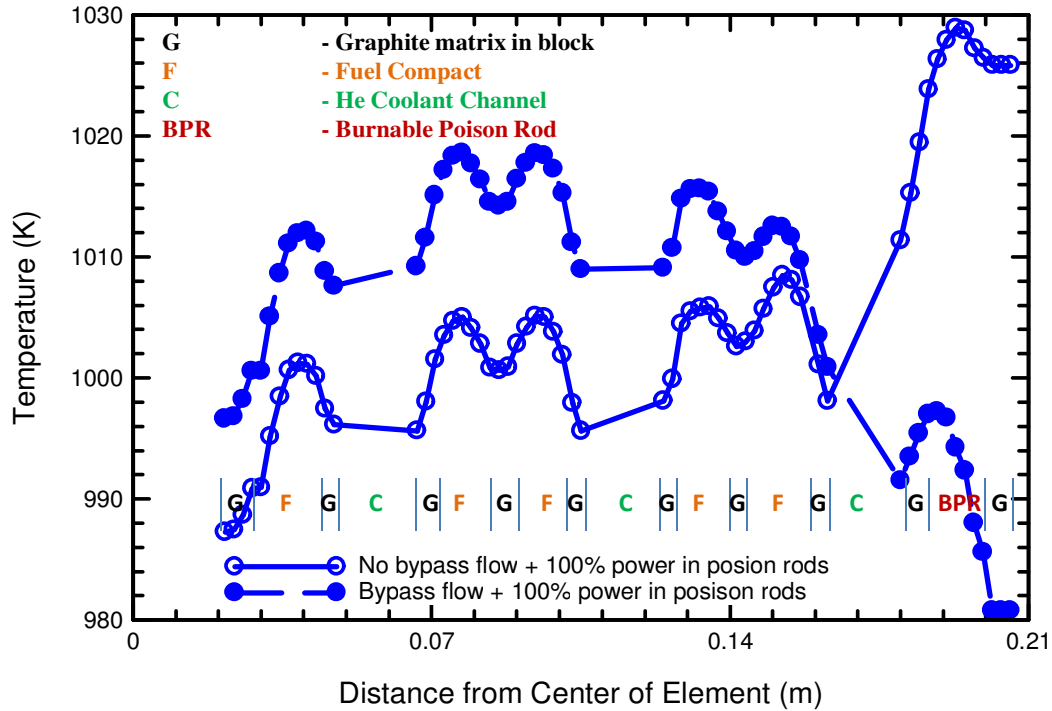


Figure 6.10. Calculated Radial Temperature Distributions along the 0° Coordinate in Fuel Element with 100% Power in Burnable Poison Rods, with and without Bypass Flow (55 cm from Top of Element).

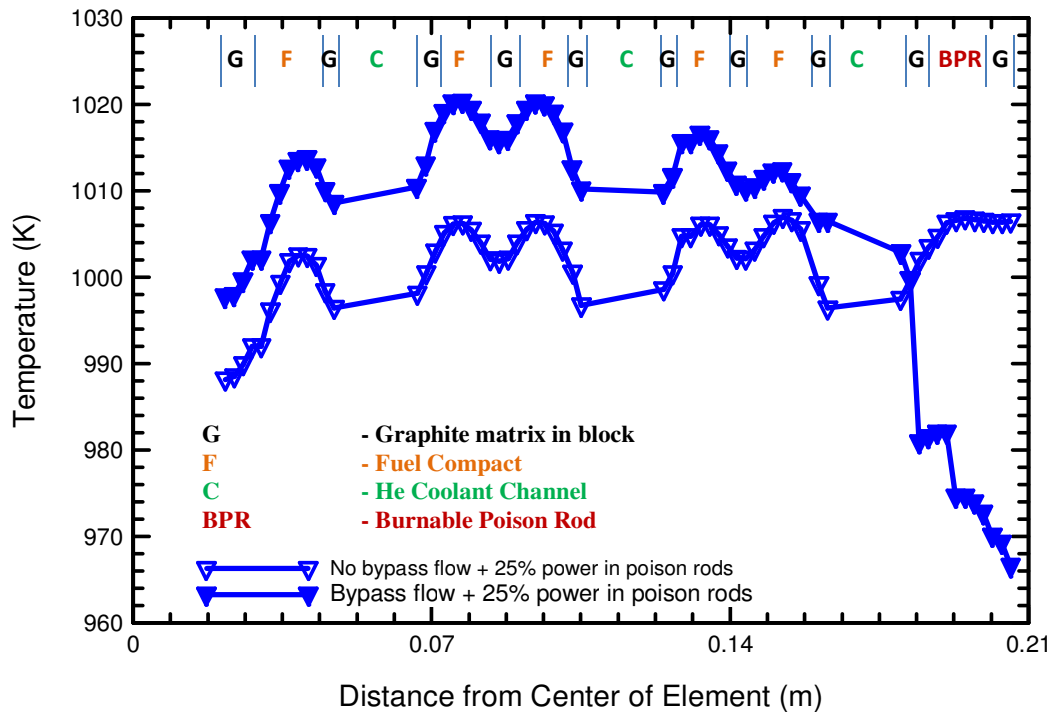


Figure 6.11. Calculated Radial Temperature Distributions along the 0° Coordinate in Fuel Element with 25% Power in Burnable Poison Rods, with and without Bypass Flow (55 cm from Top of Element).

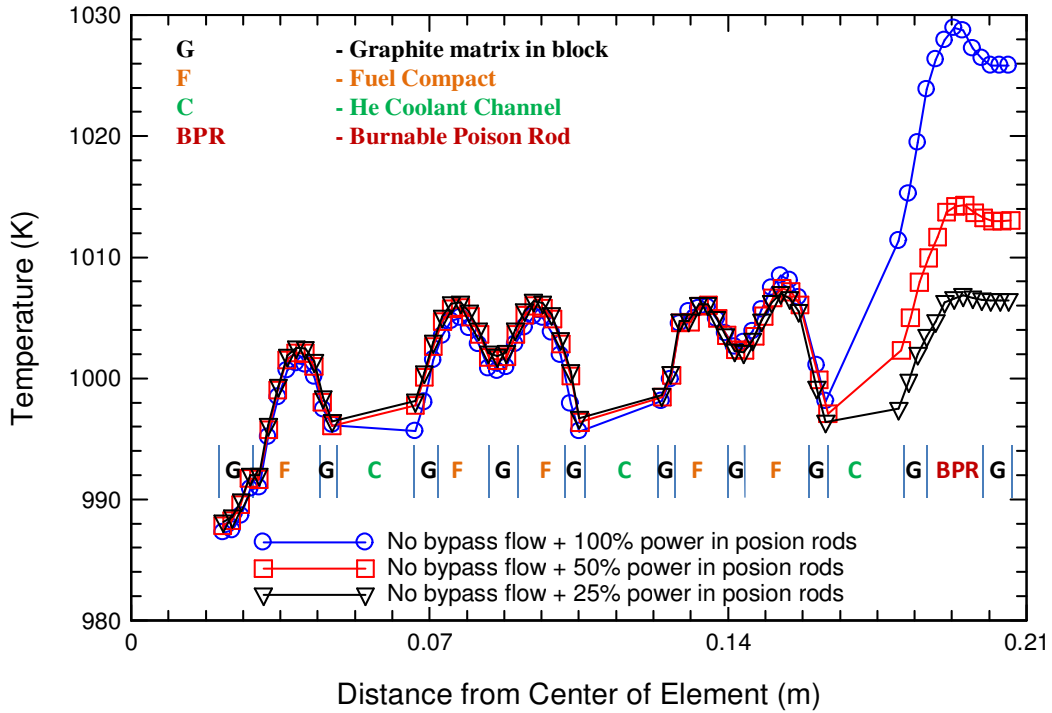


Figure 6.12. Calculated Radial Temperature Distributions along the 0° Coordinate in Fuel Element without Bypass Flow, but Different Powers in the Burnable Poison Rods (55 cm from Top of Element).

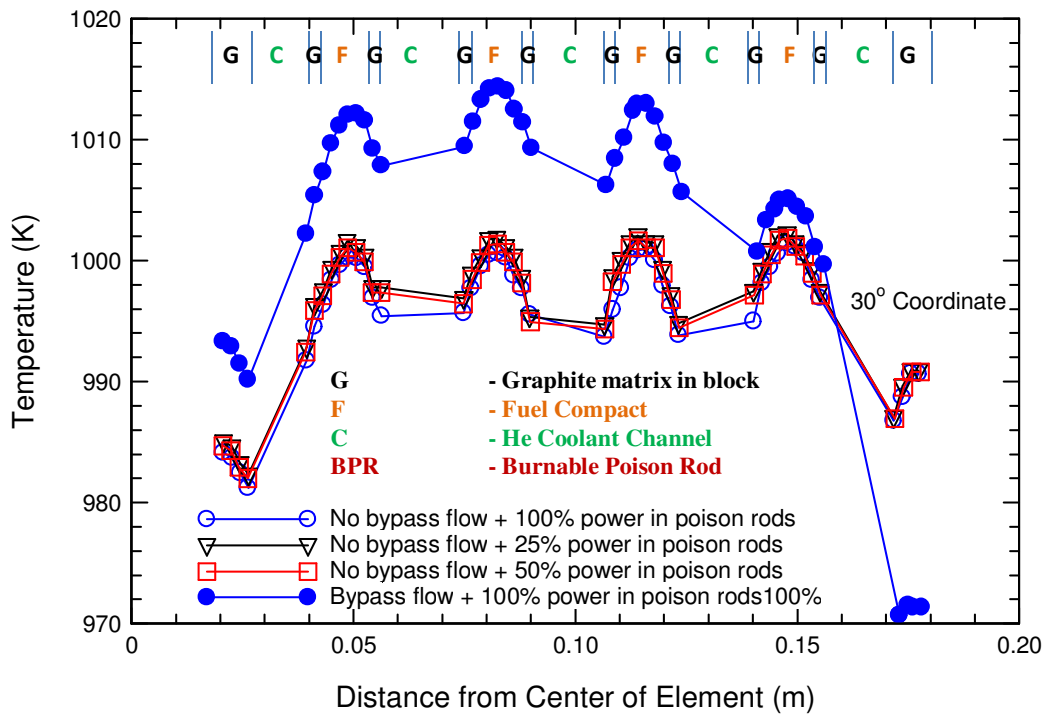


Figure 6.13. Calculated Radial Temperature Distributions along the 30° Coordinate in Fuel Element with and without Bypass Flow and Different Powers in the Burnable Poison Rods (55 cm from Top of Element).

most of the element except at the corner poison rod, where it peaks at 1029 K. In Fig. 6.10, the temperature peaks within the element correspond to the fuel compacts, and the almost flat valleys correspond to the helium coolant channels. The peak temperatures near the edge of the fuel element without a bypass flow correspond to the corner burnable poison rods.

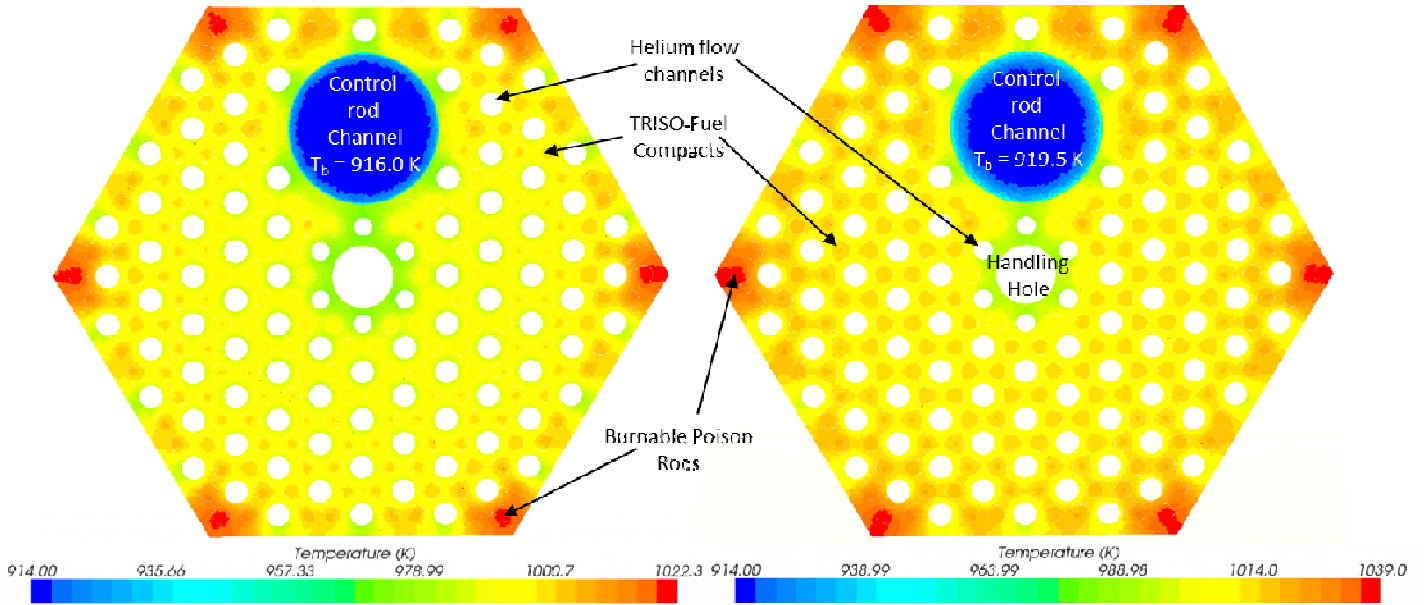
Figure 6.11 shows that reducing the power generation in the corner burnable poison rods (BPRs) to 25% of that in the fuel compact results in a little change in temperatures within the majority of the fuel elements, but noticeably decreases the temperatures of the corner burnable poison rods (BPRs). This decrease in temperature between the cases with and without helium bypass flow in Fig. 6.11 is 31 K, compared to 32 K in Fig. 6.10. The results in Fig. 6.11 show that the maximum temperature near the center of the fuel element with a helium bypass flow is 1021 K and that of the burnable poison rods is 1007 K. The latter is much lower than in Fig. 6.10, due to the lower heat generation in these rods. In general, decreasing the heat generation rate in the BPRs to what would be expected during nominal reactor operation ($\sim 25\% - 30\%$ of that in fuel compacts) insignificantly changes the temperature distribution within most of the fuel element, except those of the BPR and the graphite in its vicinity. This is shown by the results in Fig. 6.12 with no helium bypass flow. Decreasing the generated thermal power in the BPRs from 100% to 50% and 25% of that in the fuel compacts changes the average fuel element temperatures by only 1 – 2 K, but decreases that of the BPRs by 15 K and 22 K, respectively (Fig. 6.12). As indicated earlier, the temperature distributions presented in Figs. 6.10 to 6.12 are along the 0° coordinate in the fuel element. The results in Fig. 6.13, however, are for the 30° coordinate in the fuel element (Figs. 6.3 and 6.9b).

Figure 6.13 shows that the higher temperatures in the central region of the fuel element with helium bypass flow are even more prevalent. Without a bypass flow, these temperatures decrease by 10 – 15 K, while varying the generated power in the BPRs has little effects on the temperature values and distribution in the fuel element. In general, attempting to reduce the interstitial gap and hence, the helium bypass flow is desirable in terms of lowering the temperature and the differential thermal expansion of the fuel elements in a VHTR core. The next section presents the results of the effect of the helium flow through the control rod channel on the temperature in a fuel element without a helium bypass flow.

6.2.2a Effect of bleed helium flow through control rod channel

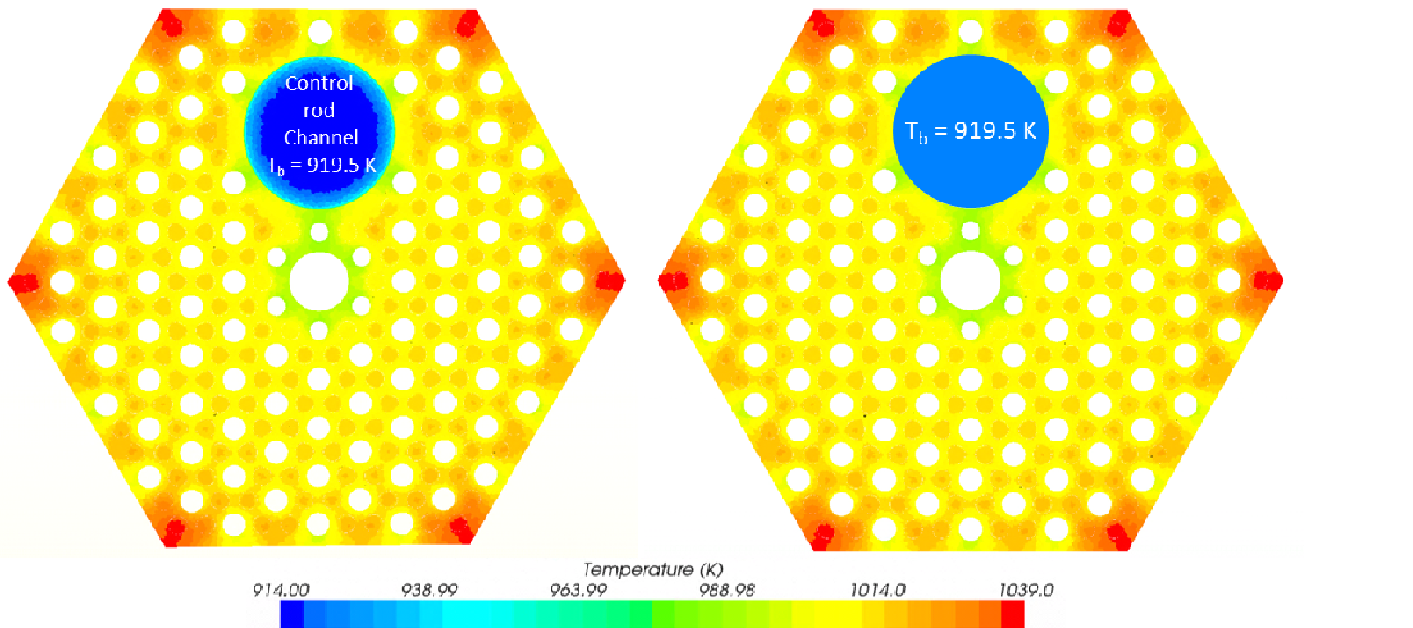
The thermal-hydraulics analysis results in this section are those calculated using both the simplified methodology as well as a full 3-D analysis of a fuel element without interstitial helium bypass flow (Figs. 6.14 and 6.15). The objective is to examine the effectiveness of the simplified methodology in which the flow through the coolant channels as well as the control rod channel is 1-D, but thermally coupled to 3-D conduction in the graphite and fuel compacts of the fuel element. The helium flow rate in the 48 control rod channels in a prismatic core totals 0.20625 kg/s, which is 3% of the total helium flow rate into the reactor, divided equally among the control rod channels. Thus, only 97% of the total helium coolant flows through the coolant channels of the core. The helium flow rate in each of the 1.5875 cm-diameter coolant channels is 0.02968 kg/s.

Figures 6.14a and 6.14b compare the calculated temperature fields in a prismatic fuel element at two axial locations from the entrance (or top); 20 cm and 55 cm, respectively. In these figures, the thermal-hydraulics analysis is performed using a full 3-D numerical simulation of the fuel element with helium flow through the control rod channel and the coolant channels, but no helium



(a) Full 3D CFD in control rod channel at 20 cm into core **(b) Full 3D CFD in control rod channel at 55 cm into core**

Figure 6.14. Calculated Temperatures Using a Full 3-D Analysis of a Prismatic Fuel Element with Helium Coolant Bleed Flow (3% of Total) in the Control Rod Channel (at 20 and 55 cm from Entrance).



(a) Full 3D CFD in control rod channel at 55 cm into core **(b) Simplified methodology in control rod channel at 55 cm into core**

Figure 6.15. Calculated Temperatures Using the Simplified Methodology and a Full 3-D Analysis of a Prismatic Fuel Element with Helium Coolant Flow (3% of Total) in Control Rod Channel (at 55 cm from Entrance).

bypass flow. In these calculations, the volumetric heat generation rate in the corner burnable poison rods is assumed the same as in the fuel compacts and the helium inlet temperature of 914 K is the same as in the coolant and the control rod channels. The axial heat generation in the fuel compact is assumed uniform, since the height of the fuel element is 1/10th of that of a VHTR active core. The results in Figs. 6.14a and 6.14b show the growth of the thermal boundary layer and the increase in the local helium coolant bulk temperature in the control rod channel with axial elevation. These figures also show the calculated temperature contours in the thermal boundary layer. The radial extent of the thermal boundary layer is limited to the region next to the channel wall, but does grow with axial distance as the flow progresses down the channel. Because of the high helium flow rate in the control rod channel, its bulk temperature is significantly lower than that in the surrounding helium coolant channels. At 55 cm from the entrance, the bulk temperature in the control rod channel is 919.5 K (Fig. 6.14b), versus 940.5 K in the coolant channels.

The simplified thermal-hydraulics analysis methodology (Travis and El-Genk, 2013) calculates almost the same temperature distribution in the fuel element, and the same helium local bulk temperatures in the control rod and coolant channels, but provides no details on the growth as well as the temperature gradient in the thermal boundary layer. It significantly reduces the number of the numerical mesh elements for the analysis and the computation time. The results calculated using the simplified methodology are compared with those obtained using a full 3-D analysis (Fig. 6.15b), at 55 cm from the entrance of the coolant channels in the fuel element. Note that Fig. 6.15b is the same as Fig. 6.14b.

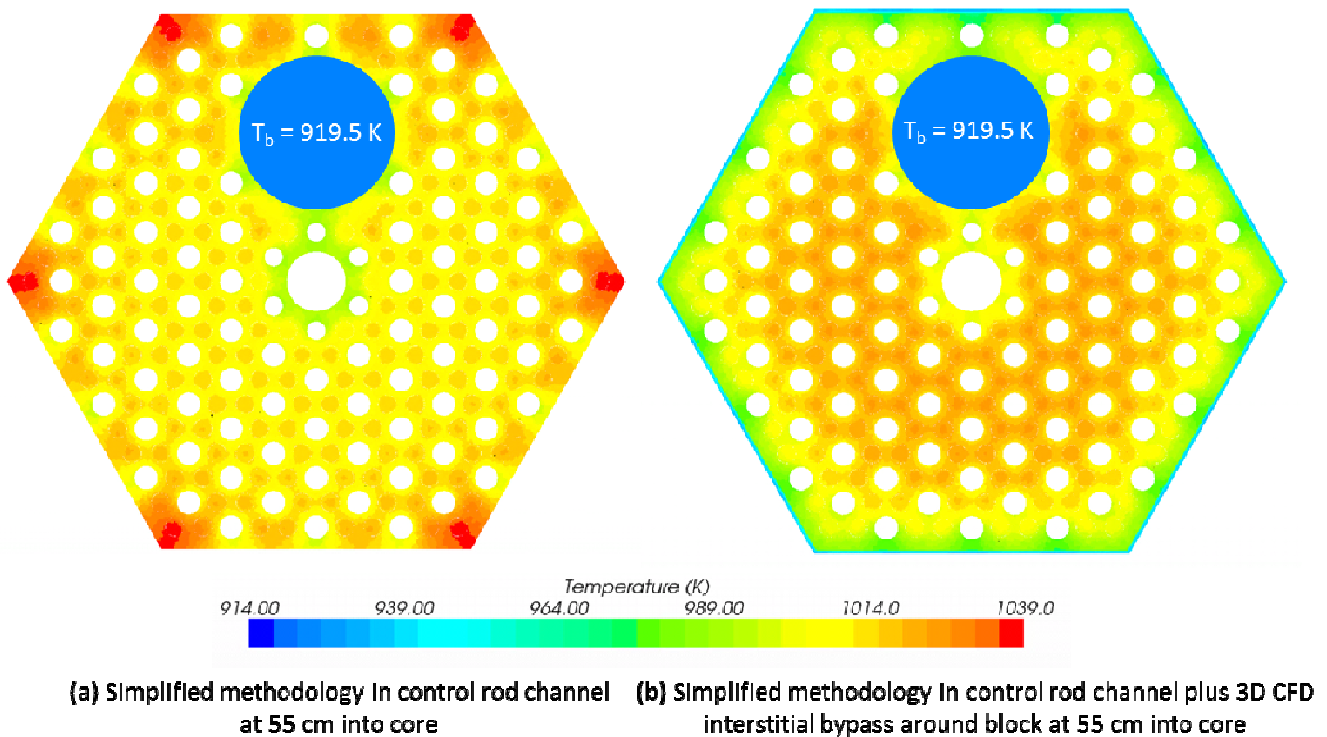


Figure 6.16. Calculated Temperatures Using the Simplified Analysis Methodology of a Prismatic Fuel Element with Helium Flow in the Control Rod Channel and Interstitial Bypass Flow (at 55 cm from Entrance).

In Fig. 6.15a, the helium flow in the control rod and helium coolant channels is simulated as 1-D in conjunction with the forced convection correlations in Equations (6.1) and (6.2). The helium coolant flow in these channels is thermally coupled to the 3-D conduction in the graphite and fuel compacts in the fuel element and exits at the same bulk temperature as that calculated using the full 3-D analysis (928.35 K). Although no meshing is required in the control rod and coolant flow channels when using the simplified methodology, in the full 3-D analysis meshing the control rod channel (Fig. 6.15b) adds approximately 560,000 numerical cells. In addition, the full 3-D simulation runs significantly slower than that with the simplified methodology. A full simulation of the fuel element in Fig. 6.15a using the simplified methodology takes 2.5 hours to complete versus ~ 26 hours using a full 3-D simulation (Fig. 6.15b). However, the calculated temperatures using both simulation methods are almost identical. The largest difference between the calculated maximum temperatures in the fuel element using the two methods is 0.3 K, and the temperature difference between Figs. 6.15a and 6.15b at the center of the element near the control rod channel is 0.12 K. These results further confirm the effectiveness of the simplified methodology for thermal-hydraulics analysis of not only the helium coolant channels but also the control rod channels in a VHTR core. In the next subsection, the simplified methodology is used in the thermal-hydraulics analysis of a prismatic fuel element with helium flow in the control rod channel and helium bypass flow in a 5-mm wide interstitial gap.

6.2.2b Fuel element analysis with helium bypass flow

The results of the combined effect of the interstitial helium bypass flow and the helium flow through the control rod channel are shown Fig. 6.16b at 55 cm from the entrance. Figure 6.16a is the same as Fig. 6.15b with helium flow in the control rod channel, but without a helium bypass flow. In both figures, the heat generation rate in the corner burnable poison rods is the same as that in the fuel compacts. The helium bypass flow cools the edges of the fuel element, including the poison rods, but raises the temperature in most of the central region of the fuel element (Fig. 6.16b).

The peak temperature in the center region of the element in Fig. 6.16b is ~ 1030 K versus 1015 K in Fig. 6.16a without a helium bypass flow. In the latter, the edge temperatures vary from 1005 K – 1018 K and peak at 1039 K in the corner burnable poison rods. The helium bypass flow in Fig. 6.16b cools the edges of the fuel element to 975 K – 980 K and the burnable poison rods to ~ 1003 K. Despite the absence of numerical meshing in the helium coolant and the control rod channels, the 3-D simulation of the helium bypass flow in Fig. 6.16b increases the total number of the numerical mesh cells in the fuel element by as much as 2.75 million cells. This extends the time to complete the calculations to ~ 48 hours, versus only ~ 2 hours in Fig. 6.16a without helium bypass flow.

6.2.3 Thermal-hydraulics analysis of a full height 1/6th core

The performed thermal-hydraulics analysis of a prismatic full height VHTR 1/6 core without a helium bypass flow used the simplified methodology (Travis and El-Genk, 2013) at the conditions listed in Table 6.2, for both uniform and cosine axial power profiles and a uniform radial power profile. This analysis took approximately 72 – 108 hours of real time to complete using two nodes, each with 8 threads, one with 36 GB of RAM and the other 48 GB of RAM. Simulations using the latter ran significantly faster, likely due to a lower reliance on the slower virtual memory.

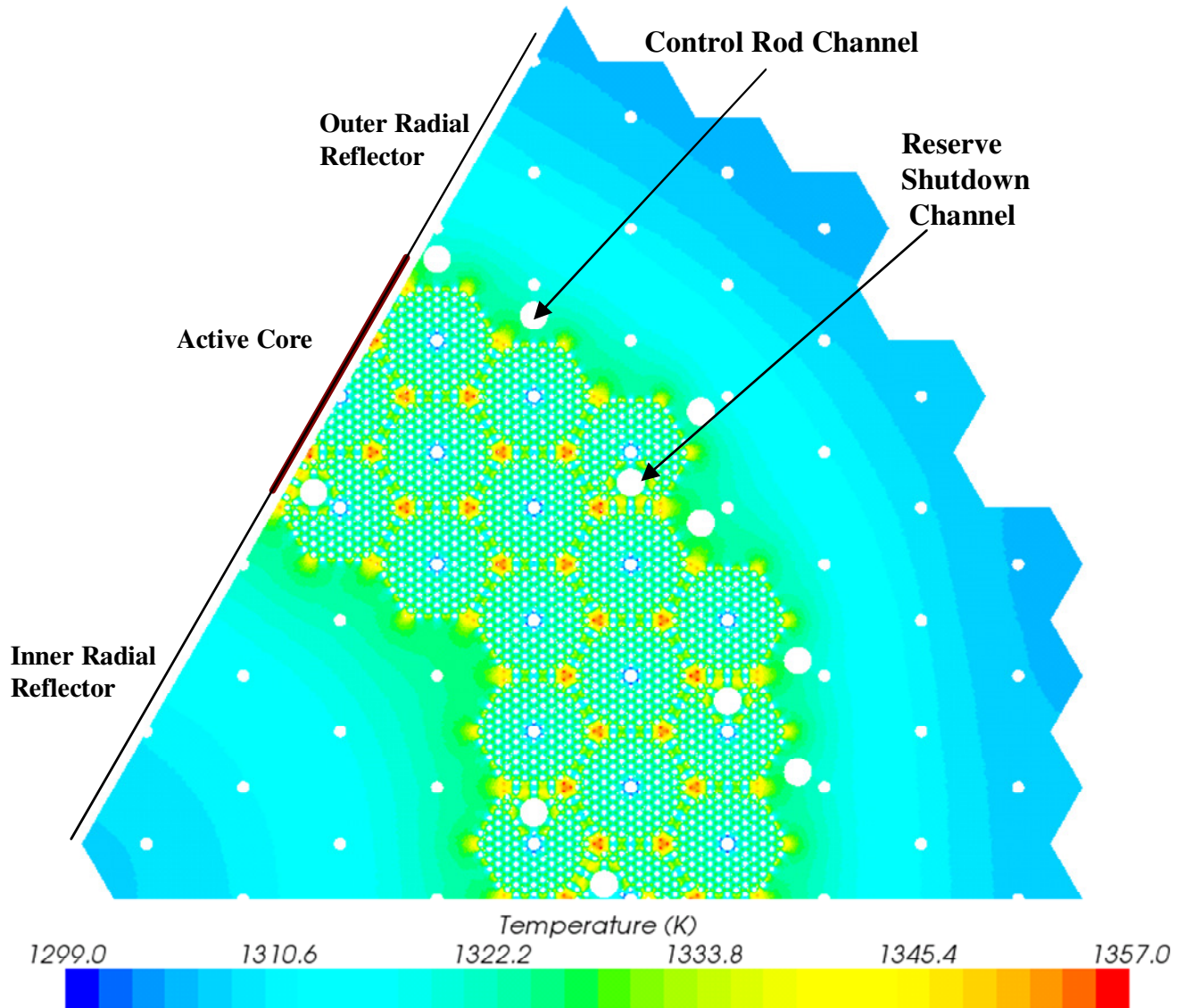
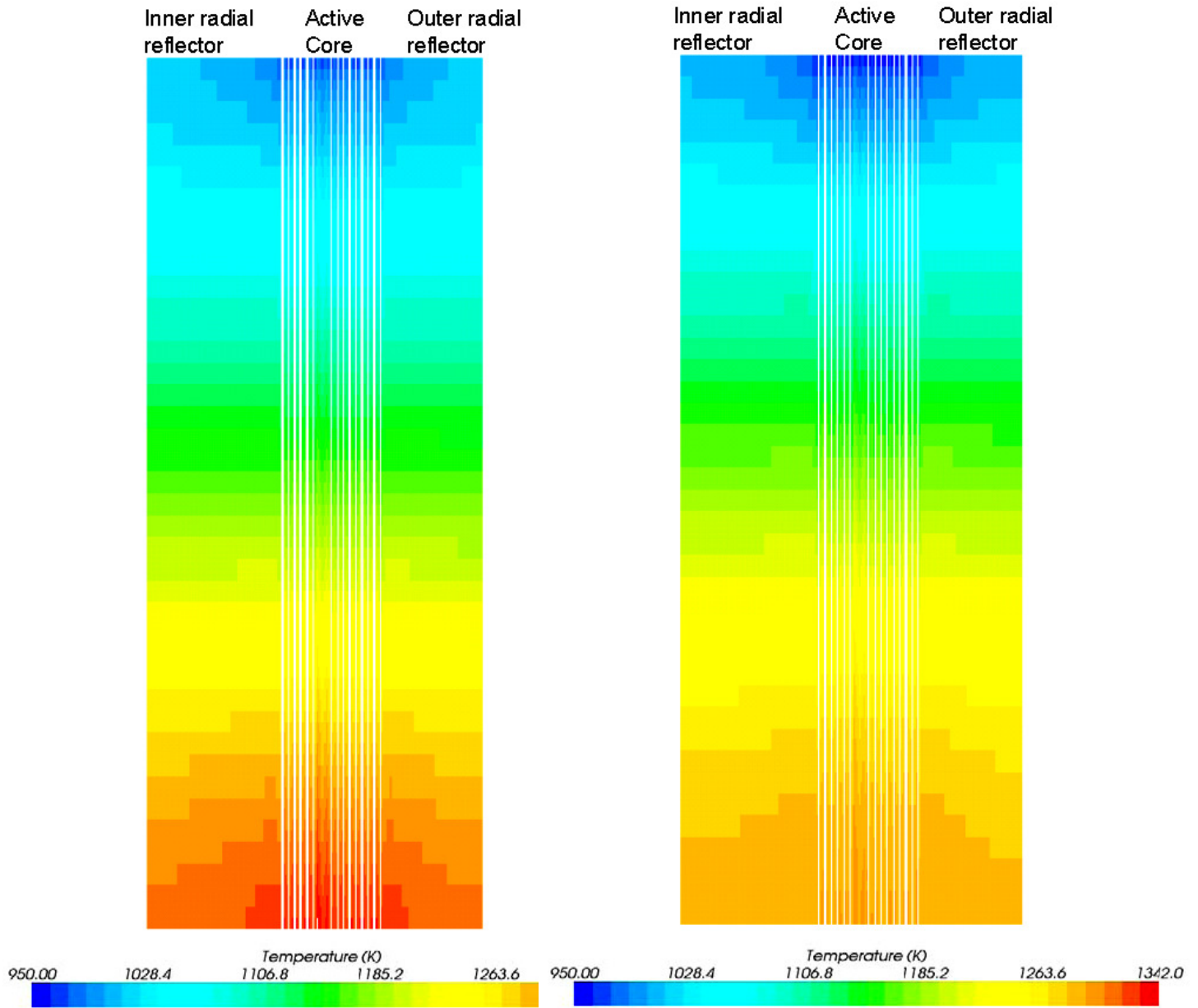


Figure 6.17. Calculated Radial Temperature Field at Mid-Plane in the Thermal-Hydraulics Analysis of a Full Height VHTR 1/6 Core with Constant Volumetric Heat Generation in Fuel Compacts, and No He Bypass Flow.

Similar runs conducted by ANL (Pointer and Thomas, 2010) of a full 3-D thermal-hydraulics analysis of a full height 1/6 core, but with lower helium inlet temperature (784 K) and volumetric heat generation in the fuel compacts of 33.59 MW/m^3 , used 24 cores of a 25.9 teraflop cluster and took over 300 hours of CPU time. These calculations also required an unknown amount of RAM, but in the authors' experience, it would have been an extensive amount.

The performed thermal-hydraulics analysis of the full height 1/6 core, whose results are presented in Figs. 6.17 and 6.18, is for a uniform volumetric heat generation in the fuel compacts, constant helium flow mass flux, but different flow rates in the standard and smaller diameter coolant channels and no bypass helium flow in interstitial gaps or the reserve shutdown and control rod channels (Figs. 6.2 and 6.3). These figures show a relatively uniform temperature in



(a) Uniform Axial Power Distribution

(a) Cosine Axial Power Distribution

Figure 6.18. Calculated Axial Temperature Distributions in the Thermal-Hydraulics Analysis of a Full Height VHTR 1/6 Core with Constant Volumetric Heat Generation and No Helium Bypass Flow.

the active core region, but hotspots at the edges of the fuel elements in the core where the burnable poison control rods are located. This analysis is overly conservative, assuming that the poison rods generate the same amount of thermal power as the fuel compacts. In reality, the hot spots at the burnable poison rods locations in the fuel elements (Fig. 6.9a) would not exist to the same extent, as the heat generated in the poison rods is typically 25% – 30% of that in the fuel

compacts. It is notable that slightly smaller hot spots occur near the reserve shutdown channels in the core because they are not actively cooled in this analysis (Fig. 6.17). The inner and outer reflector hexagonal elements in a prismatic VHTR core (Fig. 6.2) are made of the same graphite as the fuel elements. Thus, the hot spots in the active core are only a concern under non-standard flow conditions. The inevitable helium bypass flow through interstitial gaps is likely to cool the edges of the fuel elements and alleviate these hot spots, at the expense of increasing the temperature in interior regions of the core elements by as much as 30 K.

The presented images of the calculated temperature field in the core in Figs. 6.18a and 6.18b show the axial delineation in the numerical meshing. The two figures are for the same total heat generation in the reactor core ($600 \text{ MW}_{\text{th}}$), but different axial power profiles. With a uniform axial power profile, the hottest temperatures in the core and of the helium coolant are at the exit of the coolant channels (Bottom of Fig. 6.18a). With a cosine axial power profile (Fig. 6.18b) there is a notable effect on the calculated axial temperature profile, compared to that for the uniform axial power profile (Fig. 6.18a). The cosine power profile causes comparatively larger temperatures in the axial middle section of the core, while lowering the temperatures near the exit of the core (Figs. 6.18b).

6.3 SUMMARY

The results presented in this Chapter demonstrate the effectiveness of the simplified methodology for thermal-hydraulics analyses of a hexagonal fuel element with and without a helium flow through the control rod channel and an interstitial helium bypass flow, as well as of a prismatic full height VHTR 1/6 core at nominal operating conditions. The simplified methodology, which uses a 1-D helium flow in the coolant channels and 3-D conduction in the graphite and fuel compacts, is an appropriate surrogate to performing a full 3-D thermal-hydraulics analysis. The 1-D helium flow in the coolant channels is thermally coupled to the 3-D conduction in the graphite using a recently developed turbulent convection heat transfer coefficient correlation (Equation 6.1). The local values of the heat transfer coefficient are determined, including the effect of flow mixing in the entrance section ($z/D \leq 25$) of the 8.0 m long heated section of the coolant channels in the core. In addition to generating comparable results to the full 3-D thermal-hydraulics analysis of the fuel element, the simplified methodology runs much faster due to the relatively modest meshing requirements.

The thermal-hydraulics analyses of a prismatic fuel element using both the simplified methodology and a full 3-D numerical simulation are carried out on a node running 64-bit Windows Server 2007 with two, 2.27 GHz quad-core Intel Xeon processors and 48 GB of RAM. A full 3-D simulation without a helium bypass flow takes ~ 100 hours of real time to complete, versus only 3 hours with the simplified methodology. The calculated temperature fields in the fuel element using the full 3-D thermal-hydraulics analysis and the simplified methodology are similar and the values are within a few degrees (< 4 K). With the simplified methodology no meshing is required in the coolant channels, but instead is limited to the graphite, fuel compacts, bypass flow gap and the control rod channel. The latter increases the numerical mesh grid by more than 560,000 cells. A full thermal-hydraulics analysis of the fuel element with helium flow in the control rod channel using the simplified methodology takes 2.5 hours to complete versus ~ 26 hours using a full 3-D simulation. Because of the high helium flow rate in the control rod channel, its bulk temperature is lower than that in the coolant channels. The largest difference between the calculated maximum temperatures in the fuel element using the simplified methodology and the full 3-D simulation is 0.3 K, and the temperature difference near the control rod channel is 0.12 K.

Results show that the helium bypass flow cools the edges of the fuel element, including the corner burnable poison rods, but raises the temperature in most of the central region of the fuel element. The helium bypass flow has a beneficial effect on the hot spots at the corner burnable poison rods. The intensity of these hot spots dramatically decreases as the volumetric heat generation rate decreases to a level more akin to that expected during nominal reactor operation (~ 25% of that in the fuel compacts). When the volumetric heat generation rate in the corner burnable poison rods is the same as the fuel compacts, the helium bypass flow increases the temperatures in most of the fuel element by ~ 10 – 15 K, while reducing the edge temperatures by as much as ~ 32 K. With a helium bypass flow, the maximum temperature near the center of the fuel element is 1018 K. Without a helium bypass flow, however, the temperature is lower in most of the element except at the corner poison rod, where it peaks at 1029 K. Reducing the power generation in the corner burnable poison rods to 25% of that in the fuel compact results in little change in temperatures within the majority of the fuel elements, but effectively decreases the poison rods temperature. The maximum temperature near the center of the fuel element with a

helium bypass flow is 1021 K and that of the burnable poison rods is 1007 K. Decreasing the generated thermal power in the burnable poison rods from 100% to 25% of that in the fuel compacts increases the average fuel element temperature by only ~ 1 – 2 K, but decreases that of the poison rods by as much as 22 K.

In general, reducing the interstitial bypass flow gap is desirable in terms of lowering the temperature and the differential thermal expansion of the fuel elements in a VHTR core. The results obtained for a prismatic full height VHTR 1/6 core using the simplified methodology, with uniform and cosine axial power profiles are also encouraging. In addition to the significant savings in the computation time and the reduction in the numerical meshing requirement, the results are reasonably accurate, further confirming the effectiveness of the simplified methodology for thermal-hydraulics and safety analyses of prismatic VHTRs or HTGRs.

6.4 NOMENCLATURE

A	Cross-section area of flow channel (m^2)
C_p	Specific heat ($\text{J} / \text{kg.K}$)
D	Coolant channel diameter (m)
k	Thermal conductivity ($\text{W} / \text{m.K}$)
h	Heat transfer coefficient ($\text{W} / \text{m}^2.\text{K}$)
Nu	Nusselt Number, $h D/k$
Pr	Prandtl Number, $\mu C_p/k$
Re	Reynolds Number, $(\dot{m} D / A\mu)$
T	Temperature (K)
T_w	Wall temperature (K)
T_b	Bulk average temperature (K)
z	Axial distance from reactor core entrance (m)

Greek Letters

μ	Dynamic viscosity ($\text{kg} / \text{m.s}$)
ρ	Density (kg / m^3)

Subscripts / Superscripts

b	Helium coolant bulk
w	Flow channel wall surface temperature

7. SUMMARY AND CONCLUSIONS

The gasification of graphite in the core, reflector and support columns in the lower plenum of VHTRs and HTGRs is a primary safety analysis concern in the unlikely event of an air ingress accident. At low and intermediate temperatures, graphite gasification occurs within the open volume pores and its rate increases exponentially with increasing temperature, solely driven by the kinetics of the oxidation chemical reactions. At high temperatures, despite the increase in the chemical oxidation kinetics, the rate of gasification becomes limited by the diffusion of oxygen from the bulk gas mixture through the boundary layer to the external surface of the graphite. Therefore, there was a need to develop and validate a Sherwood number correlation for accurately calculating the oxygen diffusion in the surface boundary layer during the gasification of nuclear graphite at high temperatures.

In Chapter 2 of this report, an extensive database is compiled of 807 experiments measurements of forced-convection heat and mass transfer coefficients at $0.006 \leq Re \leq 2.42 \times 10^5$ and $0.68 < Sc < 2,000$ (Table 2.1), and for gasification of a cylinder of V483T nuclear graphite (300 mm long and 200 mm in diameter) at 1141 to 1393 K in ascending cross-flow of nitrogen gas containing 5 vol. % oxygen at $533 \leq Re \leq 1660$. The developed Sh correlation is within $\pm 8\%$ of the compiled experimental database and the calculated total gasification fluxes based on this correlation are within $\pm 10\%$ of the reported measurements for different size specimens of nuclear graphite grades of NBG-18, NBG-25, IG-11, IG-110, and IG-430.

Results of comparing the predictions of the developed chemical-reactions kinetics model of the gasification rates and transient weight loss for NBG-18 nuclear graphite specimens in experiments by different investigators are presented in Chapter 3. The chemical-reactions kinetics model, which also calculates the production rates of CO and CO₂ gases, employs 4 elementary reactions for the chemisorption of oxygen molecules to form un-dissociated oxygen radicals, the dissociation and adsorption of oxygen radicals to form stable surface complexes, the desorption of stable surface complexes to produce CO gas, and the desorption of CO₂ gas. The model calculations compare favorably with the reported measurements for NBG-18 nuclear graphite specimens at different temperatures in flowing atmospheric air in the experiments. This agreement validates the model and confirms that the chemical-kinetics approach for graphite gasification is more realistic and effective than the empirical approach.

The results of a parametric analysis are presented, which investigated the effects of temperature and oxygen partial pressure on the total gasification rate, the CO and CO₂ production rates, and the transient weight loss of the NBG-18 cylindrical specimens used in the experiments. The obtained continuous Arrhenius curves of the total gasification rate are in good agreement with the reported measurements at different temperatures in gasification modes (a), (b) and (c). At low and intermediate temperatures, graphite gasification is driven by the chemical kinetics of the elementary reactions. At high temperatures graphite gasification shifts to the external surface and is diffusion limited, where the total gasification rate is almost independent of temperature, but increases proportionally to the oxygen partial pressure raised to a power of unity.

The chemical kinetics parameters for the gasification of nuclear graphite grades of IG-110, IG-430, NBG-18 and NBG-25 are obtained based on the reported gasification rate and transient weight loss measurements by various investigators. These parameters for the 4 elementary chemical reactions in the graphite oxidation model include the values and Gaussian distributions

of the specific activation energies and the values of the pre-exponential rate coefficients for the adsorption of oxygen and desorption of CO and CO₂ gases. Results presented in Chapter 4 show that the chemical kinetics parameters and the surface area of free active sites for IG-110 and NBG-25 are similar, but somewhat different from those of NBG-18 and IG-430. The initial specific area of free active sites of the different grades of nuclear graphite decreases inversely proportionally to the square root of the initial graphite mass. Conversely, the initial surface area of free active sites, ASA_o, increases proportionally to the square root of initial mass. However, further work is needed to examine this finding for larger masses of nuclear graphite.

Estimates of the gasification rates are in good agreement to within $\pm 15\%$ of measurements of the total gasification rate. The values of the chemical reactions kinetics parameter are almost independent of the size of the filler particle and strongly depend on the materials of these particles. Nuclear graphite grades with petroleum coke filler particles (IG-110 and NBG-25), regardless of their size (medium or super fine), have similar chemical kinetics parameters, which are different from those of nuclear graphite grades with coal tar pitch coke filler particles (IG-430 and NBG-18).

Chapter 5 presents the results of a transient gasification analysis of NBG-18 nuclear graphite with atmospheric air in a single channel of a VHTR or HTR prismatic fuel assembly. Calculated results for the NBG-18 nuclear graphite, 0.8 m long flow channel include the local rise in graphite temperature, the local and total graphite weight loss and the productions of CO and CO₂ gases and the extent of graphite gasification along the flow channel, as functions of initial temperature of graphite and the initial atmospheric air flow (800 K to 1100 K) and the air inlet Reynolds number (5 to 20). The graphite local weight loss is non-uniform along the flow channel, and significantly higher near the entrance. This non-uniformity is caused primarily by the increase in the local graphite temperature due to the heat released by the exothermic chemical reactions for the productions of CO and CO₂ gases, and by the depletion of oxygen in the bulk gas flow along the channel. Near the flow channel entrance, the oxygen partial pressure in the bulk gas flow sustains graphite gasification. Results demonstrated the fidelity of interfacing the readout tables of graphite gasification with the diffusion and flow model. Results also show that neglecting the heats of formation of CO and CO₂ gases could significantly over estimate the total graphite loss and the transient gasification time. The practical implementation of the readout tables based on the results of the developed chemical-reactions kinetics model into CD-Adapco STAR-CCM+ commercial software is also demonstrated successfully for predicting the local production fluxes of CO and CO₂ gases and the local graphite weight loss.

Results presented in Chapter 6 show that the simplified methodology of a 1-D helium flow in the coolant channels and 3-D conduction in the graphite and fuel compacts is an appropriate surrogate to performing a full 3-D thermal-hydraulics analysis of VHTR or HTR fuel elements and full height cores. A full 3-D analysis of a prismatic fuel element on a node running 64-bit Windows Server 2007 with two, 2.27 GHz quad-core Intel Xeon processors and 48 GB of RAM took ~ 100 hours of real time to complete, versus only 3 hours with the simplified methodology. Calculated temperatures using the full 3-D thermal-hydraulics analysis and the simplified methodology are within a few degrees (< 4 K). The helium bypass flow cools the edges of the fuel element, including the corner burnable poison rods, but raises the temperature in most of the central region. The thermal-hydraulics analysis results of the fuel element with and without bypass flow and of a prismatic full height VHTR 1/6 core confirm the effectiveness of the simplified methodology for future thermal-hydraulics and safety analyses of VHTRs or HTRs.

8. REFERENCES

- Ahmed, S. and M.H. Back (1985), "The Role of the Surface Complex in the Kinetics of the Reaction of Oxygen with Carbon," *Carbon* **23** (5), 513 – 524.
- Ahmed, S., M.H. Back and J.M. Roscoe (1987), "A Kinetic Model for the Low Temperature Oxidation of Carbon," *Combustion and Flame* **70**, 1 – 16.
- Baxi, C. B., E. Perez, A. Shenoy, V. I. Kostin, N. G. Kodochigov, A. V. Vasyaev, S. E. Belov and V. F. Golovko (2006), *Evolution of the Power Conversion Unit Design of the GT-MHR*, Report No. GA-A25381, General Atomics, April 2006.
- Bhatia, S.K. and D.D. Perlmutter (1980), "A Random Pore Model for Fluid-Solid Reactions – I. Isothermal, Kinetic Control," *AIChE J.* **26** (3), 379 – 386.
- Bird, R. B., W. E. Stewart and E. N. Lightfoot (1960), *Transport Phenomena*, John Wiley & Sons, New York, NY, Chapter 16 pp. 495 – 518, and Chapter 18 pp. 554 – 591.
- Campbell, P.A. and R.E. Mitchell (2008), "The Impact of the Distributions of Surface Oxides and their Migration on Characterization of the Heterogeneous Carbon-Oxygen Reaction," *Combustion and Flame* **154**, 47 – 66.
- Chen, S.G., R.T. Yang, F. Kapteijn and J.A. Moulijn (1993), "A New Surface Oxygen Complex on Carbon: Toward a Unified Mechanism for Carbon Gasification Reactions," *Industrial & Engineering Chemistry Research* **32**, 2835 – 2840.
- Chi, A.-H. and G.-C. Kim (2008), "Comparison of the Oxidation Rate and Degree of Graphitization of Selected IG and NBG Nuclear Graphite Grades," *J. Nuclear Materials* **381**, 9–14.
- Collis, D.C. and M.J. Williams (1959), "Two-Dimensional Convection from Heated Wires at Low Reynolds Numbers," *Journal of Fluid Mechanics* **6** (3), 357–384.
- Davis, A.H. (1924), "Convective Cooling of Wires in Streams of Viscous Liquids," *Philosophical Magazine – 6th Series* **47** (282), 1057–1092.
- Du., Z., A.F. Sarofim and J.P. Longwell (1990), "Activation Energy Distribution in Temperature-Programmed Desorption: Modeling and Application to the Soot-Oxygen System," *Energy and Fuels* **4**, 296 – 302.
- Du., Z., A.F. Sarofim, J.P. Longwell and C.A. Mims (1991), "Kinetic Measurement and Modeling of Carbon Oxidation," *Energy and Fuels* **5**, 214 – 221.
- El-Genk, M. S. and J.-M. Tournier (2011), "Development and Validation of a Graphite Oxidation Model," *J. Nuclear Materials* **411**, 193 – 207.

El-Genk, M. S. and J.-M. Tournier (2012a), “Comparison of Oxidation Model Predictions with Gasification Data of IG-110, IG-430 and NBG-25 Nuclear Graphite,” *J. Nuclear Materials* **420**, 141 – 158.

El-Genk, M. S. and J.-M. Tournier (2012b), “Validation of Gasification Model for NBG-18 Nuclear Graphite,” *Nuclear Engineering and Design* **250**, 142 – 155.

El-Genk, M. S. and J.-M. Tournier (2012c), “Comparison of Gasification Kinetics Parameters of Different Types of Nuclear Graphite,” in *Proceedings 2012 International Congress on the Advances in Nuclear Power Plants (ICAPP '12)*, American Nuclear Society, Paper No. 12023, June 24-28, 2012, Chicago, IL, USA.

El-Genk, M. S. and J.-M. Tournier (2012d), “Sherwood Number Correlation for Nuclear Graphite Gasification at High Temperature,” *J. Progress in Nuclear Energy* (in press).

El-Genk, M. S. and J.-M. Tournier (2013), “Transient Gasification of NBG-18 Nuclear Graphite in a VHTR Flow Channel,” submitted August 8, 2012 for consideration for publication in *J. Progress in Nuclear Energy*.

Essenhigh, R.H. (1981), “Fundamentals of Coal Combustion,” in *Chemistry of Coal Utilization*, Second Supplementary Volume, Edited by M. A. Elliott, Chapter 19, pp. 1153 – 1312, John-Wiley & Sons, New York, USA.

Fand, R.M. (1965), “Heat Transfer by Forced Convection from a Cylinder to Water in Crossflow,” *International Journal of Heat and Mass Transfer* **8**, 995–1010.

Fand, R.M. and K.K. Keswani (1972), “A Continuous Correlation Equation for Heat Transfer from Cylinders to Air in Crossflow for Reynolds Numbers from 10^{-2} to 2×10^5 ,” *International Journal of Heat and Mass Transfer* **15**, 559–562.

Froschauer, K., G. Brähler and W. Heit (2008), “Development and Economical Aspects in the Fabrication of HTR Fuel Elements,” *2008 International Congress on Advances in Nuclear Power Plants (ICAPP '08)*, held in Anaheim, CA, June 8-12, 2008, Paper 8097.

Fuller, E.L. and J.M. Okoh (1997), “Kinetics and Mechanisms of the Reaction of Air with Nuclear Grade Graphite IG-110,” *J. Nuclear Materials* **240**, 241–250.

Gandhi, J. M. and S. C. Saxena (1966), “Thermal Conductivity of Multicomponent Mixtures of Inert Gases: Part III – Some Simpler Methods of Computation,” *Indian J. of Pure and Applied Physics* **4**, 461 – 466.

General Atomics (1996), *Gas Turbine-Modular Helium Reactor (GT-MHR) Conceptual Design Description*, Report published July 1996.

Growcock, F.B., J.J. Barry, M. Eto, J.H. III Heiser, C.A. Sastre (1980), *Oxidation-Induced Strength Loss in HTGR Graphites*, in: Advanced Reactor Safety Research Division, Quarterly Progress Report, Jan 1 – March 31, 1980, Brookhaven National Laboratory Report No. BNL-NUREG-51217, Upton NY, 1980, Chapter 1, pp. 4–24.

Hatton, A.P., D.D. James and H.W. Swire (1970), “Combined Forced and Natural Convection with Low-Speed Air Flow over Horizontal Cylinders,” *Journal of Fluid Mechanics* **42**, 17–31.

Haynes, B.S. (2001), “A Turnover Model for Carbon Reactivity – I. Development,” *Combustion and Flame* **126**, 1421 – 1432.

Hilpert, V. R. (1933), „Wärmeabgabe von Geheizten Drähten und Rohren im Luftstrom,“ *Forschung. Gebiete Ingenieurw.* **4** (5), 215 – 224 (in German).

Hinssen, H.-K., K. Kühn, R. Moorman et al. (2008), „Oxidation Experiments and Theoretical Examinations on Graphite Materials Relevant for the PBMR,“ *Nuclear Engineering and Design* **238** (11), 3018 – 3025.

Hirschfelder, J.O., C.F. Curtiss, R.B. Bird (1954), *Molecular Theory of Gases and Liquids*, John Wiley & Sons, New York, NY, 1954, Chapter 8 pp. 514–600, Table I-M pp. 1126–1127.

Hughes, A. and E. Coy (1916), “On the Cooling of Cylinder in a Stream of Air,” *Philosophical Magazine* **31**, 118–130.

Hurt, R.H. and B.S. Haynes (2005), ”Origin of Power-Law Kinetics in Carbon Oxidation,“ *Proceedings of the Combustion Institute* **30**, 2161 – 2168.

IAEA (2001), *Current Status and Future Development of Modular High Temperature Gas Cooled Reactor Technology*, Report No. IAEA-TECDOC-1198, International Atomic Energy Agency, Vienna, Austria, Feb. 2001.

INL (2007), *Next Generation Nuclear Plant Pre-Conceptual Design Report*, Idaho National Laboratory, Idaho Falls, ID, Report No. INL/EXT-07-12967 Revision 1, November 2007.

Kakaç, S., Y. Yener (1995), *Convective Heat Transfer*, second edition, CRC Press, Inc., Ann Arbor, MI, 1995, Chapter 6, pp. 119–185.

Kennelly, A.E. and H.S. Sanborn (1914), “The Influence of Atmospheric Pressure upon the Forced Thermal Convection from Small Electrically Heated Platinum Wires,” *Proceedings of the American Philosophical Society* **53**, 55–77.

Kim, E.S., K.W. Lee and H.C. No (2006), “Analysis of Geometrical Effects on Graphite Oxidation through Measurement of Internal Surface Area,” *Journal of Nuclear Materials* **348**, 174 – 180.

Kim, E.S. and H.C. No (2006), “Experimental Study on the Oxidation of Nuclear Graphite and Development of an Oxidation Model,” *J. Nuclear Materials* **349**, 182–194.

Kim, E. S., H. C. No, B. J. Kim and C. H. Oh (2008), “Estimation of Graphite Density and Mechanical Strength Variation of VHTR during Air-Ingress Accident,” *Nuclear Engineering and Design* **238** (4), 837 – 847.

King, L.V. (1914), “On the Convection of Heat from Small Cylinders in a Stream of Fluid: Determination of the Convection Constants of Small Platinum Wires with Applications to Hot-Wire Anemometry,” *Philosophical Transactions of the Royal Society of London – Series A* **214**, 373–432.

Kiryushin, A.I., Kodochigov, N.G., Kouzavkov, N.G., Ponomarev-Stepnoi, N.N., Gloushov, E.S., Grebennik, V.N. (1997), “Project of the GT-MHR High-Temperature Helium Reactor with Gas Turbine,” *J. Nuclear Engineering and Design* **173**, 119–129.

LaBar, M.P., A.S. Shenoy, W.A. Simon, E.M. Campbell, Y.A. Hassan (2004), “The Gas-Turbine Modular Helium Reactor,” *J. Nuclear Future* **43** (3), 165 – 175.

Laine, N.R., F.J. Vastola, P.L. Walker, Jr. (1963), “The Importance of Active Surface Area in the Carbon-Oxygen Reaction,” *Journal of Physical Chemistry* **67**, 2030 – 2034.

Landolt, H. and R. Börnstein (1962), *Physikalisch-Chemische Tabellen*, Edition 6, volume 2a, Section 2521, “Diffusion in Gasen,” Springer, Berlin, 1962, pp. 516 – 561 (in German).

Lim, H.S. and H.C. No (2006), “GAMMA Multi-Component Mixture Analysis to Predict Air-Ingress Phenomena in an HTGR,” *Nuclear Science and Engineering* **152**, 87–97.

MacDonald, P.E., Sterbentz, J.W., Sant, R.L., Bayless, P.D., Shultz, R.R., Gougar, H.D., Moore, R.L., Ougouag A.M., Terry, W.K. (2003), *NGNP Preliminary Point Design – Results of Initial Neutronics and Thermal-Hydraulic Assessment*, Technical Report No. INEEL/EXT-03-00870 Rev. 1, Idaho National Engineering and Environmental Laboratory, 2003.

MacDonald, P. E., P. D. Bayless, H. D. Gougar, R. L. Moore, A. M. Ougouag, R. L. Sant, J. W. Sterbentz and W. K. Terry (2004), “The Next Generation Nuclear Plant – Insights Gained from the INEEL Point Design Studies,” *2004 International Congress on Advances in Nuclear Power Plants (ICAPP '04), Embedded International Topical Meeting, 2004 American Nuclear Society Annual Meeting*, held in Pittsburgh, PA, June 13-14, 2004, Paper 3405.

Maruyama, S., A. Saikusa, T. Ikoku, K. Kunitomi, S. Shiozawa, K. Ohashi and H. Hayakawa (1995), “Evaluation of Graphite Oxidation during Water Ingress Accidents in HTTR”, in *Response of Fuel, Fuel Elements and Gas Cooled Reactor Cores under Accidental Air or Water Ingress Conditions*, Report No. IAEA-TECDOC-784, pp. 97 – 103, International Atomic Energy Agency, Vienna, Austria.

Mathur, S., P. K. Tondon and S. C. Saxena (1967), “Thermal Conductivity of Binary, Ternary and Quaternary Mixtures of Rare Gases,” *Molecular Physics* **12** (6), 569 – 579.

McAdams, W.H. (1954), *Heat Transmission*, McGraw-Hill Book Company, New York, NY, 1954, Chapter 10, pp. 252–268.

Minh, C.L., C. Li and T.C. Brown (1997), “Kinetics of Coke Combustion during Temperature-Programmed Oxidation of Deactivated Cracking Catalysts,” *Studies in Surface Science and Catalysis* **111**, 383 – 390.

Moulijn, J.A. and F. Kapteijn (1995), “Towards a Unified Theory of Reactions of Carbon with Oxygen-Containing Molecules,” *Carbon*, **33** (3), 1155 – 1165.

No, H. C., H. S. Lim, J. Kim, C.H. Oh, L. Siefken and C. Davis (2007), “Multi-Component Diffusion Analysis and Assessment of GAMMA Code and Improved RELAP5 Code,” *Nuclear Engineering and Design* **237**, 997 – 1008.

Nonal, J.P. (2001), *Graphite in High Temperature Reactors*, Technical Report CEA/DMN/SEMI/LM2E, French CEA.

Ogawa, M. (1987), “Mass Transfer of Mixed Gas Flow Crossing a High Temperature Graphite Cylinder with Chemical Reactions and in-Pore Diffusion,” *Int. J. Heat and Mass Transfer* **30** (5), 1017 – 1026.

Piret, E.L., W. James, M. Stacy (1947), “Heat Transmission from Fine Wires to Water,” *Industrial and Engineering Chemistry* **39** (9), 1098–1103.

Pointer, W.D. and Thomas, J.W. (2010), “Steady-State, Whole-Core Prismatic VHTR Simulation Including Core Bypass,” in *Proceedings ICAPP '10*, American Nuclear Society, San Diego, CA, 2010, Paper No. 10310.

Powell, R.W. (1940), “Further Experiments on the Evaporation of Water from Saturated Surfaces,” *Transactions of the Institution of Chemical Engineers (London)* **18**, 36–50.

Reiher, H. (1925), „Wärmeübergang von strömender luft an rohre und röhrenbündel im kreuzstrom (Heat transmission from flowing hot air to tubes and sets of tubes, in cross current),“ *Forschungsarbeiten auf dem Gebiete des Ingenieurwesens* **269**, 1–85 (in German).

Sato, H., R. Johnson and R. Schultz (2010), “Computational Fluid Dynamic Analysis of Core Bypass Flow Phenomena in a Prismatic VHTR,” *Annals of Nuclear Energy* **37**, 1172 – 1185.

Schultz, R.R., Nigg, D.W., Ougouag, A.M., Terry, W.K., Wolf, J.R., Gougar, H.D., Johnsen, G.W., McEligot, D.M., McCreery, G.E., Johnson, R.W., Sterbentz, J.W., MacDonald, P.E., Temitope, A., Taiwo, Thomas, Y. C., Wei, Won S. Yang, Vilim, R.B., Pointer, W.D., Khalil, H.S. (2004), *Next Generation Nuclear Plant-Design Methods Development and Validation Research*

and Development Program Plan, Technical Report No. INEEL/EXT-04-02293 Rev. 0, Idaho National Engineering and Environmental Laboratory, 2004.

Shampine, L.F., M.W. Reichelt and J.A. Kierzenka (1999), “Solving Index-1 DAEs in MATLAB and Simulink,” *SIAM Review* **41**, 538 – 552.

SIMULINK® 6.1, [retrieved 15 Sept. 2008]. <http://www.mathworks.com/products/simulink>.

STAR-CCM+ v7.04 [retrieved 12 July 2012].
http://www.cd-adapco.com/products/star_ccm_plus/index.html.

Su, J.-L. and D.D. Perlmutter (1985), “Effect of Pore Structure on Char Oxidation Kinetics,” *AIChE Journal* **31** (6), 973 – 981.

Tak, N.I., M.H. Kim and H.S. Lim (2008), “Numerical Investigation of a Heat Transfer within the Prismatic Fuel Assembly of a Very High Temperature Reactor,” *Annals of Nuclear Energy* **35**, 1892 – 1899.

Tak, N.I., M.H. Kim and H.S. Lim (2010), “A Practical Method for Thermal Analysis and Design of Prismatic Fuel Blocks,” in *Proceedings ICAPP '10*, American Nuclear Society, San Diego, CA, 2010, paper No. 10362.

Takeda, T. (2004), “Research and Development on Prevention of Air Ingress during the Primary-Pipe Rupture Accident in the HTTR,” *Nuclear Engineering and Design* **233**, 197 – 209.

Taylor, M.F. (1967), *Correlation of Local Heat-Transfer Coefficients for Single-Phase Turbulent Flow of Hydrogen in Tubes with Temperature Ratios to 23*, Technical Report No. TN D-4332, NASA Lewis Research Center, Cleveland Ohio, 1967.

Travis, B.W. and El-Genk, M.S. (2013), “Numerical Simulation and Turbulent Convection Heat Transfer Correlation for Coolant Channels in a VHTR,” *J. Heat Transfer Engineering* **34** (1), 1 – 14.

Vogtländer, P.H. and C.A.P. Bakker (1963), “An Experimental Study of Mass Transfer from a Liquid Flow to Wires and Gauges,” *Chemical Engineering Science* **18**, 583–589.

Vreeling, J.A., O. Wouters and J.G. van der Laan (2008), “Graphite Irradiation Testing for HTR Technology at the High Flux Reactor in Petten,” *J. Nuclear Materials* **381**, 68 – 75.

Walker, P.L., Jr., F. Rusinko, Jr. and L.G. Austin (1959), “Gas Reactions of Carbon,” *Advances in Catalysis* **11**, 133 – 221.

Xiaowei, L., R. Jean-Charles and Y. Suyuan (2004), “Effect of Temperature on Graphite Oxidation Behavior,” *Nuclear Engineering and Design* **227**, 273 – 280.

Xiaowei, L., R. Jean-Charles, Y. Suyuan (2005), “Comparison of Oxidation Behaviors of Different Grades of Nuclear Graphite,” *J. Nuclear Science and Engineering* **151**, 121–127.

Yu, X., L. Brissonneau, C. Bourdeloie and S. Yu (2008), “The Modeling of Graphite Oxidation Behavior for HTGR Fuel Coolant Channels under Normal Operating Conditions,” *Nuclear Engineering and Design* **238** (9), 2230 – 2238.

Zhang, Z. and S. Yu (2002), “Future HTGR Developments in China after the Criticality of the HTR-10,” *Nuclear Engineering and Design* **218**, 249–257.

Zhuang, Q., T. Kyotani and A. Tomita (1995), “Dynamics of Surface Oxygen Complexes during Carbon Gasification with Oxygen,” *Energy Fuels* **9**, 630 – 634.

APPENDIX A – PUBLICATIONS BASED ON COMPLETED RESEARCH

A-1. REFEREED JOURNAL PAPERS

El-Genk, M. S. and J-M. Tournier (2011), “Development and Validation of a Model for the Chemical Kinetics of Graphite Oxidation,” *J. Nuclear Materials*, **411**, 193 – 207.

El-Genk, M. S. and J-M. Tournier (2012a), “Comparison of Oxidation Model Predictions with Gasification Data of IG-110, IG-430 and NBG-25 Nuclear Graphite,” *J. Nuclear Materials*, **420**, 141 – 158.

El-Genk, M. S. and J-M. Tournier (2012b), “Validation of an Oxidation Model for NBG-18 Nuclear Graphite,” *J. Nuclear Engineering and Design*, **250**, 142 – 155.

El-Genk, M. S. and J-M. Tournier (2013), “Sherwood Number Correlation for Nuclear Graphite Gasification at high Temperatures,” *J. Progress in Nuclear Energy*, **62**, 26 – 36.

Travis, B. W. and M. S. El-Genk (2013), “Numerical Simulation and Turbulent Convection Heat Transfer Correlation for Coolant Channels in a Very-High-temperature Reactor,” *J. Heat Transfer Engineering*, **34** (1), 1 – 14.

Travis, B. W. and M. S. El-Genk, “Thermal-Hydraulics Analyses of 1/6 Prismatic VHTR Core and Fuel Element with and without Bypass Flow,” *J. Energy Conversion and Management* (Submitted for Review 13 Sept. 2012).

El-Genk, M. S. and J.-M. Tournier, “Transient Gasification of NBG-18 Nuclear Graphite in a Prismatic VHTR Flow Channel,” *J. Progress in Nuclear Energy* (Submitted for Review 7 August 2012).

El-Genk, M. S. and J-M. Tournier, “Chemical Kinetics Parameters of Nuclear Graphite Gasification,” *Int. J. Nuclear Energy Science and Technology* (in press 2012).

A-2. REFEREED CONFERENCE PROCEEDINGS PAPERS

El-Genk, M. S. and J-M. Tournier (2010), “On Modes and Kinetics of Nuclear Graphite Oxidation in Massive Air or Steam Ingress,” *Proceedings 10th International Congress on Advances in Nuclear Power Plants (ICAPP’10)*, paper No. 10159, 13 – 17 June 2010, San Diego, CA.

El-Genk, M. S. and J-M. Tournier (2012c), “Diffusion Velocity Correlation for Nuclear Graphite Gasification at High Temperatures and Low Reynolds Numbers” *Proceedings of 12th International Congress on Advances in Nuclear Power Plants (ICAPP’12)*, paper No. **12022**, Chicago, 24 – 28 June 2012.

El-Genk, M. S. and J.-M. Tournier (2012d), “Comparison of Gasification Kinetics Parameters of Different Types of Nuclear Graphite” *Proceedings of 12th International Congress on Advances in Nuclear Power Plants (ICAPP’12)*, paper No. **12023**, Chicago, 24 – 28 June 2012.

Travis, B. W. and M. S. El-Genk (2012), “An Effective Thermal-Hydraulics Methodology for Prismatic Core HTGR and VHTR,” *Proceedings of 12th International Congress on Advances in Nuclear Power Plants (ICAPP’12)*, paper No. **12061**, Chicago, 24 – 28 June 2012.

A-3. CONFERENCE PROCEEDINGS PAPERS

Travis, B. W. and M. S. El-Genk (2011), “A Heat Transfer Correlation for Flow Channels in a Prismatic Core VHTR,” *Proceedings 15th International Conference on Emerging Nuclear Energy Systems (ICENES-2011)*, San Francisco, CA, 15 – 19 May 2011.

A-4. TECHNICAL REPORTS

El-Genk, M. S. and J-M. Tournier (2010b), *Graphite Oxidation Simulation in HTR Accident Conditions: Development of a Graphite Oxidation Kinetics Model*, **1st Year Technical Report No. UNM-ISNPS-1-2010**, Institute for Space and Nuclear Power Studies, University of New Mexico, **October 2010**.

El-Genk, M. S., J-M. Tournier and B. W. Travis (2011), *Comparison of Oxidation Model with Gasification Data of IG-110, IG-430, and NBG-25 Nuclear Graphite, and Numerical Simulation of Turbulent Convection Heat Transfer in Coolant Channels of a VHTR*, **2nd Year Technical Report No. UNM-ISNPS-1-2011**, Institute for Space and Nuclear Power Studies, University of New Mexico, **October 2011**.

El-Genk, M. S., J-M. Tournier and B. W. Travis (2012), *Graphite Oxidation Simulation in HTR Accident Conditions – 3rd Year and Final Technical Report*, **3rd Year and Final Technical Report No. UNM-ISNPS-1-2012**, Institute for Space and Nuclear Power Studies, University of New Mexico, **October 2012**.